A PRECISION MEASUREMENT OF THE W BOSON MASS WITH 1 FB^{-1} OF DØ RUN IIA DATA

A Dissertation

Submitted to the Graduate School
of the University of Notre Dame
in Partial Fulfillment of the Requirements
for the Degree of

Doctor of Philosophy

by

Jyotsna Osta

Michael D. Hildreth, Director

Graduate Program in Physics
Notre Dame, Indiana

December 2009

© Copyright by

Jyotsna Osta

2009

All Rights Reserved

A PRECISION MEASUREMENT OF THE W BOSON MASS WITH 1 FB^{-1} OF DØ RUN IIA DATA

Abstract

by

Jyotsna Osta

This thesis is a detailed presentation of a precision measurement of the mass of the W boson. It has been obtained by analyzing $W \rightarrow e\nu$ decays. The data used for this analysis was collected from 2002 to 2006 with the DØ detector, during Run IIa of the Fermilab Tevatron collider. It corresponds to a total integrated luminosity of 1 fb^{-1}. With a sample of 499,830 $W \rightarrow e\nu$ candidate events, we obtain a mass measurement of M_W=80.401 $\pm$ 0.043 GeV. This is the most precise measurement from a single experiment to date.

Dedicated to my family, teachers and friends

I am because they are

The woods are lovely, dark and deep,

But I have promises to keep,

And miles to go before I sleep,

And miles to go before I sleep.

- *"Stopping By Woods on a Snowy Evening"* by Robert Frost

Contents

List of Figures ix

List of Tables xv

Chapter 1: An Introduction to Particle Physics 1
- 1.1 A Brief Introduction 1
- 1.2 A Timeline of the History of Particle Physics 2
  - 1.2.1 Classification of Particles - Fermions and Bosons 2
  - 1.2.2 The Beginning of the End of the Classical Era 3
  - 1.2.3 Discovering the Photon 4
  - 1.2.4 Discovering the Meson 4
  - 1.2.5 Discovering the Antiparticles 5
  - 1.2.6 Advent of the Neutrino 6
  - 1.2.7 Hadrons and the Concept of Strangeness 8
  - 1.2.8 The Particle Zoo - ca. 1960 9
  - 1.2.9 A Model for the Quarks 10
  - 1.2.10 Discovering the Charm Quark 11
  - 1.2.11 Discovering the Bottom and Top Quarks 11
- 1.3 Interactions and Fields in Particle Physics 12
  - 1.3.1 Electromagnetic Interactions 13
  - 1.3.2 Gravitational Interactions 14
  - 1.3.3 Weak Interactions 14
  - 1.3.4 Strong Interactions 16
- 1.4 The Standard Model 16
- 1.5 The W and Z Bosons in the Standard Model 19
- 1.6 Motivation for a Precise Measurement 21
- 1.7 Past Measurements of M_W 23

Chapter 2: The Theory of Electroweak Interactions 27
- 2.1 A Brief Introduction 27
- 2.2 Early Attempts at Unification 28

2.3 Gauge Invariance 29
2.4 Non-Abelian Gauge Theory 31
2.5 The Electroweak Standard Model - Weinberg-Salam SU(2)×U(1) Model 32
2.6 Spontaneous Symmetry Breaking and the Higgs Mechanism . . . 37
2.7 Parameterizing the Standard Model 42
2.7.1 Tree Level Value of W Mass 44
2.7.2 Higher Order Contributions to W Mass 45

Chapter 3: W/Z Boson Production and Decay 48
3.1 A Brief Introduction 48
3.2 Vector Boson Production 49
3.3 Determination and Use of the Parton Distribution Functions . . . 53
3.4 Transverse Momentum of the Gauge Bosons 54
3.5 Vector Boson Decay 58

Chapter 4: The Experimental Apparatus 61
4.1 A Brief Introduction 61
4.2 Fermilab's Accelerator Chain 62
4.2.1 The Cockcroft-Walton Generator 63
4.2.2 The Linear Accelerator (LINAC) 63
4.2.3 The Booster 64
4.2.4 The Main Injector 64
4.2.5 The Antiproton Source 65
4.2.6 The Recycler 67
4.2.7 The Tevatron 67
4.3 The DØ Detector 70
4.3.1 Calorimeter Coordinates 73
4.3.2 The Silicon Microstrip Tracker (SMT) 74
4.3.3 The Central Fiber Tracker (CFT) 78
4.3.4 The Solenoid 83
4.3.5 The Preshower Detectors 84
4.3.5.1 The Central Preshower (CPS) Detectors 85
4.3.5.2 The Forward Preshower (FPS) Detectors 85
4.3.6 The Calorimeter 88
4.3.7 The Inter-Cryostat Detector 94
4.3.8 Muon Detectors 95
4.3.9 Luminosity Monitor (LM) 99
4.4 The Trigger System 101
4.4.1 Calorimeter Triggers 103
4.4.2 Central Track Triggers 104

Chapter 5: The Measurement Strategy 106
5.1 A Brief Introduction 106
5.2 Kinematics of the $W \to e\nu$ Events 106
5.3 Kinematic Distributions for Determining the Mass of the W . . . 111
5.4 Parameterized Monte-Carlo Simulation (PMCS) 114
5.5 Fitting Procedure 116
5.6 Kinematics of the $Z \to e^+e^-$ Events 116
5.7 GEANT (FULL) Monte-Carlo Analysis 121
5.8 A Blind Analysis 122

Chapter 6: Introduction to Basic Calorimetry 123
6.1 A Brief Introduction 123
6.2 Bremsstrahlung by Accelerated Charged Particles 124
6.3 Pair Production by Energetic Photons 127
6.4 Showering in the Electromagnetic Calorimeter 130
6.4.1 Types of Calorimeters - Sampling and "Fully Active" . . . 132
6.4.2 Longitudinal Development of a Shower 135
6.4.3 Transverse Development of a Shower 136
6.4.4 Linearity and Resolution of a Calorimeter 137

Chapter 7: Reconstructing the EM Clusters and Tracks 139
7.1 A Brief Introduction 139
7.2 Energy Reconstruction in the Calorimeter 139
7.3 Track and Vertex Reconstruction from the Tracker 144

Chapter 8: Calibrating the Calorimeter and Tracker 148
8.1 A Brief Introduction 148
8.2 Electronics Calibration of the Calorimeter 149
8.3 Gain Calibration of the Calorimeter 150
8.3.1 The ϕ Intercalibration 150
8.3.2 The η Intercalibration 152
8.4 Results from the Gain Calibration 155
8.5 Alignment of the Tracking System 155

Chapter 9: Energy Loss Corrections due to Upstream Material 159
9.1 A Brief Introduction 159
9.2 Studying the Calorimeter Response & Resolution with GFLASH . 161
9.3 Response and Resolution of the DØ Run II Calorimeter 166
9.4 Observables Used for the MC Tuning 170
9.5 Determining the Correct Amount of Uninstrumented Material . . 172
9.6 Implementing the Energy Loss Corrections 177

Chapter 10: Selecting Events for the Analysis 194
10.1 A Brief Introduction 194
10.2 Data Samples 196
10.3 Trigger Selection 197
10.4 Determining the Electron Energy 198
10.5 Reconstructing the Track and Primary Vertex 200
10.6 Determining the Recoil 201
10.7 Determining the Missing (Neutrino) Energy 202
10.8 Criteria for Selecting the Events 203
10.9 $Z \to e^+e^-$ and $W \to e\nu$ Data Samples 206

Chapter 11: Event Generators 208
11.1 An Introduction - What is an Event Generator? 208
11.2 Simulating the Hard Scatter of the Process 211
11.3 What is Parton Showering and Hadronization? 212
11.4 How are Parton Showering and Hadronization Modeled? 214
11.5 Event Generators Used for this W Mass Analysis 215
11.6 QCD Corrections 217
11.7 Electroweak Corrections 218
11.8 PDF Uncertainties 219

Chapter 12: Parameterized Monte-Carlo Simulation (PMCS) 220
12.1 An Introduction - What is the PMCS of the Detector? 220
12.2 Modeling the Electron Energy Response and Resolution 223
12.2.1 Electron Angular Resolution 225
12.3 Modeling the Recoil System 226
12.4 Missing Transverse Energy 227

Chapter 13: Modeling the Efficiencies in PMCS 228
13.1 A Brief Introduction 228
13.2 Primary Vertex Simulation 231
13.3 Electron Geometrical Acceptance 232
13.4 Trigger Efficiency 235
13.5 Preselection Efficiency 236
13.6 EMID (HMatrix) Efficiency 237
13.7 Track Matching Efficiency 239
13.8 Overall Hadronic Activity (SET) Efficiency 242
13.9 Recoil Related ($u_{\parallel}$) Efficiency 248
13.10 Final Efficiency Corrections Based on Electron p_T: Tag and Probe 249

Chapter 14: Simulating the Electron Energy in the PMCS 252
14.1 A Brief Introduction 252
14.2 Reconstruction of the Electron Energy in Data 252
14.3 Parameterization of the Electron Energy in the FAST MC 253
14.3.1 Parameterization of the Electron Energy Response 254
14.3.2 Parameterization of the Electron Energy Resolution 256
14.3.3 Parameterization of the Underlying Energy Corrections . . 258
14.3.4 Parameterization of the Calorimeter Position Resolution . 261
14.3.5 Electron Geometrical Acceptance - PhiMod 262
14.4 Final State Photon Correction 262
14.5 Primary Vertex Simulation 268
14.6 Luminosity Profile and Run Number 268
14.7 Quality of the Electron Energy Loss Functions 268

Chapter 15: Simulating the Recoil Energy in the PMCS 271
15.1 A Brief Introduction 271
15.2 Components of the Hadronic Recoil 271
15.3 Modeling the Hadronic Recoil 273
15.3.1 Modeling the "hard" Component 273
15.3.2 Modeling the "soft" or "semi-hard" Component 276
15.3.3 The $u_{\parallel}$ Correction to the Modeled Recoil 279
15.3.4 The FSR Correction to the Modeled Recoil 280
15.4 Fine-tuning/Over-smearing the Modeled Recoil 280
15.4.1 Fine-tuning the Hadronic Response 283
15.4.2 Fine-tuning the Hadronic Resolution 284

Chapter 16: The Backgrounds in the Analysis 286
16.1 A Brief Introduction 286
16.2 QCD Background 286
16.2.1 f_{QCD} and ϵ_{trk} 288
16.3 $Z \to e^+e^-$ Background 291
16.4 $W \to \tau\nu$ Background 292
16.5 Normalization of the Backgrounds 293

Chapter 17: The FULL (Geant) MC Analysis 294
17.1 A Brief Introduction 294
17.2 FULL MC Samples 296
17.3 Electron Response and Resolution Terms 296
17.4 Recoil Response and Resolution Terms 298
17.5 Z Boson Comparison Results 299
17.6 W Boson Comparison Results 300

17.7 Fitting Procedure for Determining the W Mass 301
17.8 W Mass Results 303

Chapter 18: W Mass Results from the Collider Data 311
18.1 A Brief Introduction 311
18.2 Electron Response and Resolution Terms 312
18.3 Recoil Response and Resolution Terms 314
18.4 Z Boson Comparison Results 317
18.5 W Boson Comparison Results 318
18.6 Fitting Procedure for Determining the W Mass 319
18.7 W Mass Results 319

Chapter 19: Systematic Uncertainty on the W Mass Measurement 331
19.1 An Introduction 331
19.2 Experimental Uncertainties 335
19.2.1 Electron Energy Scale 335
19.2.2 Electron Energy Resolution 335
19.2.3 Electron Energy Non-Linearity 336
19.2.4 Recoil Momentum Scale and Resolution 337
19.2.5 Efficiencies 337
19.2.6 Backgrounds 338
19.3 Theoretical Uncertainties 338
19.3.1 Parton Distribution Functions 338
19.3.2 W and Z Boson p_T 339
19.3.3 Electroweak and FSR Photon Corrections 340
19.4 Concluding Remarks on the Uncertainties 343

Chapter 20: Consistency Checks 347
20.1 A Brief Introduction 347
20.2 Fitting Intervals 348
20.3 Instantaneous Luminosity 349
20.4 Time 352
20.5 Scalar E_T 353
20.6 Phi Fiducial Cut 355
20.7 u_T Cut 357
20.8 $u_{\|}$ 357

Chapter 21: The Combination of the W Mass Results 360
21.1 A Brief Introduction 360
21.2 Determination of Statistical Correlations for the Three M_W Measurements 360

21.3 Determination of Systematic Correlations for the Three M_W Measurements 361
21.4 Combining the three measurements using BLUE 364
21.5 Future Prospects of the M_W analysis 366

References 370

List of Figures

1.1 The Standard Model Particles and Force Propagators 20
1.2 Constraints on the Higgs Mass from M_W and M_{top} 23
1.3 Past Measurements of M_W 26

2.1 Radiative Corrections for the W Mass 47

3.1 Lowest Order Diagram for W and Z Production 49
3.2 NLO Processes in the W/Z Production 56
3.3 Spin States for W Production and Decay 59

4.1 Layout of Fermilab's Accelerators Chain 63
4.2 Components of the Antiproton Source 66
4.3 Tevatron Bunch Structure for Run I and Run II 69
4.4 Total Integrated Luminosity Delivered and Recorded at DØ . . . 70
4.5 Cross-sectional View of the DØ Run II Detector 71
4.6 The Barrel and Disk Design of the SMT 75
4.7 Readout Chain of the SMT 79
4.8 Cross-sectional View of the CFT 80
4.9 LED Spectrum Showing Photoelectron Peaks of a VLPC 81
4.10 The CFT/CPS Axial Components of the L1 CTT System 82
4.11 Views of the CPS Detector 86
4.12 View of the FPS Detector 87
4.13 Parts of the DØ Calorimeter 89
4.14 Side View of One Quarter of the Calorimeter 90
4.15 A Typical Calorimeter Cell 91
4.16 The Calorimeter Cell Configuration 92
4.17 Shape of Electronic Signal from Calorimeter 94

4.18 Readout Chain of Calorimeter 95
4.19 C-Layer of Forward Muon Scintillation Counters 97
4.20 Design of a Forward Muon Scintillation Counter 98
4.21 Cross-section of a Mini Drift Tube 99
4.22 Schematic Drawing of Luminosity Counters 100
4.23 DØ Trigger and Data Acquisition System 102

5.1 Schematic Drawing of $W \to e\nu$ Decay 108
5.2 Dominant Decay Channels for W within SM 108
5.3 Distributions of m_T and p_T^e for W Boson 113
5.4 Schematic Drawing of $Z \to ee$ Decay 117
5.5 Decay Channels for Z within SM 118

6.1 Feynman Diagram for Bremsstrahlung 125
6.2 Feynman Diagram for γ Pair Production 128
6.3 Schematic Drawing of an EM Shower 131

7.1 Isolation of an EM Cluster 142

8.1 Calibration Constants of the Calorimeter 156

9.1 Average Shower Profile for Electrons of E=45 GeV at η_{phys}=0 . . 162
9.2 Average Shower Profile for Electrons of E=45 GeV at η_{phys}=1 . . 163
9.3 Shower Fluctuations for Electrons of E=45 GeV at η_{phys}=0 164
9.4 Shower Fluctuations for Electrons of E=45 GeV at η_{phys}=1 165
9.5 Shower Fluctuations for Electrons of E=5 GeV at η_{phys}=0 165
9.6 Shower Fluctuations for Electrons of E=45 GeV at η_{phys}=0 166
9.7 Fractional Energy Resolution as a Function of η_{phys} 167
9.8 Fractional Resolution at η_{phys}=0 as a Function of E 168
9.9 Z Mass for Two Angles of Incidence of Electrons 170
9.10 E vs. η_{phys} for Electrons from W and Z 171
9.11 Comparison of Kinematic Variables for Z Events; Category 10; Default Material 180
9.12 Comparison of Kinematic Variables for Z Events; Category 23; Default Material 181

9.13 Comparison of EM Fractions for Z Events; Category 10; Default Material . . . 182
9.14 Comparison of EM Fractions for Z Events; Category 23; Default Material . . . 183
9.15 Summary of the Means of the EM Fractions for Z Events; Default Material . . . 184
9.16 Ratio of the Means of the EM Fractions for Z Events; Default Material . . . 185
9.17 Fit for nX_0 for All EM Layers . . . 186
9.18 Fit for nX_0 for Each EM Layer . . . 187
9.19 Comparison of EM Fractions for Z Events; Category 10; Tuned Material . . . 188
9.20 Comparison of EM Fractions for Z Events; Category 23; Tuned Material . . . 189
9.21 Ratio of Means of EM Fractions for Z Events; Tuned Material . . 190
9.22 Energy Loss Correction Factors . . . 191
9.23 Summary of the Means of the EM Fractions for W Events; Tuned Material . . . 192
9.24 Ratio of Means of EM Fractions for W Events; Tuned Material . . 193

11.1 Event Simulation by an Event Generator . . . 211

13.1 End View of Central Calorimeter and EM Modules . . . 233
13.2 PhiMod Shift and PhiMod Efficiency . . . 234
13.3 Trigger Efficiency vs. Electron p_T for Four Trigger Periods . . . 236
13.4 The Preselection Efficiency for Reconstructing a Loose EM Cluster 238
13.5 The EMID Efficiency as a Function of η_{det} . . . 239
13.6 The EMID Efficiency as a Function of η and p_T . . . 240
13.7 The Tracking Efficiency as a Function of η and Vertex z . . . 241
13.8 The Tracking Efficiency as a Function of η and p_T . . . 243
13.9 The Event Reconstruction Efficiency as a Function of SET . . . 245
13.10 SET Efficiency with Corrections from Electron p_T and SET . . . 247
13.11 The $u_{\parallel}$ Efficiency in Data for W and Z Events . . . 250
13.12 The p_T Dependence of HMatrix for CC Electrons . . . 251
13.13 The p_T Dependence of Track Match for CC Electrons . . . 251

14.1 M_Z vs. f_Z Distribution in FULL MC 257
14.2 $\Delta UE_{\rm rot}$ Distributon in Data 260
14.3 ΔUE_{rot} vs. Luminosity and vs. $u_{\|}$ 261
14.4 Electron ID Efficiency vs. Fractional Energy of Photon 264
14.5 Electron Energy Correction vs. Fractional Energy of Photon . . . 266
14.6 True Spectrum and Fractional Difference of Electron Energies . . 270

15.1 The Recoil p_T and ϕ Resolutions for 5 GeV 276
15.2 The Recoil p_T and ϕ Resolutions for 20 GeV 277
15.3 The $\eta - \xi$ Coordinate System 282

16.1 Method for Subtracting QCD Backgrounds from W Events 288
16.2 p_T Dependence of f_{QCD} in Bins of η^{det} 289
16.3 ϵ_{trk} in η^{det} Bins 290
16.4 η^{det} of the Two Electrons in Z Background 291
16.5 The Three Backgrounds in the Normalized Form 293

17.1 1σ Contour of E Scale and Offset in FULL MC 297
17.2 Central Value & 1σ Contour for `RelScale` & `RelOffset` 299
17.3 Comparison of the Mean of the η Imbalance for FULL and FAST MC 300
17.4 Central Value & 1σ Contour for `RelSampA` & α_{mb} 301
17.5 Comparison of the Width of the η Imbalance for FULL and FAST MC 302
17.6 Comparison Plots for Z between FULL MC and FAST MC - First Set of Histograms 304
17.7 Comparison plots for Z between FULL MC and FAST MC - Second Set of Histograms 305
17.8 Comparison plots for W between FULL MC and FAST MC - First Set of Histograms 306
17.9 Comparison plots for W between FULL MC and FAST MC - Second Set of Histograms 307
17.10 W Mass from m_T Distribution and the Likelihood Plot 308
17.11 W Mass from p_T^e Distribution and the Likelihood Plot 309
17.12 W Mass from $\not{E}_T$ Distribution and the Likelihood Plot 310

18.1 χ^2 Projections on α-β Axes and 1σ Contour in DATA 313
18.2 Central Value & 1σ Contour for `RelScale` & `RelOffset` 315
18.3 Comparison of the Mean of the η Imbalance for DATA and FAST MC 316
18.4 Central Value & 1σ Contour for `RelSampA` & α_{mb} 316
18.5 Comparison of the Width of the η Imbalance for DATA and FAST MC 317
18.6 Comparison Plots for Z between Collider Data and FAST MC - First Set of Histograms 322
18.7 Contribution of the g_2, PDF and ϕ-crack Systematics 323
18.8 Comparison Plots for Z between Collider Data and FAST MC - Second Set of Histograms 324
18.9 Comparison Plots for W between Collider Data and FAST MC - First Set of Histograms 325
18.10 Comparison Plots for W between Collider Data and FAST MC - Second Set of Histograms 326
18.11 The Reconstructed Z Mass from Data and the FAST MC 327
18.12 W Mass from m_T Distribution and the Likelihood Plot 328
18.13 W mass from p_T^e Distribution and the Likelihood Plot 329
18.14 W mass from $\not{E}_T$ Distribution and the Likelihood Plot 330
20.1 Stability of M_W Fit vs. Fit Range for m_T Distribution 350
20.2 Stability of M_W Fit vs. Fit Range for p_T^e Distribution 351
20.3 Stability of M_W Fit vs. Fit Range for $\not{E}_T$ Distribution 352
20.4 W and Z Masses along with the Mass Ratio as a Function of Instantaneous Luminosity 353
20.5 W and Z Masses along with the Mass Ratio as a Function of Data-taking Period 354
20.6 W and Z Masses along with the Mass Ratio as a Function of Scalar E_T 355
20.7 W and Z Masses along with the Mass Ratio for Variations of the Phi Fiducial Cut 356
20.8 W and Z Masses along with the Mass Ratio for Variations of the Recoil u_T Cut 358
20.9 W and Z Masses along with Mass Ratio for Variations of $u_{\parallel}$ . . . 359

21.1 The World Average Value of the W Mass 368

List of Tables

1.1 Fundamental Forces and their Carriers 13
1.2 Leptons - Elementary Particles of the Standard Model 18
1.3 Quarks - Elementary Particles of the Standard Model 19

2.1 The LH Isodoublets and RH Isosinglets of $\mathrm{SU}(2)_I$ and $\mathrm{U}(1)_Y$ . . 36
2.2 Parameters of the Electroweak Standard Model at Tree Level . . . 45

4.1 Components of the SMT Detector 78

5.1 Neutral and Axial Vector Couplings in the SM 119

7.1 Layer Weights Used for Energy Reconstruction 141

9.1 Material in front of Liquid Argon 160
9.2 Bins in terms of Electron $|\eta_{phys}|$ 172
9.3 "η" Categories for $Z \to ee$ Events 179

10.1 Single EM Triggers Used in this Analysis 207

11.1 Event Generators for W and Z Processes 216

19.1 Systematic Uncertainties for the W Mass Analysis 344
19.2 Mass Shift of W and Z due to δs Variation 345
19.3 Mass Ratio of W and Z due to δs Variation 346

21.1 Statistical Correlation Coefficients 362
21.2 Correlation Coefficients for Electron Systematics 364
21.3 Correlation Coefficients for Recoil Systematics 365
21.4 Correlation Coefficients for PDF Systematics 366
21.5 Final Correlation Coefficients from BLUE 366

CHAPTER 1

AN INTRODUCTION TO PARTICLE PHYSICS

1.1 A Brief Introduction

Ever since the beginning of time, there have been a multitude of questions that have always occupied the thoughts and thinking prowess of mankind on this earth. He has long asked himself questions like "What is the Universe made of?", "What holds it all together?", "Is there a simple explanation for the origin of matter at the most fundamental level?" and "What exactly do we mean by fundamental?". His attempts to find answers to these queries have often led him on endless quests, pursuits and research. Some of them have yielded remarkable answers that help him inch forward in solving the mysteries of the conglomeration of this universe that he lives in. Clues that help him assemble the puzzle of the creation of the world around him, including himself.

Particle physics is that quest. The pursuit to discover the laws of nature working at the most fundamental or basic level, by discovering the fundamental building blocks of the Universe and the nature of interactions that exist amongst them. Thus it involves the study of matter at the smallest possible scales. This field of physics investigates interactions occuring at high energies (trillions of electron volts) due to the extremely small dimensions ($< 10^{-15}$ m) and high masses associated with the fundamental constituents. Thus it is also rightly termed as High Energy physics.

1.2 A Timeline of the History of Particle Physics

We begin with a brief journey down memory lane, one that provides some information aimed at answering the two most important questions "What is the world made of?" and "What holds it all together?". While addressing the first one, we look at the development of particle physics from a historical point of view, the events surrounding the discoveries of the various fundamental constituents of matter as we know them at present. The second question gets answered by way of a simple description of the interactions of the particles as we know them, thus looking at the four broad categories of forces, into which we categorize the various interactions that exist around us. A detailed account of the historical development of particle physics is given in [1].

1.2.1 Classification of Particles - Fermions and Bosons

One of the most fundamental concepts regarding our understanding of the particles and their interactions comes from Pauli's spin-statistics theorem of 1940. This connects the statistics obeyed by a particle with its intrinsic property of spin angular momentum. Particles with half-integral spin ($\frac{1}{2}\hbar, \frac{3}{2}\hbar$, ...) obey "Fermi-Dirac" statistics and are called "fermions" while those with integral values of spin ($0,\ \hbar, 2\hbar$, ...) obey "Bose-Einstein" statistics and are thus referred to as "bosons". Quarks and baryons are examples of fermionic particles whereas photons and mesons are prime examples of bosons.

For particles obeying Fermi-Dirac statistics, the wavefunction describing a pair of identical particles is anti-symmetric under an interchange of coordinates of the two particles. This implies that two identical fermions cannot exist in the same quantum state [2].

For the Bose-Einstein particles, the wavefunction is symmetric under an interchange of coordinates of two particles, thus implying that bosons can and like to exist in the same quantum state.

1.2.2 The Beginning of the End of the Classical Era

The study of particle physics, in fact the subatomic world itself, had its humble yet significant beginnings in the discovery of radioactivity by Henri Becquerel [3–6] in 1896. His discovery of the invisible emanations from uranium without the presence of an initiating energy paved the way for a life-long research on radioactivity by Marie and Pierre Curie [7–9], the most unique achievement of which was the realization that radiation is an atomic property of matter. The most intelligible understandings of the structure of the atom came from the discovery of the electron by J.J. Thomson [10, 11] in 1897 and the experimental work of Ernest Rutherford in 1911. Rutherford's α-particle scattering experiments [12, 13] laid the foundation of the planetary model of the atom, in which the mass and positive charge of the atom were concentrated in its nucleus. In 1914, Niels Bohr [14] proposed a model of the Hydrogen atom and calculated its spectrum. However the proposed model did not seem to work for heavier atoms like Helium and Lithium. For although Helium has two electrons and Lithium has three, they weigh four and seven times as much as a Hydrogen atom, respectively. The dilemma was resolved with James Chadwick's discovery of the neutron in 1932 [15], an electrically neutral twin of the proton.

1.2.3 Discovering the Photon

With these significant discoveries atomic and nuclear physics had begun offering simple and satisfying answers to the questions about the constituents of matter. Planck's theory in 1900 [16] proposing that electromagnetic radiation was quantized and Einstein's rather radical explanation of the photoelectric effect in 1905 [17, 18] were additional steps aimed at consolidating the particle nature of matter at the fundamental level. However they took the scientific world by storm. Even though the results of the decade-long experiments of the photoelectric effect performed by Millikan [19] came down in favor of Einstein's theory, the acceptance of a quantized model for radiation seemed wholly untenable. The issue was finally settled in 1923 by the scattering experiments of light conducted by A.H. Compton [20]. The shift in wavelength of the light scattered by a particle at rest could only be explained by treating light as a particle of zero rest mass with energy given by Planck's equation:

$$E = h\nu \tag{1.1}$$

Here h is Planck's constant and ν is the frequency of light. This particle of light was called the photon(γ). Although the introduction of the photon received a cold reception, it offered a whole new approach to understanding electromagnetic interactions and was eventually accepted as the mediator of the electromagnetic field.

1.2.4 Discovering the Meson

However the question "What holds the nucleus together?" still loomed large. In 1934 Yukawa came forward with a theory [21] for the strong force, the ex-

tremely short-ranged force responsible for holding the protons and neutrons at close proximities inside the nucleus. He assumed that the protons and neutrons were attracted by some sort of quantized field and called the carrier of this field the meson ("middle-weight"). He estimated its mass to be one-sixth that of the proton. Cosmic ray experiments in 1947 however proved that there are two kinds of middle-weight particles, the pions(π) and muons(μ). The true Yukawa meson is the pion [22], the muon being a heavier version of the electron and thus a lepton.

1.2.5 Discovering the Antiparticles

The Dirac equation provides a description of elementary spin-$\frac{1}{2}$ particles such as electrons, consistent with both the theories of quantum mechanics and special relativity. It was formulated in 1927 [24]. However a puzzling feature of this equation was that for every positive-energy solution ($E = \sqrt{\mathbf{p}^2c^2 + m^2c^4}$) it predicted a corresponding solution with negative energy ($E = -\sqrt{\mathbf{p}^2c^2 + m^2c^4}$). The meant that the electron could spiral to increasingly negative energy states by radiating off an infinite amount of energy. To rescue his equation, Dirac postulated that the negative-energy states are all filled by a perfectly uniform, infinite "sea" of electrons. The electrons that we observe occupy the positive-energy states. However this meant that the absence of a negative-energy electron from the sea would appear as a net positive energy in that location, thus leading to the idea of "holes" appearing in the sea. Dirac at first hoped that these holes might be protons, but it was soon clear that the holes had to be identical to the electrons - 2000 times lighter than a proton. Since no such particle was known at the time, Dirac's theory seemed to be standing on shaky grounds.

The discovery of the positron by Anderson in 1931 [23] proved to be the saving

grace for Dirac's theory of relativistic quantum mechanics. It was the first antiparticle to be discovered and is also known as the antielectron, differing from the electron only by its charge. The theoretical formulations of Feynman and Stuckelberg in the 1940s expressed Dirac's negative-energy states as the positive-energy states of a different particle (positron), thus placing the electron and positron on an equal footing.

The negatively charged antiproton was first observed experimentally at the Berkeley Bevatron facility in 1955 and the neutral antineutron was discovered at the same place in 1956. However the discovery of antimatter brought with it its own set of questions on the existence of the universe, for matter and antimatter annihilate in close proximity. It thus paved the way for research on the apparent matter-antimatter asymmetry.

1.2.6 Advent of the Neutrino

The discovery of neutrinos, though, was not that straightfoward. Historically, the study of beta decay provided the first physical evidence of the neutrino. As we know, radioactive β-decay involves the underlying conversion of a neutron into a proton with the emission of an electron. Hence the kinematics of two-body decays predict a fixed energy for the electron. However, in 1911 Lise Meitner and Otto Hahn performed an experiment that showed that the energies of electrons emitted by beta decay had a continuous rather than a discrete spectrum. This was in apparent contradiction to the law of conservation of energy, as it appeared that energy was lost in the beta decay process. In 1920-1927, Charles Ellis (along with James Chadwick and colleagues) established that the beta decay spectrum is really continuous, thus ending all controversies.

Fortunately Wolfgang Pauli suggested the emission of another electrically neutral particle [25], a silent accomplice that carried away the missing energy. In 1933, Enrico Fermi presented a theory of β-decay [26] after incorporating Pauli's particle. It proved to be immensely successful and Fermi called this apparently weightless particle the "neutrino". The β-decay of the neutron thus stands as $n \rightarrow p + e^- + \bar{\nu}$. Disintegrating pions ($\pi \rightarrow \mu + \nu_\mu$) and muons ($\mu^- \rightarrow e^- + \bar{\nu}_e + \nu_\mu$) [27] in experiments conducted by C.F. Powell and his group also suggested that the neutral particle that left no footprints in the emulsion was perhaps Pauli's neutrino. The experimental confirmation came in the mid 1950s by way of experiments conducted by F. Reines and C.L. Cowan on the "inverse" β-decay reaction ($\bar{\nu}_e + p^+ \rightarrow n + e^+$) [28] with the help of antineutrino beams from the Savannah River nuclear reactor.

Now, since the particle produced in ordinary β-decay is actually an antineutrino and not a neutrino, the question of the two particles being the same or distinguishable arose. Davis and Harmer showed that the neutrino and antineutrino are actually two distinct particles, by verifying that the crossed reaction involving antineutrinos ($\bar{\nu}_e + n \rightarrow p^+ + e^-$) does not happen [29]. This led to the concept of lepton number (L) conservation in particle interactions. The leptons (e^- or μ^- or ν) were assigned a lepton number of L =1 whereas the antiparticles (e^+ or μ^+ or $\bar{\nu}$) were assigned L = -1. This was later refined to separate conservation of electron (L_e) and muon (L_μ) lepton numbers to account for all allowed and forbidden processes, thus postulating the existence of two types of neutrinos, ν_e and ν_μ, and their corresponding antineutrinos. Thus the neutron β-decay is stated as $n \rightarrow p + e^- + \bar{\nu}_e$, in a more correct way. The existence of ν_μ was proved in 1962 by the pion (π^-) decay experiments of Lederman, Schwartz and Steinberger

at Brookhaven [30].

1.2.7 Hadrons and the Concept of Strangeness

The meson family was extended to include the neutral and charged kaons (K^0 and K^+) discovered in 1947 and 1949 respectively. In due course many more mesons like the η, the ϕ, the Ω, the ρ's, etc., were also discovered.

In 1950, another neutral particle decaying into a proton and a pion was discovered by Anderson's group at Cal Tech. It was called the Λ and was categorized as a baryon. Baryons are the family of composite particles made up of three quarks. Hence they are heavier than their elementary counterparts and are strongly interacting fermions (obey Fermi-Dirac statistics). Protons and neutrons are also baryons. The next few years led to the discovery of more baryons like the Σ's, the Δ's, etc. The law of conservation of baryon number was postulated for explaining the allowed and forbidden baryonic reactions. This provided an explanation for the stability of protons, the proton being the lightest baryon, could not decay without violating baryon number conservation.

The baryons and mesons were collectively known as the hadrons. It was observed that many of these newly discovered hadrons seemed to have distinctly different production and disintegration mechanisms. In essence, they were produced copiously but decayed relatively slowly. In modern terminology, these particles are produced by the strong force but decay via the weak force. In order to explain this discrepancy Gell-Mann [31] and Nishijima [32] introduced the concept of strangeness (S), a property of the particles that is conserved in strong but not in weak interactions. Thus the Kaons carry a strangeness of S= +1 and the Σ's and Λ carry S= -1. The "ordinary" particles like the pion, proton and neutron have

S=0. Conservation of strangeness was used to explain the production of hadrons involving strong processes. Non-conservation of strangeness explained the long time scale of the decay processes that involve weak interactions. Weak interactions also violate parity. This was revealed through the $\tau - \theta$ puzzle, where two strange mesons, τ and θ, were identical in every respect, except that one decayed into two ($\theta^+ \rightarrow \pi^+ + \pi^0$) pions, the other into three ($\tau^+ \rightarrow \pi^+ + \pi^+ + \pi^-$) pions, states of opposite parity. Lee and Yang suggested that both τ and θ were the same, the K^+ meson, and parity is simply violated in one of the weak decays [33].

1.2.8 The Particle Zoo - ca. 1960

By 1960, the zoo of particles had grown immensely into different types of leptons and hadrons and thus needed classification. In 1961, Gell-Mann introduced the Eightfold Way [34] for grouping the hadrons on the basis of their charge and strangeness. The eight lightest baryons were grouped to form the baryon-octet while the eight lightest mesons formed the meson-octet. The heavier baryons were grouped to form the baryon decuplet whereas the heavier mesons formed the meson-nonets. The antibaryons were also grouped into their respective octets and decuplets possessing opposite strangeness and charge. This grouping of the hadrons into multiplets was incomplete, allowing for the prospect of many new particles to be discovered. Over the next decade every newly discovered hadron neatly found a place in the multiplets, the most exciting being the discovery of the Ω^- in 1964.

The importance of the Eightfold Way not only lay in the classification that it provided but also in the organizational structure that it set up for the hadrons. Its stupendous success thus ushered in the era of modern particle physics.

1.2.9 A Model for the Quarks

As a result of the success of the Eightfold Way, Gell-Mann [34] and Zweig [36, 37] independently postulated the sub-structure of hadrons in 1964. Gell-Mann called these elementary constituents "quarks" while Zweig referred to them as "aces". Initially three quarks were proposed, of flavors up, down and strange. The up quark (denoted as u) carried a charge Q=+2/3 and strangeness S=0, the down quark (denoted by d) had Q=-1/3 and S=0 while the strange quark (denoted by s) had Q=-1/3 and S=-1. As per the quark model, every baryon was composed of three quarks, while every meson comprised of a quark and an antiquark. The quark model helped explain the appearance of hadrons in the baryon decuplets and meson nonets, besides making room for the newly discovered η' as a singlet in the meson nonet.

The quark model however suffered from threats to its credibility since isolated quarks had never been observed. Moreover the fact that three quarks (fermions) could exist in the same state in a baryon was in direct conflict with Pauli's exclusion principle. Although the deep inelastic scattering experiments at SLAC in 1968 did conclude that the charge of the proton seemed to be concentrated in three small lumps, thus providing some first evidence for the quarks, they did little to alleviate discomfort about the exact nature of quark confinement. Besides, O.W. Greenberg's proposal of three colors [38] (red, green and blue) for each quark flavor did little to resolve the conflict with Pauli's exclusion principle. All these factors contributed to considerable doubt about the authenticity of the quark model of matter, up until 1974.

1.2.10 Discovering the Charm Quark

The discovery of the J/ψ meson in 1974, from the independent experiments of C.C. Ting and B. Richter [39] propelled some intriguing questions into the limelight. This electrically neutral, extremely heavy meson had an extraordinary long lifetime of 10^{-20} sec, 1000 times larger than usual. Although the discovery of the J/ψ was not a direct confirmation of the existence of free quarks or color hypothesis or explanation of quark confinement, the true nature of the J/ψ meson was explained by the quark model through the assumption of a fourth quark called the charm (denoted as c). The J/ψ represents a bound state of the charm and its antiquark. The charm discovery provided a parallel between the leptons (e, ν_e, μ, ν_μ) and quarks (d, u, s, c) known at the time. The evidence of hadrons containing the "bare" c quark in the form of charmed baryons (e.g. λ_c^+ (=udc) and Σ_c^{++} (=uuc)) [40] and charmed mesons (e.g. D^0 and D^+) [41] in 1975 and 1976 respectively, confirmed the charm hypothesis, established the J/ψ as $c\bar{c}$ and helped to put the quark model back on a firmer footing.

1.2.11 Discovering the Bottom and Top Quarks

At this point the quark model consisted of four quarks and the four leptons. The tau lepton was discovered in 1975 and assuming that the corresponding neutrino (ν_τ) also existed, it ruptured the symmetry of the model. However another heavy meson discovered in 1977 and called the Upsilon [42] was postulated to be a bound state of another heavy quark called the "beauty" or "bottom" (denoted by b). Hadrons such as λ_b (=udb), B^0 and B^- containing the bottom quark were discovered during 1981 to 1983. These discoveries led to a third generations of leptons and quarks being included in the quark model. Attempts at preserving

the symmetry of the quark model now required the existence of another quark, the "truth" or "top" (denoted as t). It was eventually discovered in 1995 at Fermilab [43].

The quark model thus stands at six quarks and six leptons at present. These particles form the building blocks for the Standard Model that in turn provides a theoretical framework for the fundamental particles of matter and their interactions in this universe. A detailed discussion on the Standard Model is given in the later sections.

1.3 Interactions and Fields in Particle Physics

The elementary constituents of matter interact amongst themselves by way of four distinct types of fundamental interactions or fields. Gravity is the most familiar, though it is the least important at the miniscule scales probed by particle physics. Apart from gravity, electromagnetic interactions are responsible for practically all the phenomena that we observe in daily life. Interatomic forces that act between atoms can be traced to the electromagnetic interactions existing among the protons and electrons inside the atoms. Similarly intermolecular forces acting between molecules and binding them together are electromagnetic in nature. All forms of chemical phenomena as well as the ordinary forces of "pulling" and "pushing" that we encounter in daily life are examples of electromagnetic interactions. Weak interactions are most often observed in the slow β-decay of radioactive nuclei. Strong interactions are responsible for holding the quarks together inside a nucleon and their residual effects account for the interactions between protons and neutrons that is the nuclear binding force. Table 1.1 summarizes the forces and the carriers of these force fields.

TABLE 1.1

FUNDAMENTAL FORCES AND THEIR CARRIERS

Force	Carrier	Symbol	Charge (e)	Spin	Mass (GeV/c^2)
Strong	Gluon	g	0	1	0
Electromagnetic	Photon	γ	0	1	0
Weak	W-boson	$W^{\pm}$	± 1	1	80.399 ± 0.025
	Z-boson	Z^0	0	1	91.1876 ± 0.0021
Gravitational	Graviton	G	0	2	0

1.3.1 Electromagnetic Interactions

The photon is the force carrier of electromagnetic interactions. It is massless, which accounts for the long range nature of these interactions. The coupling constant specifying the strength of the interaction between charged particles and photons is the dimensionless fine-structure constant α given as

$$\alpha = \frac{e^2}{4\pi\hbar c} = 1/137.0360 \tag{1.2}$$

The photon couples to the electron with strength $\sqrt{\alpha}$ so that the photoelectric cross-section is proportional to α. The field theory that is used to compute the cross-sections and dynamics of these electromagnetic interactions is known as Quantum Electrodynamics.

1.3.2 Gravitational Interactions

The quantum called the graviton is thought to be the carrier of the gravitational force and thus responsible for mediating the gravitational interactions, such as those existing between planets and stars. The mass of the graviton is zero due to the infinite range of the interactions. At present there is no self-consistent quantum field theory of the graviton.

1.3.3 Weak Interactions

The first evidence of weak interactions lay in the nuclear β-decay experiments of Becquerel in 1896. Typical examples are the decay of neutrons with leptons among the decay products. This is termed as β^- decay. With Pauli's suggestion of the presence of a (anti) neutrino in these interactions, Fermi developed the first theory of weak interactions, on the assumption that they were similar to electromagnetic interactions. He postulated that the interaction was point-like and used the four-fermion coupling constant G_F to describe the process. The β decays are given as follows:

$$n \rightarrow p + e^- + \bar{\nu}_e \tag{1.3}$$

Since weak interactions are charge-changing they seem to be mediated by a charged quantum acting between fermionic currents. This exchange of the charged quantum earned them the pseudonym of "charged current" interactions. The mediator was called the intermediate vector boson. The postulation of another neutral quantum that also seemed responsible for these weak interactions was confirmed in 1973 by the discovery of the "neutral current" weak interactions. However the extremely short range of the weak forces made it challenging enough for the theorists to make predictions about the properties of these mediators of the weak

interactions, except for the speculation that they had to be massive. More details about these mediators of the weak force have been provided in Section 1.5.

The weak force is also unique because it violates parity. This was postulated by Lee and Yang in 1956 [33]. The experiments of Wu et al. [44] confirmed that weak interactions violate parity maximally. Parity had previously been thought to be a conserved symmetry in any physical reaction. Interactions having the form $V - A$, where V stands for a polar vector ("true" vector) and A is an axial vector (pseudo vector), violate parity maximally. The polar and axial vectors transform differently under parity transformation. Hence due to the $V - A$ form of the weak interactions, only negative helicity (left-handed) states of the leptons participate in the weak decays. Thus in the β-decay reaction given above, only left-handed electrons and right-handed $\bar{\nu}_e$ are allowed. It is tough to measure the helicity of a neutrino directly. An indirect method is by a measurement of the muon helicity in the pion (π^+ and π^-)decay.

$$\pi^- \rightarrow \mu^- + \bar{\nu}_\mu \tag{1.4}$$

In the π^- decay, if the pion is at rest, both the muon and antineutrino come out back to back. Besides since the spin of the pion is zero, the spins of the decay products must be oppositely aligned. Therefore if the antineutrino is right-handed the muon must also be right-handed. This is precisely what the experimental results show [45]. Thus a measurement of the muon helicity gives an idea of the helicity of the antineutrino. By the same token, in the π^+ decay ($\pi^+ \rightarrow \mu^+ + \nu_\mu$) the μ^+ is always left-handed which indicates that the neutrino is left-handed.

1.3.4 Strong Interactions

Strong interactions are responsible for the binding of quarks in hadrons. The mediator of these quark interactions is called the gluon. It is a neutral, massless, flavorless (unlike the quark flavors u, d and s) particle with a spin of 1. Both quarks and gluons carry a "color" charge which is analogous to the electric charge. Depending on the colors involved, quark-quark interactions mediated via gluon exchange may be attractive or repulsive. Neither quarks nor gluons exist as isolated particles, they exist as colorless combinations with other quarks and/or gluons. The quantum field theory describing the strong interactions at the quark level is known as Quantum Chromodynamics.

The electroweak theory provides a unified description of two of the above four fundamental interactions of nature, the electromagnetic and the weak interactions. Although both these forces appear to behave very differently at everyday low energies, they are essentially two different aspects of the same force. As postulated by the Standard Model, above a unification energy on the order of 100 GeV, both the electromagnetic and weak interactions could be merged into the combined and single electroweak interaction.

The electroweak force will be discussed in great detail in the next chapter.

1.4 The Standard Model

The theoretical framework that provides a suitable explanation for the elementary particles and the fundamental interactions that exist amongst them is known as the Standard Model. This framework incorporates the related theories of Quantum Electrodynamics, Quantum Chromodynamics, the Glashow- Salam-Weinberg theory of electroweak processes [46–48] and has been very successful in

the many experimental tests that it has undergone. One of the attractive features of the Standard Model is that all the fundamental interactions derive from a single general principle, the requirement of local gauge invariance.

The Standard Model thus builds up its theoretical structure on the basis of three kinds of elementary constituents, the leptons, quarks and the mediators. There are six leptons that fall into three families or generations naturally, on the basis of their charge and lepton number. The charged leptons are the electron(e), muon(μ) and the tau(τ), each possesses a unit of negative charge. These leptons are accompanied by their respective neutrinos which are neutral. The ν_e has an electron number of +1 just like its charged counterpart the electron. Similarly the ν_μ has a muon number of +1 (like the μ) and the ν_τ has a tau number of +1 (like the τ). Conservation of charge and lepton numbers are pertinent for leptonic interactions to occur.

There are also six antileptons, consisting of the charged positron, antimuon and antitau and their respective antineutrinos. Their charges and lepton numbers are opposite to those of the leptons. The generations and properties of the leptons have been given in Table 1.2.

There are six quarks which are categorized into three families or generations on the basis of their flavors. There are six antiquarks which possess the opposite charge and flavor with respect to their corresponding quarks. Each quark or antiquark comes in three colors, which we can call red, green and blue by convention. The properties of the quarks have also been shown in Table 1.3.

Finally the mediators account for the interaction fields that the Standard Model uses to explain the different processes that are responsible for holding all

TABLE 1.2

LEPTONS - ELEMENTARY PARTICLES OF THE STANDARD MODEL

Generation	Leptons (spin=1/2)		
	Flavor	Charge(e)	Mass(GeV/c^2)
1	e	-1	0.511×10^{-3}
	ν_e	0	$< 3 \times 10^{-9}$
2	μ	-1	0.1056
	ν_μ	0	$< 0.19 \times 10^{-3}$
3	τ	-1	1.776
	ν_τ	0	$< 18.2 \times 10^{-3}$

this matter together. Every interaction has its mediator or force carrier. The photon is the mediator for the electromagnetic force, while the $W^{\pm}$ and Z bosons are the force carriers for the weak forces. The gluons mediate the strong interactions and there are eight of them in the Standard Model classified on the basis of their colors.

The elementary particles and the force propagators can be seen in the Figure 1.1. We can see that gravity has not been included in the Standard Model as yet. Hence a postulation of a quantum theory of gravity has been one of the most interesting topics of research in particle physics for a long time now. Its incorporation into the framework of the Standard Model has proven to be a daunting task.

TABLE 1.3

QUARKS - ELEMENTARY PARTICLES OF THE STANDARD MODEL

Generation	Quarks (spin=1/2)		
	Flavor	Charge(e)	Mass(GeV/c^2)
1	u	+2/3	0.0015 - 0.0045
	d	-1/3	0.005 - 0.0085
2	c	+2/3	1 - 1.4
	s	-1/3	0.08 - 0.155
3	t	+2/3	174.3
	b	-1/3	4.0 - 4.5

1.5 The W and Z Bosons in the Standard Model

With the emergence of the electroweak theory as proposed by Glashow, Salam and Weinberg, physicists were was finally able to make a firm prediction for the masses of the mediating bosons of the electroweak force field. According to the theory there were three intermediate vector bosons, two charged ($W^{\pm}$) and one neutral (Z^0). The mass of each of the W bosons and that of the Z^0 was estimated to be about 100 GeV/c^2. In 1983, all three vector bosons were discovered by the UA1 and UA2 collaborations at CERN using the Super Proton Synchrotron which produced them directly [49]. The mass of the W was measured to be $M_W = 81 \pm 5$ GeV/c^2 while that of the Z was $M_Z = 95 \pm 3$ GeV/c^2. These discoveries were of fundamental importance and aimed at establishing the importance of the

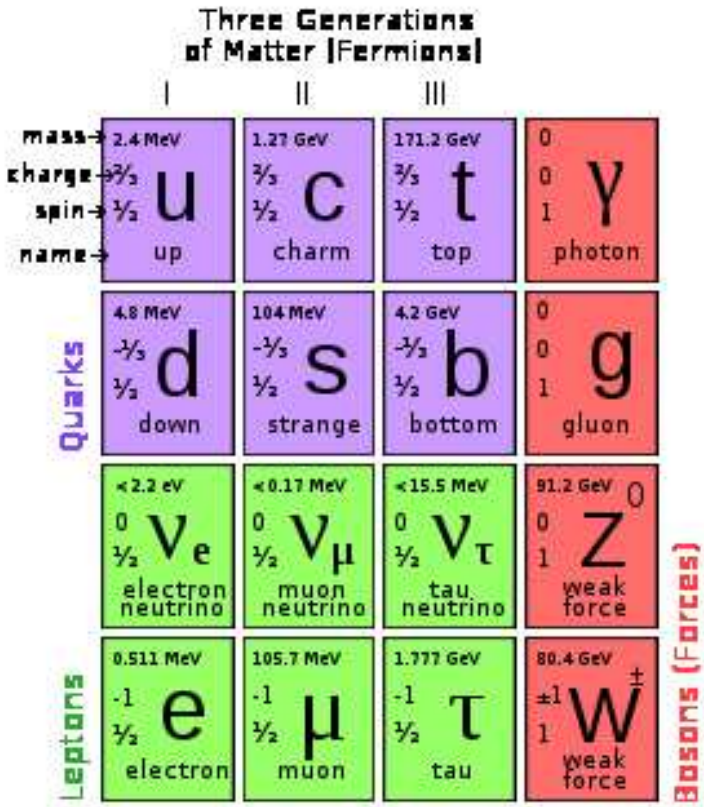

Figure 1.1. The Standard Model particles and force propagators

electroweak force in the Standard Model. They helped place the validity of the SM on a firmer pedestal.

At hadron colliders (such as the Tevatron), the W boson is produced by the annihilation of up and down quarks. The W has an extremely short lifetime $\sim 10^{-24}$ seconds and possesses both hadronic and leptonic modes of decay. The principle modes of decay of the W^+ are the hadronic modes and can be given as

$$W^+ \rightarrow u\bar{d} \tag{1.5a}$$

$$W^+ \rightarrow c\bar{s} \tag{1.5b}$$

It cannot decay into the top and bottom quarks, since the top quark is heavier than the W. The leptonic modes of decay for W^- can be written as

$$W^- \rightarrow l^- \bar{\nu}_l \tag{1.6}$$

where l^- stands for e^-, μ^- or τ^-. For the purposes of analyses, the leptonic decay modes are cleaner than the hadronic ones. Here the leptons appear as distinct, isolated signals in the detector.

1.6 Motivation for a Precise Measurement

In the Standard Model, the phenomenon of electroweak symmetry breaking is responsible for endowing the W and Z bosons with mass. This phenomenon is given a detailed treatment in the next chapter of this thesis. This symmetry breaking is brought about by the Higgs mechanism [50] which also predicts the existence of the as-yet-undiscovered Higgs boson. Considerable efforts are underway to understand the exact origins of the symmetry breaking and to prove the existence of the Higgs boson.

Thus the mass of the W boson is an important parameter for testing the validity of the Standard Model. Any discrepancies between the predicted and precisely measured values of M_W can lead to speculation for the existence of some new electroweak physics, or supersymmetry, beyond the Standard Model. More details on this have been provided in Chapter 2.

Measurements of the W mass also play a significant role in predicting the mass window of the Higgs boson. A measurement of M_W, when combined with a

measurement of the top quark mass (M_{top}), helps constrain the mass of the Higgs boson (M_{Higgs}). This is explained further in Section **??** of the next chapter. A contour plot for the Higgs has been shown in Figure 1.2. For the current world average values of the top quark mass at 173.1 $\pm$ 1.3 GeV and the W boson mass at 80.399 $\pm$ 0.025 GeV, the black and blue contours show the possible constraints on the mass of the Higgs in the Standard Model with 95% and 68% confidence levels respectively.

Detailed calculations by Marciano and Sirlin [54] show that for equal contributions to the uncertainty on the mass of the Higgs boson, the W mass needs to be known much more precisely than the top mass. In numerical terms,

$$\Delta M_W = 0.006 \times \Delta M_{top} \tag{1.7}$$

where ΔM_W is the uncertainty on the mass of the W boson and ΔM_{top} is the uncertainty on the mass of the top quark. Given the present uncertainty of ΔM_{top}=1.3 GeV, we see that the desired precision on the W mass is 8 MeV. However as stated earlier, our current best estimate of ΔM_W stands at 25 MeV. Moreover, recent precise measurements of the mass of the top quark [55] have become a big motivating factor for determining the mass of the W with even greater precision. The challenge of this single experiment measurement is to measure the W mass up to a precision of 0.05%. This thesis describes one such precise measurement done by the DØ experiment at Fermilab. This measurement has been done with 1 fb^{-1} of integrated luminosity of collider data which yields about 500,000 $W \rightarrow e\nu_e$ events after all the event selection criteria of the analysis have been implemented.

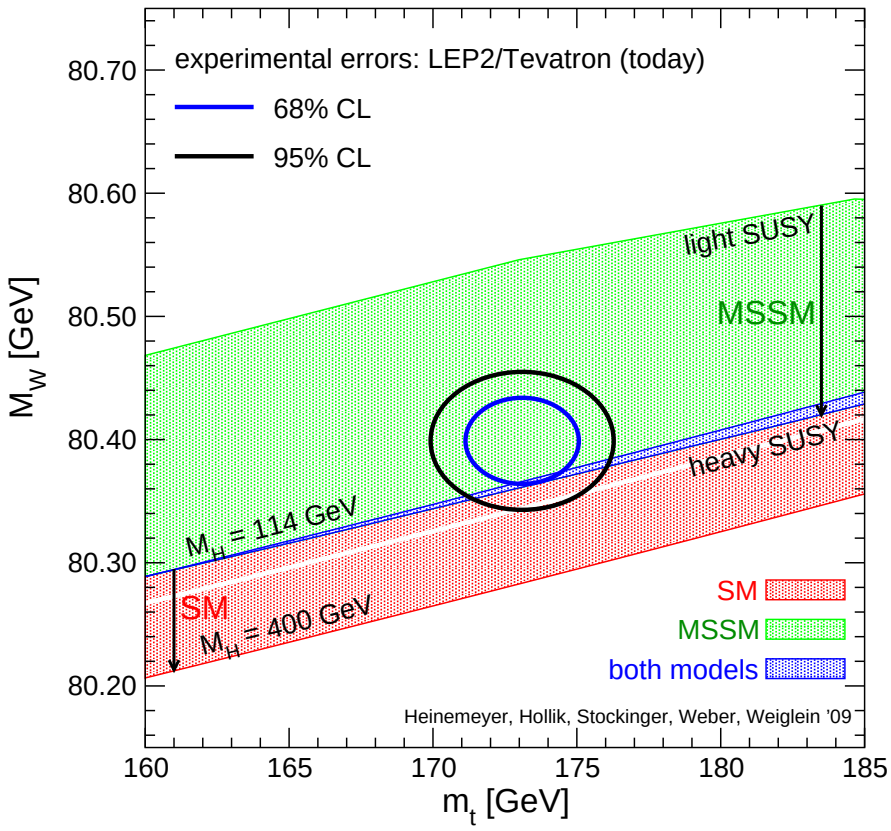

Figure 1.2. The contour plot showing the constraints on the mass of the Higgs boson from M_W and M_{top} measurements

1.7 Past Measurements of M_W

The mass of the W boson can be measured both by direct production of the boson in high-energy colliders and also by indirect methods. The indirect methods of measuring M_W usually involve measuring the weak mixing angle (θ_W) and calculating the W mass from its Standard Model predictions. This is described in detail in the next chapter. The direct methods of determination reconstruct the mass of the W boson that is produced "on-shell", from its decay products.

The Tevatron is capable of producing the W boson and both the DØ and

CDF experiments at Fermilab have measured the W mass from the data collected during the first major run of the collider (1992-1995), commonly known as Run I. DØ had obtained a measurement of M_W=80.483 ± 0.084 GeV [56] by analyzing the $W \rightarrow e\nu_e$ channel of decay in about 82 pb^{-1} of data. CDF had analyzed both the $W \rightarrow e\nu_e$ and $W \rightarrow \mu\nu_\mu$ modes of decay in about 82 pb^{-1} of data and obtained a measurement of M_W=80.433 ± 0.079 GeV [57].

Experiments such as the ALEPH [58], DELPHI [59], L3 [60] and OPAL [61] that used the e^+e^- collider LEP-2 at CERN, have also measured the W mass from data collected during their 1996-2000 run. The tunable energy of the e^+e^- collisions coupled with the experiment's insensitivity to theoretical models for W production (a considerable systematic at hadron colliders) allowed them to measure the W mass with remarkable precision. Their combined measurement stands at M_W=80.376 ± 0.033 GeV [62]. At LEP-2 the W boson was produced in pairs (W^+W^-) and both the hadronic and leptonic decay modes for each W were considered for the analyses.

A more recent measurement of M_W comes from the CDF experiment in 2007. CDF has measured the W mass with about 200 pb^{-1} of the Tevatron data collected during Run II (February 2002-September 2003). Analysis of both the electron and muon channels of the W decay has led to a measurement of M_W=80.413 ± 0.048 GeV [63].

Experiments such as SLD (SLAC Large Detector) [64] and NuTeV (Neutrinos at the Tevatron) [65] have also made indirect measurements of the W mass. Here the W mass was determined by making precise measurements of the weak mixing angle (θ_W). The value of θ_W was used in the Standard Model calculation of the W mass which is described in the next chapter.

Some of the distinguishing features of direct and indirect measurements of M_W are listed below.

1. Theoretical inputs for the cross-sections (σ_W or σ_Z) and branching ratios, $B(W \to l\nu)$, which might get contributions from non-SM couplings, are not required for the direct measurements.

2. The M_W obtained from a direct measurement can be used to derive information on the EW radiative corrections (explained in the next chapter). Since the radiative corrections modify the value of the W mass, one can test whether higher order EW corrections have any relevant impact on the W mass or not.

3. The sources of systematic errors are different. In a direct measurement an understanding of the acceptance and efficiency to obtain the $ee/e\nu$ final states is essential to the analysis. In indirect measurements the uncertainties in extracting the coupling constants are the sources of systematic errors.

4. An indirect measurement is heavily dependent on the theoretical descriptions of the production, decay and kinematics of the vector bosons. It assumes that the theoretical models are correct in its calculations of M_W. Thus a direct measurement always helps in cross-checking the theory. Any discrepancy between the direct and indirect results can lead to various speculations and suggestive clues, even the presence of non-SM couplings or interactions being present. These could lead to the higher order terms being required to explain the phenomena on a theoretical footing and also help constrain the unknown pieces. Thus a direct measurement is often an excellent means of looking for physics beyond the SM.

A plot of the direct W mass measurements in the past is shown in Figure 1.3. The present world average from all these measurements stands at M_W=80.399 $\pm$ 0.025 GeV.

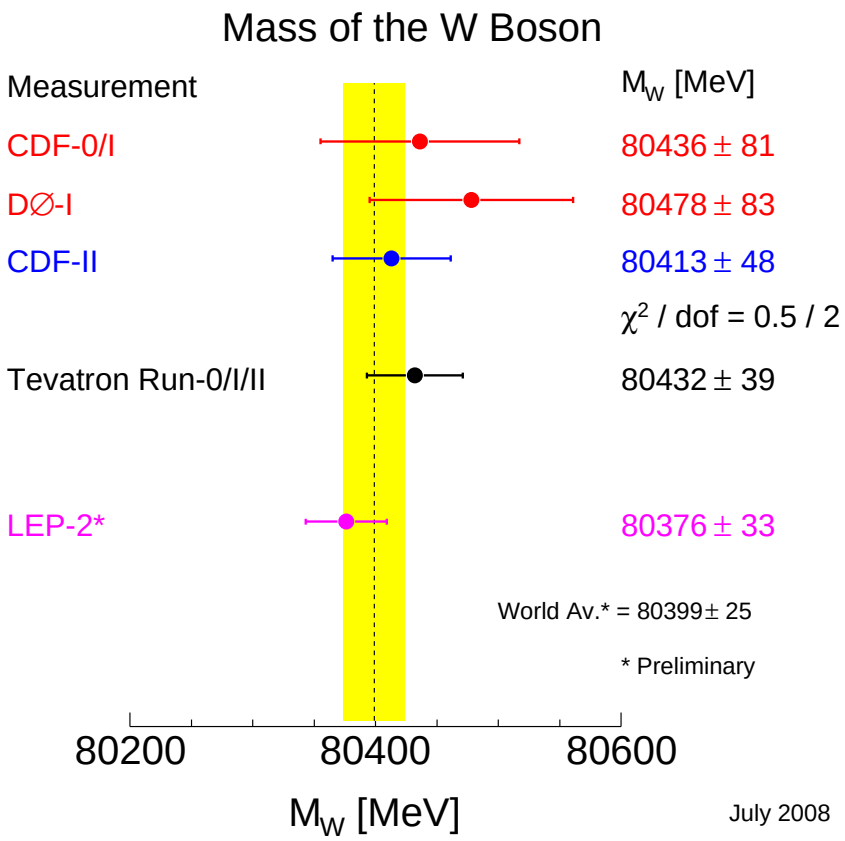

Figure 1.3. A plot showing the various direct M_W measurements over the years

CHAPTER 2

THE THEORY OF ELECTROWEAK INTERACTIONS

2.1 A Brief Introduction

The unification of the forces of electricity and magnetism was the second great unification in physics, the first being Newton's unification of terrestrial and celestial mechanics. In 1865, J.C. Maxwell postulated that both forces could be unified into a single theory involving a vector field that interacts between charges and currents. He called it the electromagnetic field. The photon (γ) was introduced as the massless carrier of the electromagnetic force and the Maxwell's equations introduced a universal constant - the velocity of light "c" - the value of c was determined experimentally.

In 1967-1968 a similar unification attempt was made by Glashow, Salam and Weinberg when they tried to show that electromagnetic and weak interactions are really two different manifestations of the same gauge theory. This symmetry between electromagnetic and weak interactions would be manifested at very large momentum transfers ($q^2 > 10^4$ GeV^2). At low energies it is a broken symmetry where out of the four mediating bosons of the electroweak force, the photon is massless whereas the W^+, W^- and Z bosons are massive. As we have read in Chapter 1, the W and Z have large masses indeed, ~ 100 GeV.

However, just like in the case of electromagnetism, the unbroken gauge theory describing the weak interactions calls for the carriers of the electroweak force to

have the same or zero mass. This is important for preserving the gauge invariance of the interaction (we will read about this later on). The fact that the W and Z bosons are massive (and not massless like the photon), is a sign that the "electroweak symmetry" is broken. This breaking of the electroweak symmetry and consequent assigning of masses to the W and Z are brought about by the "Higgs mechanism", which requires a new "Higgs field" and its accompanying Higgs boson. The Higgs boson is the particle that hides the symmetry of the Standard Model by shifting the equations in such a way that the once-massless particles now have mass.

The unification of the electromagnetic and weak interactions by way of the phenomenon of the electroweak symmetry breaking and the corresponding Higgs mechanism are the subjects of discussion in the different sections of this chapter.

2.2 Early Attempts at Unification

Unlike Quantum Electrodynamics (QED), the $V - A$ theory of weak interactions as postulated by Fermi is divergent at high energies. In Fermi's theory of β-decay the four fermions involved are assumed to have a contact (point-like) interaction with the Fermi constant, G_F, acting as the four-fermion coupling constant. At sufficiently large energies, the theory predicts cross-sections that exceed the limits set by the wave-theory, mainly due to the fact that G_F has the dimensions of an inverse power of the energy. For details on this please refer to [2]. Hence the need to redefine the weak interactions with the help of a dimensionless coupling constant.

The introduction of the neutral vector boson Z and thus the weak coupling g_W, to cancel out the divergences in neutral current interactions such as $\nu_e\bar{\nu}_e \rightarrow$

W^+W^- and $e^+e^- \rightarrow W^+W^-$ in an effective way, helped in this redefinition. From this it was pretty clear that the weak coupling constant g_W would have to be similar in magnitude to the electromagnetic coupling e. From the low q^2 limit calculations of the weak cross-sections it was estimated [2] that the approximate masses of the W and Z bosons were of the order of 100 GeV if they were to have the same coupling as in electromagnetism and an effective four fermion coupling of magnitude G_F to help explain weak interactions at low energies.

The above was the form of an early attempt at unifying the electromagnetic and weak forces, on the basis of the mediating W, Z bosons having the same intrinsic coupling strength to leptons ($g_W \sim e$).

2.3 Gauge Invariance

As the quest for unification continued, profound advancements in theory were made. In physics, a gauge theory is defined as a type of field theory in which the Lagrangian is invariant under a certain continuous group of local transformations (gauge transformations). We notice that the Dirac Lagrangian

$$\mathcal{L} = i\bar{\psi}\gamma^\mu\partial_\mu\psi - m\bar{\psi}\psi \tag{2.1}$$

is invariant under the global phase transformation given by:

$$\psi \rightarrow e^{iq\theta}\psi \tag{2.2}$$

In the above two equations ψ is the Dirac spinor wavefunction, γ^μ is the Dirac operator appropriate to a 4-component spinor field, ∂_μ is the derivative, q is the charge of the particle involved and θ is the phase factor. However, if the phase

factor is different at different space-time points, that is if θ is a function of x^μ of the form,

$$\psi(x) \rightarrow e^{iq\theta(x)}\psi(x) \tag{2.3}$$

the Lagrangian is not invariant under such a "local" phase transformation. The Lagrangian picks up an extra term from the derivative of θ such that

$$\mathcal{L} \rightarrow \mathcal{L} - (\partial_\mu\theta)\bar{\psi}\gamma^\mu\psi \tag{2.4}$$

In order that the complete Lagrangian be invariant under local phase transformations, the extra term in the above equation needs to be soaked up by redefining the Lagrangian in the following way:

$$\mathcal{L} = [i\bar{\psi}\gamma^\mu\partial_\mu\psi - m\bar{\psi}\psi] - (q\bar{\psi}\gamma^\mu\psi)A_\mu \tag{2.5}$$

where A_μ is some new field which changes according to the local phase transformations

$$A_\mu \rightarrow A_\mu + \partial_\mu\theta \tag{2.6}$$

This "new" Lagrangian compensates for the extra term in equation 2.4 and is locally invariant provided the newly introduced vector field A_μ (that couples to ψ) is massless. The added term in the equation 2.5 is brought about by considering the difference between global and local phase transformations while calculating derivatives of the fields.

$$\partial_\mu\psi \rightarrow e^{iq\theta}\Big[\partial_\mu + iq(\partial_\mu\theta)\Big]\psi \tag{2.7}$$

Here an extra piece involving $\partial_\mu \theta$ is present. If in the original (free) Lagrangian the derivative (∂_μ) is replaced by a covariant derivative (D_μ) of the form

$$D_\mu = \partial_\mu - iqA_\mu \tag{2.8}$$

the gauge transformation of A_μ will cancel the extra term in equation 2.7 and the invariance of $\mathcal{L}$ is restored.

The A_μ is identified as the electromagnetic potential and the Lagrangian is recognized as the one for Quantum Electrodynamics (QED). The global phase transformation can be thought of as multiplying ψ by a unitary 1×1 matrix:

$$\psi \rightarrow U\psi, \qquad U^\dagger U = 1 \tag{2.9}$$

This unitary group is U(1) and hence the symmetry involved is called "U(1) gauge invariance". The symmetry group U(1) is a commutative group and hence QED is an "abelian" gauge theory with one gauge field, the electromagnetic field, with the photon being the gauge boson.

2.4 Non-Abelian Gauge Theory

In an attempt to extend and generalize the original concept of gauge theory for an Abelian group, more complex phase transformations specified by non-commuting generators were considered. A "non-Abelian" gauge theory based on the SU(N) group was formulated by Yang and Mills in 1954 [66], with the intention of getting an explanation for strong interactions. This initial idea was not a success as the quanta of the Yang-Mills field must be massless in order to maintain gauge invariance but such massless particles should have had long range effects

that are not observed experimentally.

2.5 The Electroweak Standard Model - Weinberg-Salam SU(2)×U(1) Model

A gauge theory for unifying the weak and electromagnetic interactions was proposed by Glashow, Weinberg and Salam in 1967-1968. This theory of electroweak interactions was based on the SU(2) group of "weak isospin" and a U(1) group of "weak hypercharge". The generators of the weak isospin are denoted by $\vec{I}$ while the weak hypercharge is denoted by Y. In the electroweak theory the phenomenon of "spontaneous symmetry breaking" gives mass to the gauge bosons (which act as the force carriers or mediators in the electroweak field) all the while preserving the renormalizability of the theory. The crucial question of renormalizability was solved by Gerard 't Hooft in 1971. The fact that gauge theories remain renormalizable after spontaneous symmetry breaking lends credence to the theory and its purpose.

The fundamental force carriers in the GWS theory are vector bosons and consist of a massless isovector triplet denoted by $\vec{W}_\mu = \{W_\mu^{(1)}, W_\mu^{(2)}, W_\mu^{(3)}\}$ for the SU(2) part and a massless isosinglet B_μ for the U(1) contribution. Combinations of these four bosons give rise to the $W^\pm$, Z and photon, as we shall see.

From the equation 2.5 we have seen that the term representing the electromagnetic interaction in the QED Lagrangian is given by:

$$\mathcal{L} = qJ_\mu^{em} A_\mu \tag{2.10}$$

where J_μ^{em} represents the electromagnetic current.

For the electroweak interactions, the electromagnetic Lagrangian is replaced by two new terms, the first corresponds to an SU(2) weak isospin current $\vec{J}_\mu$ coupling

to the isovector triplet $\vec{W}_\mu$ and the second is a weak hypercharge current J_μ^Y which couples to the isosinglet B_μ.

Thus the interaction Lagrangian in the presence of field bosons $\vec{W}_\mu$ and B_μ can be written in the following form

$$\mathcal{L} = g\vec{J}_\mu \cdot \vec{W}_\mu + \frac{g'}{2} J_\mu^Y B_\mu \tag{2.11}$$

to first order. Here g and g' are the coupling constants of the $\vec{J}_\mu$ and J_μ^Y to $\vec{W}_\mu$ and B_μ respectively. Thus the isospin component of the interaction can be expressed as:

$$-ig\vec{J}_\mu \cdot \vec{W}_\mu = -ig\bar{\chi_L}\gamma^\mu \vec{I} \cdot \vec{W}_\mu \chi_L \tag{2.12}$$

and the hypercharge component of the interaction can be expressed as:

$$-i\frac{g'}{2} J_\mu^Y B_\mu = -ig'\bar{\psi}\gamma^\mu \frac{Y}{2}\psi B_\mu \tag{2.13}$$

The χ_L are the weak left-handed isodoublets of fermions and are explained further on in this section. The hypercharge is the "charge" of the $\mathrm{U}(1)_Y$ group and is related to the electromagnetic charge (Q) and isospin (I) by means of the Gell-Mann-Nishijima formula as:

$$Q = I^3 + \frac{Y}{2} \tag{2.14}$$

The isospin operators $\vec{I}$ which are the generators of the $\mathrm{SU}(2)_I$ weak isospin gauge group satisfy the commutation relation

$$[I^i, I^j] = i\epsilon_{ijk} I^k \tag{2.15}$$

With the help of equation 2.14 the electromagnetic current can be expressed in

terms of the isospin and hypercharge currents as follows:

$$J_\mu^{e.m.} = J_\mu^3 + \frac{J_\mu^Y}{2} \tag{2.16}$$

Here $J_\mu^{e.m.}$ is the electromagnetic current coupling to the charge Q and J_μ^3 is the third component of the isopsin current $\vec{J}_\mu$.

Now, the physical bosons of the electroweak field consist of the charged particles $W_\mu^\pm$ and the neutrals Z_μ and A_μ (the photon). The $W_\mu^\pm$ are obtained from a linear combination of the isospin components W_μ^1 and W_μ^2 while the Z_μ and A_μ are linear combinations of the components W_μ^3 and B_μ. Specifically, the $W_\mu^\pm$ can be expressed as:

$$W_\mu^\pm = \frac{1}{\sqrt{2}}(W_\mu^1 \pm W_\mu^2) \tag{2.17}$$

whereas the Z_μ and A_μ can be expressed via the following combinations of W_μ^3 and B_μ.

$$Z_\mu = \frac{gW_\mu^3 - g'B_\mu}{\sqrt{g^2 + g'^2}} \tag{2.18}$$

$$A_\mu = \frac{g'W_\mu^3 + gB_\mu}{\sqrt{g^2 + g'^2}} \tag{2.19}$$

Z_μ and A_μ are orthogonal i.e. $< Z_\mu \mid A_\mu >=0$. With the help of equation 2.16 the Lagrangian density from equation 2.11 can be written as:

$$\mathcal{L} = g(J_\mu^1 W_\mu^1 + J_\mu^2 W_\mu^2) + g(J_\mu^3 W_\mu^3) + g'(J_\mu^{e.m.} - J_\mu^3)B_\mu \tag{2.20}$$

Assuming $J_\mu^\pm = J_\mu^1 \pm iJ_\mu^2$, the Lagrangian is expressed in terms of $J_\mu^\pm$ as:

$$\mathcal{L} = \frac{g}{\sqrt{2}}(J_\mu^- W_\mu^+ + J_\mu^+ W_\mu^-) + J_\mu^3(gW_\mu^3 - g'B_\mu) + J_\mu^{e.m.} g'B_\mu \tag{2.21}$$

Inserting the expressions for W_μ^3 and B_μ from equations 2.18 and 2.19 respectively into equation 2.21 we obtain:

$$\begin{aligned}\mathcal{L} &= \frac{g}{\sqrt{2}}(J_\mu^- W_\mu^+ + J_\mu^+ W_\mu^-) + (g\cos\theta_W J_\mu^3 - g'\sin\theta_W \frac{J_\mu^Y}{2})Z_\mu \\ &+ (g'\cos\theta_W J_\mu^3 + g\sin\theta_W \frac{J_\mu^Y}{2})A_\mu \end{aligned} \tag{2.22}$$

The term (J_μ^- W_μ^+ + J_μ^+ W_μ^-) represents the charged weak current, ($g\cos\theta_W$ J_μ^3 - $g'\sin\theta_W$ $\frac{J_\mu^Y}{2}$) represents the neutral weak current term and ($g'\cos\theta_W$ J_μ^3 + $g\sin\theta_W$ $\frac{J_\mu^Y}{2}$) represents the electromagnetic neutral current term.

The A_μ term of the above equation can be identified with the electromagnetic current if and only if:

$$g'\cos\theta_W = g\sin\theta_W = e \tag{2.23}$$

Thus the relation $\frac{g'}{g} = \tan\theta_W$ also holds. Now in terms of the constant g, equation 2.22 can be written as follows:

$$\begin{aligned}\mathcal{L} &= \frac{g}{\sqrt{2}}(J_\mu^- W_\mu^+ + J_\mu^+ W_\mu^-) + \frac{g}{\cos\theta_W}(J_\mu^3 - \sin^2\theta_W J_\mu^{e.m.})Z_\mu \\ &+ g\sin\theta_W J_\mu^{e.m.} A_\mu \end{aligned} \tag{2.24}$$

The angle θ_W is called the weak mixing angle (or Weinberg angle). It is a fundamental parameter that describes how electromagnetic and weak forces mix.

The charged current $(V-A)$ weak interactions mediated by the $W^\pm$, organize the fundamental fermions and neutrinos into left-handed isodoublets (ξ_L) and right-handed isosinglets (ψ_R) which transform as

$$\xi_L \rightarrow \xi_L' = e^{i\alpha(x)\cdot I + i\beta(x)\cdot Y}\xi_L \tag{2.25}$$

$$\psi_R \rightarrow \psi'_R = e^{i\beta(x)\cdot Y}\psi_R \tag{2.26}$$

under the infinitesimal SU(2)×U(1) gauge transformations, where $\alpha(x)$ and $\beta(x)$ are gauge parameters. The grouping of the fermions is shown in Table 2.1. For a given fermionic field f, the left-handed (LH) and right-handed (RH) components can be projected out by use of the Dirac spinor γ_5:

$$f_R = 1/2(1-\gamma_5)f \tag{2.27a}$$

$$f_L = 1/2(1+\gamma_5)f \tag{2.27b}$$

TABLE 2.1

LH ISODOUBLETS AND RH ISOSINGLETS OF $SU(2)_I$ & $U(1)_Y$

Quarks		
$\begin{pmatrix} u \\ d \end{pmatrix}_L$ $(u)_R$ or $(d)_R$	$\begin{pmatrix} c \\ s \end{pmatrix}_L$ $(c)_R$ or $(s)_R$	$\begin{pmatrix} t \\ b \end{pmatrix}_L$ $(t)_R$ or $(b)_R$
Leptons		
$\begin{pmatrix} \nu_e \\ e \end{pmatrix}_L$ $(e)_R$	$\begin{pmatrix} \nu_\mu \\ \mu \end{pmatrix}_L$ $(\mu)_R$	$\begin{pmatrix} \nu_\tau \\ \tau \end{pmatrix}_L$ $(\tau)_R$

The neutral current term $J_\mu^{NC} = J_\mu^3$ - $\sin^2\theta_W$ $J_\mu^{e.m.}$ is the weak component of the two observed neutral interactions in terms of the new currents $\vec{J}_\mu$ and J_μ^Y (with the help of equation 2.16) that were introduced into the Lagrangian of the

electroweak field.

Thus the electroweak theory proposed on the basis of the SU(2)×U(1) gauge groups is capable of providing a renormalizable and gauge-invariant description of the electroweak interactions of leptons. With the help of the isotriplet vector boson $\vec{W}_\mu$ and an isosinglet vector boson B_μ, the theory incorporates both the electromagnetic and weak forces along with their appropriate properties. This model predicted neutral weak currents which were subsequently observed.

We will now take a more detailed look into the nature of the electroweak gauge bosons. As mentioned, of the four gauge bosons, one is massless and three are massive. In order to explain this, we need to discuss the phenomenon of the "electroweak symmetry breaking".

2.6 Spontaneous Symmetry Breaking and the Higgs Mechanism

In simple words, "spontaneous symmetry breaking" occurs when a system that is symmetric with respect to some symmetry group goes into a vacuum state that is not symmetric. When this happens, the system no longer appears to behave in a symmetric manner.

In the Standard Model the electroweak theory undergoes a spontaneous breakdown by the introduction of the Higgs Mechanism. This mechanism is invoked in a way that preserves the characteristics of local gauge invariance and renormalizability of the electroweak theory. A potential term (V(ϕ)) is introduced into the electroweak Lagrangian as follows:

$$\mathcal{L} =\mid (\partial_\mu - ig\vec{I}\cdot\vec{W}_\mu - \frac{ig'}{2}B_\mu)\phi \mid^2 -V(\phi) \tag{2.28}$$

where ϕ denotes an isodoublet scalar field and the potential V(ϕ) is given by:

$$V(\phi) = \mu^2 \phi^\dagger \phi + \lambda(\phi^\dagger \phi)^2 \tag{2.29}$$

In order to preserve the gauge invariance of the Lagrangian, the field ϕ must be an SU(2)×U(1) multiplet. The simplest choice is that of a Y=1 isodoublet given by:

$$\phi = \begin{pmatrix} (\phi_1 + i\phi_2)/\sqrt{2} \\ (\phi_3 + i\phi_4)/\sqrt{2} \end{pmatrix} \tag{2.30}$$

where the ϕ_i are the real scalar fields. If the parameters μ^2 <0 and λ >0, the locus of the SU(2)-invariant minimum of the potential V(ϕ) can be given by

$$\phi^\dagger \phi = \frac{1}{2}(\phi_1^2 + \phi_2^2 + \phi_3^2 + \phi_4^2) = -\frac{\mu^2}{2\lambda} \equiv \frac{v^2}{2} \tag{2.31}$$

The SU(2) symmetry can now be "spontaneously broken" by assuming that the physical vacuum is given by some specific choice of the minimum of the potential V(ϕ).

For example, one choice at minimum is given by:

$$\phi_1 = \phi_2 = \phi_4 = 0, \qquad \phi_3^2 = -\frac{\mu^2}{\lambda} \equiv v^2 \tag{2.32}$$

The vacuum state is then given by

$$\phi_0 = \sqrt{\frac{1}{2}} \begin{pmatrix} 0 \\ v \end{pmatrix} \tag{2.33}$$

Once the system falls into this specific vacuum state this SU(2) symmetry will be

lost or spontaneously broken. However the Lagrangian is still SU(2) invariant as it does not care about the location of the minimum of the vacuum state.

In order to observe the impact of this choice of vacuum, we can consider small perturbations of the fields about this minimum. These fluctuations can be parameterized in terms of the four real fields θ_1, θ_2, θ_3 and h in the following way:

$$\phi(x) = \frac{e^{i\vec{I}\cdot\vec{\theta}(x)/v}}{\sqrt{2}} \begin{pmatrix} 0 \\ v + h(x) \end{pmatrix} \tag{2.34}$$

Substituting the above form of ϕ into the equation 2.28 for the Lagrangian results in three massless fields θ_i, a term proportional to $2\mu^2 h^2$ and a number of cross terms proportional to $(W^i)_\mu \partial^\mu \theta_i$. The three massless fields characterize the three Goldstone bosons associated with the breaking of the SU(2)×U(1) symmetry down to $\mathrm{U}(1)_{em}$. The Lagrangian acquires a mass term for the h field leaving the θ fields massless.

Thus by exploiting the SU(2) gauge symmetry of the Lagrangian with the help of a gauge transformation of the type

$$\phi \rightarrow \phi' = e^{-i\vec{I}\cdot\vec{\theta}(x)/v}\phi \tag{2.35}$$

the scalar field h acquires a mass -$\frac{\lambda v^2}{2}$ and it is now called the "Higgs particle".

As discussed earlier, the Yang-Mills theory, also known as the non-Abelian gauge theory, predicts massless spin 1 gauge bosons, which (apart from the photon) have never been observed. It was Higgs' insight that when a gauge theory is combined with a spontaneous symmetry-breaking model, the massless bosons acquire a mass. These massive bosons $(W^\pm, Z)$ have been observed experimentally, thus solving the problem.

We now notice how the gauge bosons $W_\mu^\pm$, W_μ^3 and B_μ have acquired masses via the electroweak Lagrangian

$$| \, (-ig\vec{I} \cdot \vec{W}_\mu - i\frac{g'}{2}B_\mu)\phi \, |^2 \tag{2.36}$$

After some algebra, the mass terms can be expressed as follows:

$$(\frac{1}{2}vg)^2 W_\mu^+ W_\mu^- + \frac{1}{8}v^2[gW_\mu^3 - g'B_\mu]^2 + \mathcal{O}[g'W_\mu^3 + gB_\mu]^2 \tag{2.37}$$

The masses of the charged and neutral bosons can be identified from the above equation by comparing it to the standard mass terms: $M_W^2 W^+ W^-$, $\frac{1}{2}M_Z^2 Z^2$ and $\frac{1}{2}M_A^2 A^2$.

These comparisons yield

$$M_W = \frac{1}{2}vg \tag{2.38}$$

for the charged W bosons. On normalizing, for the Z_μ and A_μ vector bosons one obtains:

$$A_\mu = \frac{g'W_\mu^3 + gB_\mu}{\sqrt{g^2 + g'^2}} \qquad \text{with} \qquad M_A = 0; \tag{2.39}$$

$$Z_\mu = \frac{gW_\mu^3 - g'B_\mu}{\sqrt{g^2 + g'^2}} \qquad \text{with} \qquad M_Z = \frac{v}{2}\sqrt{g^2 + g'^2} \tag{2.40}$$

The theory now contains three massive ($W^\pm$, Z) and one massless vector boson (photon). From the above two equations the weak mixing angles can be defined in terms of the coupling constants g and g' as follows:

$$\cos\theta_W = \frac{g}{\sqrt{g^2 + g'^2}} \qquad \sin\theta_W = \frac{g'}{\sqrt{g^2 + g'^2}} \tag{2.41}$$

This helps us in attaining a new relationship between the W and Z masses.

$$\frac{M_W}{M_Z} = \frac{g}{\sqrt{g^2 + g'^2}} = \cos\theta_W \tag{2.42}$$

The boson A is associated with the photon, so M_A=0.

The phenomenon of the EW symmetry breaking can now be visualized in a simple way. In the standard model, at energies high enough so that the symmetry is unbroken, all elementary particles except the scalar Higgs boson are massless. At a critical energy, the Higgs field slides spontaneously from the point of maximum energy in a randomly chosen direction, causing the symmetry to be broken. Now the gauge boson particles such as the W and Z bosons acquire mass. The mass can be interpreted as the result of the interactions of these particles with the Higgs field.

In the Standard Model, it is postulated that fermions, such as the leptons and quarks also acquire mass as a result of their interaction with the Higgs field but not in the same way as the gauge bosons do.

As an overview, electroweak interactions are described by an SU(2)×U(1) gauge group. In the symmetric phase, the electroweak field theory predicts four massless gauge bosons. We invoke the Higgs mechanism which breaks the symmetry of the field yielding three massless Goldstone bosons and one massive scalar boson. This spontaneous breaking of the SU(2)×U(1) gauge symmetry destroys the masslessness of the gauge bosons. Three of the gauge bosons "eat" the three Goldstone bosons and are thereby endowed with mass, yielding the $W^{\pm}$ and Z. The fourth gauge boson remains massless and is the photon. In addition the theory requires the existence of a new, massive scalar called the Higgs boson.

In mathematical terms, the electroweak gauge bosons get their mass from the

breaking of the electroweak symmetry from SU(2)×U(1) to $U(1)_{em}$, caused by the Higgs mechanism. The subscript is used to indicate that these are different forms of U(1). The charge of $U(1)_{em}$ is given by $Q = Y/2 + I^3$, Y and I^3 have been mentioned before. This non-trivial, linear combination of Y and I^3 vanishes for the Higgs boson. $U(1)_{em}$ is defined to be the group generated by this linear combination, and is unbroken because the vacuum expectation value (VEV) of the Higgs boson is $U(1)_{em}$ invariant (i.e. the VEV is electrically neutral).

2.7 Parameterizing the Standard Model

The three parameters, g (the SU(2) coupling constant), g' (the U(1) coupling constant) and v (the Higgs vacuum expectation value) are important for specifying the tree level and higher order processes described by the electroweak interactions. However these parameters are not particularly well measured. Hence we need to express these parameters in terms of better measured quantities. The fine structure constant α, the Fermi coupling constant G_F and the mass of the Z boson M_Z are usually considered. With the help of equation 2.23, the coupling constants g and g' can be linked to the constant α.

$$\alpha = \frac{e^2}{4\pi\hbar c} = \frac{gg'}{4\pi\hbar c\sqrt{g^2 + g'^2}} \tag{2.43}$$

Now for obtaining the Fermi coupling constant G_F, the form of the charged current weak interaction for $\nu_e + e \rightarrow e + \nu_e$ can be parameterized as:

$$\mathcal{L}_{\mathcal{CC}} = g_W \cdot J(\text{lepton}) \cdot \text{W}^{\pm} \tag{2.44}$$

where $J(\text{lepton}) = \bar{\nu_e}\gamma^\mu(1+\gamma_5)e$. Besides, in the example $\nu_e + e \rightarrow e + \nu_e$ mediated by the $W^\pm$ which have a coupling constant g_W to the four fermions, the matrix element for the interaction is given by

$$\mathcal{M} \sim \frac{g_W^2}{q^2 + M_W^2} \tag{2.45}$$

In the low-q^2 limit, the current-current interaction is effectively pointlike and the four-fermion coupling constant G_F can be identified as

$$\frac{G_F^2}{2} \equiv \lim_{q^2 \rightarrow 0} \quad \frac{g_W^4}{(q^2 + M_W^2)^2} \tag{2.46}$$

or

$$g_W^2 = \frac{M_W^2 G_F}{\sqrt{2}} \tag{2.47}$$

Comparing equation 2.44 with the charged current component of the electroweak Lagrangian 2.22 we obtain

$$\frac{g}{2\sqrt{2}} = g_W = \left(\frac{G_F M_W^2}{\sqrt{2}}\right)^{1/2} \tag{2.48}$$

Thus the Fermi coupling constant can be expressed in the following way:

$$G_F = \frac{g^2}{4\sqrt{2}M_W^2} = \frac{1}{\sqrt{2}v^2} \tag{2.49}$$

2.7.1 Tree Level Value of W Mass

Substituting $e = g \sin\theta_W$ into the above equation we arrive at the tree level value of the mass of the W boson:

$$M_{W^\pm} = \left(\frac{g^2\sqrt{2}}{8G_F}\right)^{1/2} = \left(\frac{\sqrt{2}e^2}{8G_F \sin^2\theta_W}\right)^{1/2} \tag{2.50}$$

Inserting e^2=$4\pi\hbar c\alpha \simeq 4\pi/137$ and $G_F = 1.166 \times 10^{-5}$ GeV^{-2} we obtain:

$$M_{W^\pm} = \left(\frac{\pi\alpha}{\sqrt{2}G_F}\frac{1}{\sin^2\theta_W}\right)^{1/2} = \frac{37.4 \text{ GeV}}{\sin\theta_W} \tag{2.51}$$

to be compared with the first approximate estimate of the M_W given from equation 2.47 where in the limit g_W=e, we have $M_W^2 = \frac{e^2\sqrt{2}}{G_F}$ and hence $M_{W^\pm}, Z \simeq 100$ GeV.

It can also be shown that in the simplest gauge model (of Weinberg and Salam) with a single doublet of Higgs scalars that

$$M_Z = \frac{M_{W^\pm}}{\cos\theta_W} = \frac{75 \text{ GeV}}{\sin 2\theta_W} \tag{2.52}$$

Thus there is one free parameter in this model, namely θ_W, which determines the ratio of the couplings g and g' or equivalently the relative magnitude of the cross-sections for the charged and neutral current reactions.

The values of α, G_F and M_Z are shown in Table 2.2. The value of any other measurable combination of these three parameters such as $\sin^2\theta_W$ can be compared with its predicted value, thus testing the validity of Standard Model with the help of these parameters.

TABLE 2.2

PARAMETERS OF THE ELECTROWEAK SM AT TREE LEVEL

Parameter	Measured Value	Precision
α	1/137.0359895(61)	4.5×10^{-8}
G_F	$1.16637(2) \times 10^{-5}$ (GeV)$^{-2}$	1.7×10^{-5}
M_Z	91.187(7) GeV	7.7×10^{-5}

2.7.2 Higher Order Contributions to W Mass

At higher orders additional contributions from the masses and couplings of the fermions as well as the Higgs boson are added onto the theoretical predictions for the mass of the gauge bosons (M_W, M_Z). These extra contributions are termed as the radiative corrections and their inclusion is by means of higher orders in perturbation theory. As a result they are a potential source for changing the predictions for the observables as well as the relationships between them. Beyond the tree level estimate, the W mass expressed in terms of the higher order contributions that it includes is given as follows:

$$M_W^2 = \frac{\pi\alpha}{\sqrt{2}G_F}\frac{1}{\sin^2\theta_W}\frac{1}{(1-\Delta r)} \tag{2.53}$$

where in the "on-shell" scheme [54, 67] both masses are measurable quantities,

$$\cos\theta_W = \frac{M_W}{M_Z} \tag{2.54}$$

Here Δr signifies the contribution due to the radiative corrections. Two important contributions to Δr are those from the Higgs boson and the fermion masses. These

are shown in Figure 2.1. The first shows a one-loop correction to the W due to the virtual top and bottom quark loops. This contribution to $\Delta r \propto M_t^2$ - M_b^2 and can be expressed in the following way:

$$\Delta r_{tb} \approx \frac{-3G_F M_W^2 M_t^2}{8\sqrt{2}\pi^2(M_Z^2 - M_W^2)} \tag{2.55}$$

after neglecting terms of order M_b^2/M_t^2. The second figure shows the W radiating and then reabsorbing a Higgs boson. The contribution from this process is $\Delta r \propto \ln M_{Higgs}$, lowering M_W.

In conjunction with a measurement of the top quark mass the Standard Model predicts M_W up to a 200 MeV uncertainty [51, 52] due to the unknown mass of the Higgs boson.

Thus using the parameters of the Standard Model and the theoretical framework as an input and taking into account the higher order contributions from the radiative corrections, a value of M_W can be obtained. An experimental determination of the W mass can be compared with the theoretically calculated values, thus providing a test of the theory at the quantum level. If there are new particles that couple to the W, they may give rise to additional corrections to the W. For example the Minimal Supersymmetric Model (MSSM) can increase M_W by up to 250 MeV [68]. Thus any significant deviations of M_W from its Standard Model prediction could signal the presence of non Standard Model physics.

A disrepancy beyond the limits set by the Standard Model could be a signal of new physics. The challenge is to measure the W mass to a precision of 0.05% in order to be sensitive to these corrections.

Hence a measurement of the W mass is extremely important not only as a rigorous test of the Standard Model but as an excellent probe when searching for

some new physics.

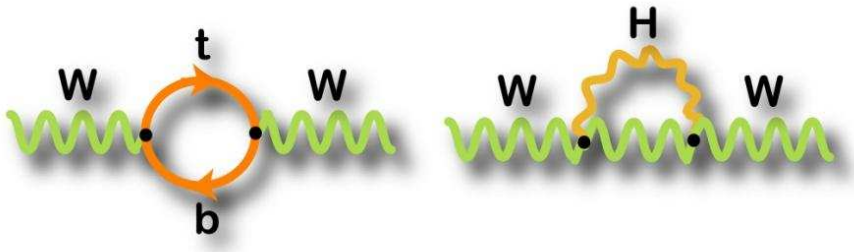

Figure 2.1. The higher order contributions to the radiative corrections for the W mass

CHAPTER 3

W/Z BOSON PRODUCTION AND DECAY

3.1 A Brief Introduction

At the center-of-mass energy $\sqrt{s}$=1.96 TeV of the colliding protons and antiprotons, the W and Z intermediate vector bosons (V) are primarily produced by the annihilation of valence quarks and antiquarks. This is referred to as a hard-scattering process [69]. During the interaction the initial proton and antiproton break up and the fragments hadronize. Figure 3.1 shows the lowest order diagrams for the $u\bar{u}$ ($d\bar{d}$) $\rightarrow Z$ and $u\bar{d}$ ($\bar{u}d$) $\rightarrow W^+(W^-)$ processes, the simplest forms of the hard scatter. However the initial state quarks can also radiate gluons which are usually soft, but could be highly energetic from time to time and give rise to hadron jets. Due to the fragmentation and hadronization of the partons subject to momentum conservation, there is a hadronic recoil in the direction opposite to the vector boson and its decay products.

The cross sections for these hard-scattering processes from hadron collisions can be computed at the parton level. Scattering processes at high energy colliders can consist of either "hard" or "soft" contributions or both. For "hard" processes that involve large momentum transfer, e.g. V or Higgs boson production or high p_T jet production, the rates and event properties can be explained quite precisely using the theories of perturbative QCD [70]. For "soft" processes

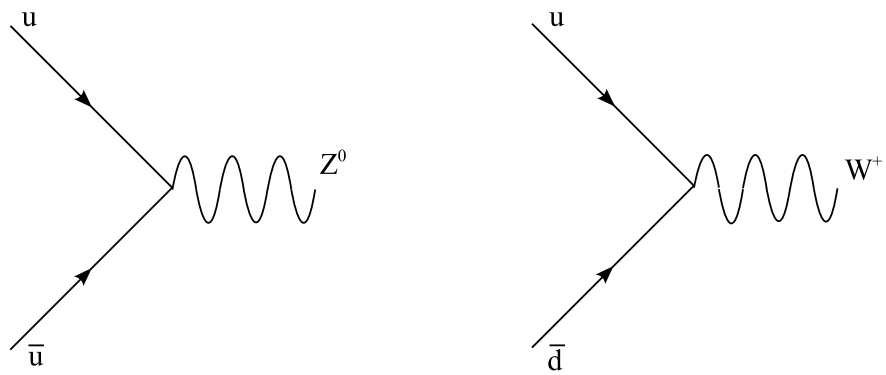

Figure 3.1. Lowest order diagram for the W and Z production

such as the emission of soft gluons and multiple parton interactions, the rates and properties lie outside the regime of perturbative QCD and are dominated by non-perturbative QCD effects. These are not adequately understood at the moment and are described by phenomenological models.

The cross-sections required for modeling the production and decay of the vector bosons are introduced in this chapter. In order to present the complete production dynamics of the vector bosons in $p\bar{p}$ collisions, the contributions from the parts describing the hard-scattering process (by means of perturbative physics) and those describing the soft processes (by means of non-perturbative physics) have been outlined below.

3.2 Vector Boson Production

For a complete description of the production dynamics of the vector bosons, we need to know the differential production cross-section in terms of the mass Q, rapidity y, and transverse momentum q_T of the produced vector bosons. For

purposes of convenience (especially while generating events as discussed in Chapter 11), we factorize this into:

$$\frac{d^3\sigma}{dq_T^2 dy dQ} \approx \left.\frac{d^2\sigma}{dq_T^2 dy}\right|_{Q^2=M_W^2} \times \frac{d\sigma}{dQ} \tag{3.1}$$

in terms of the q_T, y and Q of the bosons. Here $\left.\frac{d^2\sigma}{dq_T^2 dy}\right|_{Q^2=M_W^2}$ represents the differential cross-section for the boson production and $\frac{d\sigma}{dQ}$ represents the mass spectrum.

For $p\bar{p}$ collisions, the vector boson production cross-section is given in terms of the parton cross-section $\hat{\sigma}_{i,j}$ convoluted with the parton distribution functions (PDF) $f_i(x, Q^2)$ and summed over the parton flavors i, j. Thus

$$\frac{d^2\sigma}{dq_T^2 dy} = \sum_{i,j} \int_0^1 dx_a \int_0^1 dx_b \; f_i(x_a, Q^2) f_j(x_b, Q^2) \times \delta(s x_a x_b - Q^2) \frac{d^2\hat{\sigma}_{i,j}}{dq_T^2 dy} \tag{3.2}$$

Here $f_i(x_a)$ represents the probability density for finding a parton with flavor a in hadron A with momentum fraction x_a, whereas $f_j(x_b)$ gives the probability density to find a parton of flavor b in hadron B with momentum fraction x_b. $d^2\hat{\sigma}_{i,j}/dq_T^2 dy$ represents the differential cross section for these partons to undergo the hard-collision process. The momentum fractions x_a and x_b are defined as the ratio of the longitudinal momenta of the partons to those of the incoming parent hadrons. Thus,

$$x_a = q_a/P_A, \qquad x_b = q_b/P_B \tag{3.3}$$

where q_a and q_b are the longitudinal momenta of the quarks and P_A and P_B are the longitudinal momenta of the hadrons (protons or anti-protons).

The components of momenta of the incoming partons can be written as

$$p_a^\mu \simeq \frac{\sqrt{s}}{2}(x_a, 0, 0, x_a) \qquad p_b^\mu \simeq \frac{\sqrt{s}}{2}(x_b, 0, 0, -x_b) \tag{3.4}$$

where $\sqrt{s} = (P_A + P_B)$.

If the proton direction is defined to be along $+z$-axis, then the energy and momentum of the vector boson (V) can be written as:

$$E_V = \frac{\sqrt{s}}{2}(x_a + x_b) \tag{3.5a}$$

$$P_V = \frac{\sqrt{s}}{2}(x_a - x_b) \tag{3.5b}$$

where $\sqrt{s}$=1.96 TeV is the center-of-mass energy of the $p\bar{p}$ collision.

Several theoretical groups [71, 72] have computed $d^2\sigma/dq_T^2dy|_{Q^2=M_W^2}$ using a perturbative calculation [73] in the high-q_T regime and a non-perturbative resummation formalism [74, 75] in the low-q_T regime.

The parton cross-section can be written as:

$$\frac{d^2\hat{\sigma}}{dq_T^2dy} = \frac{\hat{\sigma}_0}{4\pi\hat{s}}\left[\int d^2I e^{i\vec{q}_T\cdot\vec{I}} \cdot \hat{W}(I) \times e^{-S} + Y\right] \tag{3.6}$$

where $\hat{\sigma}_0$ is the tree-level parton cross-section, $\hat{s}$ is the center-of-mass energy of the partons and I is the impact parameter in transverse momentum space. $\hat{W}$ and Y are the perturbative terms, while S parameterizes the non-perturbative physics. The square of the parton center-of-mass energy, $\hat{s}$, is related to the corresponding center-of-mass energy, s, by:

$$\hat{s} = x_a x_b s. \tag{3.7}$$

Now in the notation of Ref. [71],

$$S = \left[g_1 + g_2 \ln\left(\frac{Q}{2Q_0}\right) \right] I^2 + g_1 g_3 \ln(100 x_a x_b) I \tag{3.8}$$

where Q_0 is a cutoff parameter and x_a and x_b are the momentum fractions of the intial state partons. The form of the function S is motivated phenomenologically and the parameters g_1, g_2 and g_3 have to be determined from experimental datasets.

We shall see in Chapter 11 that the hard-scattering process that produces the vector boson can be described by perturbative QCD [76] to a point that there is relatively good agreement between theoretical predictions and measured cross-sections. However problems arise when the perturbative corrections from real and virtual gluon emissions (by the quarks/gluons) are computed. Soft (low energy) gluons or final state partons that are emitted collinear with the initial parton cause a double logarithmic divergence of the perturbative expansion. These large contributions to perturbative diagrams in which the emitted partons are soft or move in collinear groups and communicate over long distances while carrying small momentum fall in the regime of non-perturbative physics. This requires a separate treatment, most of which is derived on the basis of phenomenological models at present. More information on these divergences is presented in the section on the transverse momentum of the gauge bosons.

After generating the kinematics of the W/Z boson, the mass dependence of the production cross-section needs to be folded in. The line shape of the vector boson is not exactly easy to describe analytically. A Breit-Wigner curve with a mass dependent width is used to model the line shape of the resonance. However in $p\bar{p}$ production, the mass spectrum differs from the strict Breit-Wigner resonant

line shape of the partonic cross-section due to the variation of the parton flux with the parton momentum. Hence the mass spectrum is given by:

$$\frac{d\sigma}{dQ} = \mathcal{L}_{q\bar{q}}(Q)\frac{Q^2}{(Q^2 - M_W^2)^2 + Q^4\Gamma_W^2/M_W^2} \tag{3.9}$$

The intrinsic width of the W is $\Gamma_W = 2.098 \pm 0.048$ GeV [77]. The function $\mathcal{L}_{q\bar{q}}(Q)$ is called the parton luminosity and is given by:

$$\mathcal{L}_{q\bar{q}}(Q) = \frac{2Q}{s}\sum_{i,j}\int_{Q^2/s}^{1}\frac{dx}{x}f_i(x,Q^2)f_j(Q^2/sx,Q^2) \tag{3.10}$$

The parton luminosity is evaluated by generating $W \to e\nu$ events using Monte-Carlo event generators (e.g. PYTHIA, REBSOS) interfaced with parton distribution functions and subjecting them to the same kinematic and fiducial criteria as for the collider data W and Z samples.

The variables $d^2\sigma/dq_T^2dy$ and $d\sigma/dQ$ are treated as probability densities for generating the four-momenta of the vector bosons as we shall see in Chapter 11.

3.3 Determination and Use of the Parton Distribution Functions

The parton distribution functions include the contribution from the soft processes (i.e. where the momenta of the emitted gluons are much less than that of the vector boson). Hence they are derived from experiment while the cross sections ($\hat{\sigma}_{i,j}$) are calculated in QCD perturbation theory. The $\overline{\text{MS}}$ definition [76, 78] is in terms of operators and is independent of any particular physical process. These parton distributions then appear in the QCD formula for any process with one or two hadrons in the initial state.

Currently the most comprehensive derivations of the parton distributions are

being done by the CTEQ [79] collaboration in the U.S.A. and MRST [80] group in the U.K. These groups perform a global fit to the data from various experiments with the help of a parameterization for the PDFs at some standard factorization scale (μ_0).

The CTEQ 6.1 version of the PDFs [81] does a twenty parameter fit to the world data and obtains a set of parameters that are orthogonal to each other. Each parameter is varied by a positive and negative one-sigma deviation to give rise to a pair of PDFs. A set of 40 PDFs (20 pairs) is generated in this way over all the parameters. The variations are based at the 90% confidence level. The central set of the parameters (obtained from the fit) is referred to as the central PDF set for future purposes. In the FAST MC the central PDF set is used for generating the W and Z events and the 40 PDF sets are used for estimating the systematic errors associated with the PDFs.

Given some set of values for the parameters describing the PDFs at μ_0, namely $f_{a/A}(x_a, \mu_0^2)$, one can determine $f_{a/A}(x_a, \mu^2)$ for all higher values of μ by using the evolution equation [76].

3.4 Transverse Momentum of the Gauge Bosons

The initial momenta of the colliding quarks that undergo hard scatter and produce the vector (W/Z) boson is not known. Hence we cannot reconstruct a Lorentz-invariant mass for $W \rightarrow e\nu$ decays. A knowledge of the transverse momentum distribution of the W boson ($\vec{p}_T^{\,W}$) is necessary for measuring its mass from the kinematic distributions.

We can measure the W boson $\vec{p}_T$ spectrum indirectly by measuring $\vec{u}_T$, the summed $\vec{p}_T$ of all the particles that recoil against the W boson. Momentum

conservation requires the W boson $\vec{p_T}$ to be equal and opposite to $\vec{u_T}$. However the precision of the $\vec{u_T}$ measurement is insufficient, especially for small values of $\vec{u_T}$, for constraining the W spectrum as tightly as is necessary for a precise W mass measurement.

Thus, other data sets need to be used for constraining the model. Just like the rapidity distribution, one can calculate the p_T distribution of the produced vector boson. Theoretical calculations provide a formalism to describe the boson p_T spectrum, but it includes g_1, g_2, g_3 at low p_T (Eqn. 3.8) and perturbative QCD at high p_T.

Like Drell-Yan lepton pairs, most W and Z bosons (collectively referred to as V) are produced with relatively little transverse momentum, i.e., $p_T << M_V$. In the lowest order Drell-Yan mechanism, the colliding partons are assumed to be exactly collinear with the colliding hadrons, and so the vector gauge bosons are produced with p_T=0 only. This approach does not take into consideration the intrinsic (non-perturbative) transverse motion of the quarks and gluons inside the colliding hadrons, nor of the possibility of generating large transverse momentum by recoil against additional energetic partons produced in the hard-scattering.

At low transverse momenta (p_T), the intrinsic transverse motion of the partons inside the colliding hadrons, $k_T \sim \Lambda_{\mathrm{QCD}}$, cannot be ignored ($\Lambda_{\mathrm{QCD}}$ is the scale parameter in QCD theory [2]). Thus effects of multiple soft gluon emission in the initial or final state of the interacting partons could dominate the low p_T distributions of the vector bosons. In theoretical terms, these effects are of order α_s.

The dominant contribution to the production cross-section of the vector bosons comes from the leading order (LO) quark-antiquark annihilation partonic process

$q\bar{q} \to V$, the first diagram of Figure 3.2. The next-to-leading-order (NLO) partonic processes are $q\bar{q} \to Vg$ and $gq \to Vq$ (Compton scattering) as shown in the second and third diagrams of Figure 3.2. Their contribution to the physical cross-section turns out to be rather large and cannot be ignored at low p_T. Besides, processes where soft interactions occur along with hard interactions need to be understood for comparisons to the perturbative predictions.

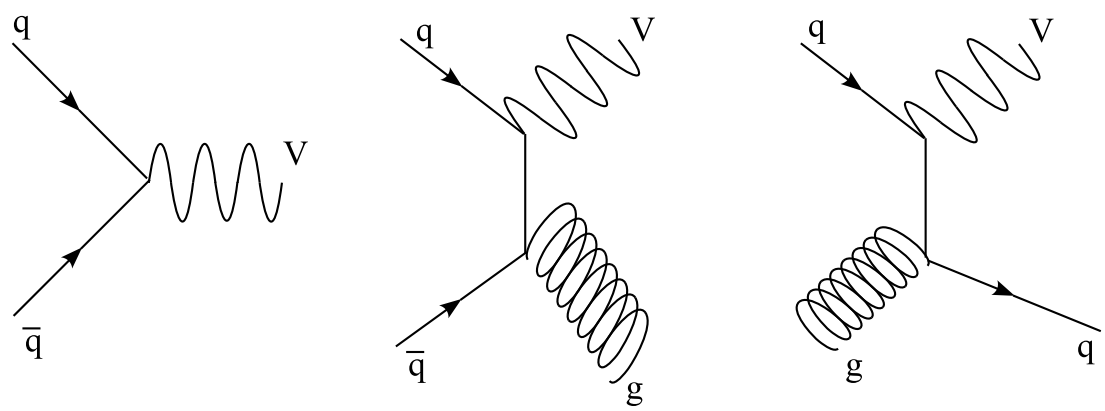

Figure 3.2. Feynman diagrams for (a) LO, and (b,c) NLO partonic processes contributing to the vector boson production

The measured p_T distribution of the lepton pairs from Drell-Yan in fixed target pN collisions is well parameterized by assuming a Gaussian distribution for the k_T with $\langle k_T \rangle \sim 700$ MeV. However this data clearly shows evidence of a hard power-law tail, which can be attributed to the momenta of one or more hard partons that could have been emitted (perturbative contribution) from higher-order processes

like $q\bar{q} \to Vg$ and $gq \to Vq$, etc.

The matrix elements for these annihilation ($q\bar{q} \to Vg$) and Compton scattering ($gq \to Vq$) processes can be computed with the help of their Feynman diagrams and the transverse momentum distribution of the V boson $d\sigma/dp_T^2$ can then be obtained by convoluting these matrix elements with the parton distribution functions in the usual way.

A major problem lies in the fact that the lowest-order perturbative contribution to the p_T distribution defined in this way is singular as $p_T \to 0$. This is because the final state partons become soft and/or are emitted collinear with the initial-state partons. In addition, higher-order contributions from processes like $q\bar{q} \to Vgg$ are also singular when the final-state gluons become collinear. The former singularity appears as logarithmic terms of the form $\log(p_T/M_V)$ which start to diverge as p_T and M_V become very disparate (i.e. $p_T << M_V$). The perturbative descriptions of these processes thus break down in these non-perturbative regimes.

In order to describe the phenomena observed at high-energy colliders and to estimate genuine non-perturbative effects correctly (in p_T distribution at $p_T << M_V$), the large logarithimic terms are brought under control by the "resummation" technique. This is an alternate approach to the systematic determinations of the higher and higher orders in the perturbative expansion of a particular observable. This approach can prove to be very useful under a different set of conditions than a fixed-order approach.

Resummation is an analytical approach in which the dominant contributions from each order in perturbation theory are singled out and "resummed" with the help of an evolution equation. Various methods for performing resummations are available [82–86].

The RESBOS program [87] is one such publicly available program that provides NLO resummed predictions at low values of the transverse momenta (p_T) of the bosons, for processes such as W, Z, $\gamma\gamma$ and Higgs boson production at hadron-hadron colliders. At high transverse momenta of the bosons ($p_T > 50$ GeV) the perturbative QCD calculations are reliable for dealing with the emission of hard partons. The hard (perturbative) and intrinsic (non-perturbative) contributions can be combined using a convolution integral in transverse momentum space, to yield a theoretical prediction that is valid for all values of p_T [71, 72, 88]. This allows RESBOS to describe the perturbative and non-perturbative regions of the partonic processes correctly, with the aid of the p_T-resummed perturbative QCD calculations for these Drell-Yan processes.

3.5 Vector Boson Decay

The W and Z are massive gauge bosons and have very short lifetimes ($\sim 10^{-24}$ sec). They decay dominantly into two fermions. Thus the Z boson can decay into a quark-antiquark pair or into a pair of leptons, keeping the lepton number conserved. Similarly the W boson can decay into a lepton pair (lepton number is conserved) or into a quark-antiquark pair. The lepton and neutrino pair, namely $l\bar{\nu}_l$ or $\bar{l}\nu_l$ is known as the leptonic channel. The quark-antiquark pair $q\bar{q}$ is known as the hadronic channel.

As the decay of W bosons into fermions has been well studied and understood to proceed via the standard $V - A$ coupling of the charged current, it is possible to predict the angular distribution of the decay fermions if the helicity of the W boson is known. At lowest order the W boson is fully polarized along the beam direction due to the $V - A$ coupling. The resulting angular distribution of the

charged lepton in the W rest frame is given by:

$$\frac{d\sigma}{d\cos\theta^*} \propto (1 - \lambda q \cos\theta^*)^2 \tag{3.11}$$

where λ is the helicity of the W with respect to the proton direction, q is the charge of the lepton and θ^* is the angle between the charged lepton and proton beam directions in the rest frame of the W boson. In the rest frame of the W, the fermions are produced back-to-back and so the energy of each is half of the mass of the W.

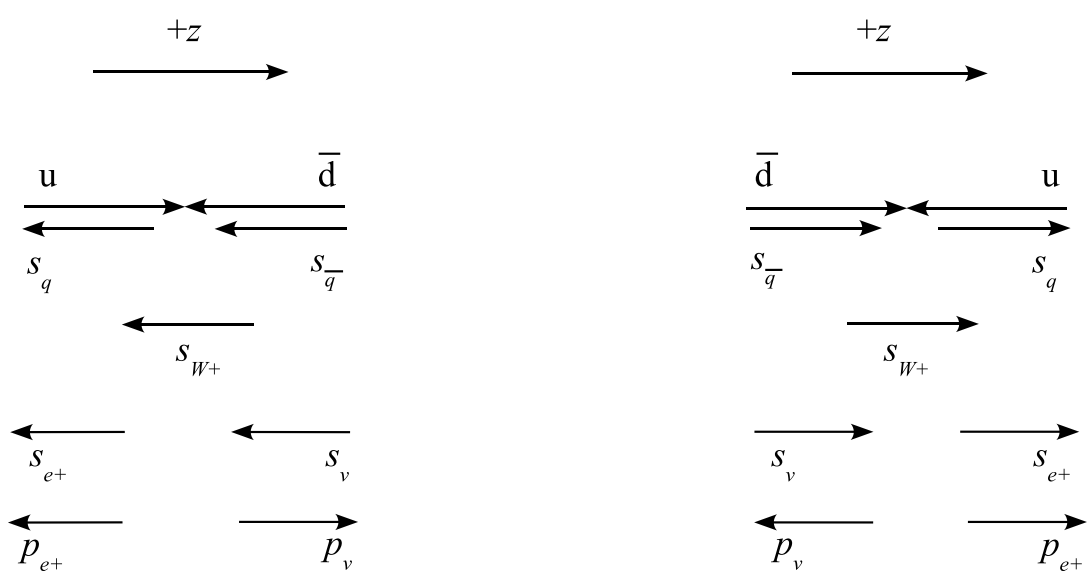

Figure 3.3. Illustration of the spin states for W production and decay. The left plot is for a W^+ produced with valence quarks while the right plot is for a W^+ produced with sea quarks

Figure 3.3 shows the polarization of the W produced in $p\bar{p}$ collisions. Since the weak interactions are left-handed, the spin of the quark is directed opposite to its momentum (left-handed) while the spin of an antiquark is along the same direction as its momentum (right-handed). Most of the time during the production of a W, the valence quark comes from the proton and the valence antiquark from the antiproton so that the spin of the W points along the direction of the incoming antiquark. The helicity λ=-1. In the event that the W is made from sea quarks, there is a 50 % chance that the quark comes from the antiproton and the antiquark from the proton so that the resulting W points in the direction of the proton and λ=1.

Radiation from the decay fermions or the W boson, known as final-state radiation, can bias the mass measurement. If the decay electron radiates a photon that is well separated from its parent so its energy cannot be included in the electron energy, or if the on-shell W boson radiates a photon and becomes off-shell at the time of its decay, the measured mass will be biased low. The energy spectrum and angular distribution of these final state photons are studied and are included as electroweak radiative corrections in the energy of the decay products up to next-to-leading-order α, while simulating the W events.

Radiation by the initial interacting quarks or the W, if the final W is still on-shell, does not affect the mass of the fermion (eν) pair from the W decay.

CHAPTER 4

THE EXPERIMENTAL APPARATUS

4.1 A Brief Introduction

The experimental apparatus used for this precise measurement of the W mass consists of the multi-purpose particle detector at the DØ experiment at Fermilab. Fermilab is home to the Tevatron - the most powerful operational particle accelerator in the world at present. It is a synchrotron that accelerates beams of protons and antiprotons to 99.99999954 % of the speed of light around a ring of four-mile circumference. Beams of protons and antiprotons, each of energy $\sim$ 1 TeV (10^{12} eV), travel in opposite directions through a vacuum pipe, mostly surrounded by superconducting electromagnets which bend the beam through the circular tunnel.

The two beams collide at the centers of two 5,000-ton particle detectors positioned around the beam pipe at two different locations inside the tunnel. The collision point BØ is the location of the CDF (Collider Detector at Fermilab) experiment, whereas the DØ experiment derives its name from its collision point. Both of these hadron collider physics experiments scour the debris of these highly energetic collisions, looking for signs of interesting physics and discoveries that could roll back the frontiers of knowledge.

The collisions occur every 396 ns at enormously high energies, with a center of mass energy (E_{cm} or $\sqrt{s}$) of 1.96 TeV. Thus they recreate conditions similar

to those present at the very early stages of the universe (moments after the Big Bang) and thus probe the structure of matter at a very small scale.

There are more than 1,000 superconducting magnets inside the Tevatron, which operate at -268° Celsius temperatures and produce magnetic fields much stronger than those of conventional magnets. The various types of magnets help to bend, focus and steer the beams in the beam pipe along the tunnel

The different accelerators in the Fermilab complex which contribute to the Tevatron's operation at these extremely high energies are described in this chapter. The DØ detector which helps physicists find the occurrence of interesting collisions and records them on tape for many an interesting analysis later on is described in details here.

4.2 Fermilab's Accelerator Chain

Fermilab uses a series of accelerators to create the world's most powerful particle beams. The first step involves creating proton and antiproton beams with hydrogen gas. Upon enough accumulation and consequent acceleration up to energies of 150 MeV , both the beams are loaded into the Tevatron. The Tevatron accelerates them further, up to energies of 1 TeV each, before allowing them to collide at the center of the two detectors, CDF and DØ. Figure 4.1 shows a layout of the different accelerators in the chain and their contributions to the production and acceleration of the protons and antiprotons, at various stages of the process are outlined below.

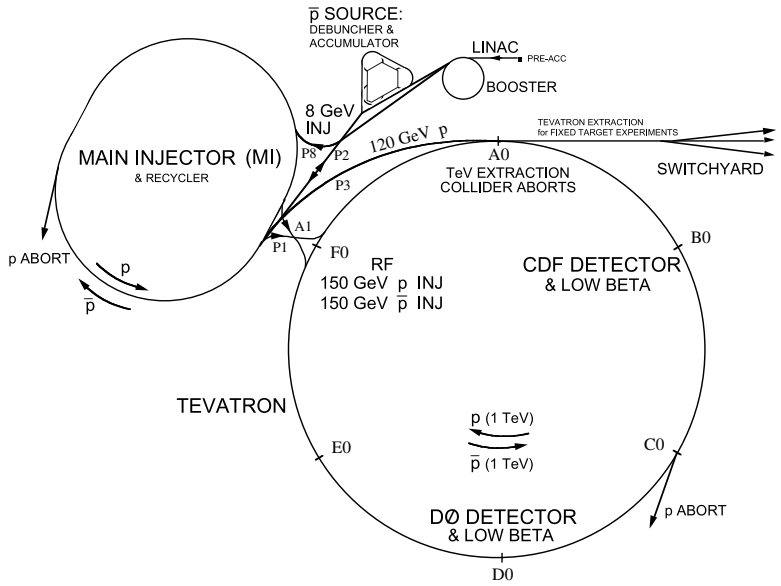

Figure 4.1. A general layout of Fermilab's accelerators chain

4.2.1 The Cockcroft-Walton Generator

The Cockcroft-Walton pre-accelerator provides the first stage of acceleration. Here hydrogen gas is ionized to create negative ions, each consisting of two electrons and one proton. The ions are accelerated by a positive voltage and reach an energy of 750 keV.

4.2.2 The Linear Accelerator (LINAC)

The negative hydrogen ions enter a linear accelerator (Linac). It is approximately 155 meters long and it accelerates the hydrogen ions up to 400 MeV by means of oscillating electric fields. Just before entering the Booster, the ions pass through a carbon foil, which strips off the electrons from the ions thus leaving only the protons.

4.2.3 The Booster

The third-stage accelerator is the Booster. It is a circular accelerator that bends the proton beams into a circular path. The protons coming in from the Linac travel around the Booster some 20,000 times. With each revolution, the radio-frequency(RF) cavities in the booster provide an accelerating force to the beam. By the end of the acceleration cycle, the energy of the protons is boosted up to 8 GeV.

4.2.4 The Main Injector

The Booster delivers protons to the Main Injector. The Main Injector completed in 1999, has become an essential part of Fermilab's accelerator complex for accelerating and transferring beams. It has four primary functions that support the Tevatron Collider.

1. It accelerates protons from 8 GeV to 150 GeV before injecting the beam into the Tevatron.

2. It produces protons of energy 120 GeV and delivers them for antiproton production.

3. It contains the Recycler (storehouse for cooling and storing antiprotons), receives antiprotons from it and accelerats them to energies of 150 GeV.

4. It injects protons and antiprotons into the Tevatron for further acceleration of up to 1 TeV.

4.2.5 The Antiproton Source

Producing antiprotons is a difficult and expensive undertaking. The antiproton source consists of three major components and Figure 4.2 is a pictorial representation of it.

1. The Target Station - Antiprotons are produced by irradiating a Nickel target with a beam of 120 GeV protons from the Main Injector every 1.5 sec. For every one million protons that hit the target, only about 20 antiprotons at energies of 8 GeV, survive to be stored in the Accumulator. The antiprotons are focussed into a beam line by a Lithium lens. The beam from the lens consists of several other particles besides antiprotons, hence the antiprotons are separated by sending the beam through a pulsed magnet which acts as charge-mass spectrometer.

2. The Debuncher - The beam in the Main Injector is accelerated using radio-frequency sources(RF), hence it is "bunched" by the time it is incident at the target station. The antiprotons produced are also bunched, but they possess a large spread in energy which is undesirable for the accelerators downstream of the target station. Thus the function of the Debuncher is to shape the beam so it possesses a narrow energy spread and large time spread.

   The Debuncher receives the low energy antiprotons at a different phase of the RF than the high energy ones, due to the difference in path lengths around the accelerator. This difference in RF phase causes the low energy particles to be accelerated while the high energy particles are decelerated. Subsequently the energy spread is reduced and the time spread is increased in this way. The debunching process takes about 100 milliseconds.

3. The Accumulator - This device accumulates the antiprotons by the momentum stacking of the successive pulses of antiprotons from the Debuncher over several hours or days. Both the RF and stochastic cooling systems (a technique used to reduce the transverse emittance of the beam) are used in the stacking process. The Accumulator is capable of cooling and storing the antiproton beam over many hours. It also transfers the antiprotons to the Recycler periodically, for additional cooling and accumulation.

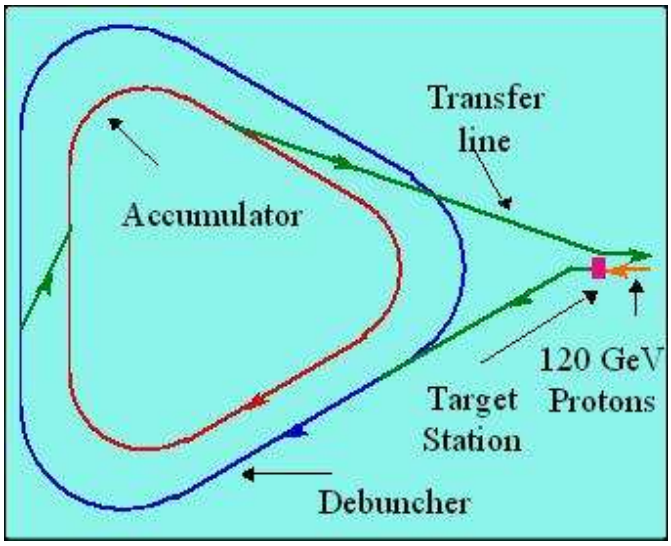

Figure 4.2. The different components of the antiproton source

4.2.6 The Recycler

Since 2005 the Recycler has become the sole storage ring for the antiprotons used in the Tevatron collider. The operational role of the Antiproton source at present, is confined to producing the antiprotons and transferring them to the Recycler periodically. The Recycler is 3.3 km in circumference located in the Main Injector tunnel, directly above the Main Injector beamline. It uses permanent magnets to store antiprotons at 8 GeV. It has an electron-cooling system which mainly reduces the longitudinal emittance of the beam by "mixing" the antiprotons with a continuous 4.3 MeV beam of electrons. These electrons are provided by a Pelletron accelerator adjacent to the ring. The electron beam, with a current of up to 0.5 Amperes and power of up to 2 MegaWatt, travels for approximately 20 m along the same path as the antiprotons, and is then sent back to the Pelletron for recirculation. The electrons interact with the antiprotons, cooling the beam and reducing the spread in longitudinal momentum. The beams are improved since the antiprotons that are traveling too fast are slowed down as they bump into the electrons and the slow antiprotons are sped up as they are hit by faster electrons. The Recycler injects the antiprotons into the Main Injector for acceleration up to energies of 150 GeV.

4.2.7 The Tevatron

The Tevatron receives the protons and antiprotons at energies of 150 GeV from the Main Injector and accelerates each beam to 980 GeV before colliding them. The Tevatron tunnel is buried 8 meters below grade, underneath an earthen berm. Its more than 1000 super-conducting magnets operate with the help of about 200,000 adjustable parameters. They operate at - 450° Fahrenheit and produce

magnetic fields of 4.2 Tesla. The dipole magnets bend the particle beam so that it stays within the beam pipe during its orbit, while the quadrupole magnets focus particle beams confining them into a thin line inside the beam pipe. Correction magnets are used for the fine-tuning of beam orbits, thus providing extra focus or horizontal and vertical steering of the beam.

The beam delivered by the Tevatron comes in "bunches" which are spaced according to the RF frequency of 53 MHz. Thus each bunch is said to occupy a RF "bucket" of about 19 ns duration. There are 1113 RF buckets around the Tevatron and thus each turn takes about 21 ms (1113 $\times$ 18.87 ns). Each of the beams consists of 36 bunches and is split into 3 trains of 12 bunches each. Each train of bunches is also called the "super bunch". In a train, each bunch is separated by the next by 21 RF buckets or 396 ns, or 3 BS (beam sync) ticks. Here 1 BS tick corresponds to 7 buckets. Two subsequent trains are separated by a gap of 20 BS ticks or 140 buckets or 2.64 μs. Thus for each turn of the beam there are 159 BS ticks. During Run I, the beam structure consisted of 6 bunches each of protons and antiprotons, separated by a 3.5 μs gap. This gap was used for developing the trigger and sampling the detector baselines before the next beam crossing. Figure 4.3 shows the bunch structure for Run I and Run II.

When colliding, the beams are focussed by collimators into a cross-sectional area of 5×10^{-5} cm^2 at the center of each detector. The length of the luminous region is described by the factor β^* and is about 30 cm.

The Tevatron has had an excellent history of performance. It has undergone two major upgrades, in 2003 and 2006, in order to maximize the integrated luminosity delivered to the CDF and DØ experiments. During its run from April 2002 to February 2006 it has delivered about 1.55 fb^{-1} of integrated luminosity to

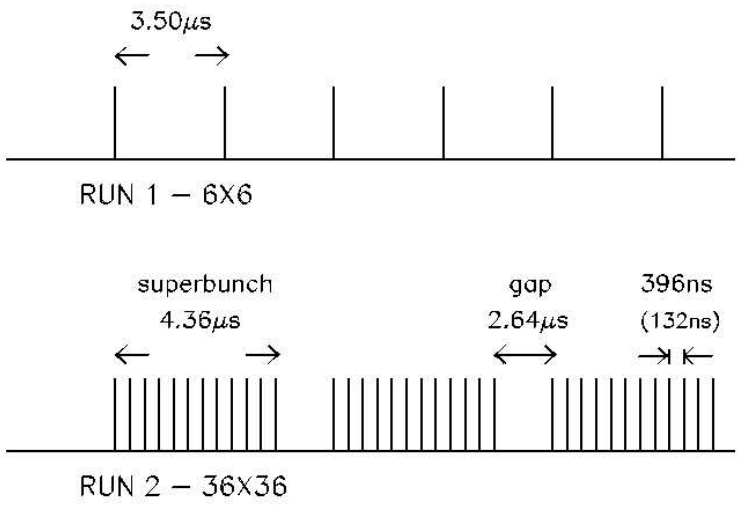

Figure 4.3. Tevatron bunch structure for Run I and Run II data taking periods

DØ. This is also referred to as the Run IIa data taking period of the experiment. The peak luminosities delivered by the Tevatron have more than doubled after the luminosity upgrade in 2006. Peak luminosities of 300×10^{30} cm^{-2} sec^{-1} are the order of the day now. The data taking run starting in June 2006 has been termed as the Run IIb of the experiment and more than 6.0 fb^{-1} of data has been delivered by June 2009, during this run.

This precise measurement has been performed with 1.0 fb^{-1} of data recorded during the DØ Run IIa data taking period.

More details on the technical aspects and operation of the Tevatron are given in [89] and [90].

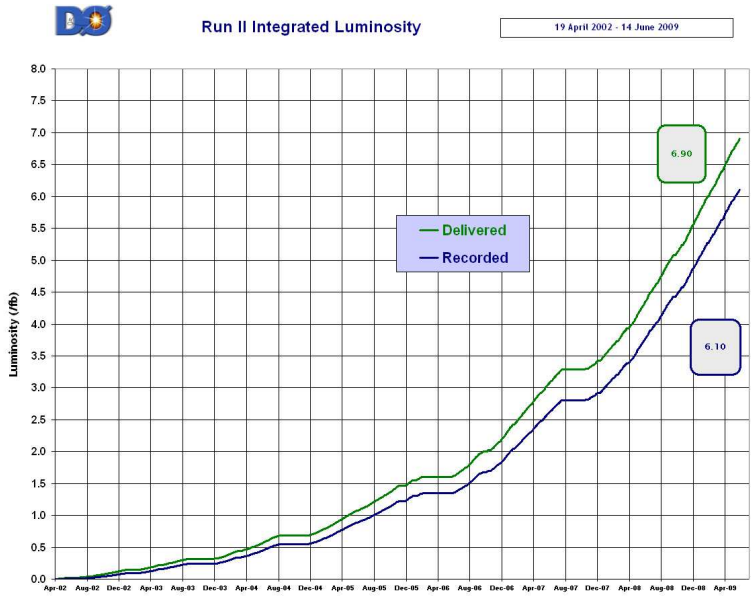

Figure 4.4. Total integrated luminosity delivered by the Tevatron and recorded by DØ during Run II

4.3 The DØ Detector

The DØ detector is a multipurpose detector made up of specialized subdetector systems. In simple words, this detector can be envisioned as a camera that is capable of taking snapshots of the debris that results from the collisions of the highly energetic protons and antiprotons at the center of the detector, every 396 ns. The collision of a proton bunch with an antiproton bunch at the Tevatron is called an "event". Since each of these collisions produce myriads of particles, some of them could prove to be new and extremely interesting for searches of new physics. Particle physicists sift through this debris of particles to look for signatures of the Higgs boson or other signs of physics beyond the Standard Model. In order to do this a complicated, algorithm-based, decision-making tool known as

the "trigger system" is used for deciding on how interesting an event is. The interesting events are recorded and stored on tapes to be used for offline analyses in the near future. The "trigger system" is described in detail later. A cross-sectional view of the DØ detector as installed in the collision hall is given in Figure 4.5. A more detailed description of the Run II DØ detector from a construction and technical point of view, can be found in [91].

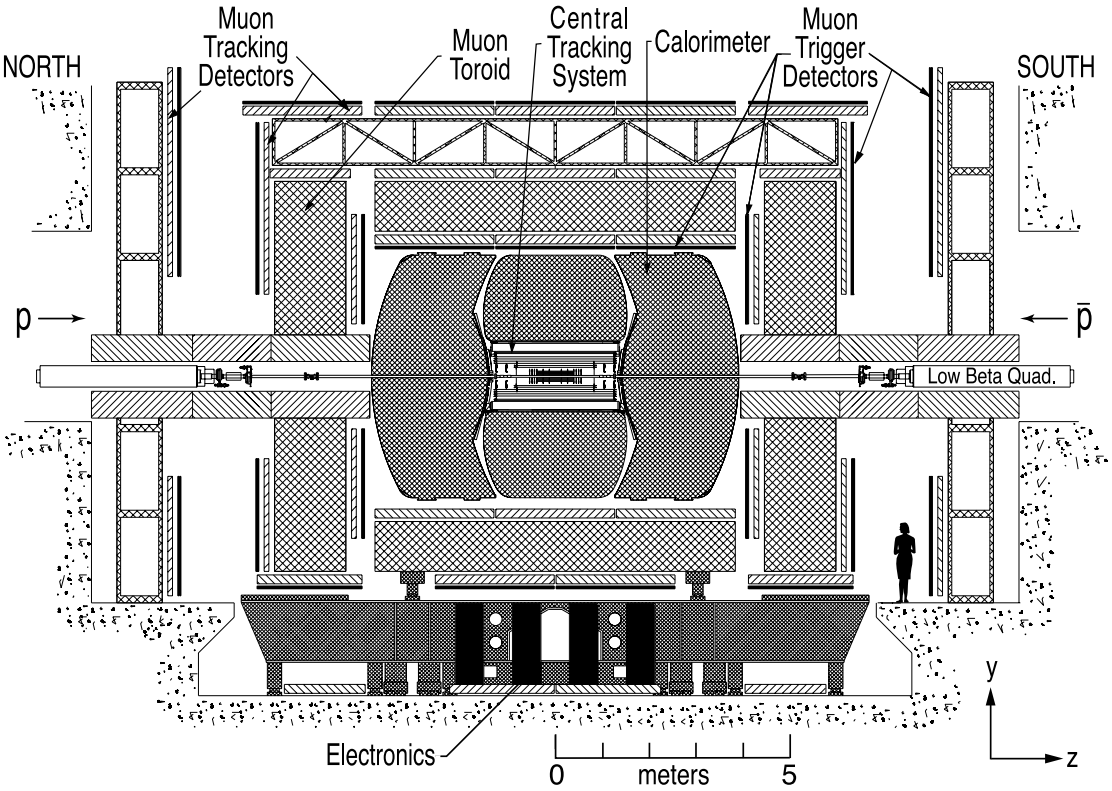

Figure 4.5. Cross-sectional view of the DØ Run II detector as viewed from inside the Tevatron ring

The importance of the sub-detectors lies in the fact that the information delivered by each one of them when put together, helps in an accurate identification of the various particles that are formed as a result of the proton-antiproton collisions. The chances of mis-identification are significantly lowered. The central tracking detectors, the uranium-liquid argon calorimeters and the muon spectrometers are the major sub-systems that constitute the DØ detector. The central tracking system includes the Silicon Microstrip Tracker (SMT) and the Central Fiber Tracker (CFT) within a 2T solenoidal magnetic field. The SMT helps identify the secondary vertices from b-quark decays while the magnetic field enables a measurement of the energy to momentum ratio (E/p) for purposes of lepton identification and calorimeter calibration. The calorimeters provide identification and energy measurements for electrons, photons and jets and also measure the transverse energy balance in events. The calorimeter consists of a central part for measuring the energy of particles emitted in the central region of the detector and two end parts for covering the forward regions of the detector. Each part consists of the electromagnetic and hadronic sections.

In the region between the solenoid and central calorimeter (CC) lie the Central Preshower (CPS) detectors which help detect the early parts of the shower development and thus improve identification of electrons, photons and jets. Similarly the Forward Preshower (FPS) detectors are placed in the forward regions near the end calorimeters (EC).

The muon detecting system consists of the central and forward muon subsystems. The central muon system consists of scintillation counters to improve muon triggering and proportional drift tubes (PDT) for tracking purposes. The forward muon system consists of mini drift tubes (MDT) and the pixel scintillation

counters that are resilient to radiation damage. Additional shielding from the beam pipe is also present. The muon toroidal magnets play an important role in the functioning of the detectors. The central and the two end iron toroids are mounted on the platform.

The SMT, CFT and calorimeters are cylindrical in shape and were mounted to be concentric around the beryllium beam pipe. The latter has a thickness of 0.508 mm, an outer diameter of 30.1 mm and is 2.37 m in length. The SMT is the innermost detector, surrounded by the CFT which in turn is surrounded by the calorimeters. The muon detectors are large, consisting of scintillator counters and drift tube chambers. They surround the calorimeter on all sides. Each of these sub-detectors is described below in more detail.

4.3.1 Calorimeter Coordinates

The calorimeter and tracking systems are the important detectors for this measurement of the W mass. The DØ detector uses a right-handed coordinate system that has its origin at the geometric center of the detector. The +z axis is along the direction of travel of the proton beam. The +y axis is directed upwards. The +x axis is horizontal and points out of the Tevatron ring. A cylindrical coordinate system is used to describe the geometry of the detector, in that the radius "r" is used to denote the distance of the point from the geometric center of the detector, the angles ϕ and θ are measures of the azimuthal and polar angles respectively.

A commonly used variable for locating polar coordinates is called the "pseudorapidity". Two types of pseudorapidity are defined, η_{det} and η_{phys}. In both

cases:

$$\eta = -\ln \tan \frac{\theta}{2} \tag{4.1}$$

For η_{det}, the angle θ is measured from the origin of the detector whereas for η_{phys}, the θ is measured from the primary interaction vertex. The primary vertex may be located up to $\pm$ 60 cm up or down the beampipe from the origin of the detector.

The pseudorapidity $\eta = -\ln[\tan(\theta/2)]$, approximates the true rapidity $y = \frac{1}{2}\ln[(E + p_z c)/(E - p_z c)]$, for finite angles in the limit that $(mc^2/E) \rightarrow 0$. The term "forward" is used for regions at large $|\eta|$, while the term "central" is usually used for $|\eta| < 1.2$ (or 1.0 in some cases).

The large reduction in the bunch spacing (396 ns) in Run II as compared to the 3.5 μs in Run I required a significant upgrade of the readout electronics for the front-end signals of the various sub-systems of the DØ detector. The calorimeter preamplifiers and pulse-shaping electronics have been upgraded and all the electronics for the muon system have also seen change. The trigger system has also undergone significant upgrade, with the introduction of three full trigger levels to cope with the high collision rate and new hardware has been added to identify the displaced secondary vertices for b-quark tagging. The design and performance of the various sub-systems of the DØ detector is described in the sections below in greater detail.

4.3.2 The Silicon Microstrip Tracker (SMT)

The Silicon Microstrip Tracker is the innermost tracker. It provides tracking and vertexing almost over the entire pseudorapidity coverage of the calorimeter and muon systems. It consists of silicon detectors which are p-n junction diodes operating at reverse bias. Two classes of beam interactions drive the design of

the SMT. The high-p_T processes give rise to highly collimated jets. These jets produce high track densities within the interaction region of length $\sim$ 25 cm. Thus the length of the interaction region sets the length scale of the device, a long detector is necessary for achieving good high-p_T acceptance. On the other hand, QCD and B-physics produce lower p_T tracks that extend into regions of high pseudorapidity. To detect these tracks, disk geometries are placed in the forward region. An isometric view of the SMT detector is shown in Figure 4.6.

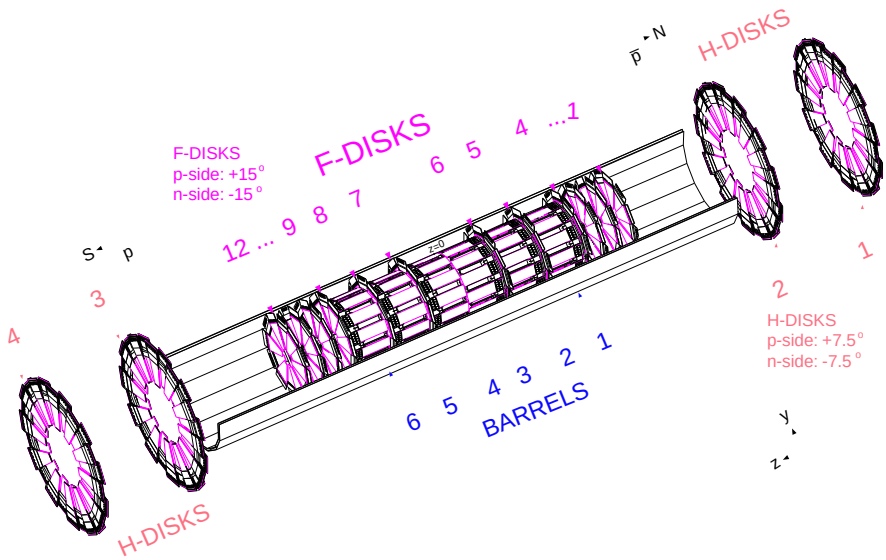

Figure 4.6. The barrel and disk design of the Silicon Microstrip Tracker

Six barrel-and-disk modules are used to measure tracks with low psuedorapidity ($|\eta| < 1.5$). Each of the 12 cm long barrels has readout layers of silicon

detectors, each silicon module is called a "ladder". The ladders are arranged in four layers, two staggered and two overlapping sub-layers. A "F" disk with 12 double sided wedge detectors caps each barrel at high $|z|$. The barrels and disks yield $r - \phi$ and $r - z$ measurements for an efficient 3D track reconstruction in the central region. The two end modules of three F disks combined with four far forward, large-diameter "H" disks provide good resolution for tracks at high pseudorapidity. Twenty four full wedge detectors consisting of two back-to-back single sided "half" wedges, are mounted on each H-disk. This design should keep momentum resolution less than 10 % at 1 GeV/c and impact parameter resolution to within 30 μm out to $|\eta| < 3$.

The five different detector types used in the SMT are shown in Table 4.1. The 4 inner barrels have 90° double sided double metal (DSDM) and 2° stereo double sided (DS) sensors. Double sided detectors are used to minimize material in the tracking volume. The two outer barrels have single sided (SS) and 2° stereo double sided (DS) sensors. This is done in order to avoid a degrading resolution of small angle tracks where the charge deposition would tend to be distributed over many strips. The ladders are mounted and aligned to 10-20 μm between two precision machined Beryllium bulkheads. These bulkheads are equipped with cooling channels. The F disk wedges are comprised of 12 wedges of double sided stereo sensors and each H disk consists of 24 wedge assemblies, each with two back-to-back single sided detectors. The barrels and F disks are mounted on 2 carbon fiber cylinders which meet at the interaction point in the detector. The H disks are mounted separately on carbon fiber cylinders.

There are approximately 800,000 readout channels from 912 readout modules of the SMT. Figure 4.7 shows the chain of electronics reading out the SMT detec-

tor. The SMT is readout by the custom-made 128-channel SVXIIe chips. These readout chips are held by the High Density Interconnectors or HDIs, these are assemblies of flex circuits laminated to the Be substrates. The SVXIIe chip performs preamplification, analog delay, digitization and data sparsification. Its features are a readout speed of 53 MHz and downloadable ADC (analog-to-digital converter) ramp, pedestal and bandwidth settings. The SVXIIe is manufactured using the 1.2 μm UTMC radiation-hard technology [92]. The preamplifier integrates the input charge for a train of beam bunches and resets during the inter-bunch gaps. This charge is delivered to a 32 cell analog pipeline. Upon a Level 1 trigger accept, a double correlated sampling [1] is performed on the appropriate cells before the analog information is sent for digitization. The digitization provides 8 bits of ADC information every 2.4 μs. Please refer to [93] for more details on this.

The SVXIIe sequencers send data from the silicon ladders and wedges to the VME readout buffer (VRB) memories viz optical link fibers. The VRBC (VRB controller) controls the operation of the VRBs with the help of the trigger information via the Serial Command Link (SCL). The SCL (Serial Command Link) carries all the trigger information required by the sequencers and VRBs to operate in a D0 RunII environment for data acquisition.

Upon a Level 2 trigger accept, a Single Board Computer (SBC) mounted on the VRB crate collects the data from all the VRBs and sends them to the Level 3 for readout and storage to tape. The second SBC present on the VRB crate is called the Power PC and is responsible for slow monitoring and calibration.

[1] Double correlated sampling is the process of subtracting the analog baseline pedestal value from the signal being measured.

TABLE 4.1

SMT DETECTOR TYPES (MODULE: LADDER OR WEDGE)

Location	Module type	Stereo angle(°)	Pitch (μm)	No. of modules	Chips/ Mod	No. of HDI
L1,L3 (outer barrels)	SS	0	50	72	3	72
L1,L3 (inner barrels)	DSDM	0/90	50/150	144	3/3=6	144
L2,L4 (outer+inner)	DS	0/±2	50/60	216	5/4=9	216
F-disks	DS	+15/-15	50/60	144	8/6	288
H-disks	SS	+7.5/-7.5	50/50	96	6/6	192

4.3.3 The Central Fiber Tracker (CFT)

The CFT is the other main component of the central tracking system. It consists of scintillating fibers mounted on eight concentric support cylinders, has an inner radius of 20 cm and an outer radius of 52 cm from the center of the beampipe. The two innermost cylinders are 1.66 m long, to accommodate the forward H-disks of the SMT, the other six cylinders are 2.52 m long. The outer cylinder provides coverage for $\eta \leq 1.7$. Each support cylinder is double walled with a 0.25 inches thick core of Rohacell [94]. Carbon fibers impregenated with 40 % resin were used for constructing the walls of the cylinders. Two doublet layers of scintillating fibers are mounted on each cylinder. The first doublet layer is aligned parallel to the beam direction (z) whereas the second layer is oriented at a stereo angle in ϕ of +3° (u) or -3° (v). Layers of fiber that are oriented along the beam direction are referred to as the axial layers while those at an angle of ±

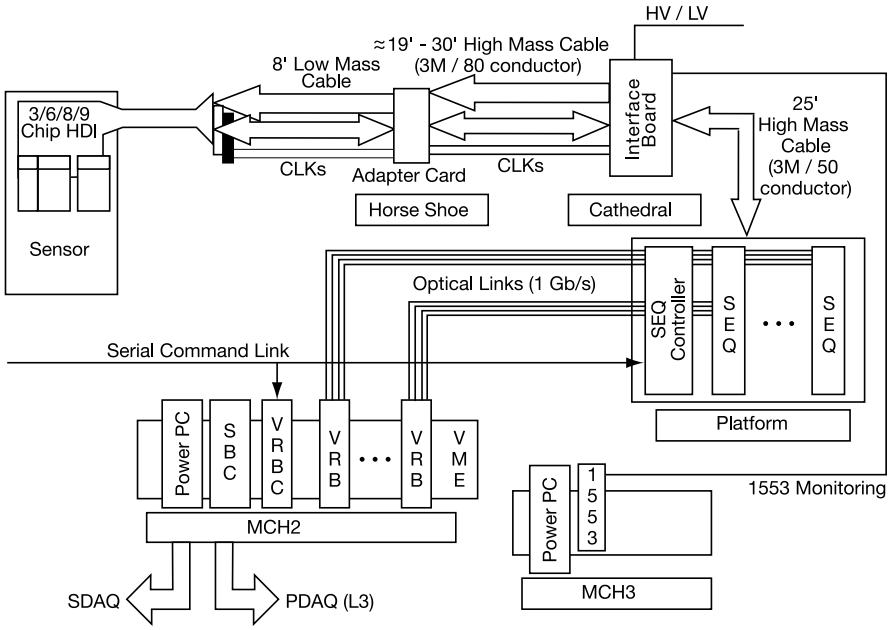

Figure 4.7. The readout chain for the SMT detector

3° are called the stereo layers. The two types of stereo layers are mounted in an alternating fashion on the support cylinders. Figure 4.8 shows the layers of the CFT and the fiber orientation.

The small fiber diameter (835 μm) gives the CFT an inherent doublet layer resolution of 100 μm provided the location of the individual fibers is known with a precision of $\sim$ 50 μm.

When charged particles pass through the scintillating fibers, light is generated. The scintillating fibers are coupled to clear fiber waveguides which bring the scintillation light to Visible Light Photon Counters (VLPCs) for readout. DØ has chosen to use the VLPC as the photosensitive device for signal readout from the CFT and preshower detectors on the basis of the high quality of its performance. VLPCs are arsenic-doped silicon diodes, originally developed at Rockwell Interna-

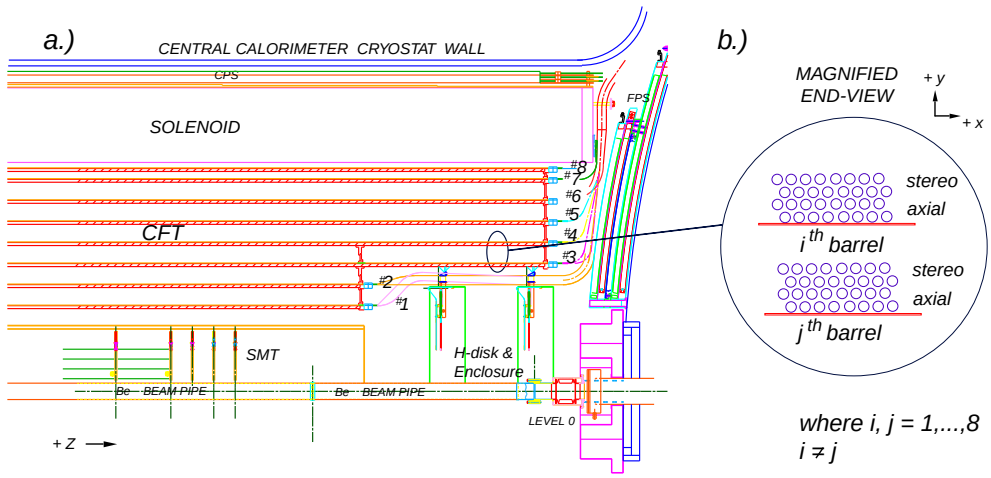

Figure 4.8. Cross-sectional view of the CFT with the 8 layers and the fiber orientation on each layer

tional and subsequently produced by the Boeing Company. They convert the light (photons) produced by the passage of charged particles through the scintillating fibers of the CFT into amplified electrical signals with an excellent time resolution. The VLPCs are capable of counting single photons. The unique features of the VLPC which enable its use as the ideal device for photon detection here are its high quantum efficiency ($\sim$ 60-80 % at visible light wavelengths), high gain (22,000 to 65,000 electrons per converted photon) and low gain dispersion ($<$ 2 %), capability of operating at high rates of at least 10 MHz (high background environment) and fast response, all of which result from the properties of its "Si:As impurity band" conduction material [95–97].

The clear fiber waveguides range in length from 7.8 to 11.9 m. The VLPC pixels are housed inside the modules of the VLPC cassettes, hence individual fibers (0.965 mm in diameter) present inside the cassettes guide the photons from the waveguides to the individual VLPC pixels. Each VLPC counts single photons

and produces amplified electrical signals. The electrical signals from the VLPCs are brought to the analog front-end (AFE) boards mounted on the cassette body by means of flex circuits. A typical LED spectrum for a single VLPC for an axial CFT fiber, is shown in Figure 4.9.

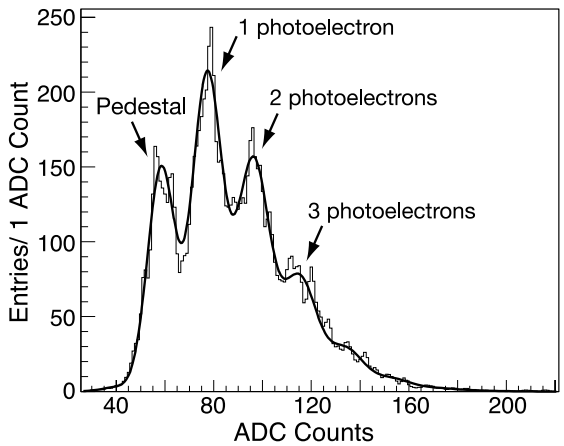

Figure 4.9. A typical LED spectrum showing the individual photoelectron peaks of a single VLPC

The discriminator signals from the axial doublet layers are sent via the high speed LVDS cable to form the fast Level 1 hardware trigger, also called the Central Track Trigger (CTT) based upon the number of track candidates above specified pT thresholds. Upon a Level 1 trigger accept the CFT provides a complete data readout for the events passing the Level 1 CTT trigger. This readout from the AFE boards is controlled by and transferred to the sequencers. Figure 4.10 provides a schematic diagram of the readout components in the path of the CTT trigger

formed from the CFT information.

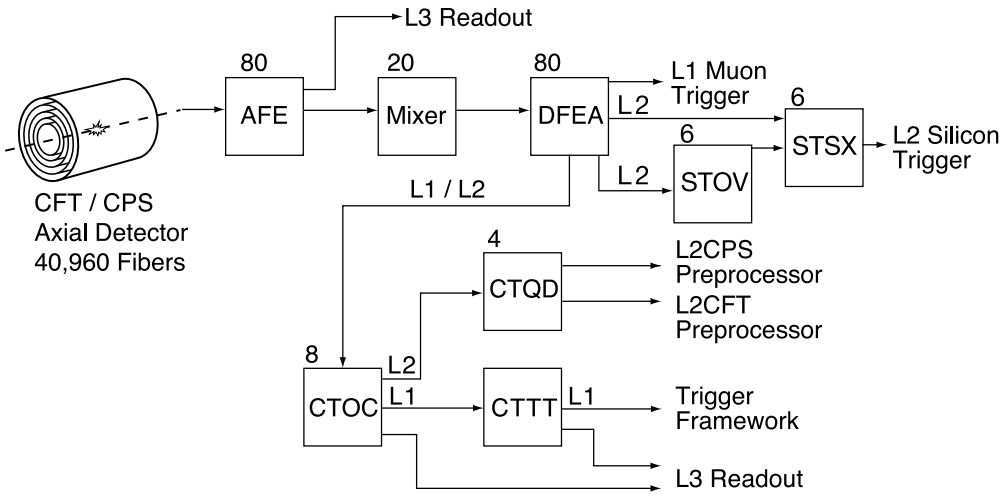

Figure 4.10. The CFT/CPS axial components of the L1 CTT system. The numbers in the top left corners of the boxes indicate the number of electronic boards of each type

The sparsified data is transferred from the sequencers to VME transition modules (VTM) via fiber optic G-Link cables. The VTMs transfer the data to the VRBs located in the VME VIPA crates. The assignment of buffers in VRBs is actually controlled by the VRB Controller (VRBC) located in each crate. Data stored in these buffers awaits the Level 2 trigger decision. A single board computer (SBC) mounted in a VME VIPA crate serves as the interface to the Level 3 readout. Upon receiving a Level 2 accept, it collects data from the VRBs and sends them to Level 3 for the formation of the Level 3 trigger. Full tracking in-

formation from the CFT for the events that pass the selection criteria at Level 3 is recorded for future analysis. There are 4 VME VIPA crates located in the Movable Counting House-2 (MCH2) for buffering the readout of the CFT and Preshower detectors.

Both the tracking detectors help locate the primary vertex of interaction with a resolution of about 35 μm along the beamline. They can tag b-quark jets with an impact parameter resolution of better than 15 μm in the $r - \phi$ direction for particles with transverse momentum $p_T > 10$ GeV/c at normal incidence (η =0). Measuring the vertex position with this high precision helps in obtaining better measurements of the lepton p_T, jet transverse energy (E_T) and missing transverse energy ($\not{E}_T$). This is turn helps the calibration of the electromagnetic calorimeter using the E/p information of the electrons.

4.3.4 The Solenoid

The superconducting solenoidal magnet was designed with the aim of optimizing the momentum resolution, $\Delta p_T/p_T$, and tracking pattern recognition within the constraints imposed by the Run I detector. Its magnetic field bends the tracks of the charged particles that cross the tracking detectors so a measurement of the momentum of the tracks can be obtained from the curvatures of their trajectories inside the tracking volume. The available space within the vacuum vessel of the central calorimeter (CC) and the need to maximize the tracking volume drive the physical size of the solenoid, it is 2.73 m long and 1.42 m in diameter. A operating central field of 2T is chosen after taking into consideration the required momentum resolution, tracking pattern recognition, available space, field uniformity over the maximum volume possible, the need to operate safely and stably with either

polarity and the need to quench safely without a protection resistor if needed. The required linear current density for the 2T field strength is achieved by wounding the solenoid with two layers of superconducting coils. The support cylinder for the solenoid is present on the outside of the windings. A control dewar provides the magnet with the cryogenic services, magnet current buses, vacuum pumpout and relief through the narrow space between the central and end calorimeter vacuum vessels.

The solenoid has an overall thickness of about 1.0 X_0 at η=0 for optimizing the performance of the Central Preshower detectors that lie just outside the solenoidal cryostat.

The solenoidal system is controlled remotely, including cooldown, warmup, energization, de-energization for reversing fields and quench recovery.

4.3.5 The Preshower Detectors

The preshower detectors aid in electron and photon identification and in background rejection by detecting the early parts of the shower development of particles passing through it. They function as tracking detectors and calorimeters, thus enhancing the spatial matching between tracks and showers in the calorimeters. Charged particles could loose a considerable fraction of their energy in the solenoid and upstream material such as the cables and supports, so the preshower detectors can be used offline to correct for these losses in the EM energy measurements of the central and end calorimeters. The fast energy and position readouts from the preshowers are also used for Level 1 trigger purposes. There are two sub-components of the preshower detectors, the central preshower detectors located between the solenoid and the central calorimeter and the forward preshower

detectors that are attached to the faces of the end calorimeters.

4.3.5.1 The Central Preshower (CPS) Detectors

The CPS consists of three concentric cylindrical layers of triangular scintillator strips. The layers are arranged in an axial u-v geometry with a u stereo angle of 23.774° and a v angle of 24.016°. Each layer contains 1280 strips. Embedded at the center of each triangular strip is a wavelength-shifting-fiber (WLS) that collects and carries the light to the end of the detector where they are read out by clear light-guide fibers. The WLS fibers are split at z=0 and are read out from each end resulting in 2560 channels per layer. A cross-sectional view of the CPS detector is shown in Figure 4.11.

A lead radiator of 1.0 X_0 thickness has been placed between the solenoid and the CPS. This lead alongwith the solenoid provides a total of about two radiation lengths of material for particles incident normally and about four radiation lengths for particles incident at extreme angles. The CPS provides coverage for particles within $\eta < 1.3$ of the detector.

The readout of the CPS is similar to that of the CFT, in that it uses clear waveguides that bring light to the VLPCs. The components of the readout electronics are the same as that used for the CFT. The information from the axial layers of the CPS is used for Level 1 triggering purposes while that from the stereo layers is used for the Level 2 trigger.

4.3.5.2 The Forward Preshower (FPS) Detectors

The two FPS detectors are mounted on the cryostats of the end calorimeters (north and south) between the luminosity monitors and the inter-cryostat detec-

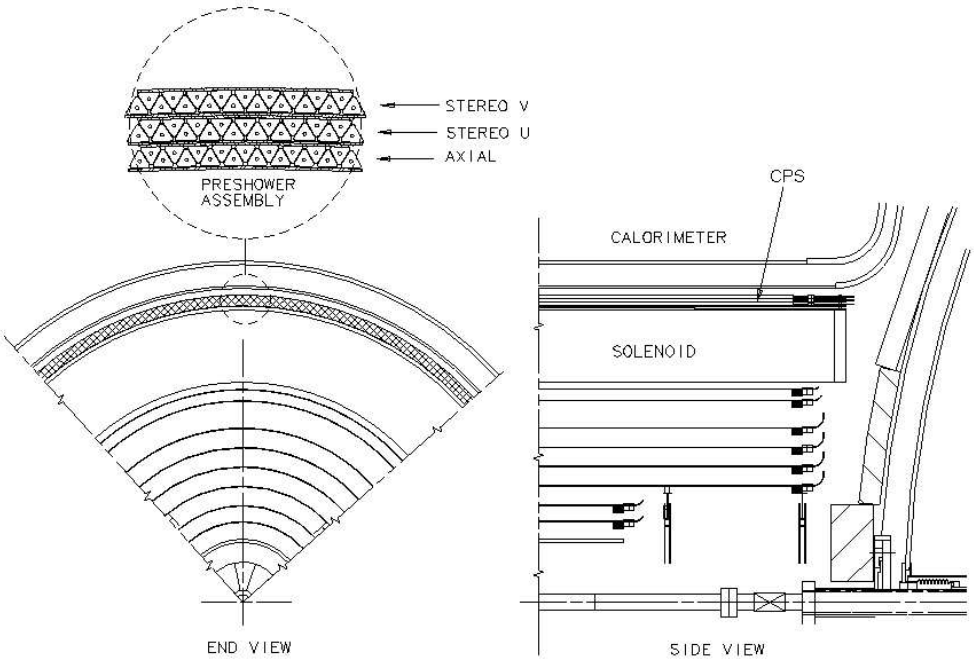

Figure 4.11. Cross-sectional end view (left) and side view (right) of the Central Preshower detector

tors (ICD). Each detector is made from two layers, of two planes of scintillator strips. The two layers are separated by a 2.0 X_0 thick lead-stainless steel absorber. The layers nearest to the interaction region (beampipe) are called the minimum ionizing particle (MIP) layers. This is because the charged particles passing through these layers of the detector leave minimum ionizing signals thus allowing a position measurement (in η, ϕ and z) of the track. The layers behind the absorber are called the shower layers. Particles such as the photon and electron will shower in these layers and form a cluster of energy spanning almost three strips. Heavier charged particles are less likely to shower and will thus leave a second MIP signal in the shower layers. The signals from the MIP layers are spatially

matched to the signals in the shower layer to identify the various electromagnetic and hadronic particles. For example the energy shower that matches with a track signal in the MIP layers is indicative of an electron, while a photon does not interact in the MIP layers, it produces a signal in the shower layers only. MIP signals from both layers are indicative of hadronic particles that pass through but do not shower. A quarter view of the FPS detector has been shown in Figure 4.12.

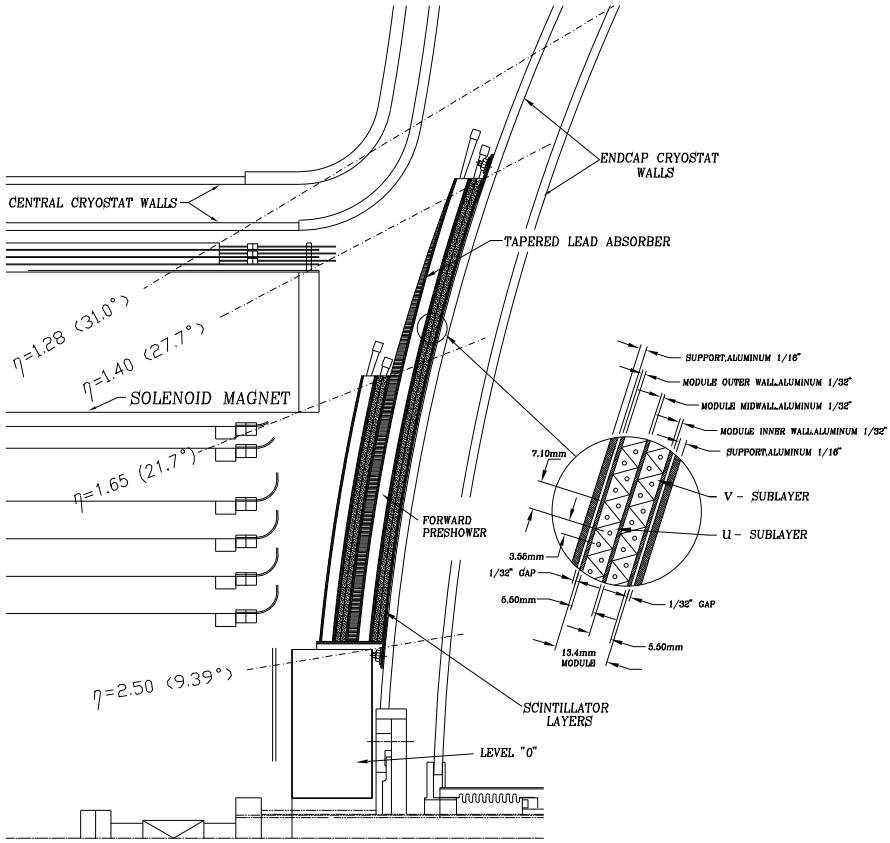

Figure 4.12. One quarter view of the Forward Preshower detector

The shower layers provide readout for $1.5 < \eta < 2.5$ whereas the MIP layers and the absorber cover the region $1.65 < \eta < 2.5$. The outer region of the FPS falls behind the solenoidal magnet which provides about $3X_0$ of material infront of it. This material reduces the possibility of showers reaching these shower layers of the FPS. The FPS detectors also share readout elements with the CFT, starting with the clear fiber waveguides and continuing through the entire readout electronics system.

4.3.6 The Calorimeter

The calorimeter is the most essential sub-detector for the measurement of the W mass. It provides energy measurements for the electromagnetic and hadronic particles, assists in the identification of particles such as electrons, photons, jets and muons and measures the transverse energy balance in events.

The calorimeter essentially consists of the central and the two end (north and south) segments commonly known as the central calorimeter (CC) and end calorimeters (ECN and ECS) respectively. DØ's central calorimeter has an η coverage of ≤ 1.2 and each of the end calorimeters provide coverage up to $\eta \leq 4.2$, thus making the calorimeter nearly hermetic. Both the central and end calorimeters contain three concentric sections with the electromagnetic (EM) section closest to the interaction region and surrounded by the fine and coarse hadronic (FH and CH) sections. Figure 4.13 is a split-open view of the barrel of the calorimeter, showing the CC and EC regions and the various segmentations (EM, FH, CH) in each region.

The EM section is essentially a barrel consisting of 32 EM modules azimuthally. Each module is sub-divided into 4 layers, EM1, EM2, EM3 and EM4 respectively.

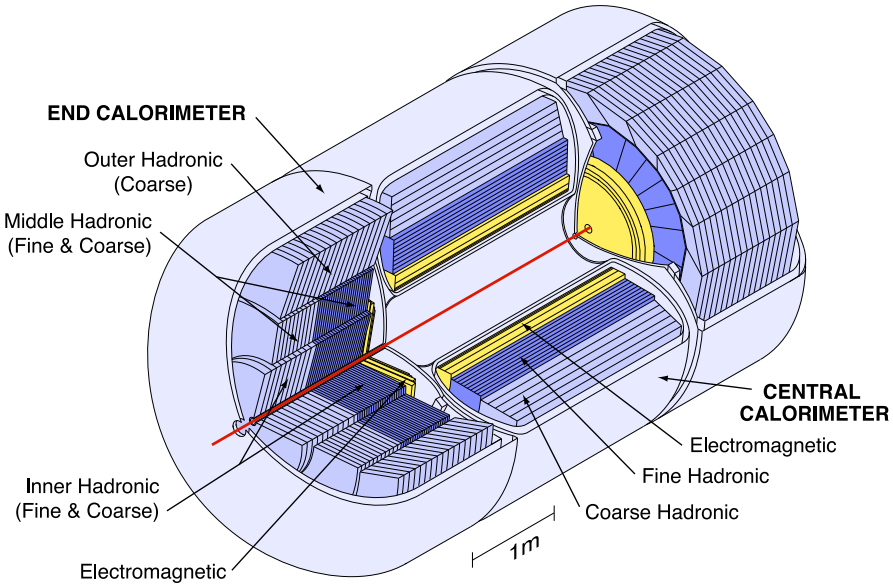

Figure 4.13. The various segmentations and parts of the DØ calorimeter

This is surrounded by the fine hadronic section which contains 16 modules, each sub-divided into 3 layers, FH1, FH2 and FH3. The FH section is surrounded by the single layer coarse hadronic section consisting of 16 modules. Thus each EM module is $\frac{2\pi}{32}$ ($\sim$0.2) radian wide in ϕ whereas each hadronic (FH and CH) module is $\frac{2\pi}{16}$ ($\sim$0.4) radian wide in ϕ. Figure 4.14 shows a cross-sectional view of one quarter of the detector with the η and depth segmentation.

Although liquid argon is the active medium for the entire calorimeter, different absorber plates are used in different sections of the central calorimeter. The EM section modules use 3 mm thick depleted Uranium plates while the FH section contains 6 mm thick Uranium-Niobium plates. The modules in the CH section use relatively thick (46.5 mm) plates of Copper as the absorber material. Each of the calorimeters is held within its own cryostat, a vacuum-vessel which maintains the temperature of the detector at approximately 90 K. The purity of the liquid

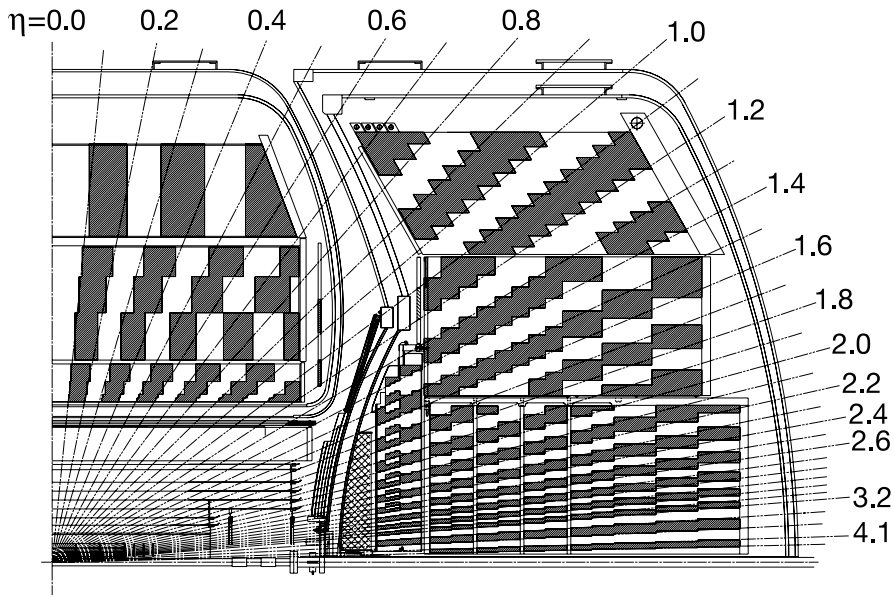

Figure 4.14. Side view of one quarter of the calorimeter, showing segmentation and tower definitions. The line extending from the center of the detector denote the pseudorapidity coverage of cells and projected towers

argon has been very stable over time and was measured to be less than 0.30 pm 0.12 ppm for all three cryostats.

A typical calorimeter "cell" is shown in Figure 4.15. A unit cell consists of two separated and grounded metal absorber plates with a signal board placed between them. The gaps between the plates and board contain liquid argon. The high positive potential (2 kV) of these signal boards establishes an electric field across the gap and the Copper pads located on the inner surfaces of these boards act as the electrodes for the gap. An assembly of these electrode-pads and the intermediate gaps, in depth, approximately at the same η and ϕ, forms a "readout cell" or "readout channel".

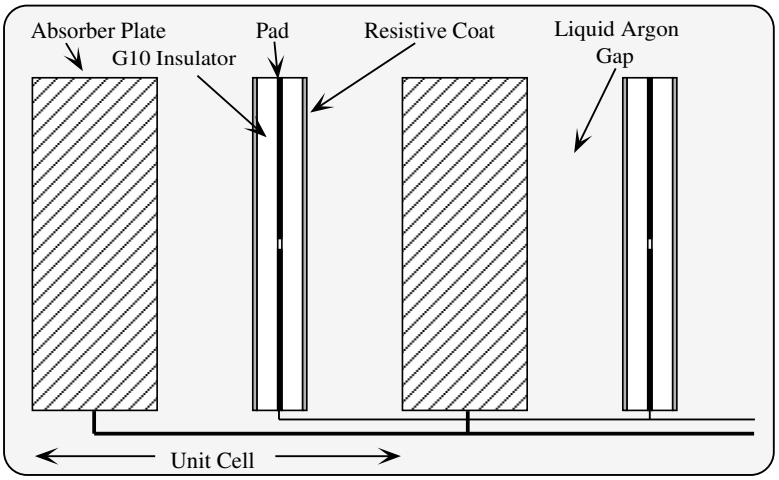

Figure 4.15. A typical calorimeter cell

Since this measurement of the W mass probes electrons in the central region of the DØ detector, let us take a look at the readout units of the EM section of the central calorimeter in a little more detail. Each of the EM1, EM2 and EM4 layers in an EM module consist of 2 readout cells at a "fixed η" width of 0.1. Thus each cell is 0.1 radian wide both in η and ϕ. The third EM layer (EM3), which contains the maximum of the EM shower is segmented twice as finely both in η and ϕ (0.05) to allow for a more precise location of the EM shower centroids. Thus in each EM module this EM3 layer contains 8 readout cells at a "fixed η" width of 0.1. Figure 4.16 shows the relative segmentation of the different layers of the calorimeter.

The readout cells over all the three sections of the calorimeter, in turn form the pseudo-projective "readout towers". These towers are 0.1 radian in width, in both η and ϕ for the EM and hadronic modules. Each readout tower consists of 11 readout cells in the CC. When sub-divided each tower comprises of the EM,

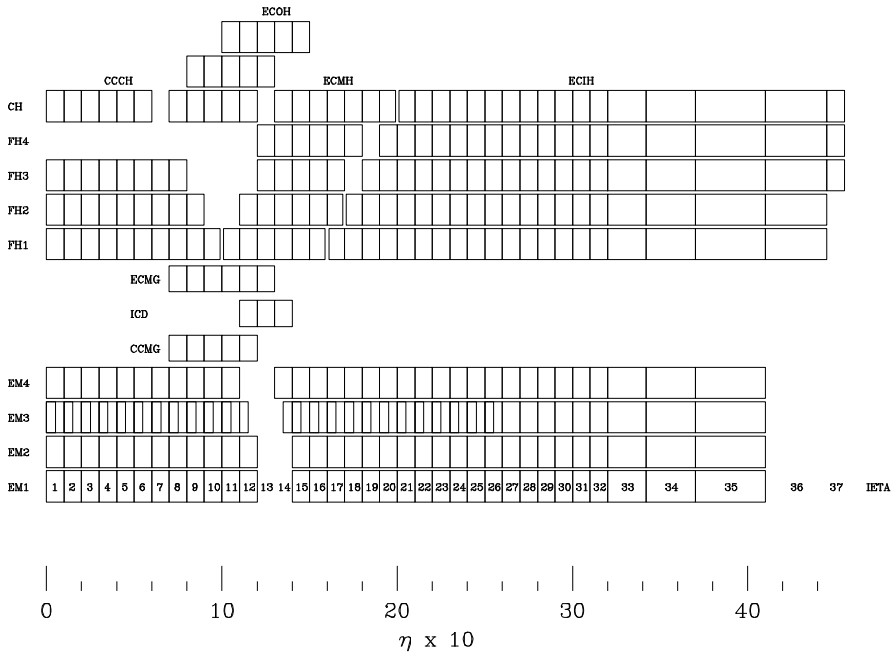

Figure 4.16. The calorimeter cell configuration in terms of depth and η

FH and the CH towers respectively. Each EM tower consists of 7 readout cells, each FH tower contains 3 readout cells and the CH tower comprises of a single readout cell.

In the CC each EM module contains 48 EM readout towers for a total η width of 2.4 (-1.2 to 1.2) and ϕ width of 0.2 (width of each module). Thus for a fixed η width of 0.1, there are 2 readout towers for the EM module.

There are about 55,300 electronics channels to be read out in the calorimeter. Figure 4.18 is a pictorial representation of the readout chain of the calorimeter. The readout is achieved in three principal stages. In the first stage, signals from the calorimeter are fed into charge preamplifiers located on the cryostats via low impedance coaxial cables. The fact that the electron drift time across the liquid argon gap is about 450 ns at 2.0 kV and the bunch collision spacing is 396 ns,

presents a challenge for the signal charge integration in Run II. The calorimeter electronics were designed to maintain a high signal-to-noise ratio in an environment of high instantaneous luminosity, in accordance with the original design of the Tevatron, that is a bunch spacing of 132 ns. The output of the preamplifier is an integral of the calorimeter signal with a rise time of 450 ns and a recovery time of $\sim 15\ \mu$s.

From the preamplifiers they are transported to the analog signal shaping and storage circuits located on the baseline subtractor (BLS) boards, located below the cryostats. The BLS provide baseline subtraction to remove any low-frequency noise or pileup from the signal. They also send faster shaped analog sums of the signals as prompt inputs for the Level 1 and Level 2 calorimeter trigger decisions and use switched capacitor arrays (SCAs) to hold the signal for about 4 μs until a Level 1 trigger decision is made and for an additional 2 ms until the Level 2 trigger accept arrives. The signal shaper circuits utilize only two-thirds of the charge collected by the preamplifier so as to minimize the effects of pileup. [2] This corresponds to the first ~ 260 ns of signal collection from the gap. The shaper circuit produces a unipolar signal peak at ~ 320 ns with a recovery time of 1.2 μs. These signals are sampled every 132 ns. Figure 4.17 depicts the signals obtained from the cell, preamplifiers and shaper circuits.

The precision signals from the BLS boards are transmitted on an analog bus with the help of analog drivers over 130 m of twisted-pair cable to ADCs (analog-to-digital converter). Upon digitization by the ADCs, these signals enter the data acquisition system to await the Level 3 trigger decision and subsequent storage to tape.

[2] Due to multiple interactions in a single beam crossing or due to interactions in multiple beam crossings

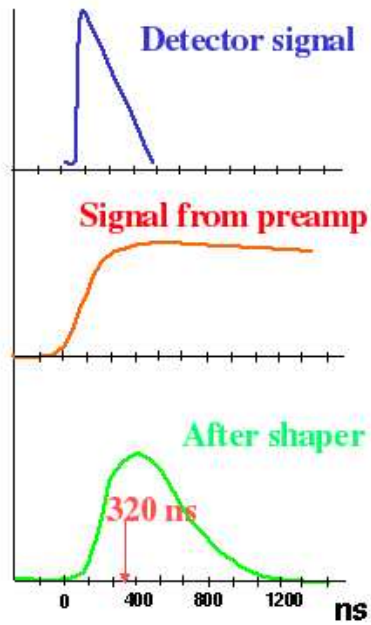

Figure 4.17. The shape of the electronic signal from calorimeter cell, preamplifier and shaper circuit

4.3.7 The Inter-Cryostat Detector

Since the central and end calorimeters are mounted in their separate cryostats, the region between the cryostats ($0.8 < \eta < 1.4$) remains uncovered. In addition there is substantial unsampled material in this region which degrades energy resolution. To address this problem, additional sampling has been provided in these regions by way of the inter-cryostat detector (ICD) and the massless gaps. The massless gaps are standard calorimeter readout cells placed infront of the first layer of uranium. The ICD is a series of 0.5 inches thick scintillating tiles that are attached to the exterior surface of the end cryostats and are read out via WLS fibers. These fibers are fed to clear optical fibers which in turn terminate at a photomultiplier tube (PMT).

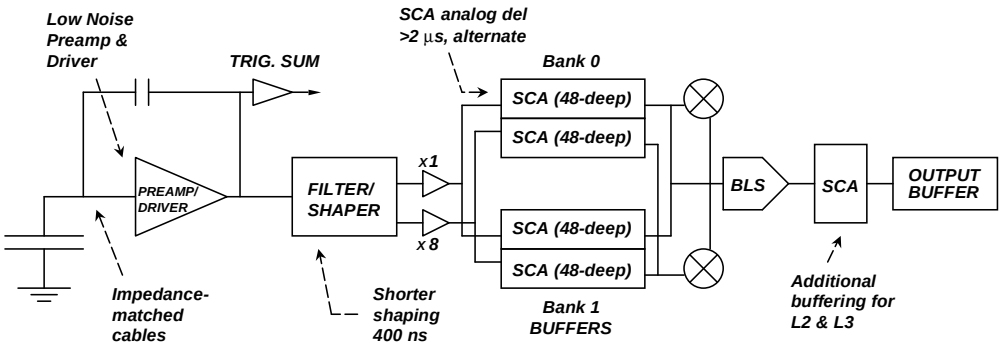

Figure 4.18. The electronic components in the readout chain of the calorimeter

The sampling of the ICD provides coverage within the $1.1 < \eta < 1.4$ region.

4.3.8 Muon Detectors

The muon detection system comprises of the central and forward muon systems. The central muon system uses proportional drift tubes (PDTs), central toroidal magnets and trigger scintillation counters. The forward muon system uses mini drift tubes (MDTs), trigger scintillation counters and the end toroidal magnets.

The toroidal magnets enable the muon system to obtain an independent measurement of the muon momenta. This is turn allows for a cleaner matching with the muon tracks from the central tracking detectors, helps reject pion/kaon decays, enables for a low p_T cutoff in the muon trigger at Level 1 and improves momentum resolution for high momentum muons.

The central muon system provides coverage up to $\eta \leq 1.0$. Here the scintillation counters, called the A_ϕ counters have been installed on the PDTs that are mounted between the calorimeter and the toroidal magnets. These provide a readout fast

enough for associating a muon in a PDT with the appropriate bunch crossing and thus reducing cosmic background. The PDTs are essentially drift chambers made of rectangular extruded aluminum tubes and typically consist of 72 to 96 cells that are 10.1 cm across. The anode wire at the center of each cell alongwith the vernier cathode pads located above and below the wires provide precise measurements of the coordinates of the track-hit along the wire. The tubes are filled with a gaseous mixture of 84 % argon, 8 % methane and 8 % CF_4. The drift velocity of the charge inside the tubes is about 10cm/μs for a maximum drift time of 500 ns. Thus they are used for precise coordinate measurements and triggering. Both the scintillation counters and PDTs contribute to the background rejection. The PDTs are mounted in three layers, A, B and C, with the A layer situated inside the toroidal magnet while the B and C layers are outside the magnet.

The forward muon system provides coverage over the $1.0 \leq \eta \leq 2.0$ region and consists of four major parts, the end toroidal magnets, three layers of MDTs for detecting muon tracks, three layers of scintillation counters for triggering on events with muons and the shielding around the beam pipe. The MDTs are arranged in three layers, A, B and C, with the A layer closest to the interaction region and inside the toroidal magnet and the B and C layers outside it. The MDTs of the forward muon system provide a short drift time for the electrons ($<$ 132 ns), good coordinate resolution ($<$ 1mm), resilience to radiation damage, high segmentation and low occupancy. The MDT tubes are made out of aluminum extrusions and stainless steel and possess eight readout cells. Each cell possesses a W-Au anode wire in the center. The MDT system uses a CH_4-CF_4 (90-10 %) gas mixture and the maximum drift time for tracks normal to the detector plane is about 40 ns. The trigger scintillation counters help in triggering and identifying muons and

thus rejecting background events. The stand-alone momentum resolution from the forward muon system is 20 % for muon momentum below 40 GeV/c. This system contributes significantly towards improving the momentum resolution for muons with high momenta, especially in the region $1.6 \leq \eta \leq 2.0$, i.e. those muons which did not pass through all layers of the CFT. Figure 4.19 is a photograph of the C-layer of muon trigger scintillation counters and Figure 4.20 shows the design of the scintillation counter. Figure 4.21 is a cross-sectional view of a mini drift tube.

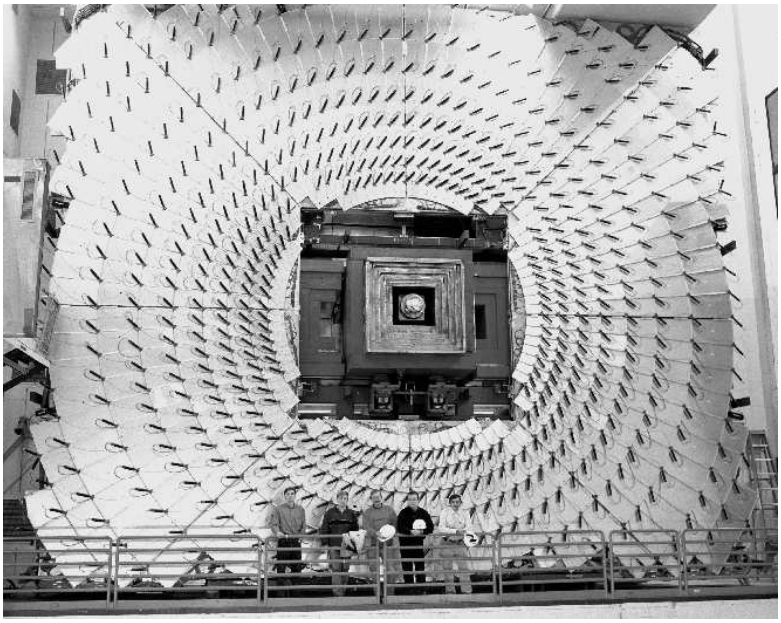

Figure 4.19. Photograph of the C-layer of muon trigger scintillation counters of the forward muon system

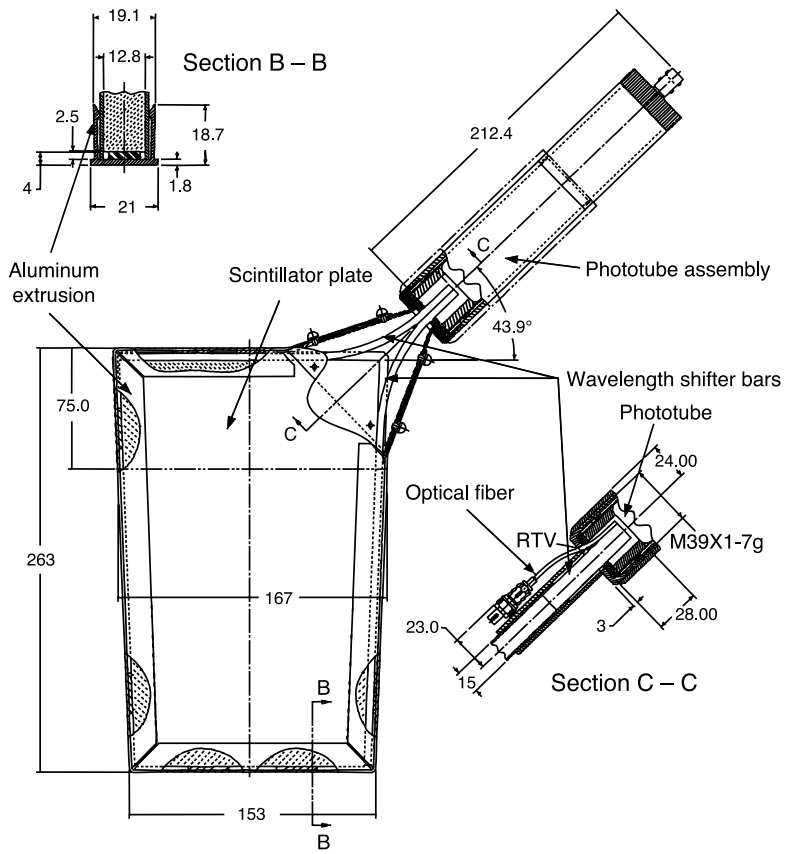

Figure 4.20. Design of a scintillation counter for the forward muon trigger system

The hit information from the MDTs and the drift times are sent to the trigger and data acquisition system.

Scattered proton and antiproton fragments that interact with the end of the calorimeter or beampipe or with the low-beta quadrupole magnets produce hits in the central and forward muon systems, thus contributing to non-muon backgrounds. Hence shielding in the form of iron, polyethylene and lead is provided in a steel structure around the beampipe. Iron is used to absorb the EM and hadronic components of the fragements due to its short interaction (16.8 cm) and

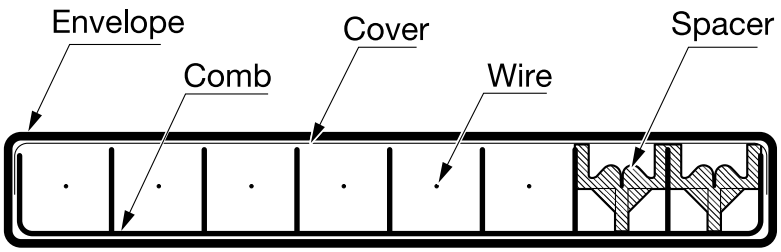

Figure 4.21. Cross-sectional view of a mini drift tube

radiation (1.76 cm) lengths. Polyethylene because of its high hydrogen content is used to absorb the neutrons, while lead is used to absorb gamma rays.

4.3.9 Luminosity Monitor (LM)

The luminosity monitor is made up of 24 plastic wedge-shaped scintillating counters with PMT readouts mounted on each one of the wedges. The monitors are located at z = +-140 cm and very close to the beam pipe. They are mounted infront of the two end calorimeters and occupy the radial space between the beam pipe and Forward Preshower detectors. The counters are 15 cm long and they provide coverage in the $2.7 \leq \eta \leq 4.4$ region. Scintillation light produced by the wedges are collected by the PMTs and are amplified by a factor of five by the preamplifiers present in the PMTs. Analog sums are formed from these signals for each of the two arrays and are fed into a Time-to-Digital-Converter (TDC) to help identify $p\bar{p}$ collisions. Figure 4.22 shows a schematic diagram for the position of the luminosity detectors in the far forward regions.

The luminosity $\mathcal{L}$ is determined from the average number of inelastic collisions

per beam crossing (N_{LM}) as measured by the LM.

$$L = fN_{LM}/\sigma_{LM} \tag{4.2}$$

where f is the beam crossing frequency and σ_{LM} is the effective cross-section for the LM that takes into account the acceptance and efficiency of the detector. Since N_{LM} is usually greater than one, it is important to account for the number of multiple $p\bar{p}$ collisions that occur in a single beam crossing. This is done by noting the fraction of beam crossings that do not have any collisions and then using Poisson statistics to determine N_{LM}.

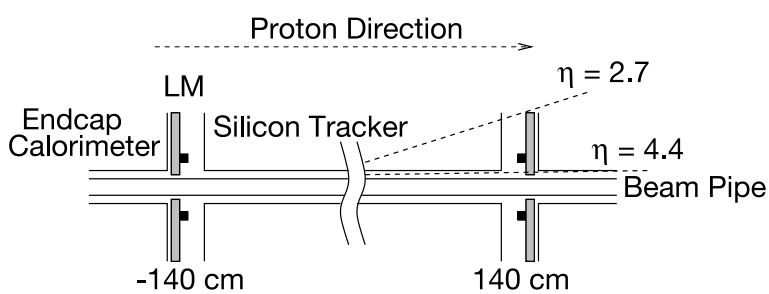

Figure 4.22. Schematic drawing showing the location of the luminosity counters

4.4 The Trigger System

The increased luminosity and higher interaction rate of the upgraded Tevatron provides almost 1.7 million collisions per second at the center of the detectors. An event is described as everything that occurs in the collision of a proton-antiproton pair in the collider. However not every event is "interesting" from the perspective of a physics analysis. Actually, only a few events out of the millions are considered to possess interesting physics information and are deemed fit to be recorded on tape. This ability to select interesting physics events and record them for future off-line analyzes belongs to an enhanced trigger system at DØ.

This trigger system consists of three distinct levels, with each succeeding level examining fewer events than the preceeding one, albeit in greater detail and with more complexity. The first stage (Level 1 or L1) comprises of a collection of hardware trigger elements, from the fast readouts of the different sub-detectors. This can be likened to the formation of individual trigger objects such as hits from tracks, energy deposits. The L1 has an output rate of about 2 kHz. If the object is deemed interesting by the trigger, the relevant information is passed onto the next trigger level. In technical terms this is referred to as a "L1 trigger accept". The second stage of the trigger (Level 2 or L2) receives the information from the specific sub-detectors (L1) and a global processor here constructs a trigger decision based on the individual trigger objects and the correlations between them. Thus it moves one step closer to identifying the candidates as potential physics objects such as tracks, electrons, jets, etc. The L2 trigger system reduces the trigger rate by a factor of about two and has an accept rate of about 1 kHz. Upon receiving a "L2 trigger accept", the event information is sent onto the third and final stage, Level 3 or L3. This stage is a high level fully programmable software trigger and

performs a limited reconstruction of events, reducing a 1 kHz input rate to 50 Hz. Level 3 contains a farm of microprocessors, where sophisticated object-specific software algorithms (known as filter tools) generate candidate physics objects or relations between them (such as the rapidity, azimuthal angle separating the objects or invariant mass). The L3 trigger decisions are based on the complete physics objects and their relationships. It then records the event information for offline reconstruction and analyses. Figure 4.23 gives an overview of the DØ trigger and data acquisition system.

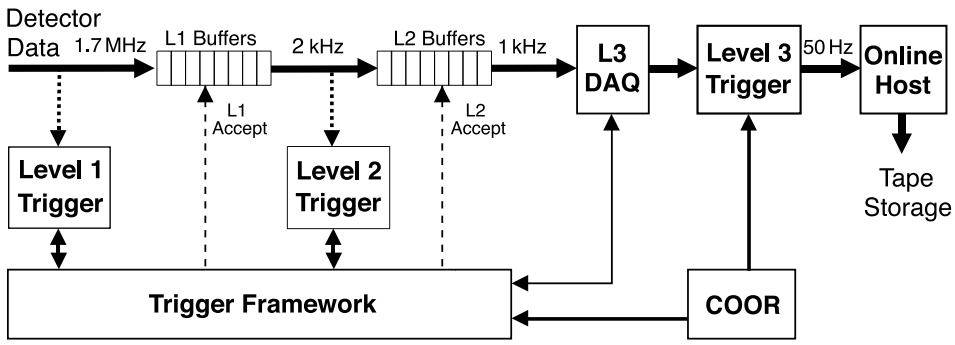

Figure 4.23. Overview of the DØ trigger and data acquisition system

As evident the trigger system is integrated with the readout of data from the detector. Each event that passes the trigger conditions of L1 and L2 is completely digitized and all of the data blocks for the event are transferred to a single commodity processor in the L3 farm.

The trigger framework (TFW) is an essential part of the system and serves

as a common interface for the different trigger levels and the data acquisition system. It collects all digital information from each of the specific L1 trigger devices and decides whether a particular event is worth a further examination. In addition it coordinates various vetoes that can inhibit triggers, enables the prescaling of triggers to reduce their rates, correlates the trigger and readout functions, manages the communication tasks with the front-end electronics and the trigger control computer (TCC) and accounts for trigger rates and deadtimes. It makes extensive use of FPGA [98, 99] technology for implementing different functions.

Since this analysis of the W mass makes use of the calorimeter for determining the energy of the electrons and the tracker for matching the energy cluster to a track, the calorimeter and track triggers have been discussed in a little more detail here.

4.4.1 Calorimeter Triggers

The L1 calorimeter trigger (L1Cal) look for energy deposition patterns that exceed the programmed limits on transverse energy deposits. The readout cells of the calorimeter form readout towers ($\Delta\eta \times \Delta\phi = 0.2 \times 0.2$) and these form the inputs to the L1 calorimeter trigger. These comprise of the sums of energy in depth and transverse coordinates of fast analog pickoffs. The tower energies are converted to E_T on input, have the pedestals subtracted and energy scales adjusted if necessary. Both the EM transverse energies and the total transverse energies (EM + H) above a certain threshold are read out and used to form the trigger.

At the L2 stage of the calorimeter trigger, the $\not\!\!E_T$ algorithm calculates the

vector sum E_T from the individual trigger tower E_T energies passed on from L1. For this, the preprocessor system identifies jets, electrons or photons and calculates the $\not{E}_T$ of the event for the global processor.

The basic electron tool at L3 has requirements on E_T, EM fraction (> 0.9), transverse shower shape and simple $\sqrt{\Delta\eta^2 + \Delta\phi^2} = 0.25$ jet cone. The position of the primary vertex is of importance for the jet selection which is made on the basis of E_T. By utilizing a simple cone algorithm and suppressing the hot calorimeter cells, the L3 jet tool is able to sharpen the turn-on curve to nearly 100% for both jet and electron filters.

4.4.2 Central Track Triggers

The L1CTT reconstructs the trajectories of the charged particles using fast discriminator data from the CFT and the central and forward preshower detectors. Although the L1CTT is optimized for making fast L1 trigger decisions, its electronics also store other event information such as sorted list of tracks, preshower clusters, for later readout to L2/L3 or for use as seeds by other DØ systems. The input to the L1CTT are discriminator bits, generated every 132 ns from the front-end electronics of the CFT system, the AFE boards. These bits are sent over point-to-point low-voltage differential signal (LVDS) links to digital front-end (DFE) boards. The discriminator bits pass through the mixer system [100] which handles their data reorganization and duplication.

The L2CTT preprocessor receives its input from the L1CTT and L2STT. The L2STT performs the online pattern recognition in the data readout from the SMT. It utilizes the finer spatial resolution of the SMT to reconstruct the charged particle tracks found in the CFT at Level 1. Hence it improves the momentum

resolution of the tracks at the trigger level.

At L3, CFT track finding utilizes the x, y and ϕ positions of the fiber. Adjacent hits are merged into clusters with their x, y and ϕ positions averaged. A global (SMT + CFT) high-momentum-track finder starts from axial CFT tracks that are matched to stereo clusters and then propagates them into the SMT. If the CFT axial/stereo match fails, then the CFT-SMT match is done in x, y only. In this way the L3 tracker makes an independent selection of individual charged high-p_T tracks. The algorithm with a 60 μm distance-of-closest-approach (DCA) resolution for central tracks runs in less than 200 ms. Off-line studies of track-matched electrons in a $Z \rightarrow e^+e^-$ data sample show a 60% overall efficiency.

CHAPTER 5

THE MEASUREMENT STRATEGY

5.1 A Brief Introduction

In Chapter 1 we read that the leptonic decay modes of the W are usually chosen for the purposes of analyses. This chapter contains more information about the $W \rightarrow e\nu$ events, the production and decay modes of the W boson and the choice of the leptonic decay mode for this measurement of M_W. The kinematic distributions of the W that contain its mass information are also described here. The production and decay modes of the Z boson are similar to that of the W from a kinematic point of view. Besides, the electrons from the $Z \rightarrow e^+e^-$ decay are completely detected. Hence the $Z \rightarrow e^+e^-$ events are used as a control sample for the $W \rightarrow e\nu$ mass analysis. The kinematics of the $Z \rightarrow e^+e^-$ events are described here. A synopsis of the strategy adopted by the DØ W mass group and the main features (and tools) of the strategy are also presented in this Chapter.

5.2 Kinematics of the $W \rightarrow e\nu$ Events

At the Tevatron the W bosons are mainly produced by the annihilation of valence quarks and antiquarks. The annihilation and consequent production of the vector boson (W or Z) can be viewed as being caused by a "hard scatter" (head-on collision) between the quark and antiquark. Figure 5.1 shows a schematic

diagram of a W event along with the kinematic quantities of the event.

$$u + \bar{d} \rightarrow W^+ \tag{5.1a}$$

$$\bar{u} + d \rightarrow W^- \tag{5.1b}$$

If the quark or antiquark radiates a gluon before it annihilates (this is called "initial-state gluon radiation") it imparts a boost or momentum to the newly created W boson, the transverse component of which is represented by p_T^W. In order to conserve momentum, the radiated gluon (parton) forms the recoil in the direction opposite to the W boson. The W boson can also emit a photon and continue on as a real (on-shell) or virtual (off-shell) W boson with some momentum.

The Figure 5.1 shows a $W \rightarrow e\nu$ decay in the transverse plane of the detector. This plane is perpendicular to the beam line (z) of the detector. The W boson decays into an electron and a neutrino. A hadronic recoil shown in the direction opposite to the W, conserves transverse momentum. This recoil includes the partons (undergo hadronization) emerging from the hard scatter, from the interactions of the spectator quarks in the event and hadrons from the previous beam crossings. The energy deposition from the electron and hadronic particles are detected in the calorimeter. The neutrino leaves no signatures of interactions in the calorimeter and hence its energy is termed as "missing energy".

The W boson possesses both hadronic and leptonic modes of decay. These are shown in Figure 5.2. The dominant hadronic modes yield the following decay products:

$$W^+ \rightarrow c + \bar{s} \tag{5.2a}$$

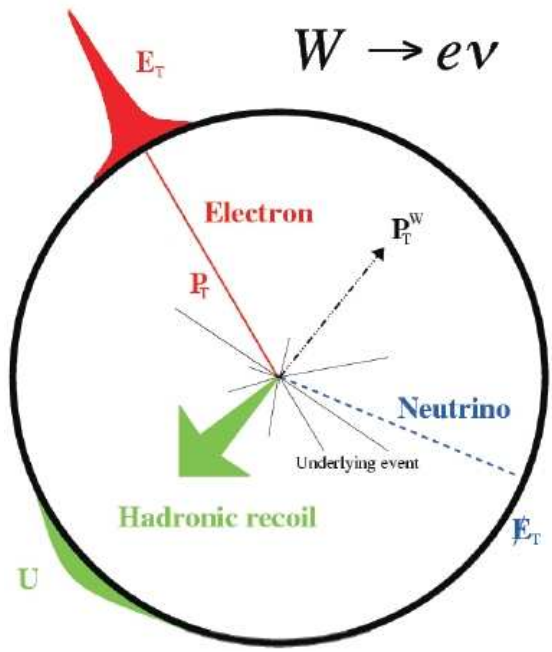

Figure 5.1. A schematic diagram of a $W \rightarrow e\nu$ decay

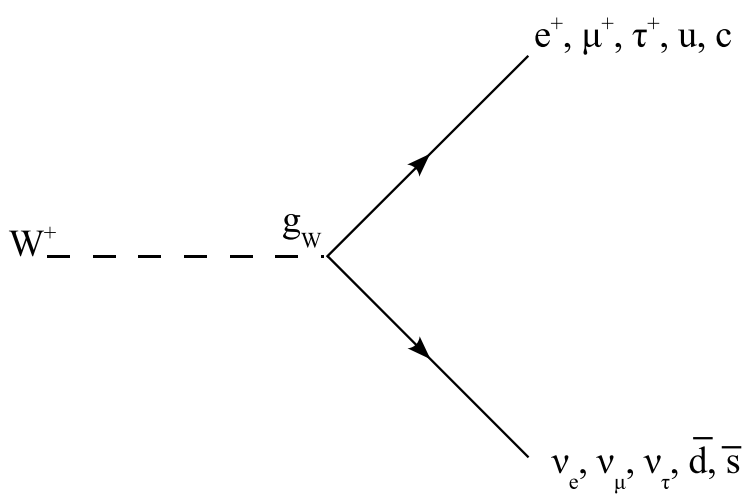

Figure 5.2. Dominant decay channels for W within SM

$$W^+ \rightarrow u + \bar{d} \tag{5.2b}$$

The W^- modes are charge conjugates of the above modes. The $W^+ \rightarrow t + \bar{b}$ or $W^- \rightarrow \bar{t} + b$ decay modes do not exist since the top quark, with a mass of $\sim$ 175 GeV, is much heavier than the W boson. Each hadronic mode is really three individual modes, one for each color of the product quarks. The branching fraction for the W into all the hadronic modes above is given simply by:

$$\Gamma_{\text{hadrons}}/\Gamma\ (W \rightarrow \text{hadrons}) \sim \frac{6}{9} = 66.67\% \tag{5.3a}$$

which is close to its PDG value of

$$\Gamma_{\text{hadrons}}/\Gamma\ (W \rightarrow \text{hadrons}) = (67.96 \pm 0.35)\% \tag{5.3b}$$

When decaying via the leptonic mode, the W^+ (or W^-) boson decays into the charged antileptons (leptons) and their corresponding neutrinos (antineutrinos) via:

$$W^+ \rightarrow l^+ + \nu_l \tag{5.4a}$$

$$W^- \rightarrow l^- + \bar{\nu}_l \tag{5.4b}$$

where l stands for any of the leptons (antileptons) $e^-(e^+)$, $\mu^-(\mu^+)$ and $\tau^-(\tau^+)$. Since leptons do not carry color the branching fraction for any of the leptonic modes above can be approximated as:

$$\Gamma_l/\Gamma\ (W \rightarrow l\nu) \sim \frac{1}{9} = 11.11\% \tag{5.5a}$$

which is close to its PDG value of

$$\Gamma_l/\Gamma\ (W \to l\nu) = (10.68 \pm 0.12)\% \tag{5.5b}$$

From the above numbers for the branching ratios, it is evident that hadronic decays of the W are more probable than the ones involving leptons. However the leptonic decay channels have very clear signatures when compared to the hadronic modes. The hadronic decay modes of the W are hard to distinguish due to the presence of other hadronic jets. Multijets arising from $p\bar{p}$ collisions are also capable of faking the hadronic decays from the W boson. The jets from the W boson events need to be dissociated from those present from other sources. The charged leptons from the W decay carry large momenta and are well isolated. The clean and relatively easy detectability, coupled with minimal backgrounds make the leptonic decay modes highly favored candidates for analyses involving the W boson at hadron colliders, especially when it comes to precision measurements of its mass (M_W).

By design, the DØ calorimeter is well suited for measuring energies of particles arising from the $p\bar{p}$ collisions. It can provide an energy resolution of about 5% for electrons at energies of 50 GeV, making the $W \to e\nu$ mode, a promising candidate for study.

Thus this precision analysis probes the leptonic mode of the W decay, where the $W^-(W^+)$ decays into an electron (positron) and an antineutrino (neutrino). The energy deposition from the electron is mainly contained in the EM calorimeter whereas the energy of the neutrino contributes to the missing energy ($\not{E}_T$) of the event.

In the hard scatter that produces a vector boson event, the initial proton and antiproton break up and the fragments hadronize. These hadronic particles

recoil against the vector boson, so they're directed opposite to the boson. Besides this, interactions from the other particles present in the same or previous beam crossings and calorimeter noise [101, 102] also contribute to the hadronic flux.

The "hadronic recoil" (denoted by $\vec{u}_T$) is thus a collective term used for everything in the event except for the vector boson and its decay products. Hence in a $W(Z)$ event the recoil constitutes of all the particles recoiling against the W (or Z) boson in order to conserve momentum. Thus at their point of production, the net transverse momenta of the recoiling particles must balance the transverse momentum of the vector boson (denoted by $\vec{p}_T^{\,W}$), i.e.

$$\vec{u}_T = -\vec{p}_T^{\,W} \tag{5.6}$$

Once the W boson decays into the electron and neutrino, the transverse momentum of the W boson equals the vector sum of these decay products. From the above relation, the W recoil can also be obtained from the sum of the decay products. Hence,

$$\vec{u}_T = -\vec{p}_T^{\,W} = -(\vec{p}_T^{\,e} + \vec{\not{E}}_T) \tag{5.7}$$

5.3 Kinematic Distributions for Determining the Mass of the W

In $p\bar{p}$ collisons, the exact longitudinal momenta of the colliding quarks is not known. The DØ calorimeter has coverage up to $|\eta| \leq 4.2$, but it does not have complete coverage, especially in the area around and near the beampipe of the detector. As a result an appreciable number of particles resulting from a $p\bar{p}$ collision could escape undetected down the beampipe. This means that the energy (momentum) of the neutrino which escapes undetected might not be measured correctly, thus impacting the invariant mass of the W boson.

In order to avoid these pitfalls, the W mass is reconstructed on a plane that is transverse to the beam direction. Momentum conservation allow us to obtain precise measurements of the transverse momenta (energy) of the electron and recoil in this plane. The neutrino momentum is inferred from the p_T balance of the event and is referred to as the "missing transverse energy" of the event. From these measurements the "transverse mass" of the W boson is computed. In the transverse plane, the p_T balance is given by the following expression:

$$\vec{p}_T^{\,\nu} \;=\; -\,(\vec{p}_T^{\,e} \;+\; \vec{p}_T^{\,\mathrm{Recoil}}) \tag{5.8}$$

The transverse mass of the W can be constructed from the difference of its energies and momenta and is given by the following expression:

$$m_T = \sqrt{(|E_T^e| + |E_T^\nu|)^2 - (\vec{p}_T^{\,e} + \vec{p}_T^{\,\nu})^2} \tag{5.9a}$$

which can be simplified to the following

$$m_T = \sqrt{2p_T^e p_T^\nu (1 - \cos\phi_{e\nu})} \tag{5.9b}$$

where p_T^e and p_T^ν are the magnitudes of the transverse momenta of the electron and neutrino respectively and $\cos\phi_{e\nu}$ is the angle between the two.

It should be noted that the transverse mass of the W is analogous to its invariant mass, $M(e,\nu)$.

$$M(e,\nu) = \sqrt{(|E^e| + |E^\nu|)^2 - (\vec{p}^{\,e} + \vec{p}^{\,\nu})^2} \tag{5.10}$$

It is obtained in the transverse momentum subspace where the laws of momentum

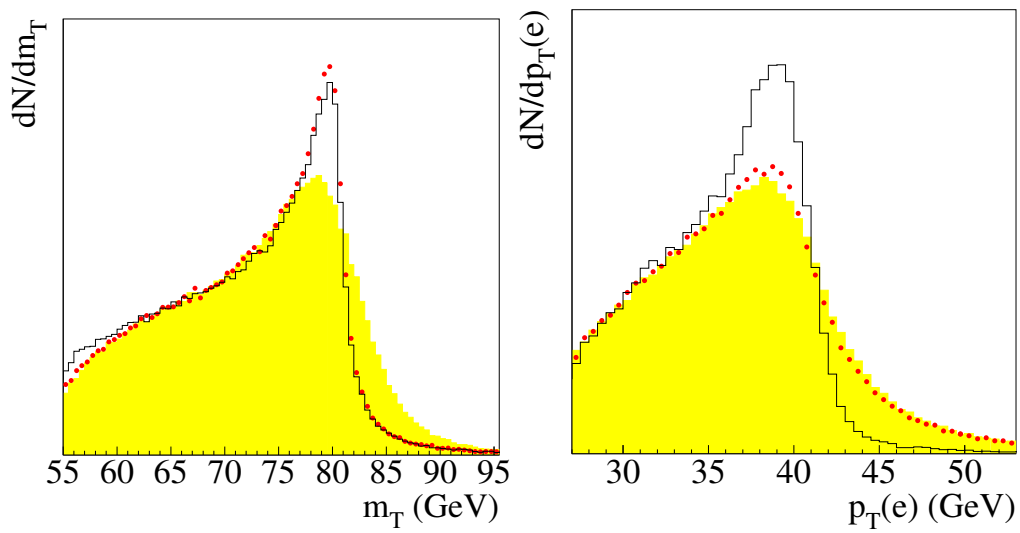

Figure 5.3. m_T and p_T^e spectra for W boson for p_T^W=0 (solid line), finite p_T^W (red dots) and with detector resolution (yellow)

conservation can be applied successfully.

Besides the transverse mass (m_T), the mass of the W can also be extracted from the transverse momenta distributions of the electron (p_T^e) and neutrino (p_T^ν). Since the neutrino escapes undetected, its momentum is also known as the missing energy denoted by $\not{E}_T$. The determination of M_W depends on the two body nature of the W decay, $W \rightarrow l\nu_l$. The kinematical Jacobian peak and sharp edge at the value $M_W/2$ is easily observed in the distributions of the transverse momentum of either of the leptons. This "Jacobian edge" contains the mass information of the W from its two-body decay [103].

The Jacobian peak in the p_T distribution gets smeared out by the W width, detector resolution effects and particularly by the effect of the finite transverse momentum of the W boson (p_T^W). Figure 5.3 shows a transverse momentum distribution of the electron (p_T^e) for three different cases. The solid black histogram

shows p_T^e without any detector effects and for $p_T^W = 0$. The red dots include the effects of a finite p_T^W while the shaded yellow histogram includes the effects of detector resolutions. Evidently, p_T^e is very sensitive to the transverse motion of the W boson. Figure 5.3 also shows a distribution of the transverse mass of the W. The solid black histogram shows m_T without detector smearing and for $p_T^W = 0$. The red dots show the effects of adding a finite p_T^W while the yellow histogram includes the effects of detector resolutions. Evidently, m_T is impacted significantly by the effects of the detector.

Thus, a fit to the p_T^e distribution provides a cross-check of the production model for the W. The modeling of the p_T^W is important because it has a big impact on the p_T^e distribution. On the other hand, the p_T^ν distribution checks how well the hadronic recoil has been modeled. Its reconstruction is sensitive to the hadronic response and multiple interactions. The m_T which is a combination of the p_T^e and p_T^ν, is a relatively robust variable. It is not sensitive to the boost of the W boson (p_T^W) to first order and is thus a complementary measurement to those from the lepton p_T distributions. Obtaining the W mass from these three different distributions is a way to test the production models and the detector modeling used.

5.4 Parameterized Monte-Carlo Simulation (PMCS)

Due to the complex interplay of the detector and kinematic effects, the shapes of the above distributions cannot be predicted analytically. A standard procedure for determining the mass of the W boson (M_W) involves comparing the distributions of m_T, p_T^e or p_T^ν taken from the collider data to the simulated template distributions. Such high statistics templates are generated at different values of the

electroweak parameter being measured (M_W in this case), from a fast, parameterized, Monte-Carlo simulated (PMCS) model of the detector. This parameterized detector models the relevant observables from the real detector as accurately as necessary with the help of parameters that are tuned to $Z \rightarrow e^+e^-$ data. Since the effects of the real detector are modeled on the basis of parameters only, this parameterized detector model works fast, enabling us to carry out extensive studies of the various aspects of this W mass analysis or make large sets of templates, unlike a detailed simulation of the detector (e.g. GEANT) which would be very slow for these purposes. This ability of the parameterized detector model has earned it the nickname "FAST MC", which will often be used to denote it in this thesis. The FAST MC modeling of the detector will be described in greater detail in Chapter 12 and in [104]. Since this is a Monte-Carlo based method, the values of the kinematic variables (such as energy, momentum, mass, etc.), which are generated by the MC and serve as input to the analysis procedure, are known. These will be referred to as E_{true}, p_{true}, M_{true}, etc. in this thesis.

The $Z \rightarrow e^+e^-$ events serve as an excellent control sample for the W due to the fact that the Z, with its two decay electrons, is a well-known and precisely-measured resonance [105] in the detector. Its signature is very similar to that of the W, with the second lepton being replaced by the neutrino for the W. Besides, its mass of $\sim$ 90 GeV is pretty close to that of the W at $\sim$ 80 GeV.

The $Z \rightarrow e^+e^-$ events are also used for the inter-η calibration of the EM calorimeter as described in Chapter 8.

An important thing to bear in mind is that since the $Z \rightarrow e^+e^-$ events are used as a control sample for the W mass analysis, we are effectively measuring a ratio of the W to Z masses in this analysis.

5.5 Fitting Procedure

As mentioned above, the W mass is extracted by comparing the collider data and FAST MC distributions of m_T, p_T^e and $\not{E}_T$. The FAST MC distributions are a set of templates generated over a range of input values of M_W in steps. The background contributions to the $W \to e\nu$ signal are added to these simulated distributions to help them resemble the actual distributions obtained from collider data.

The method of comparison consists of computing a binned likelihood between the two distributions. The likelihood is determined by calculating the product of the Poisson probability for each bin of the distribution containing n_i observed events and expecting m_i events. The probability is defined as:

$$\mathcal{L} = \prod_{i=1}^{N} \frac{e^{-m_i} m_i^{n_i}}{n_i} \tag{5.11}$$

We take the logarithm of the likelihood and obtain:

$$-\ln\ \mathcal{L} = \sum_{i=1}^{N} (-n_i \ln\ m_i + m_i + \ln\ n_i) \tag{5.12}$$

With the help of MINUIT [106] we minimize -ln $\mathcal{L}$ and obtain the corresponding W mass. The $\pm 1\sigma$ error on the optimal value is obtained by varying -ln $\mathcal{L}$ by 0.5. The fits are performed separately for each of the m_T, p_T^e and $\not{E}_T$ distributions.

5.6 Kinematics of the $Z \to e^+e^-$ Events

Since we use the $Z \to e^+e^-$ events from collider data as a standard candle in this analysis, both for calibrating the EM calorimeter and parameterizing several

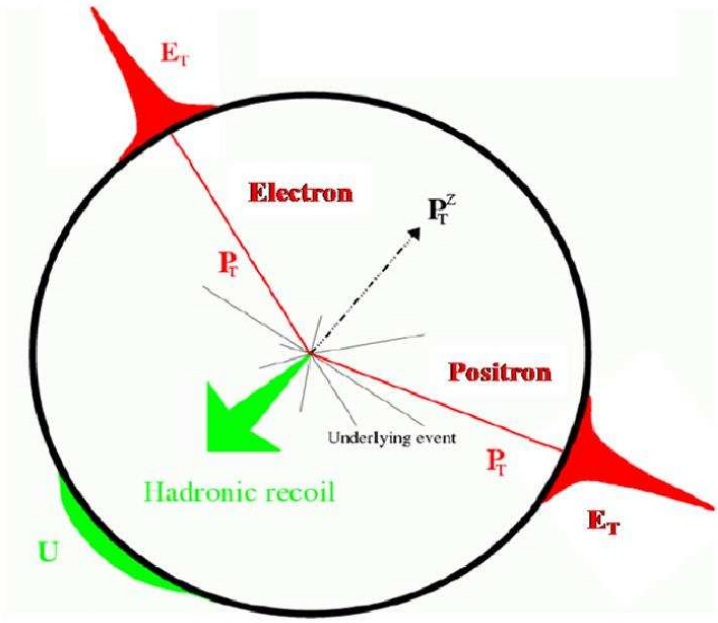

Figure 5.4. A schematic diagram of a $Z \rightarrow ee$ decay

systems of the FAST MC, it is important to familiarize ourselves with the Z boson, its production and decay modes and some of the reconstructed variables that are prominent and will often find mention in the subsequent sections here. Figure 5.4 represents a schematic of the Z boson decaying into its lepton-antilepton pair, in this figure the electron and positron.

Like the W, the Z boson is also produced by the annihilation of the valence quarks and antiquarks at the Tevatron. Initial state radiation from the colliding quarks or the Z propagator itself can impart some transverse momentum to the Z boson, referred to as p_T^Z in the transverse plane.

$$u + \bar{u} \rightarrow Z^0 \tag{5.13a}$$

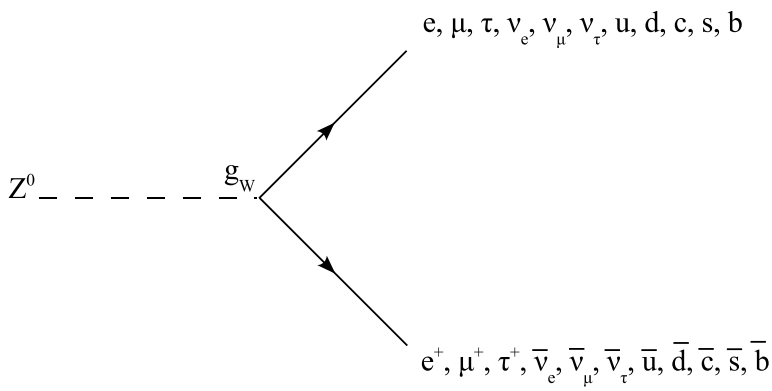

Figure 5.5. Possible decay channels for Z within SM

$$d + \bar{d} \rightarrow Z^0 \tag{5.13b}$$

The Z boson also possesses both hadronic and leptonic modes of decay. These have been shown in Figure 5.5. However the coupling of the Z to the quarks and leptons is not like that of the W (a universal $V - A$ form). The Z vertex factor is given as follows:

$$\frac{ig_z}{2}\gamma^\mu(c_V^f - c_A^f\gamma^5) \tag{5.14}$$

where g_z is the neutral coupling constant and the coefficients c_V^f and c_A^f depend on the particular quark or lepton (f) involved. In the Glashow-Weinberg-Salam model, all these numbers are determined by a single fundamental parameter θ_W, called the "weak mixing angle" or Weinberg angle. These have been shown in Table 5.1.

The branching ratios for the various decay modes of the Z can be computed by taking into account their respective coupling factors, and they are different, depending on the quark or lepton involved. Like the W, the Z does not decay

TABLE 5.1

NEUTRAL & AXIAL VECTOR COUPLINGS IN THE SM

Quark/Lepton	c_V^f	c_A^f
ν_e,ν_μ, ν_τ	$\frac{1}{2}$	$\frac{1}{2}$
e^-, μ^-, τ^-	-$\frac{1}{2}$ + 2 $\sin^2\theta_W$	-$\frac{1}{2}$
u, c, t	$\frac{1}{2}$ - $\frac{4}{3}\sin^2\theta_W$	$\frac{1}{2}$
d, s, b	-$\frac{1}{2}$ + $\frac{2}{3}\sin^2\theta_W$	-$\frac{1}{2}$

into the heavier top quark. Each hadronic mode can be considered to represent three individual modes for each color of the product quark. The overall branching ratio for the Z decay into all of its hadronic modes can be given by:

$$\Gamma_{\text{hadrons}}/\Gamma\ (Z \to \text{hadrons}) \sim \frac{15}{21} = 71.43\% \tag{5.15a}$$

obtained via a simple determination. This is quite close to its PDG value of

$$\Gamma_{\text{hadrons}}/\Gamma\ (Z \to \text{hadrons}) = (69.91 \pm 0.06)\% \tag{5.15b}$$

However if we look at some of the hadronic modes of the Z, the branching ratios are given as follows:

$$Z \to (u\bar{u} + c\bar{c})/2 \qquad (10.1 \pm 1.1)\% \tag{5.16a}$$

$$Z \to (d\bar{d} + s\bar{s} + b\bar{b})/3 \qquad (16.6 \pm 0.6)\% \tag{5.16b}$$

$$Z \rightarrow c\bar{c} \qquad (11.76 \pm 0.33)\% \tag{5.16c}$$

$$Z \rightarrow b\bar{b} \qquad (15.14 \pm 0.05)\% \tag{5.16d}$$

Evidently they are quite different. When decaying leptonically, the Z decays into a lepton and an antilepton. This can be represented as:

$$Z \rightarrow l^+ + l^- \tag{5.17}$$

where l^- stands for any of the leptons (e^-, μ^-, τ^- or ν_e, ν_μ, ν_τ) and l^+ for the corresponding antileptons.

Taking into account the couplings of the Z to leptons, the branching fraction for the leptonic modes can also be determined. However from a simple calculation, the branching ratio for the Z decaying into any of its leptonic modes can be given by:

$$\Gamma_l/\Gamma \ (Z \rightarrow l^+l^-) \sim \frac{1}{21} = 4.76\% \tag{5.18a}$$

which again is reasonably close to its PDG value of

$$\Gamma_l/\Gamma \ (Z \rightarrow l^+l^-) = (3.36 \pm 0.0023)\% \tag{5.18b}$$

When making use of $Z \rightarrow e^+e^-$ events in collider data as a control sample for the W events, some of the variables that are often used are similar to those of the W. They are given below as follows:

1. The transverse momentum of the Z or the dielectron transverse momentum

$$\vec{p}_T^{\,ee} = \vec{p}_T^{\,e1} + \vec{p}_T^{\,e2} \tag{5.19}$$

2. The transverse momentum of the hadronic recoil of the Z

$$\vec{u}_T = -\vec{p}_T^{\,e1} - \vec{p}_T^{\,e2} - \vec{\not{E}}_T = \vec{p}_T^{\,ee} - \vec{\not{E}}_T \tag{5.20}$$

3. The reconstructed invariant mass of the Z boson

$$M_{ee} = \sqrt{2E^{e1}E^{e2}(1-\cos\omega)} \tag{5.21}$$

where ω is the opening angle between the two electrons.

5.7 GEANT (FULL) Monte-Carlo Analysis

The *modus operandi* for the W mass analysis adopted by the DØ W mass group is to first perform a GEANT-based Monte Carlo measurement [104] before performing a measurement on actual collider data. Here a $W \to e\nu$ events sample containing events generated using Monte-Carlo (e.g. PYTHIA) [107] and processed through a full chain of the DØ detector simulation and reconstruction software [108] is considered as the "data" sample. The use of Monte-Carlo signifies that the input W mass value to the generated sample is known beforehand. We go through the entire rigmarole of the W mass analysis, checking for compatibility between the expected and the obtained results at each step. Finally the obtained W mass from this analysis should be within reasonable agreement of the initial (M_W) input.

Because of the detailed (or full) detector geometry involved with the GEANT3-based Monte-Carlo simulation, this sample is also nicknamed as the "FULL MC" and will be referred to as such, throughout this thesis, henceforth.

The MC measurement serves as a good warm-up exercise, testing out the

functionality, accuracy and performance of the various tools and procedures that have been developed by the group, for the analysis. The FULL MC analysis will be described in greater detail in Chapter 17.

5.8 A Blind Analysis

The actual W mass measurement with the collider data has been performed as a "blind analysis" [109]. This is a standard technique adopted by analyzers to avoid any bias towards a previously measured value or a statistical pattern from previous measurements. The central values are deliberately hidden from analyzers and reviewers until the analysis has gained approval. In this case it was done by inserting a recoverable but randomly generated offset in the fitting package (`wz_fitter`) [110] that provides the fitted mass (M_W) values by comparing the data and templates. The random offset was generated in an interval [-2,2] GeV around the true M_W value of 80.450 GeV. The introduction of this offset reports true differences between the different mass fits, thus allowing for systematic studies to be conducted but the central values are hidden until the last stage of approval.

CHAPTER 6

INTRODUCTION TO BASIC CALORIMETRY

6.1 A Brief Introduction

Since this measurement of the W mass involves measuring the energy of the electron ($W \rightarrow e\nu$) from the W, the calorimeter is an important subdetector for this measurement. The next few chapters detail the use of a calorimeter for this aspect of the measurement. They deal with a description of the behavior of a particle inside a calorimeter, how this information is put to use for tracking down the particle and how the calorimeter is made to function in the best effective way possible, for the above purpose.

This chapter outlines the physics behind the operation of an ideal calorimeter. Here we look at some of the main processes by which particles interact in the calorimeter with the consequent signatures (profiles) that help us identify the particle. Chapter 7 discusses how these profiles are employed for reconstructing and identifying the particles successfully. Chapter 8 describes the settings and corrections needed by the real DØ calorimeter in order to understand its response to the incident particles, so that it stands optimized for the energy measurements.

Calorimetry refers to the destructive detection of the energy of an incident particle. Most (if not all) of the energy of the particle, charged or neutral, is absorbed in a detecting medium, thus recording its energy. In addition, the momenta

of charged particles are also measured by means of their curvatures, while passing through the magnetic fields of tracking detectors. These track measurements are often helpful in identifying the particles along with their energy depositions in the calorimeter. Using the coalesced information from one or more detectors, thus helps in cleaning up the backgrounds present, especially in studies of rare processes.

Calorimetry is useful in measuring all energy, even of those particles that are neutral and thus invisible to tracking detectors, such as photons (γ), K_L^0 and neutrons. It mainly involves the calorimetric measurements of the electromagnetic (electrons, photons) and hadronic (mesons, baryons) particles. Hence most calorimeters used in particle physics experiments fall into two broad categories, electromagnetic and hadronic calorimeters. Particles such as electrons and photons interact electromagnetically, via Bremsstrahlung ($e \rightarrow e\gamma$) and pair production ($\gamma \rightarrow e^+e^-$). Thus they lose most of their energy and form EM "showers" in the electromagnetic sections of the calorimeter, via these two processes. Hadronic particles such as protons, pions and kaons interact via strong interactions of the nuclei. They deposit their energy in the form of hadronic showers in the hadronic sections of the calorimeter. For more details on calorimetry please refer to [2, 111, 112].

6.2 Bremsstrahlung by Accelerated Charged Particles

Bremsstrahlung (braking radiation) is the emission of photons by charged particles being accelerated or decelerated in the Coulomb field of a nucleus 6.1. In the rest frame of the charged particle, the electric field of the incoming nucleus (Ze) can be visualized as a distribution of soft photons [113–115] that will Thom-

son scatter [112] off the projectile (i.e. charged particle). The Bremsstrahlung cross section, σ_B, is thus described as the Thomson scattering, σ_T, of the soft virtual photons, N_γ, that describe the coherent field of the nucleus off the projectile charge. Thus,

$$\frac{d\sigma_B}{d\omega} \sim Z^2 \frac{dN_\gamma}{d\omega} \sigma_T \tag{6.1a}$$

$$\frac{d\sigma_B}{d\omega} \sim \frac{(Z^2\alpha)}{\omega} (\alpha\lambda_p)^2 [ln(\ )] \tag{6.1b}$$

Here the Compton wavelength λ_p is the wavelength of the projectile ($\lambda_p = \hbar/m_p c$).

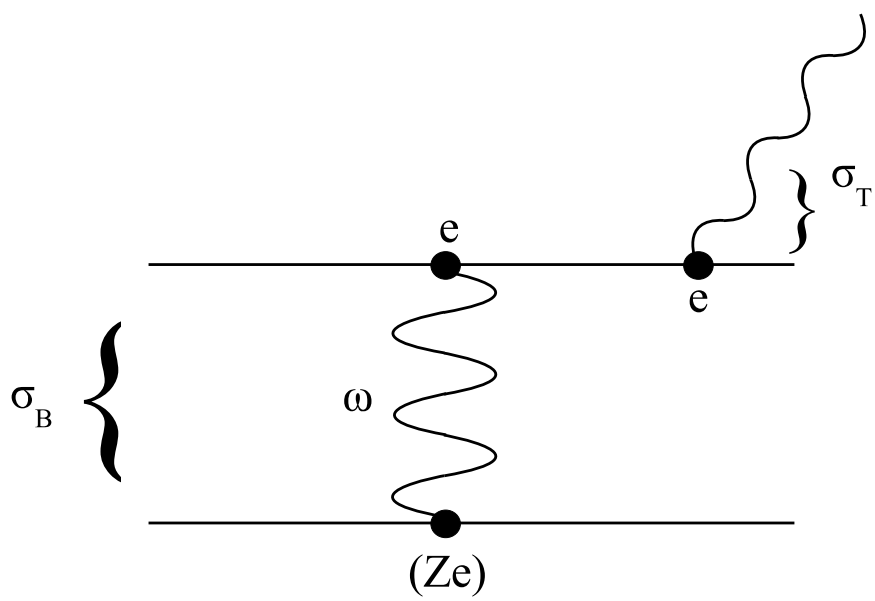

Figure 6.1. Feynman diagram for Bremsstrahlung in the field of a nucleus

Since the Bremsstrahlung cross section $\sigma_B \sim [Z^2\alpha^3/m^2]\ln(\ )$, we notice that it is numerically larger ($\sigma_B \sim$ Z^2[0.58 mb]) than the typical hadronic cross section given below by equation 6.10.

The total emitted energy or radiative energy loss, dE, is obtained by integrating the Bremsstrahlung distribution over all frequencies and weight by the energy of the emitted photon. Thus,

$$dE \sim \int_0^E (\hbar\omega)(\frac{N_0\rho\ dx}{A})(\frac{d\sigma_B}{d\omega})d\omega \tag{6.2}$$

The fractional energy loss per path length, ρ dx (in g/cm^2), is given by $\frac{1}{E}(\frac{dE}{\rho\ dx})$ and it also represents the radiative mean free path for emitting Bremsstrahlung radiation, X_0, or simply put, the radiation length.

$$\frac{1}{E}(\frac{dE}{\rho\ dx}) = \frac{1}{X_0}, \qquad E(x) = E(0)e^{-(\rho x/X_0)} \tag{6.3}$$

From equation 6.2, $dE \sim (\mathrm{Z}^2\alpha)(\alpha\lambda)^2(N_0\rho\ dx/A)E$, and the radiation length is given by,

$$X_0^{-1} = \frac{16}{3}(\frac{N_0}{A})(Z^2\alpha)(\alpha\lambda_p)^2[ln(\ )] \tag{6.4a}$$

$$\sim (Z/A)Z \sim Z \tag{6.4b}$$

A reasonable representation of the numerical value in g/cm^2 is given as,

$$X_0(\mathrm{g/cm^2}) = 180(\frac{A}{Z^2}) \tag{6.5}$$

The radiation length can also be expressed in units of length (cm) if the value of X_0 obtained from the above equation is divided by the density of the material involved. Thus the radiation length for lead is 6.37 g/cm^2 or 0.56 cm. The depth (t) in the material is expressed in units of the radiation length as follows:

$$t = x/X_0 \tag{6.6}$$

Since the radiation length for Bremsstrahlung dependent processes decreases as $1/Z^2$, heavier metals like Pb can be used for shielding against the photons. Besides, we see that the radiation length varies as the mass of the projectile ($\lambda_p = \hbar/m_p c$). Thus electrons will radiate more easily than muons which are 200 times heavier, even though the muons couple in the same way as the electrons. Since the forces acting upon the electrons and muons are the same, the acceleration experienced by the two, due to these radiative processes are quite different. Muons ionize and 'range out' of an electromagnetic calorimeter. They do not shower and deposit much energy in it.

The critical energy, E_c, is also vital for describing the energy loss mechanism for electrons. It is defined as that energy above which radiative processes dominate. The electron energy is often defined in units of the critical energy. Thus,

$$\frac{dE}{dx} \sim \frac{-E_c}{X_0} \tag{6.7a}$$

$$E_c \sim [550MeV]/Z \tag{6.7b}$$

$$y = E/E_c \tag{6.7c}$$

Thus the critical energy has a $1/Z$ dependence. In Uranium the radiation length is 0.32 cm, the critical energy is about 6 MeV and the minimum ionization loss ($\frac{dE}{dx}|_{min}$) is 1.082 $\frac{\text{MeV}}{\text{g/cm}^2}$. For lead the $\frac{dE}{dx}|_{min}$ is 1.13 $\frac{\text{MeV}}{\text{g/cm}^2}$.

6.3 Pair Production by Energetic Photons

The phenomenon of pair production by photons is shown in Figure 6.2. The Feynman diagrams of Bremsstrahlung and photon pair conversion are very similar

and their cross sections are almost equal :

$$\sigma_{pair} = \frac{7}{9}\sigma_B \tag{6.8}$$

The process of pair production can be likened to the isotropic "decay" of a virtual photon of some non-zero mass or a "virtual mass" ('m_γ' $> 2m_e$). This virtual mass is acquired by the interaction with a nuclear Coulomb field to produce the electron-positron pair. The opening angle for the e^+e^- pair is approximately given by the ratio of the mass to the energy of the electron ($\sim m_e/E_e$). Thus the opening angle can be very small initially. It increases gradually due to the opposite sense of rotation of the electron and positron momenta in the magnetic field [112].

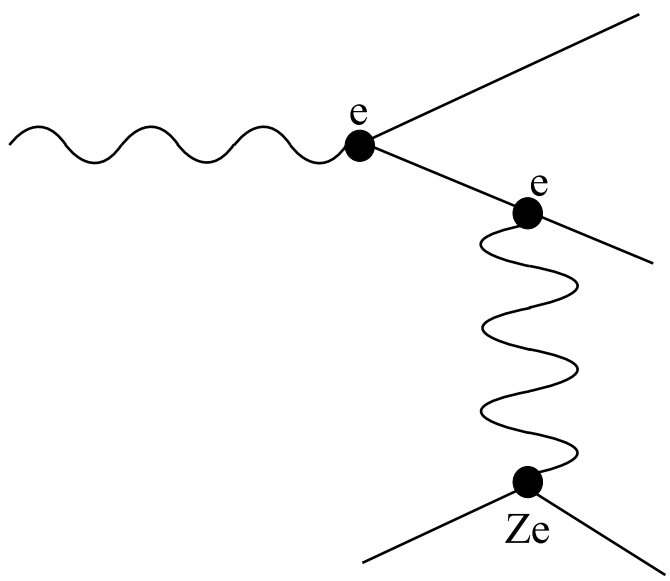

Figure 6.2. Feynman diagram for γ pair production in the field of a nucleus

Thus in electromagnetic calorimetry, an electromagnetic cascade develops. An

accelerated or decelerated electron emits photons due to Bremsstrahlung. If these photons are sufficiently energetic they pair-produce into electrons and positrons, which in turn make more Bremsstrahlung photons. This results in a shower of particles with reducing energy in the calorimeter. A sufficiently dense material such as lead or uranium is capable of absorbing these particles. An active medium such as liquid argon placed in the vicinity of the absorber material is ionized by these particles passing through it. When instrumented it yields a measurement of their energy. Details of the techniques used by calorimeters for obtaining the energies of incident particles are given in Section 6.4.1.

In hadronic interactions the charged particles interact with the nucleus by way of strong interactions. If the protons and neutrons can be thought of as spherical objects with a size of the order of the Compton wavelength of a proton (λ_p), packed together inside a nucleus of volume V, the size of the nucleus given by a_N and

$$V = 4\pi/3a_N^3 = A\ 4\pi/3\lambda_p^3 \tag{6.9}$$

Hence $a_N \sim \lambda_p\ A^{1/3}$.

The geometrical interpretation of the cross section of interaction with a nucleus is given by:

$$\sigma_N \sim \pi a_N^2 \sim A^{2/3} \tag{6.10}$$

Thus the mean free path for a nuclear interaction $\langle L \rangle$, in g/cm^2 units scales as $A^{1/3}$ and from here the nuclear interaction length (λ_1) can be derived to be

$$\lambda_1 \sim (35)A^{1/3} \qquad \text{g/cm}^2 \tag{6.11}$$

The depth in the material (ν) is expressed in terms of the nuclear interaction

lengths, λ_1, and is given by :

$$\nu = x/\lambda_1 \tag{6.12}$$

In materials such as uranium, the radiation length is ~ 0.32 cm (6.0 g/cm^2) and the nuclear interaction length is ~ 10.5 cm (200 g/cm^2). Thus the interaction length is at least 30 times greater than the radiative length. Therefore if a photon is incident on an electromagnetic calorimeter that is 20 X_0 deep, it will be almost totally absorbed. However the probability of a hadronic interaction to occur is only about 48 %. Those that do interact create a cascade occupying several λ_1 in depth. Thus electromagnetic and hadronic showers differ in their longitudinal development and transverse sizes, the former deposit their energy before the hadronic showers. This difference is exploited in the electromagnetic and hadronic calorimeters that are used for identifying electrons, photons and hadrons on the basis of the showers produced by them in the dense material of these calorimeters.

6.4 Showering in the Electromagnetic Calorimeter

The processes of Bremsstrahlung and pair production lead to a runaway showering process for the incident electron or photon inside the calorimeter, leading to a rapid, geometric, increase in the number of particles with depth. The energy of the secondary particles being created are subsequently lower than their parent particles and the "cascade" process stops when the secondary particles are not energetic enough to multiply. At this point, the shower is said to have the maximum number of particles, N_{max} and is of maximum depth, t_{max}. Beyond this range of shower maximum, the electrons die out due to ionization range out and the photons die away by Compton scattering and photoelectric absorption.

A simple schematic view of an electromagnetic shower is shown in Figure 6.3.

The mean energy of the photon emerging from Bremsstrahlung or the electron or positron emerging from pair production is assigned to be half of the energy of the parent particle, as the energy spectrum of the decay products is basically uniform from zero to the energy of the parent particle. For purposes of simplicity, the fluctuations both at the interaction points and in the secondary energies are ignored.

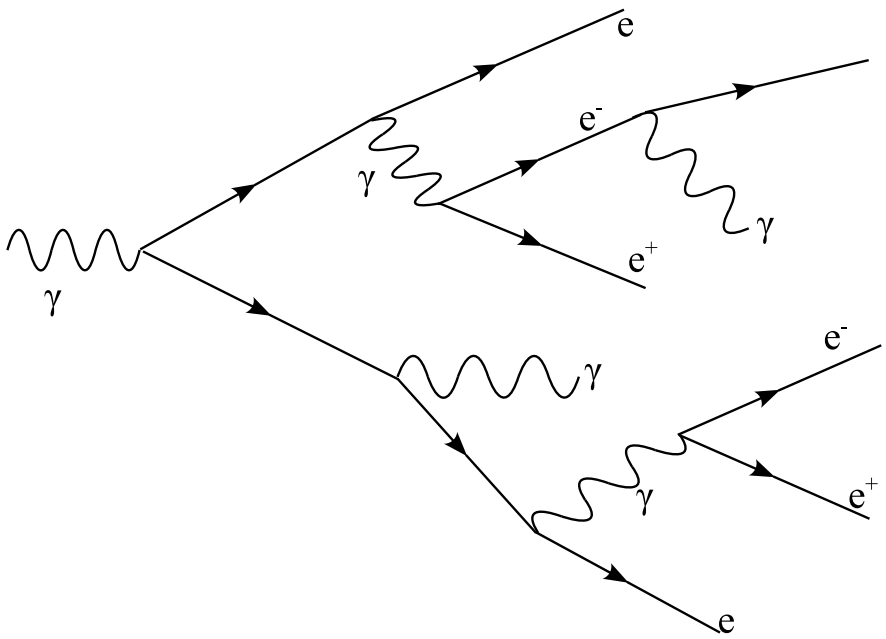

Figure 6.3. Schematic view of the development of an EM shower

Let us consider a particle with energy E decaying into massless particles. Since the number of particles, *N(t)*, in the cascade grows geometrically with the depth (t) of the cascade, the energy and number of particles can be expressed as a

function of depth in the following way:

$$e(t) = E/2^t = E/N(t) \tag{6.13}$$

$$N(t) = 2^t \tag{6.14}$$

The showering processes causing the multiplication of particles go on until the mean energy of the particles in the cascade reach the critical energy (E_c). This energy, E_c is defined as the energy above which the radiative processes dominate. As the energy falls below the critical energy, the multiplicative processes stop and the cascade dies off. Hence

$$E_c = E/2^{t_{max}} = \varepsilon(t_{max}) = yE \qquad \text{MeV} \tag{6.15}$$

where $y = E/E_c$ is the scaled incident energy. From here we see that $t_{max} \sim \ln y \sim \ln(E/E_c) \sim \ln(ZE)$ since the critical energy E_c has a $1/Z$ dependence. Thus the depth of the location of the shower maximum in units of radiation length is partially dependent on the material used for making the calorimeter.

$$N_{max} \sim E/E_c = N(t_{max}) = y \tag{6.16}$$

Thus for example, a 3.2 GeV shower in Pb has a shower maximum at a depth of t_{max}=6. There are about 400 particles in the cascade at the shower maximum.

6.4.1 Types of Calorimeters - Sampling and "Fully Active"

The two main types of calorimeters that are used for measuring the energies of incident particles are the sampling and the "fully active" calorimeters. Since

the DØ calorimeter is a sampling calorimeter, let us look into this type first. In a sampling calorimeter, the high Z absorber plates usually made of materials such as lead or uranium are interspersed with layers made of a low Z material such as scintillator plastic or liquid argon. The two different kinds of layers being used lead to the calorimeter being called a "non-homogeneous" calorimeter. The shower develops in the inert layers of the absorber medium where most of the energy is lost. The shower energy is detected (or sampled) in the active layers of the low Z material. The small fraction of energy sampled should be proportional to the total energy that is absorbed in the inert layers.

If the high Z absorber plates are of thickness $> X_0$ (radiation length of the material), the shower evolves rapidly and there is no correlation between the consecutive active layers of sampling. Thus the total number of particles traversing the active layers, N_s, is the total number in the shower. This can be obtained from the total path length, L, divided by the thickness of the inert layers, Δt, placed between the active layers. Thus,

$$N_s = L/\Delta t \sim (E/E_c)/\Delta t \tag{6.17}$$

The error due to fluctuations in the fraction of energy that appears in the active sampling layers, δE, should be the fluctuation in the total number of sampled particles, N_s. Thus the energy resolution of a sampling calorimeter has a "stochastic coefficient" term (also called sampling term), a_{samp}. This stochastic term depends on the thickness of the inert plates and thus scales as $\sqrt{\Delta t}$. If the plates become very thick, the sampled energy is not a good representation of the full shower

energy and the fluctuations increase.

$$(\frac{dE}{E})_{samp} = 1/\sqrt{N_s} \equiv a_{samp}/\sqrt{E} \tag{6.18}$$

Since $N_{max} \sim E/E_c$, a lower critical energy means more shower particles (N_s), which implies a smaller stochastic term.

Also, the energy deposited by ionization, ΔE, when going through a plate of thickness Δt at the critical energy E_c is simply $E_c \Delta t$. Hence

$$a_{samp} \sim \sqrt{E_c \Delta t} \sim \sqrt{\Delta E} \tag{6.19}$$

The other broad category of calorimeters are those which are "fully active" and consequently possess very fine sampling. Here the shower developing medium is itself active and is usually made up of crystals such as BGO, lead tungstate ($PbWO_4$) or lead glass. The uniform composition and transparency of the crystals used lead to it being called a "homogeneous" calorimeter.

In this type of calorimetry, multiple scattering of the shower particles becomes important as their numbers increase and their energy slowly decreases to the critical energy E_c at shower maximum. As a result, the scattering angle may become very large since E_c becomes comparable to the scattering energy E_s=21 MeV. This would cause the path length to exceed the usual one dimensional path length at normal incidence, deltat, since particles traverse the sampling layers at finite angles. A rough estimate of the increase is given by

$$\Delta t \rightarrow \Delta t / \langle \cos \theta_{MS} \rangle \tag{6.20a}$$

$$\theta_{MS} \sim (E_s/E_c)\sqrt{\Delta t \sim 1} \tag{6.20b}$$

The effects due to changes with the fine sampling and multiple scattering are incorporated into a theoretically motivated phenomenological formula for the sampling coefficient a_{samp}.

$$a_{samp} \sim \left[(1-W)\left(\frac{\Delta E + \delta E}{\langle \cos\theta_{MS} \rangle}\right)^{\frac{1-W}{2}} \right] \tag{6.21}$$

Here $W = \delta E/(\delta E + \Delta E)$ is the ratio of the sampled energy to the total energy lost in a layer. As the parameter $W \rightarrow 0$ we are ignoring the effects of the active sampling layers and we notice that the equation 6.21 collapses to equation 6.19, appropriate for a sampling calorimeter. For a fully active and perfect calorimeter $W \rightarrow 1$ and $a_{samp} \rightarrow 0$. However this is an unrealistisc situation because even though the stochastic errors might become negligible, other sources of error such as ionization fluctuations start to contribute.

6.4.2 Longitudinal Development of a Shower

The "total path length", L, for all generations in the shower is obtained by summing over the distance travelled by all the particles. Assuming that each particle in the shower travels a X_0 in depth before interacting, the total path length is given by,

$$L \sim X_0 \sum_{i=1}^{t_{max}} N(t) \tag{6.22a}$$

$$\frac{L}{X_0} \sim \int_0^{N_{max}} N(t)dt \sim \int_0^{t_{max}} 2^t dt \tag{6.22b}$$

$$\sim (E/E_c)/\ln 2 = N_{max}[\ln 2] \tag{6.22c}$$

Thus L $\sim X_0 N_{max}$ and the result can be visualized as the N_{max} particles of the last "generation" travelling the final one radiation length of material (X_0) in depth before ranging out and loosing energy (E_c) to ionization.

6.4.3 Transverse Development of a Shower

The transverse momentum scale is defined by the physics of the atomic electrons that shower inside the calorimeter. The characteristic transverse momentum in these collisons is the mass of the electron, m_e. In the early stages of a shower development, the transverse angles are only a few mrad, $\theta \sim m_e/\varepsilon \sim 0.51$ mrad at ε=1GeV. However as the shower progresses the energy of the cascading particles softens, as the energy is shared between the particles newly produced. Now the shower becomes more isotropic more rapidly,

$$\langle p_T \rangle \sim m_e \tag{6.23}$$

$$\langle \theta \rangle \sim m_e/\varepsilon(t) \tag{6.24}$$

Since the energy of the particles at a depth 't' defines the angle, at shower maximum (SM), the typical energy is the critical energy so that the typical angle of a particle at shower maximum is given by

$$\langle \theta \rangle_{SM} \sim m_e/E_c \tag{6.25}$$

In lead, the pair production angle at shower maximum is about 4°. However the transverse shower development is guided more by the processes of multiple scattering than finite production angles, since $E_s >> m_e$. Thus the transverse momentum of a particle of energy E_s, from multiple scattering at a depth t is given by

$$\langle p_T \rangle_{MS} \sim E_s\sqrt{t}, \qquad \sqrt{t} \equiv 1 \tag{6.26}$$

Thus the multiple scattering angle at shower maximum is given by:

$$\langle\theta\rangle_{SM}^{MS} \sim \; E_s/E_c \tag{6.27}$$

The transverse size of a showering particle is usually described in terms of the Moliere radius (r_M), which can be conceptualized as the transverse distance travelled by a particle at the critical energy while traversing the final radiation length (X_0) before dying off. Hence

$$r_M \sim \; E_s X_0/E_c = \langle\theta\rangle_{SM}^{MS} X_0 \tag{6.28a}$$

$$r_M \sim \; 7(A/Z) \qquad \text{g/cm}^2 \tag{6.28b}$$

Thus the Moliere radius depends on the multiple scattering energy E_s, the critical energy E_c and the radiation length X_0. For most of the elements where A $\sim 2Z$, the Moliere radius is about 14 g/cm^2. 90 % of the energy of a shower is contained within about 1 Moliere radius while 95 % is contained within about 2 Moliere radii, which is about 3.0 cm in lead.

6.4.4 Linearity and Resolution of a Calorimeter

Fluctuations in the shower development lead to fluctuations in the number of particles in the shower. The path length also exhibits fluctuations since cascading is a random process. The fluctuation in the number of particles goes as dN $\sim \sqrt{N}$. The measurement of energy by the calorimeter contains a "stochastic term" due to these fluctuations and consequently the fractional error in the energy measurements (energy resolution) of the calorimeter varies as $1/\sqrt{E}$

Since $N_{max} = E/E_c$, we have

$$dE/E \sim \ 1/\sqrt{E} \sim \ dN/N \tag{6.29}$$

The energy resolution of a sampling calorimeter is typically expressed by the following equation:

$$\frac{\sigma_E}{E} = \sqrt{C^2 + \frac{S^2}{E} + \frac{N^2}{E^2}} \tag{6.30}$$

The term $\frac{\sigma_E}{E}$ represents the fractional energy resolution. The noise term (N_{EM}) accounts for the electronics noise, latent radioactivity from Uranium and the underlying events in the calorimeter. It becomes an insignificant contributor at higher energies due to its $1/E^2$ dependence. The constant term (C_{EM}) incorporates the effects of imperfections in the relative channel-to-channel calibrations of the calorimeter. Since this term is independent of energy, it dominates at high energies. The sampling term (S_{EM}) accounts for the fact that we sample only a fraction of the total energy (signal) from the calorimeter. The effects of fluctuations in the shower development due to the material in front of the calorimeter are also included in this term. At high electron energies the contribution from the sampling term is suppressed due to its $1/E$ behavior. Details on the calorimeter resolution are presented in the Chapter 14

This dependence of the energy resolution can be sharply contrasted with that of tracking devices where the fractional error $dp/p \sim p$. The momentum resolution degrades linearly with momentum in a tracking device of fixed length, whereas the energy resolution of a calorimeter actually improves with increase of energy.

CHAPTER 7

RECONSTRUCTING THE EM CLUSTERS AND TRACKS

7.1 A Brief Introduction

Since this analysis of the W mass involves the leptonic decay channels ($W \rightarrow e^-\bar{\nu}$ or $W \rightarrow e^+\nu$) of the W boson, a precise reconstruction of the electron (positron) from the signals in the detectors is very important here. The electron is identified by means of its energy deposit (cluster) in the calorimeter and a corresponding track in the tracker which points to the energy cluster. Thus the electron reconstruction comprises the reconstruction of the energy cluster and the track. This chapter describes how the energy deposits and track signatures are reconstructed so as to represent the depositions of these single particles.

7.2 Energy Reconstruction in the Calorimeter

The clustering algorithm for finding and identifying electromagnetic showers is used by the reconstruction procedure of the DØ experiment. Here a cluster (list) of the EM readout towers possessing significant energy are chosen, with the tower possessing the maximum energy acting as the "seed" for the clustering process. The energy of an EM readout tower is obtained by summing up the energy contributions of the calorimeter readout cells from the four EM layers and the frist FH layer contained within a 0.1×0.1 dimension in $\Delta\eta \times \Delta\phi$. With

the seed tower as the center of the cluster, the algorithm looks at the energies of all the neighboring readout towers and sums up their energies while forming the energy of the cluster. This process continues till the region is depleted of neighbors whose tower energies are above the threshold of $\sim$ 50 MeV. The energy of the reconstructed cluster has to be above 1.5 GeV for it to escape rejection. Besides the cluster is required to pass some inital, rather crude selection criteria imposed in the early stages of the reconstruction program.

During the reconstruction procedure individual layer weights are assigned to the energy readout from the different layers, in an effort to compensate partially for the energy lost in the dead material. Higher weights are assigned to the early layers (EM1 and EM2) since most of the energy deposition takes place here. These layer weights are derived from GEANT (FULL MC) simulation and new weights have been derived using Run II Monte Carlo before taking data. These weights are very different from those used in Run I due to the fact that even though the DØ calorimeter has remain unchanged between the runs, the readout timing is very different (from 2.2 μs in Run I to 450 ns in RunII) and the material infront of the calorimeter has increased significantly. Table 7.1 gives the approximate layer weights that are used for the energy reconstruction.

The two variables of EM fraction and isolation are used as the main criteria for identifying electromagnetic candidates. The EM fraction f_{EM}, is defined as the ratio of the energy contained only in the EM layers to the total energy of the cluster and is required to be above 0.9 for the cluster to be identified as an EM cluster. The isolation variable f_{iso}, is a measure of how well isolated the cluster

TABLE 7.1

INDIVIDUAL LAYER WEIGHTS USED FOR ENERGY RECONSTRUCTION

Layer	Depth (X_0)	Weight (a.u.)	Weight/X_0
EM1	2.0	31.199	15.6
EM2	2.0	9.399	4.7
EM3	6.8	25.716	3.8
EM4	9.1	28.033	3.1
FH1	≈ 40	24.885	≈ 0.6

is from other objects such as hadronic jets. It is defined as:

$$f_{iso} = \frac{E_{cone} - E_{core}}{E_{core}} \tag{7.1}$$

Here E_{cone} is the total energy of the readout towers summed over the four EM and first FH layers. The towers lie within a cone of radius R = $\sqrt{\Delta\eta^2 + \Delta\phi^2}$ = 0.4, around the center of a cluster in the η-ϕ space. The cluster is centered on the tower with the highest transverse energy. E_{core} is the total energy of the readout towers within a cone of radius R=0.2, summed over the four EM layers only. Figure 7.1 is a pictorial representation of the energy variables that help define the isolation for an EM cluster.

The isolation variable is also a measure of how deep and narrow a cluster is. Small values of isolation point to the fact that a large amount of energy is concentrated in a narrow region of the EM cluster and is likely to be deposited

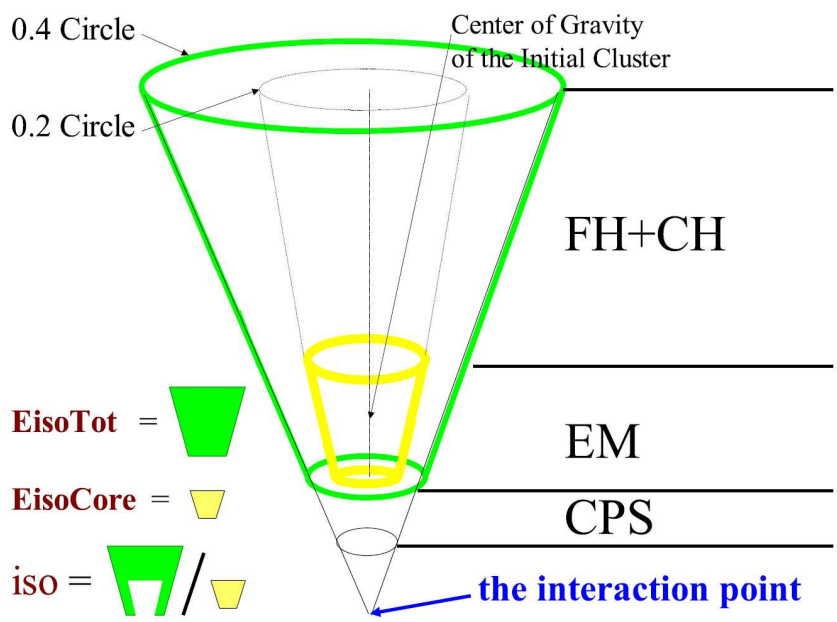

Figure 7.1. Defining the isolation of an EM cluster

by an electron or a photon. Hence an initial threshold of 0.2 is required for the cluster to satisfy the isolation criterion at the reconstruction level. Later on in the analysis this cut is tightened to 0.15.

Since charged hadrons deposit less than 10 % of their energy in the EM calorimeter and the electrons from W and Z boson decays tend to be well isolated from other particles, the variables of f_{EM} and f_{iso} prove to be powerful discriminants aimed at distinguishing between electromagnetic objects and hadronic jets.

Besides the EM fraction and isolation discriminants, the shape of an electron shower is also tested to see how well it compares to that expected for a typical electromagnetic shower. This is done with the help of a multi-variate tool called

the H-matrix. This H-matrix is the inverse of the covariance matrix that is built up using the following seven variables - the fractional energies in the four EM layers, shower width in the eta direction, the logarithm of the cluster energy and the position of the primary vertex. The seven dimensional covariance matrix is built up with all this information obtained from the detailed simulations of electromagnetic showers using the GEANT based Monte Carlo.

A cluster that passes all the default thresholds in the initial stages of selection is subject to the final stage of reconstruction. At this stage various quantities that describe cluster properties, such as cluster energy, cluster p_T, η, ϕ, are computed and stored.

The electron energy is obtained by summing over the energies of all EM towers within a window of 0.5 $\times$ 0.5 in the $\eta - \phi$ space (5 $\times$ 5 towers), in the central region (CC) or within a cone of radius 10 cm in EM3 in the end-cap regions (EC) of the calorimeter. Both these regions are centered on the tower that registers the highest fraction of the electron energy. The centroid of the calorimeter shower is determined from a log-energy-weighted algorithm. The energy depositions in the third EM layer, EM3, are used to compute the weighted means of the positions $\vec{x_i}$ of the cell centers.

$$\vec{x}_{cluster} = \frac{\sum_i \omega_i \vec{x_i}}{\sum_i \omega_i} \tag{7.2}$$

The weights are given by

$$\omega_i = \max(0, \omega_0 + \log(E_i/E(e))) \tag{7.3}$$

where E_i is the energy in cell i, ω_0 is a parameter that depends on η_e and E(e), the pseudorapidity and energy of the electron. The algorithm is calibrated using

electrons from GEANT based MC simulations. If an electron cluster is found to have a matched track, then the direction of the track is assigned to the direction of the electron. If the cluster cannot be matched to a track, then the positions of the calorimeter centroid and the primary vertex are used to derive a direction for the electron cluster. The momentum of the electron is given by:

$$\vec{p_e} = E(e) \begin{pmatrix} \sin\theta(e)\cos\phi(e) \\ \sin\theta(e)\sin\phi(e) \\ \cos\theta(e) \end{pmatrix} \tag{7.4}$$

The transverse momentum of the electron is given by $p_T(e) = E_T(e) = E(e)\sin\theta(e)$

7.3 Track and Vertex Reconstruction from the Tracker

Trajectories of charged particles are reconstructed from the hit information that is available from the SMT and CFT. The tracks are then used to find the primary event vertices and also the displaced secondary vertices for some long-lived particles such as b-quarks, K_S^0, D and λ_s mesons that have finite decay lengths.

The hits are first subject to the pattern-recognition procedure that searches through all the possible combinations of hit patterns, as predicted by the GEANT-based MC simulations, in order to find the pattern that matches the data best. This pattern search is done in parts, it starts with the outermost layers of the tracking detectors and works its way outside in, step 1 considers the 2 outermost layers, step 2 looks at hits in the next 2 outer layers lying inside the ones that were looked at in step 1 and step 3 looks at the 4 inner layers. This way the search at each step is narrower due to the previous search results and results in quick

decisions. After the pattern-recognition algorithms finish working, they yield a complete set of track candidates.

The next major step in the track-finding algorithm is the implementation of the Kalman fitting technique. The use of the Kalman fitter for track-finding and fitting with the DØ Run II tracker is part of the `trf` software package [116]. This fitting algorithm is an elegant and simple way of solving the mathematical problem of determining the optimal track parameters with errors, from a set of measurements, on any surface. It starts with an inital guess or a partially reconstructed track and extends the track by including additional measurements. In essence, the track parameters and error matrix from one set of measurements is propagated to the surface of the next set of measurements, thus creating a prediction for that surface. The predictions can be used as a filter, to help the pattern-recognition in the selection of new measurements of the track candidates. These predictions alongwith the actual measurements of the new surface are used to produce an improved or "filtered" estimate of the track parameters and errors on that surface. This continues until an optimal estimate of the track parameters with the errors is obtained on the surface of the final measurement. The Kalman fitter works well with the addition of several sets of measurements and the track parameters are well determined to form gobal track candidates.

The method used for the vertex fitting is based on the Kalman Filter algorithm [117] but uses a fast global least squares fit instead of a recursive approach. The primary vertex is the point of interaction of the proton-antiproton in a hard scatter event when the two beam bunches collide with each other. As we know, the positions of these $p\bar{p}$ interactions are distributed along the z direction according to a Gaussian distribution with a width of ~ 25 cm. In the transverse plane, the

beam is only about 30 μm wide in x and y. The primary vertex identification consists of two steps - reconstruction of all interactions in a given event and selection of the hard scatter primary vertex. All suitable primary vertices in an event are obtained via the Impact Parameter Primary Vertex algorithm. This can also be called the "tear-down" procedure for determining the primary vertex of an event. Here all the selected tracks are fitted to a common vertex and the χ^2 contribution of each track to the vertex is computed. The track that is furthest from the vertex (highest χ^2) is dropped from the selection while the remaining tracks are refit for a new common vertex. This process is reiterated until the χ^2/dof is < 10 at the vertex. After a vertex has been found the whole procedure of finding another common vertex is repeated with the remainder of the tracks in the event, until no more tracks can be vertexed.

The selection of the hard scatter event vertex is based on a probabilistic approach described in detail in [117]. Based on the momentum (p_T) difference of tracks from hard and minimum-bias interactions, a track minimum-bias (MB) probability is built by integrating over the track momenta distribution from minimum-bias events from a given track p_T to infinity. This parameter is the probability for a track from the minimum-bias event to be reconstructed with a momentum p_T or higher. For each vertex, the individual track MB probabilities are combined to yield a "vertex MB probability". The vertex with the smallest MB probability is chosen as the hard scatter primary vertex of the event.

The search for the secondary vertices consists of four steps, track-based jet reconstruction, track selection, vertex finding and vertex selection. The reconstruction of track-based jets helps to keep the secondary vertex finding algorithm free from biases due to calorimeter reconstruction. Track-based jets exploit the 3-

dimensional capabilities of the tracking detector to obtain 3D jets and are usually not affected by noisy jets or calorimeter-tracker misalignments. For each reconstructed track-jet, a set of displaced tracks is selected based on the significance of the impact parameter (S = $dca/\sigma(dca)$).

For every track-based jet with at least two selected tracks, attempts are made to find a secondary vertex from the tracks. Two complementary methods are used, the first is the "tear-down" procedure which has been described in the section above on finding primary vertices. The other is known as the "build-up" algorithm which starts finding seed vertices by fitting all combinations of pairs of selected tracks in jets. It then attempts to associate more tracks with the seeds based on a χ^2 contribution to the vertex until no more tracks can be associated with the seeds. This procedure often results in vertices sharing tracks. The "tear-down" method has a higher level of purity but lower efficiency than the "build-up" method of finding secondary vertices.

CHAPTER 8

CALIBRATING THE CALORIMETER AND TRACKER

8.1 A Brief Introduction

An accurate reconstruction of the electron energy is critical to the W mass measurement. We have read about some of the operational principles of a calorimeter in Chapter 6 and reconstruction of the electron signature from the calorimeter readouts in Chapter 7. We now read about how the DØ calorimeter is set up for an optimal measurement of the energies of the particles that are incident on it. This ensures that the response of the calorimeter to the particles is optimized uniformly as a function of the calorimeter dimensions of η and ϕ. This is referred to as "calibrating" the calorimeter for the energy measurements.

As we have read in Chapter 4, the readout of the calorimeter is in the form of digitized signals that are proportional to the energy deposits of each cell. This ADC signal is first corrected by applying the gain- and pedestal-corrections [118] to it and then converted to its correponding energy value by applying a series of calibration factors to it. These calibration factors are a combination of an overall calibration which determines the absolute energy scale and the use of individual layer weights which correct for energy lost in the dead material in front of the calorimeter (will be discussed in Chapter 9). We discuss both these calibrations in detail in this chapter.

The DØ calorimeter is fine-grained and has 32 azimuthal segments. Physical and electronic non-uniformities of the calorimeter can affect its readout in a way that disables an accurate energy measurement of the signatures of a W or Z event. The mechanical non-uniformities such as mis-alignment, granularity, etc. increase the energy resolution of the partons in the calorimeter. This effect is indicated by the "constant term" in the standard expression (Chapter 14) used for the energy resolution of the calorimeter and is independent of the incident energy. Hence for high energy electrons, this term dominates their energy resolution. Miscalibrated segments of the calorimeter can introduce significant non-Gaussian effects on the physical observables of event signatures. Thus an accurate calibration of the calorimeter is very essential for precision measurements such as the W mass.

There are two parts of the calibration procedure, calibrating out the channel-to-channel biases in the readout electronics and calibrating the mechanical non-uniformities of the detector.

8.2 Electronics Calibration of the Calorimeter

The non-uniformities in the channel-to-channel responses are ascertained with the help of pulser signals. Pulser signals of known charge are injected into the readout and the measured charge is documented, thus providing a handle for getting rid of the differences in response of the readout channels. However there are some differences between the signal used for the calibration and the actual physical signals. For example the shapes of the two signals are different - the physical signal is a triangle-shaped signal possessing about 450 ns of drift time, whereas the calibration signal is an exponential signal that falls off rapidly. Moreover since the pulser signals are injected between the calorimeter and the electronics,

the signals are reflected from the calorimeter, making them more sensitive to cable length and variations in cell capacitances than the physical signal. Thus they are altered in shape and behavior by the time they reach the readout and affect the accuracy of the electronics calibration.

By taking sample measurements of the same signal at three different times, with the nominal peak sample taken at the time defined by the trigger, and two samples taken 132 ns before and after the peak one, we can determine the nominal sampling position with respect to the shaped signal peak. We ascertain that the variation in the peak value of the sampled signal due to timing differences from channel-to-channel is less than 0.1%. The electronics calibration helps in correcting the variation of the physical signal with an accuracy of 1%.

8.3 Gain Calibration of the Calorimeter

In this section we discuss the calibrations that are necessary due to the mechanical non-uniformities of the calorimeter. Calibrating out the effects of the physical deformities that impact the response and resolution of the calorimeter is also termed as "gain calibration" of the detector. The basic idea is to adjust the relative weights of the different segments of the detector on the basis of their actual energy response so as to obtain a uniform and expected energy response over all regions of the calorimeter. The gain calibration involves two major procedures, the ϕ and η intercalibrations.

8.3.1 The ϕ Intercalibration

At the Tevatron the proton and anti-proton beams are non-polarized. This implies that the calorimeter should exhibit a uniform response in the azimuthal

(ϕ) direction. Any deviations from this indicates the presence of physical non-uniformities in the segments. Thus calibrating the detector in the azimuthal (ϕ) direction at fixed values of η (the notation $i\eta = 10\times\eta$ is also used often) is referred to as "ϕ intercalibration". This equalizes the response of all towers inside a ϕ ring at a given value of $i\eta$. In the central region of the calorimeter the readout precision-towers have been calibrated with a precision of about 1%, whereas the EM layers have been calibrated with a precision of about 2 %.

Collider data events above a certain EM energy threshold are used for the calibration. In principal, the observed transverse energy (E_T^i) of each precision-tower is multiplied by a weight factor (α_i) to match the tower's occupancy with the average ocupancy (over all the towers in the specified η ring). Thus,

$$E_T^{i\prime} = \alpha_i E_T^i \tag{8.1}$$

In practice, the number of events above a fixed lower cut on transverse energy L, is determined in each calibrated tower. The cut L is sufficiently high to avoid trigger biases. In a similar way, the average number of events per ϕ-tower for the entire uncalibrated eta-ring is estimated. Now for each tower in ϕ, an movable lower energy cut, L_i' is adjusted so that the occupancy of the tower matches the average occupancy.

Hence from our assumption of proportionality the calibration constant α_i can also be determined as follows:

$$L_i' = \alpha_i L_i \tag{8.2}$$

The four EM layers of the calorimeter within each precision-tower are also calibrated via the same concept. That is, the relative calibrations of the layers are

adjusted so that the distribution of the fractional energy for each layer in a tower reflects the average energy distribution for that layer for all values of ϕ.

These tower and layer calibrations performed over successive iterations, give rise to stable and consistent results for the calibration constants. The ϕ intercalibration is performed with the help of inclusive EM and jet events from the collider data.

8.3.2 The η Intercalibration

Having calibrated out the variations in the azimuthal (ϕ) response of the calorimeter we now equalize the energy response of the calorimeter at different rapidities (η), that is at the different rings represented by the values of "$i\eta$". The central region of the calorimeter (CC) extends up to η =1.2 and the end-cap regions (EC) extend up to η =4.2. The η calibration has been done at the precision-tower level in the EC region and at the layer level in the CC region of the calorimeter.

$Z \rightarrow e^+e^-$ events from data are used for this calibration. For each η region represented by a value of $i\eta$, the reconstructed electron energies are obtained from the corresponding raw energies. These energies have been corrected with the help of multiplicative constants ($c_{i\eta}(j)$), $\vec{\alpha}$ and $\vec{\beta}$. $\vec{\alpha}$ is an array of parameters that are used to correct for the average loss of energy by the electron in front of the calorimeter while $\vec{\beta}$ is an array of variables used for correcting the energy lost by electrons too close to the ϕ-cracks (intermodular) regions of the calorimeter.

In terms of the energies, the invariant mass of the Z boson is given by:

$$m_Z = \sqrt{2E_1E_2(1-\cos\theta)} \tag{8.3}$$

where E_1 and E_2 are the reconstructed energies of the two electrons and θ is the angle between them. The reconstructed energies E_i (i = 1,2) can be represented by

$$E_i = E_i^{\text{raw}} + K(E_i^{\text{raw}}, \vec{\alpha}) + L(E_i^{\text{raw}}, \vec{\beta}) \tag{8.4a}$$

with

$$E_i^{\text{raw}} = \sum_{j=(\text{allcells})} E_j \tag{8.4b}$$

Thus the "raw energy" E_i^{raw}, is the sum of all the energies in the EM cluster. However as we have read earlier in Chapter 4, our calorimeter possesses $\sim 4.0\ X_0$ of material in front of it and so the electrons might lose an appreciable amount of their energies before they reach the first detecting (active) regions of the calorimeter. This energy loss primarily depends on the energy of the electrons and their angle of incidence (η) on the calorimeter. This energy loss is described in greater detail in Chapter 9. Due to the appreciable loss in energy of the electrons, the reconstructed cluster energy E_i^{raw} can underestimate the true energy of the electron. Hence a correction function in form of $K(E_i^{\text{raw}}, \vec{\alpha})$ is required to describe the average energy loss as a function of the reconstructed electron energy E_i^{raw}. The vector α describes the dependence of the average energy loss of the electrons on the material encountered in front of the calorimeter. Similarly we have read that the response of the calorimeter in its intermodular regions (ϕ-cracks) and the intercryostat regions (ICR) is poor. Thus the energies of electrons lying close to these regions need a correction in order to reflect their true energies. The function $L(E_i^{\text{raw}}, \vec{\beta})$ is used to correct for the energy lost by electrons of this type. Inside the "fiducial" region of the calorimeter, the corrections for the edge effects are smaller than the those due to the material upstream of the calorimeter.

Since we are dealing with the calibration procedure, the raw energies in equation 8.4a can be replaced by the following expression:

$$E_i^{\text{raw}} = \sum_{j=(\text{allcells})} c_{i\eta}(j) E'_j \tag{8.5}$$

where E'_j denotes the cell energies E_j after the multiplicative calibration factors obtained from the ϕ intercalibration have been applied to it. In addition, a multiplicative energy correction factor $c_{i\eta}(j)$, defined for each η ring (denoted by $i\eta$) has been applied to the energy of each cell (E'_j), the value of $c_{i\eta}(j)$ applied depending on the position (η) of the cell.

The goal of the η intercalibration procedure is to equalize the response at different rapidities and thereby help in determining the absolute energy scale. This is done by determining the values of the multiplicative calibration constants ($c_{i\eta}(j)$), by adjusting them till the electron energies are tuned enough to match the observed Z boson mass to its (standard) LEP value and possess minimum experimental width.

This tuning is attained with the help of a fitting procedure that utilizes the standard method of unbinned likelihood for purposes of comparison between the reference and the observable that is being tuned.

As noted above, the η intercalibration for the EM calorimeter is performed with the help of $Z \rightarrow e^+e^-$ events. For the hadronic calorimeter, back-to-back di-jet events are used for the calibration.

The absolute energy scale determination has been described in the chapter on electron simulation. The calibration constants of the ϕ and η intercalibrations along with those of the readout electronics have been implemented in the p17 release of the offline data reconstruction algorithm for this analysis.

8.4 Results from the Gain Calibration

Figure 8.1 shows the calibration constants obtained after the ϕ and η calibrations of the calorimeter. The horizontal axis represents $i\eta$ and the vertical axis represents the fit results for $c_{i\eta}(j)$. The η calibration is done for -2.6 $\leq \eta \leq$ 2.6. The grey areas show regions in which we do not attempt to determine $c_{i\eta}(j)$. This area is the inter-cryostat region (ICR) and lies between the cryostats of the central and end calorimeters. Due to paucity of statistics at higher η values we group the η regions together and obtain one calibration constant for that region. Thus the point at $i\eta$=-27 represents the combined constant for all the extreme η bins -3.7 $\leq \eta \leq$ -2.7. Similarly the point at $i\eta$=27 includes the contribution from the extreme eta bins 2.7 $\leq \eta \leq$ 3.7. The triangles represent the result for data taken before the Sept-Nov 2003 shutdown, while the dots represent the result for data taken after that shutdown. The constants determined over the two data taking periods do not show any significant deviation thus showing that the calibrations remain fairly constant over time and no drastic changes have occured to our calorimeter system.

The calibration resulted in a 10% improvement in the resolution of the Z mass distribution. The resolution of the calorimeter due to mechanical non-uniformities (indicated by the constant term C_{EM}) is at 2% in agreement with the design goals for Run II.

8.5 Alignment of the Tracking System

The tracking system consists of the SMT and CFT detectors. The structure of the SMT is rather complicated and includes rectangular and wedge-shaped elements, called “ladders” and “wedges” respectively. The ladders are grouped

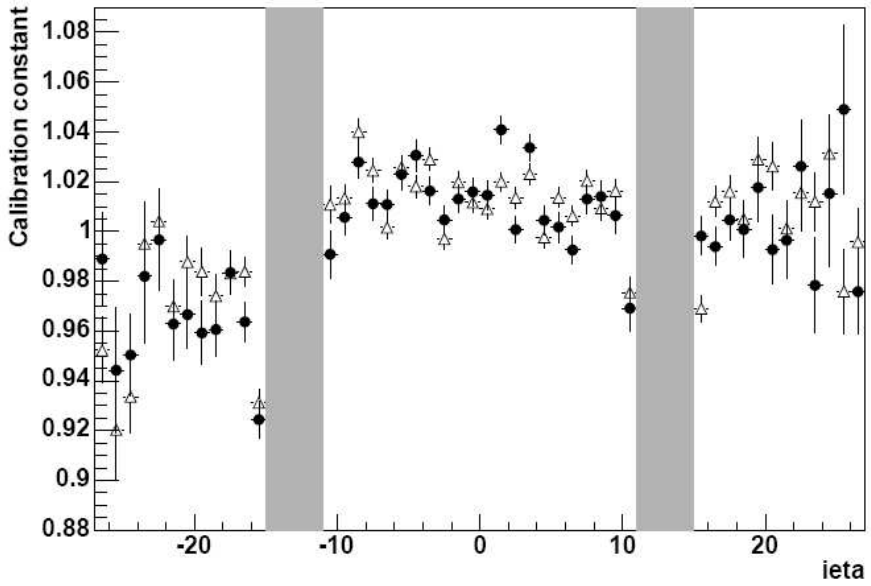

Figure 8.1. Calibration constants obtained for the gain calibration of the calorimeter

into six barrels with each barrel consisting of four layers of ladders. The wedges are grouped into disks, namely the 12 F-disks supporting the barrels at their ends and the 4 outer H-disks. The planes of the disks are perpendicular to the beam axis.

The design of the CFT is comparatively simple. It contains of scintillating fibers mounted on eight concentric support cylinders. Each cylinder supports one doublet layer of fibers oriented along the direction of the beam (z) and a second doublet layer oriented at a stereo angle in ϕ of +3° (u) or -3° (v). The former is called the "axial layer" while the latter is called the "stereo layer". The fibers in each layer are grouped into ribbons, there are 10 such ribbons in the first CFT layer and 28 in the last layer.

Two different types of data, cosmic muons and collision data are used for

aligning both the tracking detectors. The comic muons are reconstructed and used to determine the position of the CFT detector. After the position of the CFT detector is fixed, $p\bar{p}$ collision data is used to determine the position of the SMT detector by keeping the position of the CFT detector fixed.

The basic elements of the SMT for purposes of detector alignment are a ladder and a wedge, while that of the CFT is a ribbon. The alignment procedure aims at determining the position and orientation angles of these basic detector elements of the DØ tracking system. The shape of a ladder and a wedge is approximated by the plane whereas that of a ribbon is approximated by the segment of a cylinder. In the first step of alignment, a selection of a large number of tracks passing through a given detector element is obtained and a residual for each track is determined. The residual is the difference between the measurement of the track as obtained in an element of the detector and the expected track position. The latter is determined after excluding the detector element from the track fit. Thus any non-zero value of the residual mean indicates a misalignment of that detector element. A sufficiently large collection of residuals can be used to derive the shifts of a given detector element from the aligned position and orientation. In turn, the geometrical constants describing the aligned position can be obtained by applying these shifts to the initial position and orientation of the detector element.

In the alignment procedure, the correlations between the different detector elements are accounted for by iterating the alignment several times. At each iterative step the positions of all the detector elements are determined. A new measurement of the track parameters are performed and the new residuals are computed using these new track measurements. These are in turn used to extract the new geometry shifts. This procedure is repeated until the resulting shifts of

all detectors are below a predefined threshold value.

Both the cosmic muons and collision data are collected with the DØ magnets switched off in order to keep the tracks from being bent due to the magnetic field. The cosmic muons pass through the whole detector and are thus reconstructed as a single straight track passing through the entire detector by matching two tracks. They can be used to connect the opposite parts of the detector. They are used to align the positions of the CFT ribbons. However the number of cosmic muon events available are not enough to align the many elements of the SMT detector, especially the wedges which are prependicular to the beam direction and thus have very low exposure to the cosmic muons. The position of the SMT is aligned using the collision data. All the tracks in the collison data sample are required to have a common primary vertex, which acts like an additional constraint for connecting one part of the detector to the other.

CHAPTER 9

ENERGY LOSS CORRECTIONS DUE TO UPSTREAM MATERIAL

9.1 A Brief Introduction

As a result of the significant upgrades between the two major data taking periods at the Tevatron, the D0 Run II detector is very different from the detector used in Run I. While the calorimeter itself remains unchanged, the drift chambers of Run I have been replaced with the tracking detectors (CFT and SMT) in Run II. A magnetic field of about 2 Tesla has also been established with the help of an aluminum-cored solenoid for obtaining curvature measurements from the CFT. In order to catch the early development of the particle showers the preshower detectors (CPS and FPS) have also been installed. All these new introductions have increased the amount of material in front of the calorimeter. Table 9.1 is a tabulation of the amount of material in front of the first active layer of liquid Argon as seen by an electron traveling from the interaction point to the CC at normal incidence in the calorimeter. It should be kept in mind that particles traveling at other angles of incidence will encounter even more material than shown here.

While the detectors are well instrumented, materials such as the aluminum core of the solenoid and lead for the preshowers are not or very poorly instrumented. Hence they are also referred to as "dead" or uninstrumented material. It is not possible to garner information about the energy that particles lose at each step in

TABLE 9.1

MATERIAL IN FRONT OF THE FIRST ACTIVE LAYER OF LIQUID ARGON

Detector Element	Material Thickness
Inner Detector (CFT + SMT)	0.2 X_0
Solenoid	0.9 X_0
Preshower (Detector)	0.3 X_0
Preshower (Lead)	1.0 X_0
Calorimeter Cryostat	1.3 X_0

these materials while passing through them. There is almost 4.0 X_0 of material in front of the calorimeter.

The introduction of these additional materials in front of the calorimeter causes particles to lose a considerable fraction of their energy when passing through it, before they reach the first detecting layer of liquid Argon inside the calorimeter. This leads to an early development of the showers, especially for the electrons. The information from these early showers is accessed by the central and two forward preshower detectors

For the purposes of this analysis, we know that the calorimeter measures the energy of the incident electrons. Thus for an accurate reconstruction of the energy of the electrons in an event, it is imperative to determine the amount of energy lost by them in the material before they reach the calorimeter. A precise and detailed mapping of the amount, position and nature of the material contributes to an accurate determination of the energy loss corrections for the electrons that pass

through it. Due to a significant amount of material in front of the calorimeter, these corrections are derived as a function of energy (E) and angle of incidence (η), from the detailed detector simulation (GEANT3-based) FULL MC. These energy-loss corrections are then applied to the energy detected in the calorimeter, thus reconstructing the original energy associated with the event.

From the previous chapters we have learned about the reconstruction of the electron energy and the calibrations of the calorimeter that make it well suited for a precise and unbiased (stable) energy measurement. With the help of all this background information, this chapter now details our understanding of the DØ calorimeter for this precision measurement of M_W. It describes the nature of energy loss upstream of the DØ calorimeter, the correct estimation of the material in front of the DØ calorimeter and the subsequent estimation of the energy loss corrections for the electrons incident on the calorimeter.

9.2 Studying the Calorimeter Response & Resolution with GFLASH

The energy response of the calorimeter is highly non-linear due to the presence of an appreciable amount of dead material. This means that the energy response of a 5 GeV electron reaching the calorimeter is not necessarily proportional to that of a 30 GeV electron. Let us take a look at the impact that an appreciable amount of dead material in front of a calorimeter has on the development of an electron shower.

GFLASH [119, 120] is a fast, parameterized MC simulation used for modeling EM showers and their fluctuations. It is used for the above study. Parameterized simulations of the shower development of electrons are used to show and study the longitudinal segmentation and radial profiles of the showers developed

in the EM layers of a calorimeter. The simulations are performed for a variety of kinematic and diagnostic variables such as angle of incidence on the dead material and calorimeter, incident electron energies, amount of material in front of the calorimeter, etc. The commonly used variable for locating polar coordinates, namely "pseudorapidity" is used as the coordinate system here 4. Physics η (denoted as η_{phys}) is used as a measure of the angle of incidence here and is defined as:

$$\eta = -\ln \tan \frac{\theta}{2} \tag{9.1}$$

The angle θ is measured from the primary vertex of interaction.

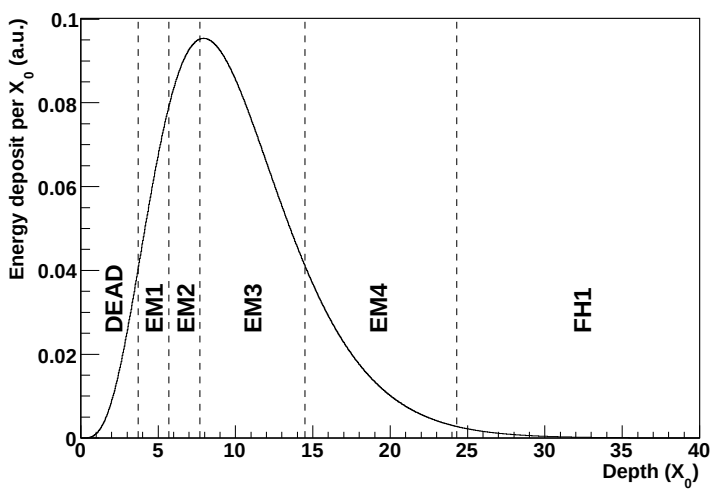

Figure 9.1. Average shower profile for electrons of energy E=45 GeV at normal incidence (η_{phys} =0)

Figure 9.1 shows an average longitudinal shower profile for electrons of energy= 45 GeV at normal incidence (η_{phys} =0) on the calorimeter. The position of the active parts of the CC are indicated in the Figure assuming a normal incidence.

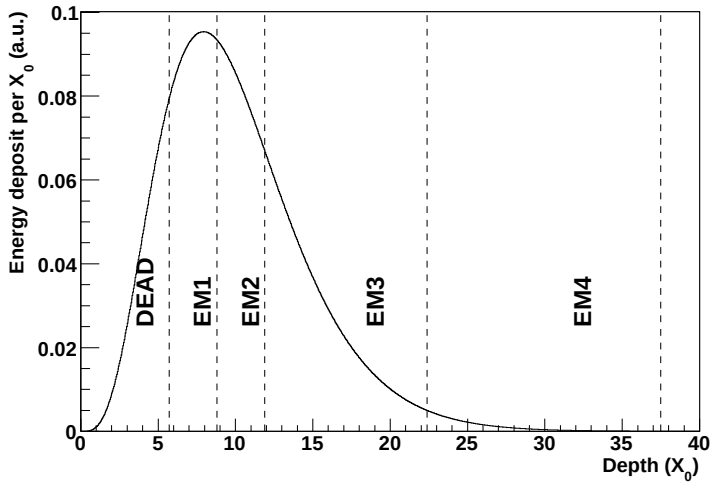

Figure 9.2. Average shower profile for electrons of energy E=45 GeV at an extreme angle of incidence (η_{phys} =1)

In the reconstruction procedure, artificial weights are applied to the individual layers, EM1 to FH1, in an attempt to compensate for the energy losses in the dead material, with the early layers such as EM1 having higher weights than the others. Figure 9.2 illustrates the situation for a shower at the same energy of 45 GeV but at an extreme angle of incidence (i.e. η_{phys} =1). This time the active parts of the CC are indicated for a highly non-normal incidence. We notice the change in the position of the shower. When the electrons travel at extreme angles of incidence they encounter more dead material in front of the active EM layers than at normal incidence. The amount of energy deposited in the dead material as a function of depth is more in the second case thus causing the shower maximum to shift into the early layers and appear in EM1 !

Figures 9.3 and 9.4 depict the shower-to-shower fluctuations for electrons of energy E=45 GeV for two different angles of incidence, normal (η =0) and an

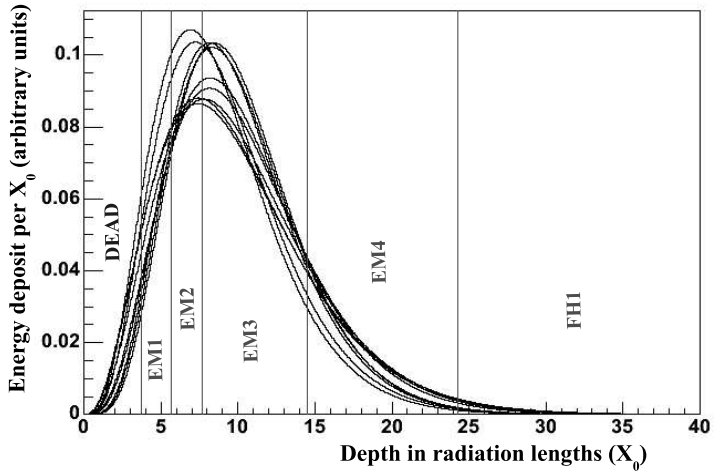

Figure 9.3. Shower-to-shower fluctuations for electrons of energy E=45 GeV at normal incidence (η_{phys} =0)

extreme value (η =1). Notice that the nature of the fluctuations are different for the two angles of incidence and are detrimental for the energy resolution, especially for large η values. This indicates that the energy resolution of the calorimeter has an angular dependence. As can be seen from the above four figures, the energy resolution will depend on the angle of incidence of the electron energies that are sampled.

Figures 9.5 and 9.6 show the shower-to-shower fluctuations in the longitudinal shower profiles for two different electron energies, E=5 GeV and E=45 GeV, both at normal incidence (η_{phys} =0). As seen from here, the average shower development and the fluctuations around the average also depend on the energy of the incident electrons, as a considerable amount of energy is lost in the dead material. Thus the resolution of the EM calorimeter also depends on the energy of the electron being sampled.

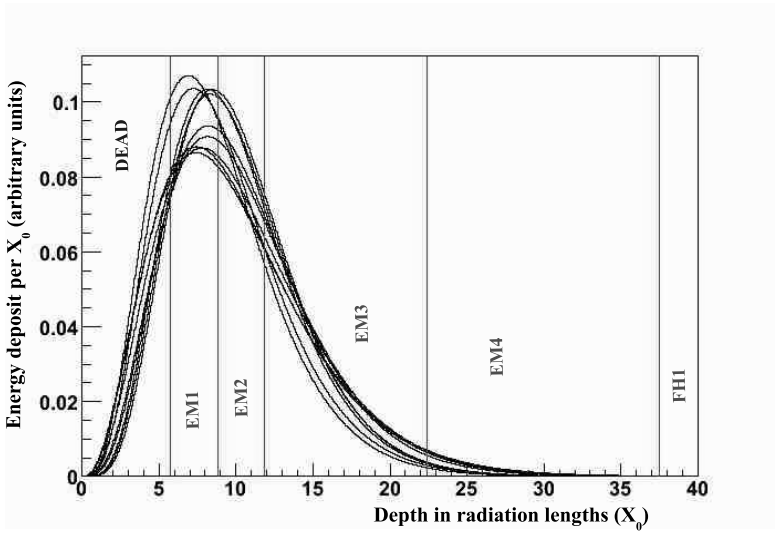

Figure 9.4. Shower-to-shower fluctuations for electrons of energy E=45 GeV at an extreme angle of incidence (η_{phys} =1)

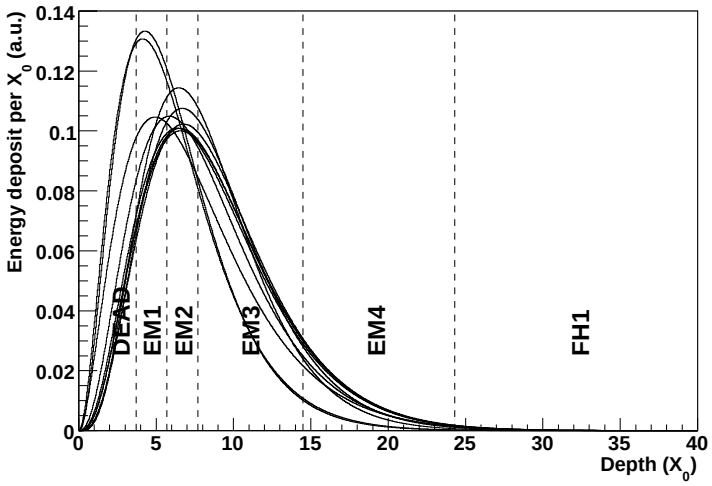

Figure 9.5. Shower-to-shower fluctuations for electrons of energy E=5 GeV at normal incidence (η_{phys} =0)

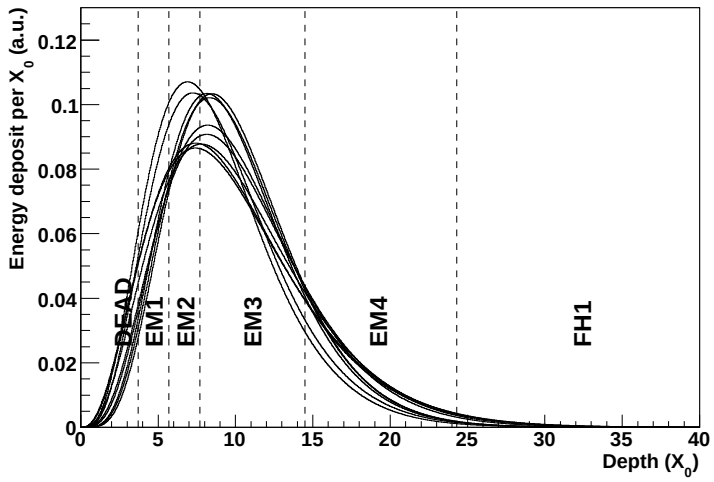

Figure 9.6. Shower-to-shower fluctuations for electrons of energy E=45 GeV at normal incidence (η_{phys} =0)

All the above toy MC figures show that significant energy is lost when there is an appreciable amount of dead material in front of the calorimeter. Small variations in this material can have a significant impact on the reconstructed energy. The EM1 and EM2 layers are particularly sensitive since their energies are reconstructed with larger weights and they contribute to the steeply rising edge of the shower profile. Thus determining the amount of dead material is critical for getting a handle on the linearity of the energy response and resolution of the calorimeter.

9.3 Response and Resolution of the DØ Run II Calorimeter

Both the η and energy dependence of the resolution are artifacts of the sampling fluctuations due to the additional dead material in front of the Run II EM calorimeter. The energy resolution of the Run I calorimeter was described by the

standard expression for the resolution of an ideal sampling calorimeter at normal incidence (η=0). It is given as follows:

$$\frac{\sigma_E}{E} = \sqrt{C_{EM}^2 + \frac{S_{EM}^2}{E} + \frac{N_{EM}^2}{E^2}} \tag{9.2}$$

Now let us look at the scaling laws of the energy resolution of the Run II calorimeter with the help of single electrons of energy E=45 GeV which are passed through `d0gstar`, the GEANT-based detailed simulation of the DØ detector.

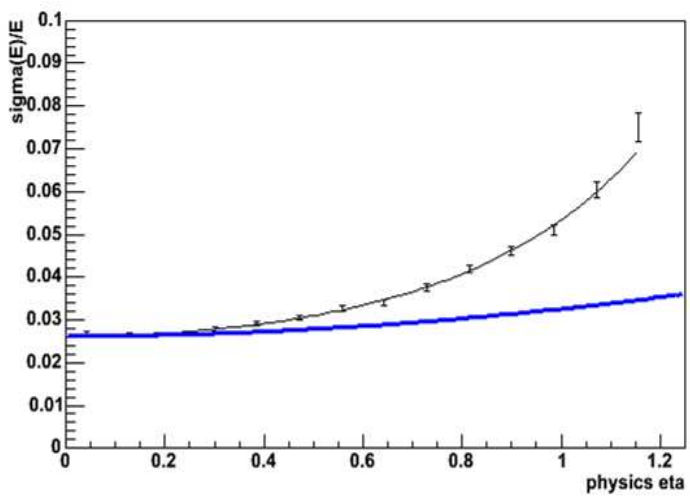

Figure 9.7. Fractional energy resolution $\sigma(E)/E$ as a function of η_{phys})

Figure 9.7 depicts the dependence of the fractional energy resolution ($\sigma(E)/E$) as a function of the angle of incidence, η_{phys}. The blue line represents the usual, almost flat model given by the functional form of $1/\sqrt{\sin\theta}$ for an ideal calorimeter

whereas the black line has been fit to a functional form of

$$\frac{\sigma_E}{E}(\theta) = \frac{p_0}{e^{p_1}} \times e^{\frac{p_1}{\sin\theta}} \tag{9.3}$$

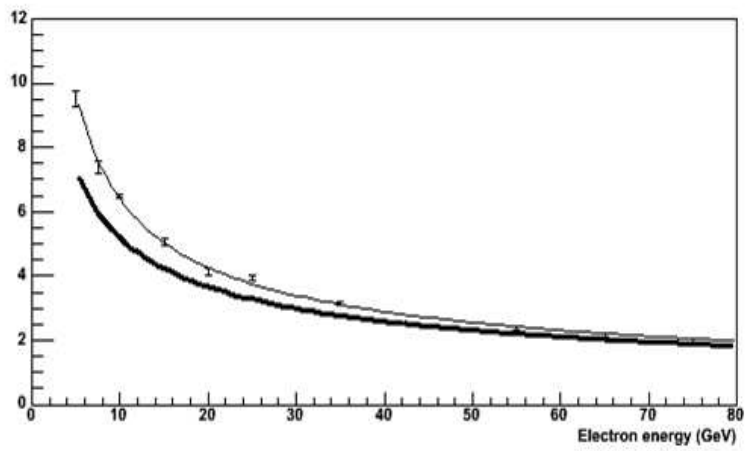

Figure 9.8. p_0 (fractional resolution at normal incidence) as a function of energy E)

Here p_0 is the fractional resolution at normal incidence (η_{phys}=0) whereas the contribution from the coefficient p_1 becomes large in case of a large angular dependence. Thus we observe a strong dependence of the energy resolution on the angle of incidence. This is due to the significant amount of material in front of the calorimeter. Figure 9.8 shows the energy dependence of the term p_0 in the new expression for the fractional energy resolution of our Run II calorimeter as expressed in the above form. The solid black line indicates the usual scaling of the sampling fluctuations as a function of energy and is given by:

$$\frac{\sigma_E}{E} = \frac{16.4\%}{\sqrt{E}} \tag{9.4}$$

However the fitted black line is given by the following functional form

$$\frac{\sigma_E}{E} = \frac{16.4\%}{\sqrt{E}} + \frac{12.2\%}{E} \tag{9.5}$$

From here it's evident that it does not follow the $1/\sqrt{E}$ trend that is expected for an ideal sampling calorimeter.

The third example shows the anomalies in the response of the calorimeter. The reconstructed Z mass from the FULL MC should be predicted accurately and be constant if the electron energies are being reconstructed accurately and the final energy scale and offset determined from a fit to the Z mass spectrum are of sufficient quality. Figure 9.9 shows the di-electron mass spectrum of the $Z \rightarrow e^+e^-$ for two cases. The red plot is when both electrons are close to normal incidence to the calorimeter ($|\eta_{phys}| < 0.2$), the blue plot is when both are at extreme angles of incidence to the calorimeter ($|\eta_{phys}| > 0.8$). It can be clearly seen that the two peaks are not at the same Z mass. The spectra clearly indicate an inaccuracy with the angular dependence in the calibration.

This startling result indicates a potential problem with two aspects of the energy reconstruction. Either the MC-based energy loss corrections which depend on the modeling of the passive material in front of the calorimeter are not right or the gain calibrations (inter-ϕ and inter-η) have been performed incorrectly. Besides, as we have read earlier, the latter also depends on the energy loss corrections.

All these deviations call for a visit to the calibrations and energy-loss corrections that contribute to the reconstructed energies of the particles detected in the calorimeter. Both the response and resolution of the Run II calorimeter differ from those of an ideal and hint at problems with the energy reconstruction in the calorimeter. This will also lead to a new parameterized model of the DØ Run II

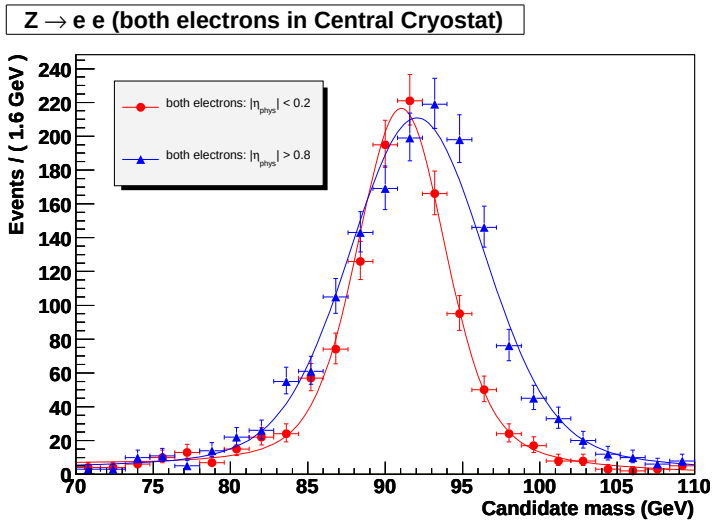

Figure 9.9. The reconstructed Z mass for two different angles of incidence of the electrons. The regions are $|\eta_{phys}| < 0.2$ (red) and $|\eta_{phys}| > 0.8$ (blue)

calorimeter. This will be described in detail in Chapter 12. The new parameterization includes the angular and energy dependence of the sampling fluctuations.

9.4 Observables Used for the MC Tuning

In order to study the average energy response and resolution as a function of the energy and angle of incidence we choose collider data $Z \rightarrow e^+e^-$ events. The reconstructed mass and width obtained from the two Z electrons can be compared with the well known world average value. Each of the two electrons of the Z has its own η_{phys} (pseudorapidity). Hence if we split the Z events into different kinematic regions, we gain more information compared to when we use the values of the mass and width averaged over the entire Z sample. Since we need to study the energy and angular dependence of the electron reconstruction, a two-dimensional splitting

of the electrons on the basis of their energy and η_{phys} would be ideal. However as seen from Figure 9.10, these two are strongly correlated. Hence the Z sample is divided on the basis of η_{phys} and not energy. We bin each electron on the basis of its angle of incident, η_{phys}. This has the advantage that the bins are defined without the help of any calorimeter-based measurement.

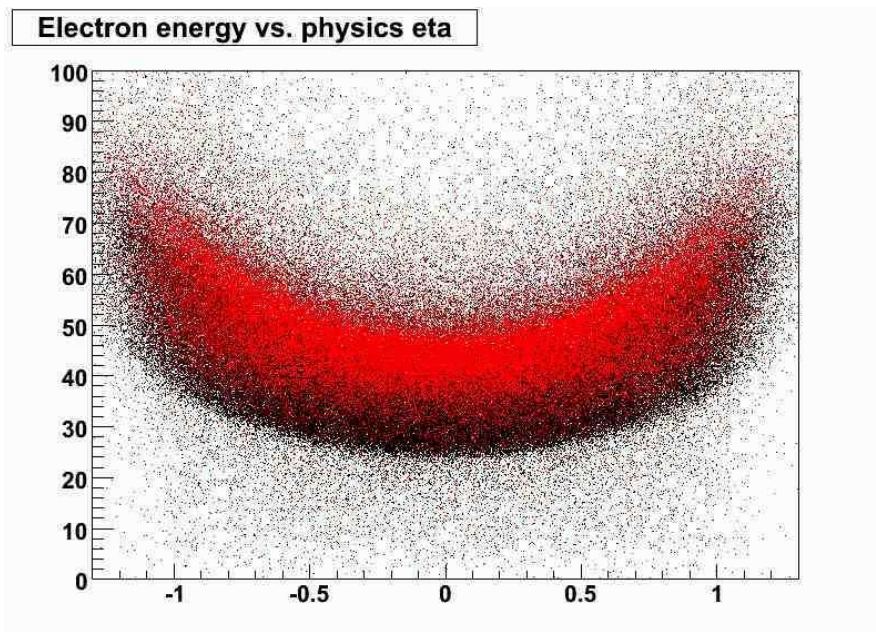

Figure 9.10. Electron energy vs. η_{phys} for electrons from $W \to e\nu$ (black) and from $Z \to e^+e^-$ (red)

The five distinct η_{phys} bins are shown in Table 9.2.

Since the Z has two electrons we end up splitting the $Z \to e^+e^-$ sample into 15 different categories on the basis of the bins in which each of the electrons fall. We do not distinguish between the leading and the subleading electron. The different

TABLE 9.2

DEFINITION OF THE BINS IN TERMS OF ELECTRON $|\eta_{phys}|$

Bin Number	Range of $|\eta_{phys}|$
bin0	$0.0 \leq |\eta_{phys}| < 0.2$
bin1	$0.2 \leq |\eta_{phys}| < 0.4$
bin2	$0.4 \leq |\eta_{phys}| < 0.6$
bin3	$0.6 \leq |\eta_{phys}| < 0.8$
bin4	$0.8 \leq |\eta_{phys}|$

categories are shown in Table 9.3. We study the measured Z mass and resolution in each of the 15 categories.

9.5 Determining the Correct Amount of Uninstrumented Material

In order to improve the electron energy reconstruction, the first step is to ensure that GEANT models the electromagnetic showers with an acceptable precision and accuracy. Several studies that involve detailed comparisons of GEANT, the EGS simulation program [121, 122] and a priori calculations were carried out to ascertain this. The studies used toy calorimeter geometries for both GEANT and EGS and compared e/γ productions rates, energies, particle flow and energy depositions. It was found that GEANT as operated in its standard mode at the DØ farms processing FULL MC samples is inadequate with respect to the following:

1. The fundamental Bremsstrahlung and pair production cross sections as de-

scribed within GEANT are insufficient

2. The Moliere theory is used outside its domain of validity

3. The energy cut off for tracking δ-rays is too high (particularly for regions near the Uranium and Argon boundary)

These have been addressed by using a special version of GEANT where the fundamental cross-sections have been updated and various operating parameters have been adjusted. In particular the parameter representing the step size (STMIN) is set to 1.0×10^{-7} cm, just like in EGS, so it improves the validity of the Moliere theory and the low-energy tracking, thereby improving the energy flow [1]

This special version of GEANT was used to generate the FULL MC $Z \rightarrow e^+e^-$ and $W \rightarrow e\nu$ event samples.

The special version of GEANT mentioned above does model the physical processes precisely enough for the W mass measurement. However we still need to understand the discrepancy between the reconstructed energies at the two values of $|\eta_{phys}|$ as shown in Figure 9.9.

Now, we know that at large angles of incidence, particles traverse larger amounts of material than at normal incidence. Could an inaccuracy in the description of the material in front of the calorimeter be the reason for this discrepancy in Figure 9.9? Or are the gain-calibrations (ϕ and η intercalibrations) of the calorimeter at fault? The diagnostic plots of kinematic variables help us probe further into these questions and as mentioned later on in this Section, the layer-intercalibrations of the calorimeter are not the main source of the discrepancies

[1] Although these changes result in a simulation of a suitable quality for the W mass measurement, the processing time unfortunately increases by a factor of 20. Thus it cannot be used for the general GEANT-MC production.

that we observe. The material upstream of the calorimeter seems to be a more probable cause of the problem. Thus we revisit the amount of uninstrumented material lying in front of the calorimeter, before doubting the calibrations.

This section describes the modifications to the dead material in front of the central calorimeter (CC). The simulation used here is a combination of the improved and detailed GEANT-based detector simulation (also called FULL MC) and the FAST MC (parameterized MC). The FULL MC is used to exploit the longitudinal segmentation of the EM calorimeter in order to get a handle on the correct amount of uninstrumented material lying in front of it. The concept is a simple one - varying the size of the passive material will cause different fractions of the shower energy to be sampled by each of the four active EM layers (EM1 - EM4). Thus the FULL MC is used to study the mean EM fractions and the fluctuations around the average in single electron events. The single electrons are generated at various values of energy and η_{phys} and thus span the entire region of the energy-η_{phys} plane that is relevant for $Z \rightarrow e^+e^-$. A parameterization for the mean EM fractions and their fluctuations as a function of true electron energy and η_{phys} is built from these FULL MC events and is implemented in the FAST MC to be used for all essential aspects of the W mass measurements.

In order to get started on studying the amount of material upstream, we start with a FULL MC which contains a nominal model of the detector geometry and has been generated using the special version of GEANT. As a first step we compare the standard kinematic variables (such as invariant mass of the electron pair and their transverse momenta) to data, to ensure that our simulation reproduces the electron distributions for the entire E-η_{phys} space in reasonable agreement with data. Figures 9.11 and 9.12 show a data-FULL MC comparison of the kinematic

variables for two of the 15 categories. The data shown in these two has been calibrated using the energy-loss functions based on the default DØ simulation. Small potential disagreements like for the leading electron in category 23 are not a concern since the average shower depth depends $\sim \ln(E)$. The disagreement in the mass distribution in category 23 could arise if the energy loss is not being reproduced properly as a function of η.

Now we begin to study the EM fractions, that is the fraction of the EM energy that is sampled by each of the four EM layers. Figures 9.13 and 9.14 show a comparison of the fractional energy deposits from the collider data and the FULL MC simulation of the detector for categories 10 and 23 respectively. As can be seen, the mismatch in each layer suggests the presence of some additional material in the detector that is eluding decription in the material description of the FULL MC. The simulation predicts tends to predict too little energy in the early layers.

A summary of the information from all four layers and all 15 categories is shown in Figure 9.15. It shows the average means of the EM fractions separately for data and simulation. The strong trends visible in the variations of the mean EM fractions from one category to another, reinforces the importance of the "effective" amount of dead material traversed by the electrons at different angles of incidence. We notice that even though our simulation tracks the shape of these variations well, there are systematic "shifts" visible which could be attributed to the missing material in the FULL MC simulation.

Figure 9.16 shows the ratios of the data to FULL MC simulation for the mean EM fractions. We notice that the spread around unity here is larger than that expected from errors due to the gain-calibrations of the calorimeter alone. This figure also points to missing material from the FULL MC.

Hence we decide to tune the GEANT-based model of the detector by adding more material to its already existing description. This is in the form of some "effective" material that would play the role of some other unidentified material that is missing from the nominal material map. Since most of the material in front of the CC (e.g. solenoid, CPS lead) is largely cylindrical in geometry, the effective missing material is also chosen to be a copper (low Z) cylinder placed concentrically inside the solenoid.

The thickness of this copper cylinder is varied in increments, in terms of X_0, and a detailed simulation of the detector is produced each time with the help of the special version of GEANT and the single electrons. From the full scans of the energy/η_{phys} plane the respective parameterizations of the mean EM fractions and their fluctuations about the average are obtained, as a function of energy, η_{phys} and number of additional radiation lengths of material, nX_0.

The distributions of the fractional energy deposits in each of the three EM layers (EM1, EM2, EM3) are compared to those from collider data for each of the 15 η_{phys} categories. Based on the agreement between the FULL simulation and the data for the EM fractions, a χ^2 is determined. The total χ^2 is the sum over all of the 3 layers. The value of nX_0 is varied in a way so as to minimize this total χ^2. Due to the very small energy deposits in EM4 especially at non-normal incidence, the layer has a negligible effect on the total sum and is not taken into account here. The use of the three EM layers is also akin to adjusting the per layer weights (or layer-intercalibrations).

This method works well and helps us determine the amount of missing material to an accuracy of 0.01 X_0. We find that on an average there is about 0.16 X_0 of additional material in front of the calorimeter which was not being modeled in

the GEANT-based detailed simulation model of the detector. Figure 9.17 shows the minimization of the χ^2 as a function of the additional dead material. As a cross-check, we repeat the fit for nX_0 for each of the layers individually and the results are shown in Figure 9.18. Good agreement is found between the results from each of the individual layers.

After adding this additional material to the FULL MC, the fractional energy deposits in the four EM layers agree remarkably well with data. Figures 9.19 and 9.20 show the fractional EM deposits for categories 10 and 23 again, this time for an optimal value of nX_0. Figure 9.21 shows the ratios of the data to FULL MC simulation for the mean EM fractions for all the EM layers and all 15 categories after including the 0.1633 X_0 of additional material in the simulation.

9.6 Implementing the Energy Loss Corrections

Once the amount of uninstrumented material has been determined with reasonable accuracy, the final energy-loss corrections are re-determined and are incorporated into the algorithms that fit for the gain calibrations of the calorimeter, so that the reconstructed energies of the electrons stand corrected before the response of the calorimeter is determined. Figure 9.22 shows the electron energy loss corrections for normal and extreme cases of incidence. The blue curve shows the energy loss corections for η_{phys}= 0.2 while the red one shows the corrections for η_{phys}= 1.1. The $Z \rightarrow e^+e^-$ and $W \rightarrow e\nu$ collider data samples were reconstructed again after the implementation of the new energy-loss corrections. New samples of $Z \rightarrow e^+e^-$ and $W \rightarrow e\nu$ FULL MC were also produced. The parameterizations obtained in the full energy/η_{phys} space with the additional material included is incorporated into the FAST MC for the W mass measurement.

It should be kept in mind that these corrections have been derived from $Z \rightarrow e^+e^-$ events and need to be extrapolated or "transported" down to the lower electron energies of the $W \rightarrow e\nu$ boson events. A powerful check of the quality of this extrapolation is done by passing the electrons from $W \rightarrow e\nu$ events through the detailed detector simulation that has been tuned to the $Z \rightarrow e^+e^-$ events and comparing the EM fractions obtained from here to data. Figure 9.23 shows the EM fractions for $W \rightarrow e\nu$ events, for all four layers and all η_{phys} categories, for data and the simulation, after the optimal amount of material has been implemented. We observe the characteristic trends in the η-dependence here as in the $Z \rightarrow e^+e^-$ EM fractions. We also note that the agreement between $W \rightarrow e\nu$ data and the tuned simulation is very good. Figure 9.24 shows the data/simulation ratios corresponding to Figure 9.23. The ratios are consistent with unity thus proving that the tuned simulation does model the electrons from $W \rightarrow e\nu$ events very accurately.

However as we know, the W and Z electrons probe rather distinct regions of the energy-eta space. There is a small overlap in their energy-η bands as seen in Figure 9.10. Because of this incomplete overlap, there is a minor dependence of the "transportation of the energy scale" from the Z to the W, which depends on the quality of the energy loss parameterizations. A measure of the impact of the imperfections in the energy loss corrections when transported from the Z to the W is given by a bias of 8+-10 MeV. More details on this estimation is given in Chapter 19.

TABLE 9.3

DEFINITION OF THE "η" CATEGORIES FOR $Z \rightarrow ee$ EVENTS

Category	Combination of $\lvert\eta_{phys}\rvert$ bins
10	0 - 0
11	0 - 1
12	0 - 2
13	0 - 3
14	0 - 4
15	1 - 1
16	1 - 2
17	1 - 3
18	1 - 4
19	2 - 2
20	2 - 3
21	2 - 4
22	3 - 3
23	3 - 4
24	4 - 4

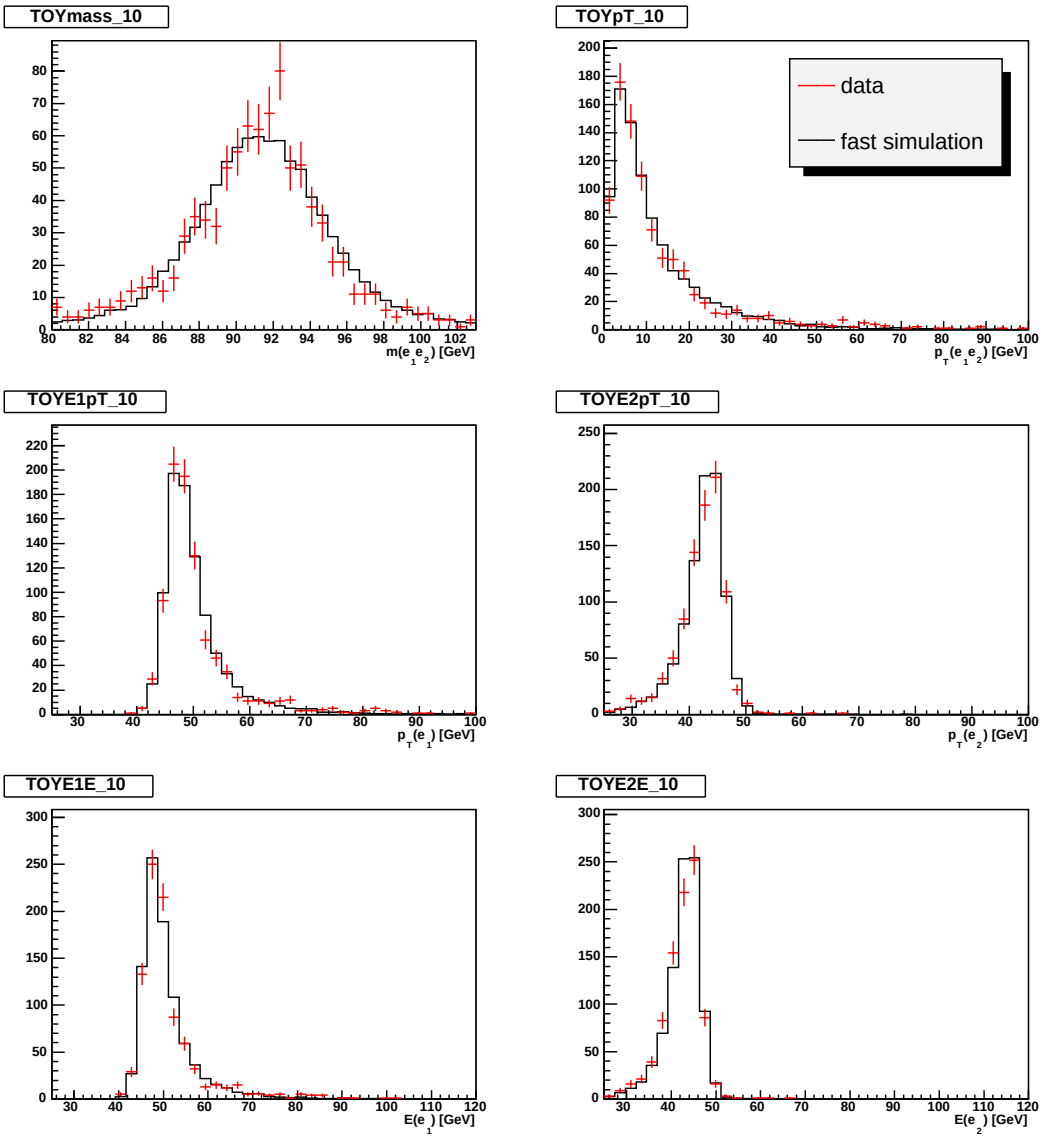

Figure 9.11. Comparison of data and FULL MC simulation for $Z \to e^+e^-$ events in category 10. Top Left: The invariant mass of the electron pair. Top Right: Transverse momentum of the electron pair. Middle Left: Transverse momentum of leading electron. Middle Right: Transverse momentum of subleading electron. Bottom Left: The energy of the leading electron. Bottom Right: Energy of subleading electron

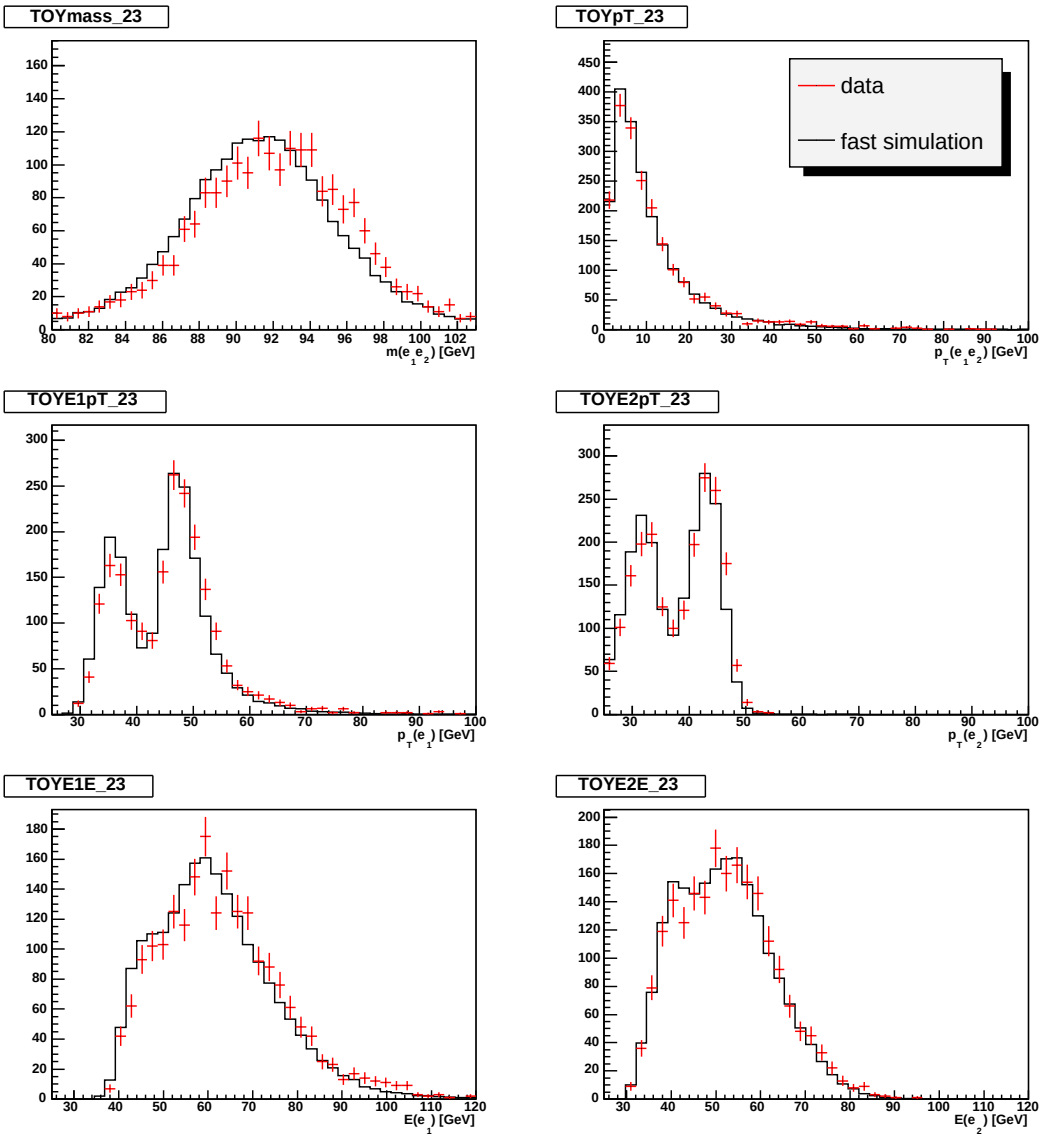

Figure 9.12. Comparison of data and FULL MC simulation for $Z \rightarrow e^+e^-$ events in category 23. Top Left: The invariant mass of the electron pair. Top Right: Transverse momentum of the electron pair. Middle Left: Transverse momentum of leading electron. Middle Right: Transverse momentum of subleading electron. Bottom Left: The energy of the leading electron. Bottom Right: Energy of subleading electron

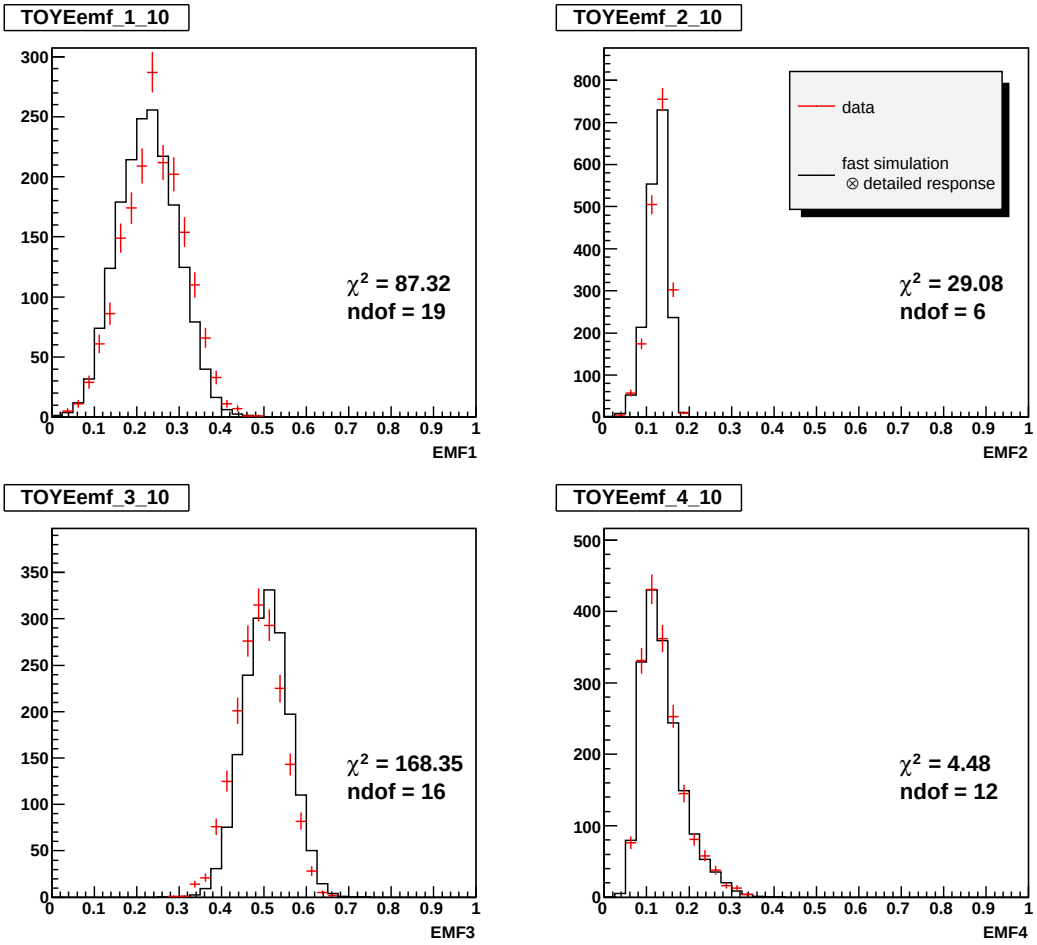

Figure 9.13. Comparison of EM fractions for electrons from $Z \rightarrow e^+e^-$ events in category 10 in data and simulation. The four individual plots show the energy fraction in each of the four EM layers. The detailed response simulation uses the default accounting of the dead material

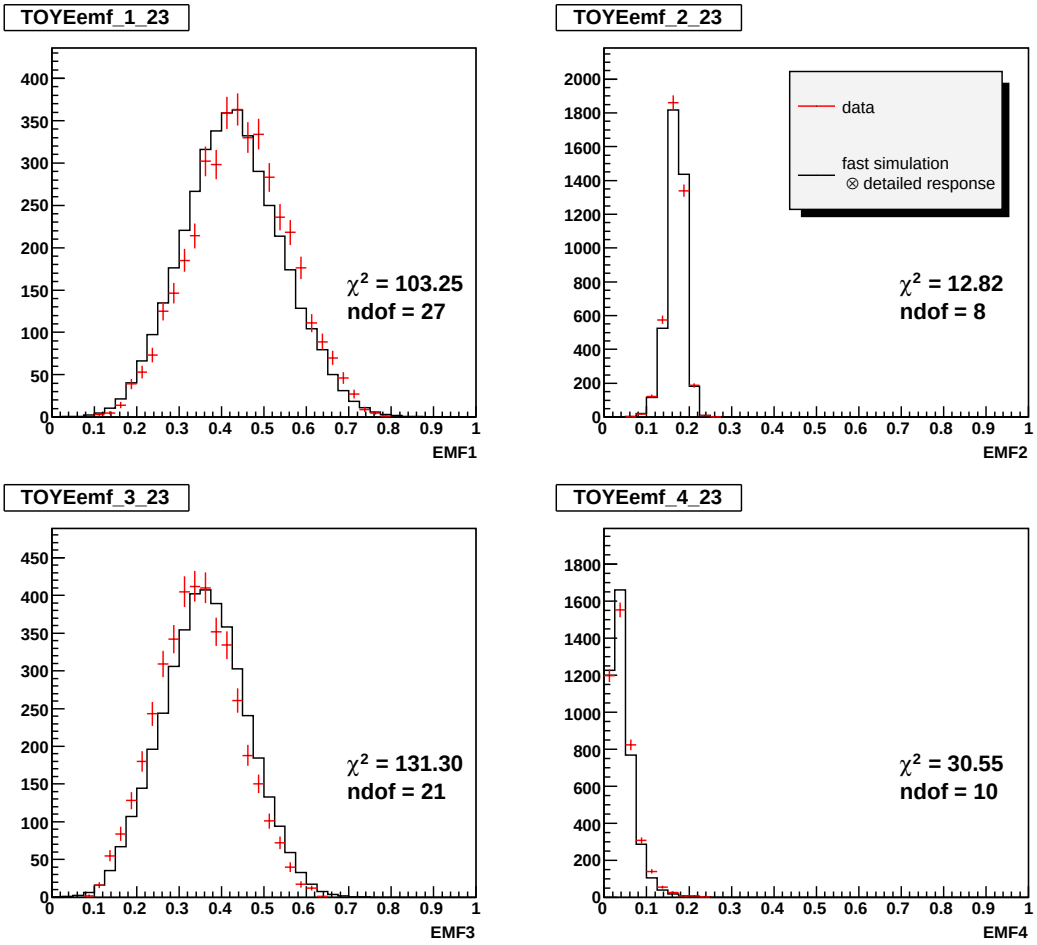

Figure 9.14. Comparison of EM fractions for electrons from $Z \rightarrow e^+e^-$ events in category 23 in data and simulation. The four individual plots show the energy fraction in each of the four EM layers. The detailed response simulation uses the default accounting of dead material

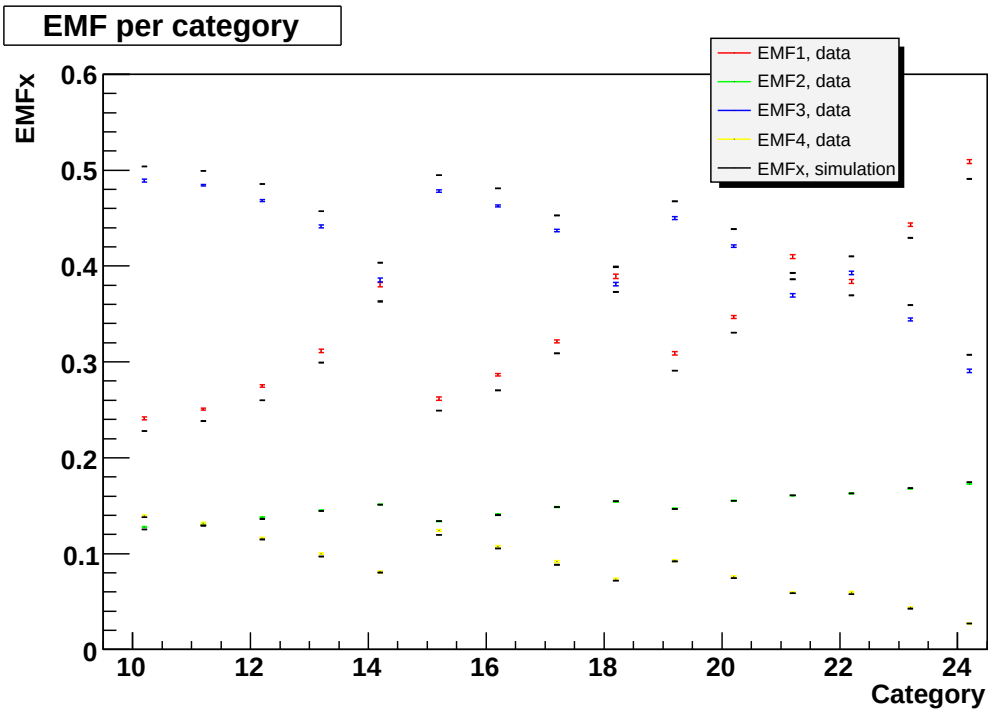

Figure 9.15. A summary of the means of the EM fraction distributions in $Z \rightarrow e^+e^-$ events for each of the four EM layers and each of the 15 η categories, separately for data and FULL MC simulation

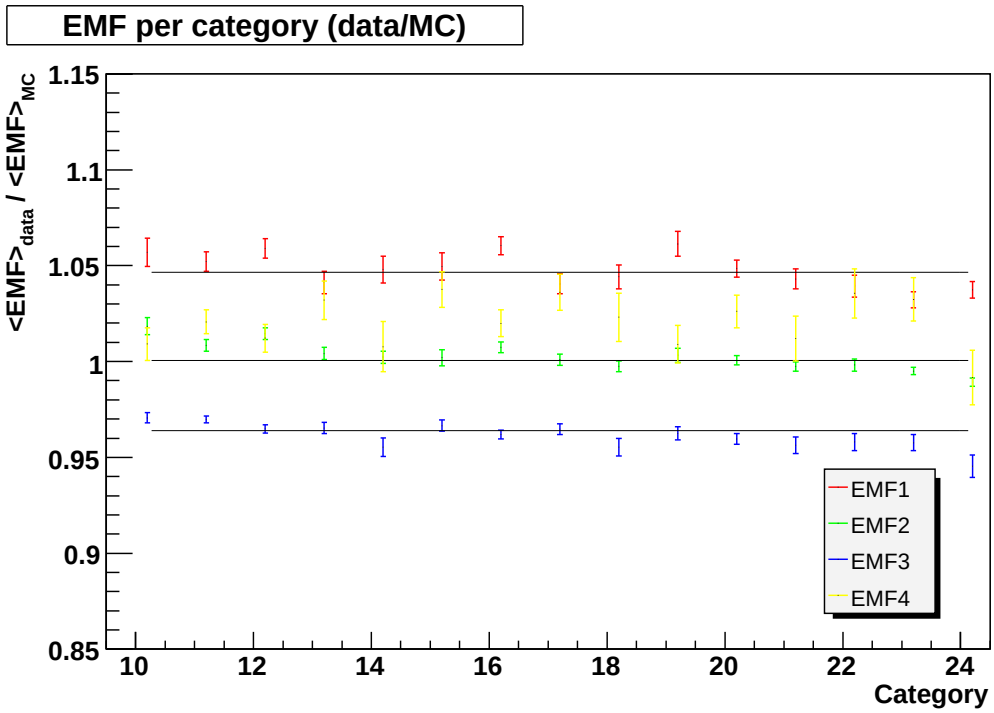

Figure 9.16. Ratios for the means of the EM fraction distributions in $Z \rightarrow e^+e^-$ events for each of the four EM layers and each of the 15 η categories. Each of the three horizontal lines indicates the result of a fit to a common constant of the 15 data points from a given EM layer. The fit was performed for EM1, EM2 and EM3

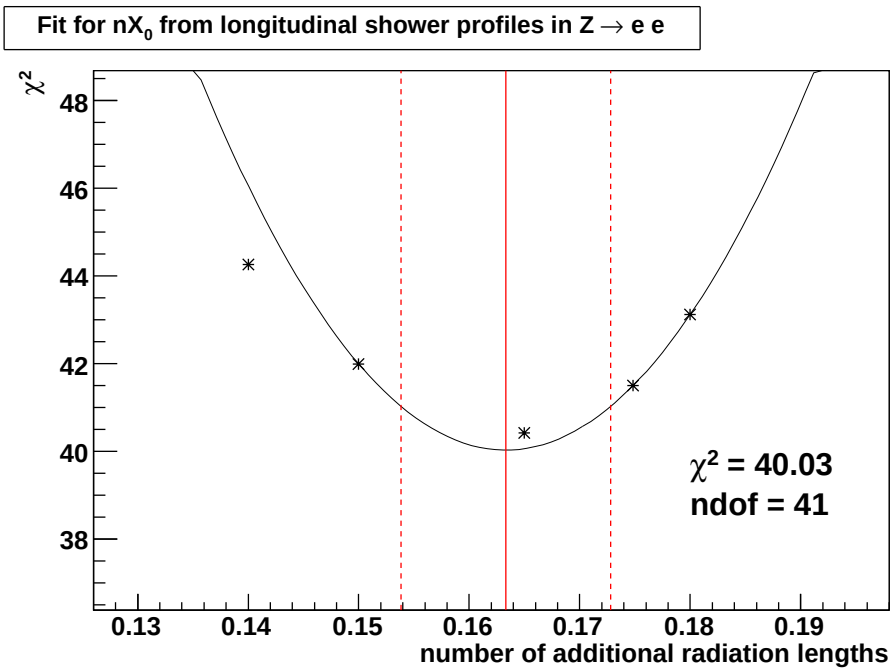

Figure 9.17. Fit for nX_0, the amount of uninstrumented material (in radiation lengths) missing from the nominal material map in the detailed simulation of the DØ detector. The five stars indicate the value of the combined χ^2 for EM1-EM3, evaluated for five values of nX_0. A parabola is fit through these points in order to determine the minimum of the combined χ^2. Also shown in the figure are the values of the combined χ^2 at its minimum as well as the one-sigma variations of nX_0

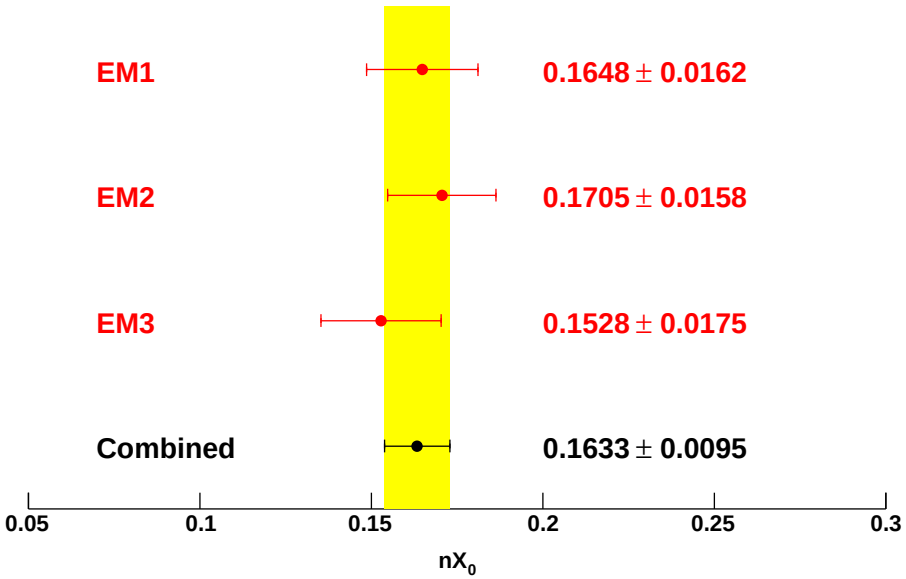

Figure 9.18. Stability check: Results of the fit for nX_0, performed separately for each of the three layers (EM1, EM2 and EM3). The result of the combined fit is also shown for comparison

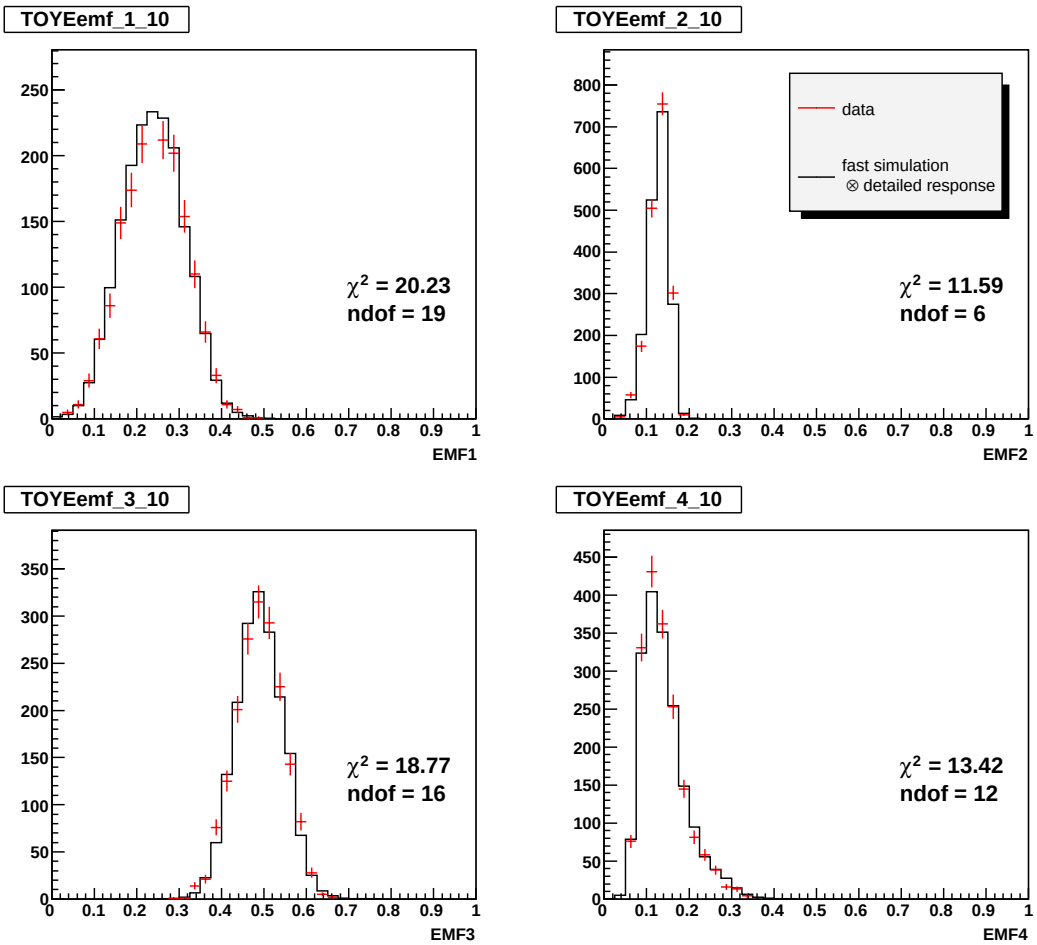

Figure 9.19. Comparison of EM fractions for electrons from $Z \rightarrow e^+e^-$ events in category 10 in data and simulation. The simulation used here includes $nX_0 = 0.1633$ radiation lengths of extra uninstrumented material in front of the CC calorimeter. The four individual plots show the energy fraction in each of the four EM layers

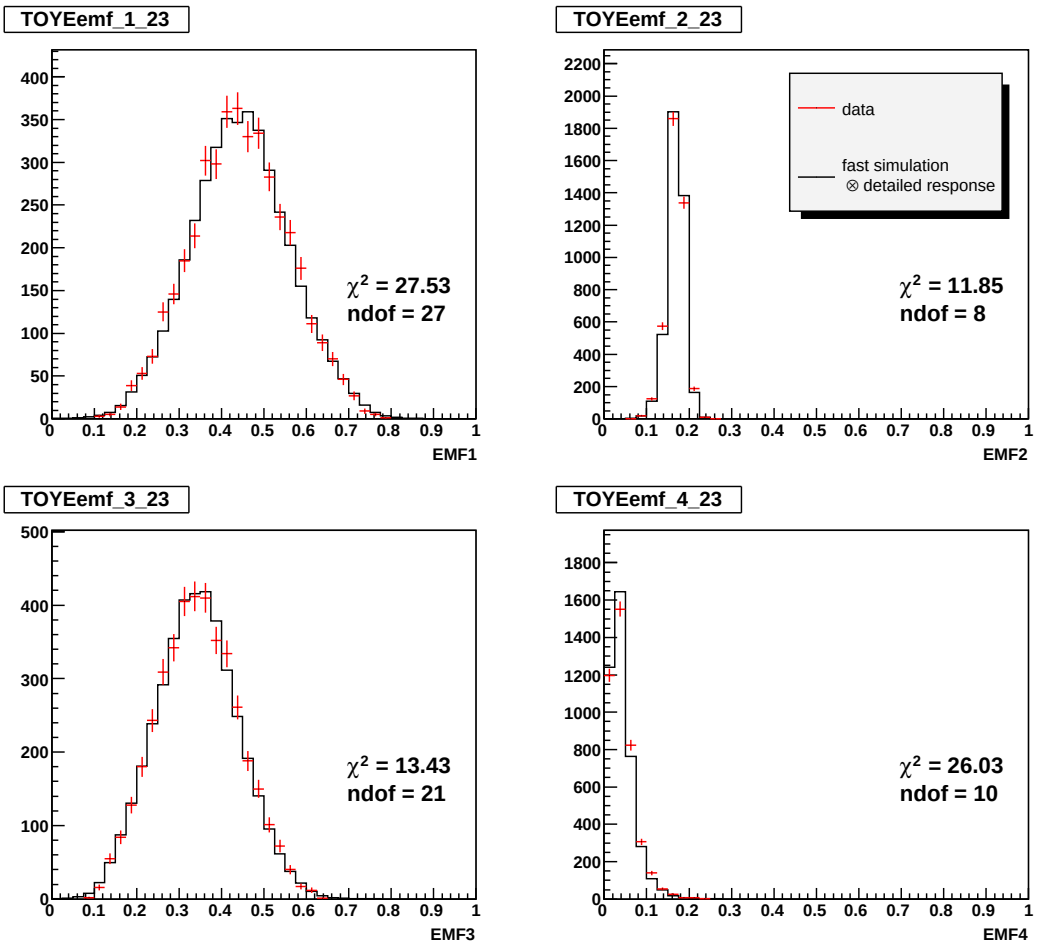

Figure 9.20. Comparison of EM fractions for electrons from $Z \rightarrow e^+e^-$ events in category 23 in data and simulation. The simulation used here includes $nX_0 = 0.1633$ radiation lengths of extra uninstrumented material in front of the CC calorimeter. The four individual plots show the energy fraction in each of the four EM layers

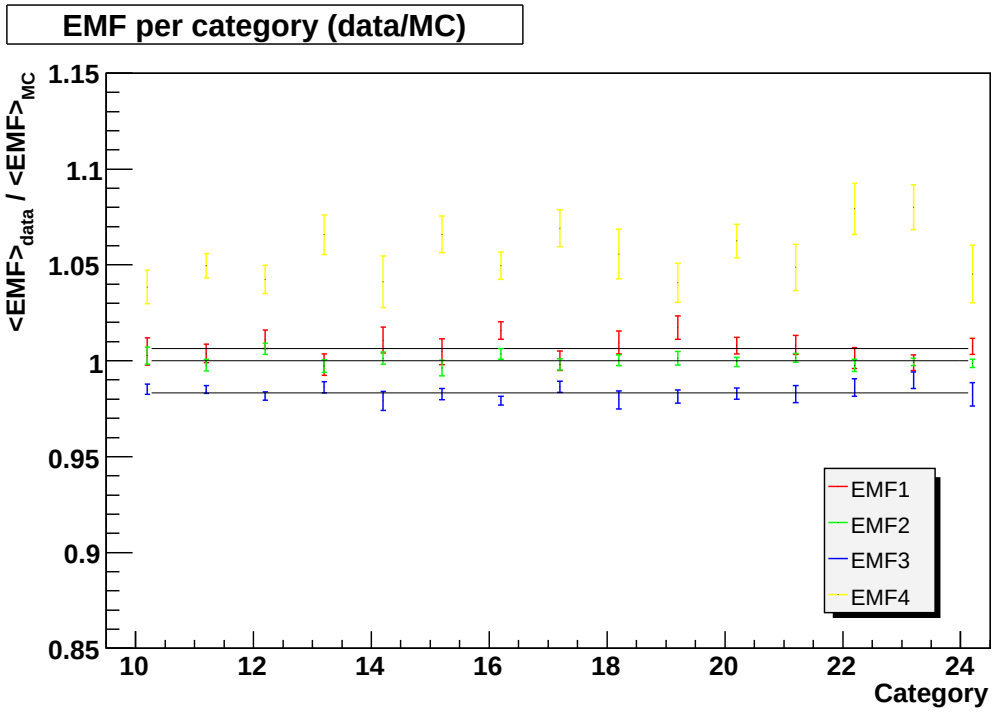

Figure 9.21. Ratios for the means of the EM fraction distributions in $Z \rightarrow e^+e^-$ events for each of the four EM layers and each of the 15 η categories. The simulation used here includes $nX_0 = 0.1633$ radiation lengths of extra uninstrumented material in front of the central calorimeter. Each of the three horizontal lines indicates the result of a fit to a common constant of the 15 data points from a given EM layer. The fit was performed for EM1, EM2 and EM3

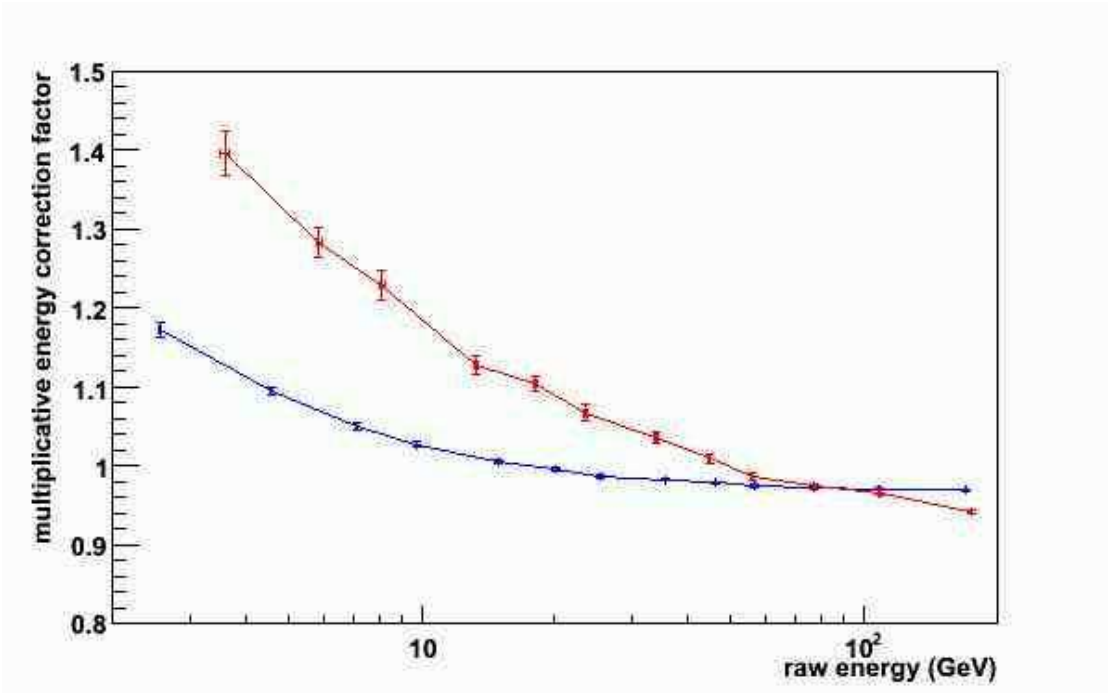

Figure 9.22. The correction factors used for obtaining the original incident energy of the electrons. Blue:η_{phys}= 0.2; Red:η_{phys}= 1.1

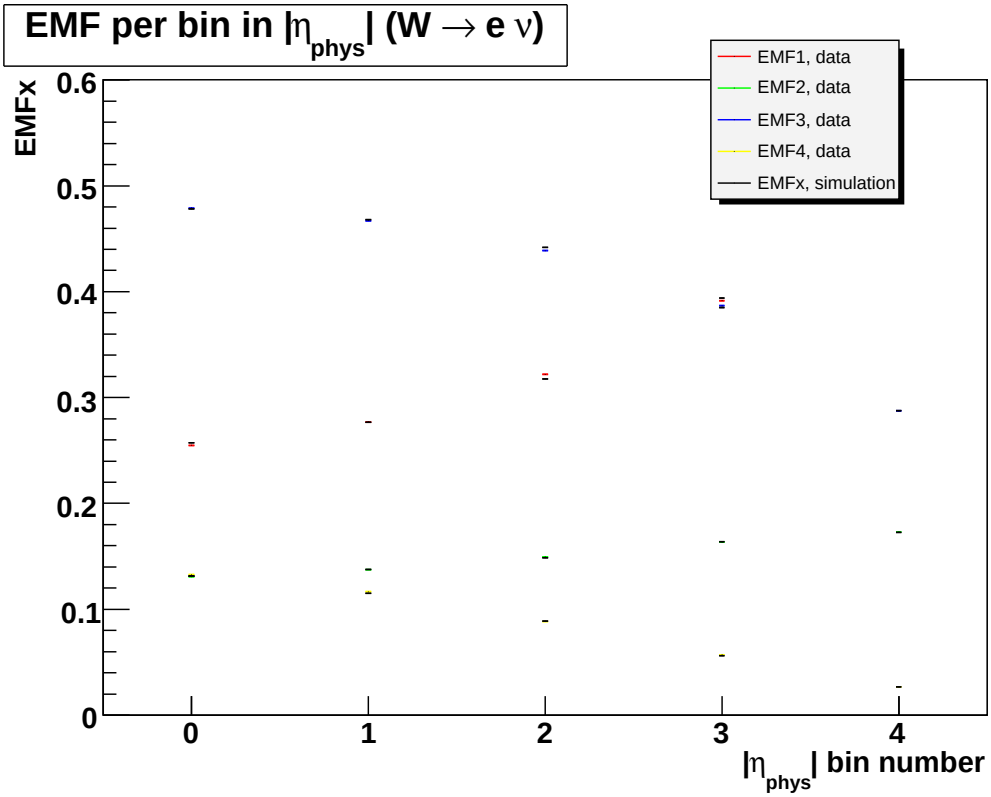

Figure 9.23. A summary of the means of the EM fraction distributions in $W \rightarrow e\nu$ events for each of the four EM layers and each of the five η bins, separately for data and FULL MC simulation

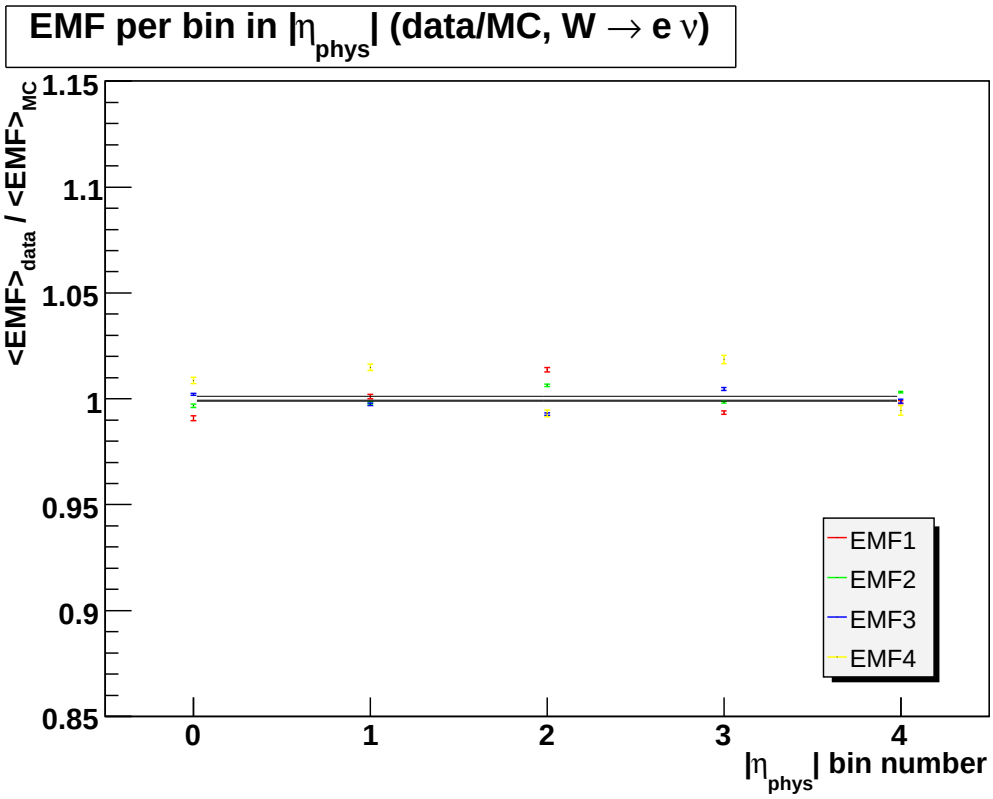

Figure 9.24. Ratios for the means of the EM fraction distributions in $W \rightarrow e\nu$ events for each of the four EM layers and each of the 5 η categories. Each of the three horizontal lines indicates the result of a fit of a common constant of the 5 data points from a given EM layer. The fit was performed for EM1, EM2 and EM3

CHAPTER 10

SELECTING EVENTS FOR THE ANALYSIS

10.1 A Brief Introduction

Now that we are finished with getting the calorimeter ready for optimal energy measurements of the W events, it is time to start talking about the details of the analysis ! The requirements and criteria for event selection plays an important role in any analysis. In our analysis, it is used for selecting the W events in collider data, for the FULL MC analysis and for parameterizing the FAST MC. The latter two have been mentioned briefly in Chapter 5 and will be discussed in the chapters that follow. Hence the event selection criteria described in this chapter will be referenced in the later chapters too.

The data sample used for this measurement of the W mass was collected between April 2002 to February 2006, the Run IIa period of data taking of the DØ detector. It represents about 1 fb^{-1} of integrated luminosity delivered by the Tevatron and recorded by the DØ detector as shown in Figure 4.4. The average instantaneous luminosity during this period of taking data was about 50×10^{30} cm^{-1} s^{-1} with an average of 1.2 interactions per bunch crossing.

The DØ detector records information for events that it deems interesting, in the form of digital signals. These signals are interpreted as physics objects by the reconstruction software DØRECO, used by the experiment. During the first stage

of reconstruction the raw data is processed into high-level physics objects such as energy clusters detected by the calorimeters or tracks recorded by the tracking systems when a charged particle passes through them. In the next stages these objects are combined to form particles such as photons, electrons, muons and jets. The missing energy is also determined with the help of all the detected energy in an event. During the course of an analysis these particles are used to identify an event, for e.g. a Z boson event is identified with the help of two high momentum leptons whereas a high momentum lepton along with a considerable amount of missing energy identifies a W event. The particles are also used for determining the primary and secondary vertices of events in the detector.

The W mass analysis described in this thesis deals with the electron and neutrino as decay products of the W boson ($W \rightarrow e\nu$). The electron leaves a clear signature in the detector while the neutrino escapes undetected and its energy is determined from the missing energy of the W event. Hence the electron identification and determination of the missing energy are important for tracking down the decay products of the W. In order to ensure that the decaying particles actually come from a W produced from the collisions of the $p\bar{p}$, the reconstruction of the primary vertex of the event is also of concern here.

As we know, the electron is reconstructed with the help of the tracking detectors. Hence we will look at both the track and energy reconstructions for purposes of identifying the electron. From the kinematics of the W boson, we know that the energy of the neutrino (missing energy) is determined from the those of the electron and the recoil, following the laws of momentum balance. Hence we will also consider the reconstruction of the recoil and the missing energy in this chapter. However let us start with a tabulation of all the trigger requirements of the

detector that contribute to the identification and recording of prospective W and Z events from the numerous $p\bar{p}$ collisions and take a look at the types of data samples that were used for this analysis.

10.2 Data Samples

The data used for this analysis have been obtained from the "EM Inclusive skims" prepared by the Common Samples Group at DØ. The p17 refixed versions of DØRECO, p17.09.03, p17.09.06 and p17.09.06b have been used for the reconstruction. The three main samples that have been skimmed are the EM+$\not\!\!E_T$ sample for finding W events, the 2EM sample for studying Z events and EM+Jet sample for estimating the probability of jets faking an electron. The three EM inclusive samples must satisfy the following requirements :

- EM + $\not\!\!E_T$:

  1 EM with $p_T > 20$ GeV, $|\eta_{det}| < 1.2$, $f_{EM} > 0.9$ and raw $\not\!\!E_T > 20$ GeV

- 2 EM :

  2 EM with $p_T > 20$ GeV, $f_{EM} > 0.9$ and isolation < 0.2

- EM + Jet :

  1 EM with $p_T > 20$ GeV, $|\eta_{det}| < 1.2$, $f_{EM} > 0.9$, isolation < 0.2

  1 Jet with $p_T > 20$ GeV, $|\eta_{det}| < 0.8$ or $1.5 < |\eta_{det}| < 2.5$

  $0.05 < f_{EM} < 0.95$, chfrac < 0.4, hotcellratio < 10 and n90 > 10

Here f_{EM} is the EM fraction, it refers to the fraction of the electron energy deposited in the 4 electromagnetic (EM) layers of the calorimeter whereas chfrac refers to the fraction of the jet energy deposited in the coarse hadronic (CH) layer of the calorimeter. The hotcellratio is the ratio of the hottest cell to the next to

hottest cell (in terms of transverse energy) in the calorimeter. n90 stands for the number of towers containing 90% of the energy of the jet.

The corresponding sam dataset for the skimmed samples are :

- EM + $\not\!\!E_T$:

  WMASSskim3-EMMET-WMRESK_p17.09.03-ROOT-wml,

  WMASSskim3-EMMET-WMRESK_p17.09.06-ROOT-wml,

  WMASSskim3-EMMET-WMRESK_p17.09.06b-ROOT-wml,

- 2EM :

  WMASSskim3-2EM-WMRESK_p17.09.03-ROOT-wml,

  WMASSskim3-2EM-WMRESK_p17.09.06-ROOT-wml,

  WMASSskim3-2EM-WMRESK_p17.09.06b-ROOT-wml,

- EM + Jet :

  tmb_WMASSskim3-EMJET-WMRESK_p17.09.03,

  tmb_WMASSskim3-EMJET-WMRESK_p17.09.06,

  tmb_WMASSskim3-EMJET-WMRESK_p17.09.06b.

10.3 Trigger Selection

In the data sample collected from the detector, a combination of single EM triggers are used for identifying electrons that might be the decay products of W and Z bosons. Different triggers of this type are used at each of the three levels (L1, L2 and L3) of the trigger system. An electron candidate must fire one of these triggers in order to qualify as an interesting candidate for the offline analysis.

The trigger lists for the dataset are divided into four periods, v8-11, v12, v13 and v14. The L1/L2/L3 requirements are different for the different trigger

periods [124]. For each trigger period, the single electron trigger that has the highest efficiency is chosen. Thus the trigger EM_HI_SH has been chosen for trigger list v8-11, E1_SHT20 for v12, E1_SHT22 for v13 and E1_SHT25 for v14. Events that passed these unprescaled trigger requirements are used for the final analysis.

The fraction of data taken during the v8-11 trigger period is 11.6%, for v12 period it is 21.2%, for v13 it is 34.3% and for v14 trigger period it is 32.7%.

The lists below enumerate and explain all the L1/L2/L3 conditions for each of the triggers used in this analysis.

10.4 Determining the Electron Energy

The energy of the electron is reconstructed from the clusters formed by the readout towers of the calorimeter. The energy of the cluster is obtained by summing over the energies of all EM towers within a window of 0.5×0.5 in the $\eta - \phi$ space (5×5 towers) in the central region (CC), or within a cone of radius 10 cm in EM3 in the end-cap regions (EC) of the calorimeter. Both these regions are centered on the tower that possesses the highest fraction of the electron energy. At DØ the reconstruction software package for electromagnetic clusters is known as EMRECO. For details please refer to Chapter 7.

The two variables of EM fraction and isolation are used as the main criteria for identifying electromagnetic candidates. A high value of the EM fraction f_{EM} indicates that most of the energy of the shower is contained in the four EM layers of the calorimeter. The isolation variable f_{iso}, is a measure of how well isolated the energy cluster is from other objects such as hadronic jets. The electrons from W and Z decays tend to be pretty well isolated and so for these EM clusters the

isolation value is required to be < 0.15.

Besides the EM fraction and isolation discriminants, the shape of an electron shower is also compared to that of a typical electromagnetic shower for conformity. This is done with the help of the H-Matrix, HMx7 is used for the central region (CC) of the calorimeter whereas HMx8 is used for the end-cap regions of the calorimeter.

An identification tag (ID) is assigned to each reconstructed cluster. An ID of 10 for those clusters which have transverse energy $E_T > 1.5$ GeV and $f_{EM} > 0.9$. If the cluster also has a track matched to it, it is assigned an ID=$\pm$11, depending on the sign of the track.

If an electron cluster is found to have a matched track, then the direction of the track is assigned to the direction of the electron. Thus,

$$\theta_e = \theta_{track} \qquad \phi_e = \phi_{track} \tag{10.1}$$

If the energy cluster cannot be matched to a track, then the positions of the calorimeter shower centroid $(x_{cal}, y_{cal}, z_{cal})$ and the primary vertices $(x_{vtx}, y_{vtx}, z_{vtx})$ are used to define a direction for the electron cluster. This is given by,

$$\tan\theta_e = \frac{\sqrt{x_{cal}^2 + y_{cal}^2} - \sqrt{x_{vtx}^2 + y_{vtx}^2}}{z_{cal} - z_{vtx}} \tag{10.2a}$$

$$\tan\phi_e = \frac{y_{cal} - y_{vtx}}{x_{cal} - x_{vtx}} \tag{10.2b}$$

With the help of the angles, θ_e and ϕ_e, the momentum of the electron is given by :

$$\vec{p_e} = E_e \begin{pmatrix} \sin\theta_e \cos\phi_e \\ \sin\theta_e \sin\phi_e \\ \cos\theta_e \end{pmatrix} \tag{10.3}$$

The transverse momentum of the electron is given by $p_T^e = E_T^e = E_e \sin\theta_e$.

As we know the calorimeter is made up of 32 modules in the EM layer, each of which is $2\pi/32$ radian wide in ϕ. The intermodular regions possess a lower response than the central regions due to their geometry and a paucity of instrumentation in these regions. This results in a loss of signals thus leading to an improper reconstruction of the energy clusters. Hence the "in fiducial" requirement on the electron clusters requires them to be located away from the intermodular regions of the calorimeter.

10.5 Reconstructing the Track and Primary Vertex

Since the electron is a charged particle, it should leave a trail in the tracking detector which gets registered in the form of hits both in the SMT and CFT. For this analysis we require an electromagnetic energy cluster to be "spatially matched" to a track which is reconstructed with the hits from the CFT and at least one hit from the SMT. In other words if the particle is an electron there should be a track pointing exactly at its energy cluster. This track matching helps reduce the backgrounds from particles such as photons (from π^0 or η decays).

The details of track reconstruction using the pattern recognition method and Kalman fitting procedure have been described in detail in Chapter 7. Since the W and Z bosons have extremely short lifetimes (10^{-24} sec) the primary vertex of the interaction is more significant. The reconstructed tracks of the electrons

are used to find the primary vertex. Details of the reconstruction of the primary vertex has also been described in the same section.

10.6 Determining the Recoil

In the $p\bar{p} \to (W \to e\nu) + X$ or $p\bar{p} \to (Z \to e^+e^-) + X$ events, where X stands for the hadronic recoil, we measure the energies of the recoiling particles having pseudorapidities $|\eta| < 4$.

In the calorimeter, individual recoil particles are not resolved but we measure their energies summed over detector segments. However particles with $|\eta| \geq 4$ escape unmeasured down the beam pipe and quite possibly carry away substantial momenta along the beam direction (z). Hence it is not possible to measure precisely, the sum of the longitudinal components of the recoil momenta (u_z). Since these escaping particles are at very small angles with respect to the beam, their contribution to the transverse momentum of the recoil ($\vec{u_T}$) is small and can be neglected. The recoil is thus constructed and analyzed in the plane transverse to the beam. It is easier to obtain the transverse component of the recoil momentum from the event kinematics by applying momentum conservation laws here.

The hadronic transverse momentum $\vec{u}_T$ is reconstructed by summing over the transverse momenta of all the calorimeter cells being read out, excluding those that belong to the electron clusters. Hence,

$$\vec{u_T} = \sum_i E_i \sin\theta_i \begin{pmatrix} \cos\phi_i \\ \sin\phi_i \end{pmatrix} = \sum_i \vec{E_T^i} \tag{10.4}$$

where the sum runs over all calorimeter cells that were read out except cells in the coarse hadronic (CH) calorimeter and ICD. Cells that belong to the electron clusters are also not included here. The CH calorimeter was excluded because of

its large noise factor and the ICD is not well calibrated[1] in the Run IIa data. The calorimeter cells that are read out pass the offline 2.5σ zero suppression threshold and the T42 algorithms[2] [101]. E_i are the cell energies, and ϕ_i and θ_i are the azimuth and colatitude of center of cell i with respect to the primary vertex.

10.7 Determining the Missing (Neutrino) Energy

The neutrino from the W decay escapes undetected and therefore its energy is referred to as the missing energy. A reconstruction of the missing energy in the 3-dimensional plane is not possible due to the incomplete coverage of the detector. We do not have an estimate of the neutrino energy travelling down the beam pipe. Hence the neutrino energy is determined from the momentum imbalance of the event, with the aid of the energies of the electron and the recoil, in the transverse plane of the detector. It is referred to as the transverse missing energy ($\not\!\!E_T$) of the event.

Since momentum is conserved in the transverse plane, a large amount of transverse missing energy indicates the production of a neutrino with high energy.

$$\not\!\!E_T = -(p_T^e + p_T^{\text{Recoil}}) \tag{10.5}$$

The missing transverse momentum is estimated by taking the vector sum

[1] What do we mean by saying "the ICD is not well calibrated in the Run IIa data" ? In addition to huge non-uniformities throughout the device, there is a non-trivial number of PMTs that just go "berserk" at high instantaneous luminosities (their gain explodes and they start to dominated the $\not\!\!E_T$ measurement). This is why many DØ Run IIa analyses use a tool that kills regions in the ICD. For us this is not an option since we would never have been able to model the effects of such cuts and vetoes. However the ICD has been calibrated well in the DØ Run IIb dataset. For more details on the ICD problem please refer to [123].

[2] A cell is said to pass the T42 algorithm is its energy is positive and $+4\sigma$ above the threshold or if it is $+2\sigma$ above the threshold but has a neighboring cell which exceeds the threshold by $+4\sigma$

$$\vec{\not{E}}_T^{\,raw} = -\sum_i E_i \sin\theta_i \begin{pmatrix} \cos\theta_i \\ \sin\theta_i \end{pmatrix} = -\sum_i \vec{E}_T^i \tag{10.6}$$

where the sum i runs over all calorimeter cells read out except cells belonging to the coarse hadronic (CH) calorimeter and the ICD. The calorimeter cells that are read out pass the offline 2.5σ zero suppression threshold and the T42 algorithms. E_i are the cell energies and ϕ_i and θ_i are the azimuthal and colatitude angles of the center of cell i with respect to the primary vertex.

The "raw" transverse component of the missing energy ($\vec{\not{E}}_T^{\,raw}$) results from the direct summation of the cell energies. This is corrected further by way of the electron energy corrections to obtain the corrected transverse missing energy.

10.8 Criteria for Selecting the Events

This section deals with the conditions imposed for the selection of ideal W and Z candidates from the detector signals for the purposes of this analysis. Since both W and Z are massive bosons and decay instantly (lifetime $\sim 10^{-24}$ sec), the location of the primary vertex (point of $p\bar{p}$ collision) is important here. Besides both types of events involve the detection of highly energetic well-defined electrons, so the selection criteria for electrons is the same for both W and Z. Apart from this there are a few specific conditions that apply to each of the events. All these criteria have been described here under their appropriate categories.

First, the primary vertex of the W or Z event needs to be located well within the detecting regions of the SMT. Thus,

- $|z|_{\text{vertex}} < 60$ cm

Second, an ideal electron candidate must satisfy the following criteria in order

to get selected :

- Confirm with electron/photon identification number, id = 10, ± 11
- $\eta_{det} < 1.05$
- $f_{EM} > 0.9$
- $f_{iso} < 0.15$
- HMx7 < 12 in CC and HMx8 < 20 in EC
- In the fiducial region of the calorimeter (in_eta_fiducial and in_phi_fiducial)
- p_T^e (or E_T^e) > 25 GeV
- Energy cluster must be spatially matched to a track
- Associated track should have at least one SMT hit and $p_T > 10$ GeV
- Calorimeter cuts for data quality
- Electrons should not be inside CC-EM module 17

To ensure that the electron energy windows (0.5×0.5 in $\Delta\eta - \Delta\phi$) are not clipped in any way the clusters are required to be in the region $\eta_{det} < 1.05$.

The "fiducial" requirement keeps electron clusters away from the intermodular regions of the calorimeter. It excludes the region mod(ϕ, $2\pi/320 < 0.1$ and mod(ϕ, $2\pi/320 > 0.9$, where (ϕ) is the azimuthal angle of the cluster.

Spatial conformity between a track and a cluster is achieved with the help of the χ^2 variable which is defined as follows :

$$\chi^2 = \left(\frac{\Delta\phi}{\sigma_\phi}\right)^2 + \left(\frac{\Delta z}{\sigma_z}\right)^2 \tag{10.7}$$

here $\Delta\phi$ and Δz are the angle difference and spatial difference between the positions of the electromagnetic cluster and the extrapolated track. The quantities σ_ϕ and σ_z represent the experimental resolutions on their respective parameters. Tracks with a track match significance probability of $P(\chi^2) > 0.01$ to EM clusters are selected.

Data quality cuts are imposed to eliminate those regions of the calorimeter that have improper readouts due to problems or failure with the readout hardware. Besides module 17 was damaged during the reassembly of the DØ calorimeter for Run II and so electron signals from this part are avoided.

Stringent conditions are imposed for the selection of ideal Z candidates in order to select well defined events and minimize the background contamination in the samples. The criteria for the selection of Z candidates are listed below :

- Should possess two "well-defined" electron candidates
- At least one electron must pass the trigger requirements (L1/L2/L3)
- Transverse momentum of the Z recoil (p_T^{Recoil}) must be low (soft), < 15 GeV
- Reconstructed invariant mass of Z (M_{ee}) should be between 70 and 110 GeV
- Z event should possess negligible amount of missing energy (mainly due to low response of recoil system)

The candidates which satisfy all the requirements of the electron selection listed above, are said to be "well-defined" candidates. If both the reconstructed electrons lie in the central region (CC) of the calorimeter, we term it a "CC-CC" Z candidate whereas if both of them lie in the end-cap regions (EC) of the calorimeter, we call it a "EC-EC" Z candidate. Similarly if one of the electrons

lies in the central region while the other lies in the end-cap region we term it a "CC-EC" Z event.

A cut on the recoil of the Z is chosen for minimizing systematic errors in the detector modeling.

This analysis focuses on the reconstructed CC-CC $Z \rightarrow ee$ events only.

Finally the requirements for the selection of ideal $W \rightarrow e\nu$ events are given as follows :

- Should possess a "well-defined" electron
- Electron must pass the trigger requirements (L1/L2/L3)
- Missing transverse energy, $\not\!\!E_T > 25$ GeV
- Transverse momentum of the W recoil (p_T^{Recoil}) must be low (soft), < 15 GeV
- Reconstructed transverse mass of the W boson should lie between 50 and 200 GeV.

A cut on the W recoil is chosen for minimizing the systematics due to the detector modeling. In addition they also reduce the QCD background associated with events at larger values of the W recoil.

Again, this analysis considers only those $W \rightarrow e\nu$ events whose electrons lie in the central region (CC) of the calorimeter.

10.9 $Z \rightarrow e^+e^-$ and $W \rightarrow e\nu$ Data Samples

So for our analysis with 1.0 fb^{-1} of collider data we obtain only 18,725 $Z \rightarrow ee$ events and 499,830 $W \rightarrow e\nu$ events, after satisfying all the above selection requirements.

TABLE 10.1

SINGLE EM TRIGGERS USED IN THIS ANALYSIS

Trigger	L1	L2	L3
EM_HI_SH	CEM(1, 10)	EM(1,12) for runs > 169523	ELE_LOOSE_SH_T(1, 20)
E1_SHT20	CEM(1, 11)	none	ELE_NLV_SHT(1, 20)
E1_SHT22	CEM(1, 11)	EM(1, 15)	ELE_NLV_SHT(1, 22)
E1_SHT25	CEM(1, 12)	EM(1, 15)	ELE_NLV_SHT(1, 25)

L1 triggers

CEM(1,10)	one EM trigger tower $E_T > 10$ GeV
CEM(1,11)	one EM trigger tower $E_T > 11$ GeV
CEM(1,12)	one EM trigger tower $E_T > 12$ GeV

L2 triggers

EM(1,12)	one EM candidate with $E_T > 12$ GeV (not present for runs below 169523)
EM(1,15)	one EM candidate with $E_T > 15$ GeV

L3 triggers

ELE_LOOSE_SH_T (1,20)	one electron with $\|\eta\|$ <3.0 and E_T >20 GeV passing loose requirements including shower shape
ELE_NLV_SHT (1,20)	one electron with $\|\eta\|$ <3.6 and E_T >20 GeV passing tight shower shape
ELE_NLV_SHT (1,22)	one electron with $\|\eta\|$ <3.6 and E_T >22 GeV passing tight shower shape
ELE_NLV_SHT (1,25)	one electron with $\|\eta\|$ <3.6 and E_T >25 GeV passing tight shower shape

CHAPTER 11

EVENT GENERATORS

11.1 An Introduction - What is an Event Generator?

We have read in Chapter 5 about a parameterized FAST MC model of the detector which is used extensively both for the FULL MC and collider data analyses. Hence the next few chapters will be devoted to some information on the Monte-Carlo. In this chapter we read about the basics of event generation in Monte-Carlo, the event generators chosen specifically for this M_W analysis and some of the important corrections that need to be considered while generating MC events. The next three chapters focus on the parameterized FAST MC detector model. We present an overview of the parameterizations of the two major (electron and recoil) systems necessary for the $W \rightarrow e\nu$ events in Chapter 12, followed by a description of each of the two systems in Chapters 14 and 15.

An "event" is a list of particles (mesons, hadrons, etc.) along with their energies and momenta, produced by the collision of a proton-antiproton pair in the collider. Both theorists and experimentalists have a strong motivation for simulating these events artificially, with the help of the Monte-Carlo (MC) software packages. The theorists need it to obtain artificial "data" for exploring analysis techniques (rather new discoveries or measurements of parameters) while the experimentalists would like to use it for similar reasons as well as study the experimental backgrounds especially when probing for new physics coming from the

Standard Model (SM). These calculational techniques can be used for the numerical simulation of artificial events for these purposes. These are known as "event generators" and are capable of simulating highly energetic events such as those actually produced in particle accelerators of collider experiments.

In this technique, a computer program generates events, which are a list of particles (π, p, ρ, ...) and their momenta p_1, p_2, p_3, ... that constitute a final state that could arise from the aftermath of a collision. The program is constructed in such a way that the probability of generating a final state f is approximately proportional to the physical probability of getting this same final state in the SM (or the theory being tested). Thus if the event generator generates weights w_n for the events, the predicted value for an observable described by a measurement function $S(f)$ is given by

$$< S >= \frac{1}{N} \sum_{n=1}^{N} w_n S(f_n) \tag{11.1}$$

Since these MC-based event generators are capable of generating complete final states, one can use detector simulations to analyze the effects of a deviation from the ideal detector on measurements. Besides, they are very important for predicting event rates and topologies, for studies of detector requirements (thus optimizing detector or trigger designs) and for studies of detector imperfections (by evaluating acceptance corrections).

The probability to generate an event is proportional to the cross-section for the event. A typical description of an event simulation has been shown pictorially in Figure 11.1 and includes the following processes:

1. The incoming hadrons and their momenta which are usually described by the parton distribution functions.

2. The "hard scatter" of the process i.e. the direct interaction between the incoming partons, producing new particles (e.g. W/Z, t quark). In the MC simulation this is taken care of by the Matrix Element calculations at the leading order (LO) and/or next-to-leading order (NLO) levels.

3. The QCD radiation from the incoming partons (called initial-state radiation) and the products of the hard interaction (known as final-state radiation). Most of this is in the form of soft gluons. This is accounted for by the "parton shower" (PS) calculations which need to be matched to those describing the hard interactions [125].

4. The "underlying event" or the interactions from the other partons in the incoming hadrons, those that did not partake in the hard scatter. This contribution is built from models based on multiple parton interactions.

5. The "hadronization" process where the radiated partons combine with other partons to form hadrons. Thus radiated gluons give rise to $q\bar{q}$ pairs which combine with other quarks to form hadrons. A variety of models (e.g. Lund String Model, Cluster Model) attempt to help model this process.

6. Hadron decays, i.e. the ultimate decay products that result from the breakup of these hadrons

The difference between the different MC event generators in the market is usually on the basis of the approximations and models that they use for simulating the above processes.

Thus event generating is built on an extensively theoretical framework. Their construction and function involves the use of many libraries and models for simulating the hard processes, the intial- and final-state parton radiations, multiple

parton-parton interactions, beam remnants, hadronization and particle decays of the complex physics processes. These topics are the subjects of discussion in the sections of this chapter with an emphasis on the simulations necessary for this analysis of the W mass.

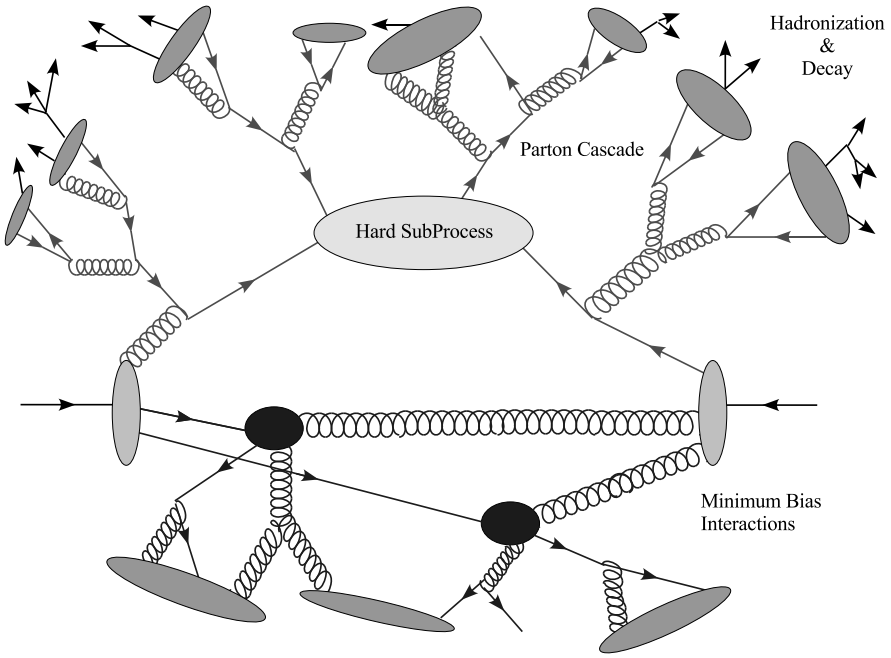

Figure 11.1. The typical simulation of an event by an event generator (H signifies the hard process)

11.2 Simulating the Hard Scatter of the Process

The cross-section of the hard scatter between the incoming quarks is based on perturbative QCD calculations [126] and is determined by means of the Matrix Element followed by integration over the phase space. The latter is the crucial part and is rather difficult. For more details on the Matrix Element technique please

refer to [127]. The parton showers involve soft and collinear gluon radiation and the Matrix Element technique cannot be used in this non-perturbative regime of low momenta. Before we delve into the details of how they are determined, let us consider the need of simulating the parton showers and hadronizations.

In a hard scatter that produces a vector (W/Z) boson, the production of the vector boson is simulated first, by generating the four-momentum of the boson using the model for the differential cross-section describing the boson production and the mass spectrum, as discussed in Chapter 3. The variables $d^2\sigma/dq_T^2dy$ and $d\sigma/dQ$ are treated as probability densities for generating the four-momenta of the vector bosons. A pair of values of y (rapidity) and q_T (transverse momentum) are picked from the former while a value of Q (mass) is picked from the latter for the produced boson. Depending on the types of quarks involved in the interactions, sea or valence, the helicity ($\lambda = +1$ or -1) differs. The other characteristics of the event like the z position of the interaction vertex (z_{vtx}) and the luminosity number are also generated. The decay of the boson is simulated next. At this point we know the true p_T of the boson and the momenta of its decay products. These kinematic variables are then used to simulate the observed transverse momentum of the recoil and the electron, by applying the parameterized detector model.

11.3 What is Parton Showering and Hadronization?

As we know the calculations for the perturbative cross-section just include the first two processes given above. However it should be kept in mind that we need the predictions for the "entire event" at the colliders (Tevatron and LHC). The LO and NLO perturbation theory can give predictions only for the very inclusive cross-sections and describe the final state in terms of quarks, gluons,

leptons and photons. These final states are not close to the physical final states. In an experiment an event is observed by detecting the hadrons (mesons, baryons), leptons and photons. As we know from quark confinement [1, 2], individual, free quarks are not found in nature. A high energy parton (quark or gluon) slowed by the increasing magnitude of the strong force, splits into two daughter partons, each of which splits into two or more partons. This process can be likened to the Brehmsstrahlung radiation that occurs in the case of the electron. As this process continues, the energy of the daughter partons consequently decreases and a parton shower develops. The partons then combine with other partons giving rise to many different hadronic states, which are actually observed.

So in order to get the predictions for the complete final state approximately right, we need to obtain realistic final states, where the outgoing partons are used to generate the parton showers and subsequent hadronizations as well. This is accomplished by the parton showering algorithm in the event generators.

Thus all outgoing colored partons must first undergo parton showering and then combination of the produced partons into hadrons [128]. The term fragmentation is used to describe the soft QCD radiation, splitting and showering of the partons while the term hadronization is used to describe the subsequent formation of hadrons. As the parton which was produced in a hard scatter exits the interaction, the strong coupling constant will increase with its separation. This increases the probability for QCD radiation, which is predominantly at small angles with respect to the originating parton. Thus, one parton will radiate gluons, which will in turn radiate $q\bar{q}$ pairs with each new parton nearly collinear with its parent. The $q\bar{q}$ combine with others of their species to form stable colorless hadrons and so on.

11.4 How are Parton Showering and Hadronization Modeled?

Since parton showering produces partons of successively lower energy, it exits the region of validity for perturbative QCD. Analytical calculations of gluon radiation possesses divergences that make it impossible to calculate the Matrix Element for all the partons in the given phase space. Furthermore, the calculations are only possible up to a fixed perturbative order. MC event generators solve this problem through parton shower models that add gluon radiation to the output of the Matrix Element calculations [129]. These models are essentially phenomenological and must then be applied to describe the length of time when showering occurs, and then the combination of colored partons into bound states of colorless hadrons, in an inherently non-perturbative way. These phenomenological descriptions are usually parameterized or expressed with the help of information from experimental data. Some of the phenomenological models that are used for describing the parton showering are the Lund String Model (used by PYTHIA) and Cluster Model (used by HERWIG) and the Fragmentation model. Detailed discussions of these models are beyond the scope of this thesis.

Thus, despite the simple structure of the tree-level QCD perturbative theory's description of the collision and decay processes in an event, the observed high-energy process usually contains significant amount of modifications, like photon and gluon bremsstrahlung or loop diagram corrections, that are usually too complex to be evaluated easily in real calculations directly on the diagrammatic level. The method of modeling the parton showering and hadronization processes is described below in the context of the event generators used for this W mass analysis.

11.5 Event Generators Used for this W Mass Analysis

Two event generators that have been extensively used for the purposes of this analysis are PYTHIA and RESBOS. PYTHIA has been used for the FULL MC analysis, since the FULL MC sample was also generated using PYTHIA. RESBOS describes the collider data better, hence it was used as the event generator in the FAST MC simulation for the actual data analysis.

The PYTHIA program is a standard tool for the generation of physics processes that actually occur during the high-energy collisions of nucleons (pp or $p\bar{p}$). It comprises of a set of physics models that work coherently for the evolution from a few-body hard process to a complex multi-hadronic (partonic) final state. Its objective is to provide a representation of event properties in a wide range of reactions, within and beyond the Standard Model, with emphasis on those where strong interactions play a direct or indirect role, thereby producing multi-hadronic (partonic) final states. Since the physics is not understood well enough to give an exact description, the program has to be based on a combination of analytical results and various QCD-based models.

RESBOS, as the name indicates, is another Monte-Carlo event generator that caters to generating events that model the production and decay of vector bosons. It utilizes a resummation technique for on-shell vector boson production so as to correctly include the effects of the polarization and width of the boson to the distributions of the decay leptons. RESBOS computes the triple differential cross-section $d^3\sigma/dq_T^2 dy dQ$ for W and Z/γ^* processes at hadron colliders. As also mentioned in Chapter 3, it performs a gluon resummation calculation at low values of the boson p_T and perturbative QCD calculations at large values of the boson p_T.

As mentioned earlier, the W mass is affected by QCD and electroweak (EW) radiations (emission of gluons or photons). Hence corrections for these effects are necessary for obtaining the correct W mass. There exist a few Monte-Carlo event generators for modeling the production and decay mechanisms of $p\bar{p} \rightarrow W/Z + X$ but none of them are adequate enough for incorporating all of the QCD and electroweak corrections associated with the mechanisms. There also exist MC programs that cater specifically to determining the electroweak corrections to vector boson production such as WGRAD [130] and ZGRAD [131]. Table 11.1 shows some of the existing generators and programs for $p\bar{p} \rightarrow V + X$, where $V = W/Z$, that we have used for purposes of W and Z event generation and determining electroweak corrections.

TABLE 11.1

AVAILABLE EVENT GENERATORS FOR W AND Z PROCESSES AT HADRON COLLIDERS

Event Gen.	Process	QCD	EW
RESBOS	W, Z	NLO	-
WGRAD	W	LO	complete $\mathcal{O}(\alpha)$, Matrix Element, ≤ 1 photon
ZGRAD	Z	LO	complete $\mathcal{O}(\alpha)$, Matrix Element, ≤ 1 photon
PHOTOS			QED FSR, ≤ 2 photons

For the electroweak corrections we have used generators like WGRAD and ZGRAD. These are MC programs for calculating the electroweak radiative corrections to W/Z boson production at hadron colliders. Thus they are well suited for cross section measurements since they calculate full matrix elements. They include the initial-state radiation (ISR), final-state radiation (FSR), photon radiation off the W propagator and other radiative corrections e.g. the interference between ISR and FSR, self-energy and W and Z box diagrams. PHOTOS [132] has been used extensively for modeling the corrections due to the emission of up to two FSR photons. As regards to the effect of the electroweak corrections on the W mass, the dominant effect comes from the radiation of a single photon off the final stage charged lepton. The effect from radiation of the second photon comes next.

Thus, RESBOS interfaced with PHOTOS is used for the purposes of generating Monte-Carlo events for this analysis. We used WGRAD and ZGRAD to study the effect of the ISR and other electroweak corrections on the W mass.

11.6 QCD Corrections

We have read in Chapter 5 that the $\not{E}_T$ and m_T distributions are more influenced by the response of the detector to the recoiling particles, since they makes use of the inferred neutrino momentum (missing energy). On the other hand, the shape of the p_T^e distribution is directly sensitive to the momentum of the W boson (p_T^W). The p_T^e also contributes in the determination of the transverse mass m_T. Thus a good understanding of the transverse momentum of the W boson is necessary for measuring the mass from the kinematic distributions.

As mentioned earlier, the p_T^W spectrum can be measured more precisely from

a measurement of the p_T distribution of the Z boson (p_T^Z). The idea behind this is that the formalism that describes the p_T of the W has to describe the p_T of the Z and the dilepton p_T spectrum from the Drell-Yan [133] production simultaneously. The p_T of the Z bosons can be measured more precisely than the p_T of the W bosons due to the clear signature of their e^+e^- decay pairs.

At low values of the W and Z momenta, we have read (in Chapter 3) that the main corrections to the overall cross-section comes from the emission of multiple soft and collinear gluons. These non-perturbative corrections are carried out through the gluon resummation formalism described earlier. Theoretical calculations provide a formalism to describe these non-perturbative physics in the boson p_T spectrum, with the help of three phenomenological parameters g_1, g_2 and g_3. These three need to be determined experimentally from $Z \to e^+e^-$ data. In addition, the p_T distribution also depends on the choice of parton distributions and Λ_{QCD}, the scale parameter in QCD theory [2]. For higher values of boson momenta, the p_T distribution relies on perturbative QCD calculations.

11.7 Electroweak Corrections

As mentioned earlier, the colliding quarks in the intial state, the newly created W boson and the final-state electron are all capable of radiating photons. Other electroweak (EW) processes such as interactions with virtual photons or Z bosons could also lead to photon radiation. All these contribute to an uncertainty on the W mass. An incorrect estimate of the EW corrections due to photon radiation can lead to an inaccurate determination of the W mass. The determination of this systematics will be described in detail in Chapter 19.

11.8 PDF Uncertainties

The parton distribution functions (PDF) used in the description of the cross-sections in the event generators also have an uncertainty associated with them. This stems from the fact that the PDFs are derived from a set of orthogonal parameters (20 parameters plus the central one in the case of CTEQ6.1 PDF set) that have been obtained from a fit to the experimental data at a 90% confidence level. The PDFs have been described in detail in Chapter 3. Details on the estimation of the systematics will be presented in Chapter 19.

CHAPTER 12

PARAMETERIZED MONTE-CARLO SIMULATION (PMCS)

12.1 An Introduction - What is the PMCS of the Detector?

In the real world of physics experiments that involve the study of the structure of matter, collisions between atoms or nuclei or nucleons produce 'events' which could be described as sets of outgoing newly created particles produced via the interactions between two incoming particles, in generic terminology. These events can be observed by the detector and stored via the data acquisition system of the experiment, for offline reconstruction and analysis later on.

As part of the requisites for ensuring that the recorded data is the effect of the true physical processes occuring as a result of the collisions, convoluted with the effects of the detector on the outgoing products, we need a "virtual reality" tool that is capable of modeling these physical processes that allow us to carry out theoretical and experimental studies of these complex multi-particle physics. The results from the exercise of this tool are compared with the actual results from the detector and are often used for formulating analysis strategies, setting detector requirements, estimating corrections and in general, help understand the ongoing physical processes at an enhanced level of detail.

This indispensible tool that can be used generate physical processes and store events, pass them through a simulation of the detector so as to convolute its

effects with the physics of the generated events and furnish them in a format that can be reconstructed and analyzed later, is called a Monte-Carlo simulation. The two main types of detector simulations described in the context of this thesis are the GEANT-based FULL MC simulation and the parameterized FAST MC simulation. The FULL MC is a minutely detailed, nut-by-bolt, slowly processed, modeling of the detector. The information from every aspect of the detector is incorporated into the simulation to ensure that the output is reasonably close to that from the actual DØ detector. The FAST MC is a fast simulation that emulates the effects of the detector, as accurately as necessary, with the help of various parameters. Hence it is aptly referred to as the "Parameterized Monte-Carlo simulation" (PMCS). It is important here to consider the fact that it only simulates the effects of the detector, it does not actually model the detector unlike the FULL MC.

Thus both the FULL and FAST MC simulate the final stage products of particle ($p\bar{p}$) collisions at the center of the detector. The starting points are the "event generators" that are convoluted with the simulations of the detector effects. In this way, we emulate the same effects on the particles emerging from the simulated detector as in the real detector. Event generators have been described in detail in Chapter 11.

Since the FAST MC is developed on the basis of parameters, it is much faster for use and reuse as compared to the FULL MC. The fact that it incorporates a very detailed modeling of the structure of the detector for emulating its effects makes the FULL MC rather slow in its performance.

More details on the FULL MC and the purpose behind using it have been given in Chapter 17. This chapter deals with the FAST MC. Let us now look

into the reason behind the FAST MC finding extensive use in the context of the W mass analysis followed by a mention of some of the important aspects of the FAST MC simulation.

A standard procedure for determining the W mass or width (M_W or Γ_W) involves fitting the distributions of m_T, p_T^e or p_T^ν ($\not{E}_T$) measured from the collider data to the simulated template distributions. These high statistics templates are generated at different values of the electroweak parameter being measured (M_W or Γ_W). This demand for many such templates necessitates the development of the FAST MC model of the detector. The parameterized detector should model the relevant observables from the real detector as accurately as necessary by recreating the underlying physics of the W boson produced in $p\bar{p}$ collisions and by simulating the response of the DØ detector for these events. It accomplishes all of the above requirements with the help of various parameters that are tuned to describe the effects of the detector. The use of parameters for modeling the detector effects makes the FAST MC a fast-to-use and relatively easy-to-handle executable, which is extremely important, given the fact that it can be used repeatedly for obtaining results over a short time scale when performing a diagnostic study or generating templates of different varieties or testing a part (or whole) of the analysis for a range of parameters, etc.

The W mass group employs the following approach for its parameterized detector simulation - use of PYTHIA [107] or RESBOS [87] Monte Carlo generators for the production and decay of the vector (W/Z) bosons followed by the smearing of the four momenta of the decay products (E, p_x, p_y, p_z) using the custom-built software package called `wz_epmcs` [134]. This wz_epmcs contains the modeling of the detector effects in a parameterized form [104]. Such a parameterized, Monte-

Carlo based, detector simulation is always referred to as the "Fast Monte Carlo" (FAST MC) throughout this thesis.

In order to emulate the effects of the detector for the W mass analysis, the FAST MC makes use of various efficiencies which help it to identify correctly and thus select the required signatures of the electron and neutrino, as precisely as necessary for the analysis. Broadly speaking, these efficiencies are like probabilities modeled as a function of the event selection requirements or detector conditions, such as the efficiency of matching an EM cluster to a track or the efficiency of triggering on electron-like objects. They are derived from the behavior of the real detector to the decay products of the events. A detailed discussion of the types and functions of the efficiencies has been given in the next chapter.

The FAST MC is also an indispensable tool for modeling the signatures of the W (or Z) events as observed in the real detector. In other words, for a W event, it models the electron energy, recoil energy and consequently the missing energy. For modeling these energies with the help of parameters, it is essential to know the effects of the detector on these signature particles, in terms of its response, resolution (smearing effect), addition of energies from other sources such as photons emitted from the leptons, etc. In the subsequent sections let's get an overview of the way the signatures of the W event are modeled in the FAST MC. Further details of the modelings are given in the subsequent Chapters 13, 14 and 15.

12.2 Modeling the Electron Energy Response and Resolution

In the FAST MC, the energy from the FSR photons that are very close to the electrons are added to the electron energy. The electron energy is then modeled

in the following way:

$$p_T^e(\text{meas}) = E^e(\text{meas}) = R_{EM}(E_0) \oplus \sigma_{EM}(E_0) + \Delta E(\mathcal{L}, u_{\parallel}) \tag{12.1}$$

Here E^e is the smeared energy (equivalent of reconstructed energy in data) while E_0 is the true (generated) energy of the electron. R_{EM} is the response and σ_{EM} is the resolution of the detector for EM objects. ΔE is the energy in the electron reconstruction cone from sources other than the electron, such as the hard recoil (see Section 12.3), energy from the underlying event, pileup and zero-suppression effects. Since the contribution from additional $p\bar{p}$ interactions depends on luminosity ($\mathcal{L}$), ΔE is parameterized as a function of luminosity and $u_{\parallel}$. It needs to be subtracted from the smeared energy of the electron.

The energy response of the EM calorimeter for the electron is modeled with the help of the following parameters:

$$R_{EM}(E_0) = \alpha \times E_0 + \beta \tag{12.2}$$

where α is the scale factor of the calorimeter and β is an offset.

The resolution of the EM calorimeter is modeled as in the usual case of a sampling calorimeter.

$$\frac{\sigma_{EM}(E_0)}{E_0} = \sqrt{C_{EM}^2 + \frac{S_{EM}^2}{E_0} + \frac{N_{EM}^2}{E_0^2}} \tag{12.3}$$

Here C_{EM} is the constant term, N_{EM} is the noise term and S_{EM} is the sampling term for the EM calorimeter. Due to the presence of extra material in front of the calorimeter in Run II as compared to Run I, the sampling term now depends on

the electron energy and angle of incidence of the electron. More information on these terms have been provided in the Chapter 14.

The final smeared energy of the electron can be given in a combined way as:

$$E^e(\text{meas}) = R_{EM}(E_0) + x * \sigma_{EM}(E_0) + \Delta E(\mathcal{L}, u_{\|}) \tag{12.4}$$

where x is a random variable from a normal gaussian distribution constructed at zero mean and unit width.

12.2.1 Electron Angular Resolution

The angular resolution of the electron is modeled in the following way:

$$\eta_{\text{meas}} = \eta_{\text{gen}} + y * \sigma_\eta \tag{12.5a}$$

$$\phi_{\text{meas}} = \phi_{\text{gen}} + z * \sigma_\phi \tag{12.5b}$$

Here σ_η and σ_ϕ are the η and ϕ resolutions of the tracking system. The amount of smearing is determined with the help of random variables (y and z) chosen from a gaussian distribution with zero mean and unit width. The values of the two parameters were determined to be $\sigma_\eta = 2 \times 10^{-3}$ and $\sigma_\phi = 0.4$ mradian, by comparing the $\Delta\eta$ and $\Delta\phi$ of the two reconstructed muons with those of a single cosmic muon that went straight through the detector.

For a thorough description of the electron modeling please refer to Chapter 14.

12.3 Modeling the Recoil System

The hadronic recoil for this analysis is modeled by splitting it up into two components, modeling each one of them separately and then combining them with the help of some tunable parameters. The two basic components are called the "hard" and "soft" components. The hard component as the name suggests, comprises of all the partons that recoil against the vector (W/Z) boson in the hard scatter. The soft component is made up of the contributions from the underlying event, the additional $p\bar{p}$ interactions, pileup and noise from the same or previous beam crossings.

The underlying event refers to the interactions of the spectator partons in the same $p\bar{p}$ hard scatter that produced the vector boson. The additional energy contribution comes from the other $p\bar{p}$ interactions that occur in the same bunch crossing, pile-up and noise effects. The part of the recoil present under the electron cluster is added back to the recoil. The energy of the FSR photons that are very far away from the parent electron are considered as part of the recoil and are added to it. Thus in the FAST MC, the observed recoil momentum is modeled in the following way:

$$\vec{u}_T(\text{meas}) = \vec{u}_T^{\,\text{HARD}} + \vec{u}_T^{\,\text{SOFT}} + \vec{u}_T^{\,\text{ELEC}} + \vec{u}_T^{\,\text{FSR}} \tag{12.6}$$

where $\vec{u}_T^{\,\text{HARD}}$ is the hard component obtained in a parameterized form from the recoil of $Z \to \nu\nu$ events, $\vec{u}_T^{\,\text{SOFT}}$ is the soft contribution modeled from minimum bias and zero bias events. $\vec{u}_T^{\,\text{ELEC}}$ represents the part of the recoil under the electron window and $\vec{u}_T^{\,\text{FSR}}$ is the contribution from the FSR photons that are too far away from their parent electrons and thus form part of the recoil.

A detailed description of the recoil modeling has been provided in Chapter 15.

12.4 Missing Transverse Energy

In the FAST MC, the transverse component of the missing energy is calculated from the transverse momenta of the electron and recoil. Since we model the electron and recoil momenta, the missing energy is inferred from the two systems by means of the following:

$$\vec{\not{E}}_T(\text{meas}) = -\vec{p}_T^{\,e}(\text{meas}) - \vec{u}_T(\text{meas}) \tag{12.7}$$

CHAPTER 13

MODELING THE EFFICIENCIES IN PMCS

13.1 A Brief Introduction

In this chapter we describe the efficiency model that helps simulate the effects of the detector on the electron in the FAST MC. In data and FULL MC, the electron is identified, reconstructed and selected on the basis of certain conditions that are imposed to ensure that only genuine electron candidates which fulfill the kinematic and geometrical acceptance requirements of the analysis are selected. These criteria have to be modeled in the form of electron reconstruction, identification and selection efficiencies in the FAST MC if it is to emulate the detector effects correctly. For example any p_T or energy (E) dependent electron efficiency shapes the electron p_T and m_T distributions and the electron resolution depends on the detector η (pseudorapidity), so it is imperative that these efficiencies are modeled well.

A detailed look at the factors that make electron efficiencies important:

1. Geometric acceptance - An electron cluster can only be reconstructed if it is present in the fiducial regions of the calorimeter. Clusters that fall inside the poorly instrumented intermodular (or phi-crack) regions of the calorimeter, partially or entirely, are often reconstructed with an incomplete amount of information and thus possess a bias.

2. Non-uniform Detector efficiency - Physical imperfections of the detector and the presence of uninstrumented or passive material in front of the detector could make some regions more efficient than others.

3. Dependence on SMT - The requirement of at least one SMT hit on the electron tracks for purposes of track reconstruction is only feasible if the track actually passes through the SMT. Besides, the efficiency of the SMT could depend on the angle of incidence of the particles.

Electron efficiencies depend not only on the single electron but also depend strongly on the information carried by the rest of the event. For example the "amount" of hadronic activity in an event influences the electron reconstruction and ID efficiencies. This is described by the scalar E_T (SET) of the event which is a measure of the total transverse energy flow in the event. The orientation of the hadronic activity with respect to the electron can also impact its reconstruction as shown in 5.1. The powerful variable of $u_{\|}$ is used to describe this effect. The $u_{\|}$ is defined as the component of the recoil vector lying in the direction of the electron. Hence our electron efficiencies are built on a per-event basis which takes into account the correlations existing between the electron and the rest of the event.

The description of the electron efficiencies in the FAST MC simulation is rather complex. We follow a step-by-step approach to build our model. With the help of single electrons we model the basic effects like geometrical acceptance, angular effects of the detector, efficiencies dependent on the transverse momenta of the particles, etc. Then we add the "perturbative effects", they are small variations to the model based on the effects from the additional activities in the event as seen by the entire calorimeter. These effects are parameterized as a function of

SET and the electron p_T. These additions are followed by another iteration of refining the efficiency model by taking into account the relative orientation of the hadronic activity and the electron, in the form of a parameterization as a function of $u_{\parallel}$.

The initial studies of the p_T dependences of the electron efficiencies are done with the help of single electron FULL Monte Carlo (MC) events. These are simple counting experiments performed conveniently since the generator-level and reconstructed-level information about the MC electrons is known well. The perturbative effects due to the "rest of the event" are also derived from FULL MC events. This is because the FULL MC model is rather detailed and provides a lot of information on the correlations between the different observables like $u_{\parallel}$ and SET. It is not possible to obtain this from data alone. However since the efficiency model has to be tuned to reflect the effects as seen in real data in the end, there is a final accounting of the p_T-dependences using a data-driven method.

Another factor that needs to be considered here is that in our step-by-step model, where we incorporate the effects from one observable at a time, the kinematics of the $Z \rightarrow e^+e^-$ production and decay lead to correlations between the different observables. For example using a p_T-dependent-only electron efficiency to generate $Z \rightarrow e^+e^-$ events causes the observed electron efficiency to have a $u_{\parallel}$ dependence and vice versa. Similarly any SET dependent efficiency will be a strong source of an apparent $u_{\parallel}$ dependence, as a result of an interplay between the efficiency model and the kinematics of the event. Hence these correlations lead to double or multiple counting of the inefficiencies when building the efficiency model with one observable at a time. This "double counting" needs to be removed. This is done by considering the ratios of data to FULL MC efficiencies

and then refining the apparent efficiency in the FAST MC to make it look like data.

Let us now look at the geometrical acceptance conditions for the electrons and the different efficiencies employed for the electron reconstruction and identification in more detail. However, first let us read about the simulation of the primary vertex in the parameterized Monte-Carlo.

13.2 Primary Vertex Simulation

We require that the primary vertex of events lie within $|z| < 60$ cm and the electrons be centrally located (i.e. $\eta_{det} < 1.05$) for the final analysis. Since the electron η_{det} depends on its physics η (η_{phys}) and position of the primary vertex , it is necessary to have a model for predicting the primary vertex distribution in the FAST MC. The shape of the luminous region depends on the shapes of the p and $\bar{p}$ bunches and on the β_x^* and β_y^*[1] of the interaction region. This translates to the width of the primary vertex distribution (σ_z) depending on the run range and instantaneous luminosity. The σ_z is determined from the zero bias (ZB) events collected from each of the 15 data taking epochs, each epoch differing from the other on the basis of the trigger list and change in the luminosity electronics. The primary vertex distribution (z_{vtx}) from each of the data taking epochs is parameterized and expressed with the help of three parameters [135]. This parameterization is used to simulate the z_{vtx} in the FAST MC.

[1]The β function is a measure of the beam width. This amplitude function details how the beam changes around the accelerator. There are separate β functions for the x and y planes. The square root of β_x^* is proportional to the beam's x-axis extent in phase space.

13.3 Electron Geometrical Acceptance

For the W mass measurement, we require that the electrons be located in the fiducial region of the CC. This means that we impose a fiducial requirement for the reconstructed EM cluster to be located away from the EM module boundaries. This requirement retains the interior 80% in azimuthal space of each module. Figure 13.1 shows the end view of the central calorimeter and the detailed design of the EM calorimeter in the vicinity of the edges of two modules. Near the very edge of each EM module, there are no electrode pads and the electric field is not uniform. Due to the shortening of the time for charge integration in Run II, we collect a much smaller fraction of the total charge. Therefore, the electron response near the boundary region is more degraded in Run II than in Run I.

The EM section of the CC consists of 32 modules azimuthally, hence each module is about $2\pi/32 \sim 0.2$ radian wide in ϕ and covers the CC region of -1.2 $\leq \eta \leq 1.2$. The EM1, EM2 and EM4 layers of an EM module possess 2 readout cells each, at a "fixed η" width of 0.1. The EM3 layer contains four readout cells at a "fixed η" width of 0.1, so each cell is 0.05 radian wide both in η and ϕ. A special intra-module variable called PhiMod=fmod$(32\phi/2\pi, 1.0)$ is used to denote the ϕ of the cluster or track position within a module of unit width. The central value of PhiMod (0.5) is thus the inter-cell boundary, the values close to 0 and 1 are the two edges of the module boundaries.

The cluster position (ϕ_{EM}) is given by the ϕ of the reconstructed EM cluster while the track position (ϕ_{trk}) is defined by the extrapolation of the electron trajectory from the primary vertex to the third layer of the EM calorimeter (EM3).

There are two effects resulting from the geometrical structure of the calorimeter modules.

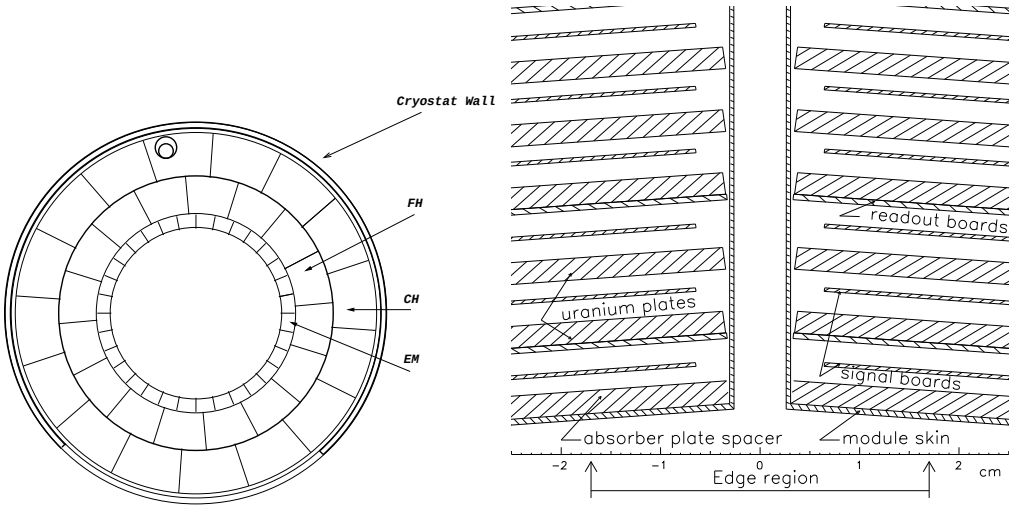

Figure 13.1. Left: End view of the central calorimeter showing the arrangement for electromagnetic (EM), fine Hadronic (FH) and coarse hadronic (CH) modules. Right: Construction of central calorimeter EM modules in the region near module boundaries. Signal boards have the electrode pads for signal collections, readout boards carry traces bringing the signals to the module ends

1. PhiMod Efficiency: Due to the arrangement of the electrode pads and the non-uniform electric fields, the efficiency to find electron clusters within a module varies with the ϕ of the incident particle [136].

2. PhiMod Shift (or bias): Due to the current EM clustering algorithms and the electronics used, the azimuthal angle ϕ_{EM} of the electron cluster, calculated from the electron energy deposited in the third EM layer, is biased towards the center of the module [137, 138].

An understanding of the PhiMod effect (both efficiency and bias) is important for understanding the measured Z boson transverse momentum (p_T^Z) distribution, which in turn affects both the electron transverse momentum (p_T^e) and recoil

system p_T distributions. Both the efficiency and bias are measured using electrons from $Z \rightarrow e^+e^-$ decays. After extrapolating the track to the EM3 layer we determine the probability for matching it to a reconstructed EM cluster, thus giving us the efficiency. We also measure the distance between the extrapolated track and EM cluster positions which gives us an idea on the bias present.

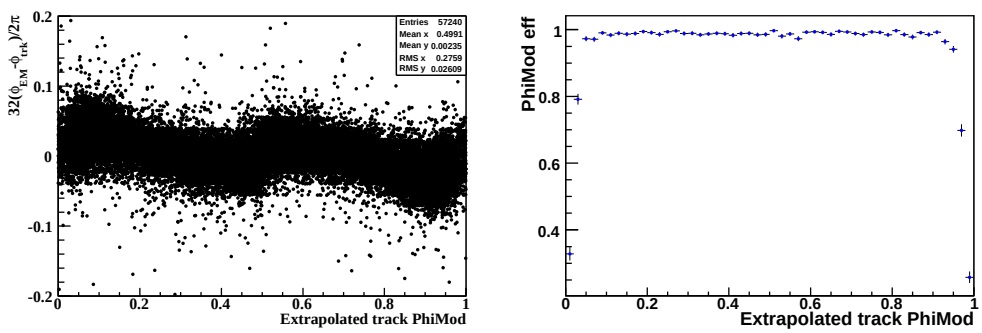

Figure 13.2. Left: Difference between ϕ_{EM} and ϕ_{trk} (fmod$(32(\phi_{EM} - \phi_{trk})/2\pi, 1.0)$) in module units vs track Phimod (fmod$(32\phi_{trk}/2\pi, 1.0)$). Right: PhiMod efficiency as a function of the extrapolated track PhiMod

Figure 13.2 on the left shows the PhiMod bias, namely fmod$(32(\phi_{EM}-\phi_{trk})/2\pi, 1.0)$ vs the PhiMod of the extrapolated track position across the module (fmod$(32\phi_{trk}/2\pi, 1.0)$). Since ϕ_{trk} is unbiased, we can see a strong tendency for the ϕ_{EM} to move towards the center of the module. Figure 13.2 on the right shows the efficiency of finding an EM cluster vs PhiMod in data. For the final analysis, we only keep electrons with $0.1 <$ PhiMod < 0.9. For more details on the phimod efficiency and bias

please refer to [139].

13.4 Trigger Efficiency

The DØRun IIa $W \rightarrow e\nu$ data taking epoch spanned four trigger periods. The trigger selection efficiencies are parameterized using the "tag-and-probe" method and are shown in Figure 13.3 for all the four trigger periods.

The "tag-and-probe" method considers one electron from the $Z \rightarrow e^+e^-$ events as the "tag electron", this electron is required to satisfy all of the required selection criteria (both loose and strict cuts). The other electron is required to satisfy the loose selection criteria that are not correlated with the selection cut that is being tested first, for it to be called a "probe". After passing the initial selection the probe is now tested for qualifying the particular selection cut for which the efficiency is being made. The efficiency is plotted as the ratio of the number of events that qualify to the total number of events.

In the case of trigger efficiency, the tag electron is required to pass all the standard electron selection criteria and the trigger requirements. Then the probe electron is checked to see if it satisfies the trigger requirements or not. To pass a trigger requirement an electron must have a matching trigger object at each of the trigger levels (L1/L2/L3) which passes all the cuts for the corresponding trigger. The electron candidate to trigger object matching requirements are $\Delta R = \sqrt{\Delta\eta^2 + \Delta\phi^2}$ for L1, L2 and L3. The correct trigger efficiency for the FAST MC is obtained by sampling from the measured efficiency distributions.

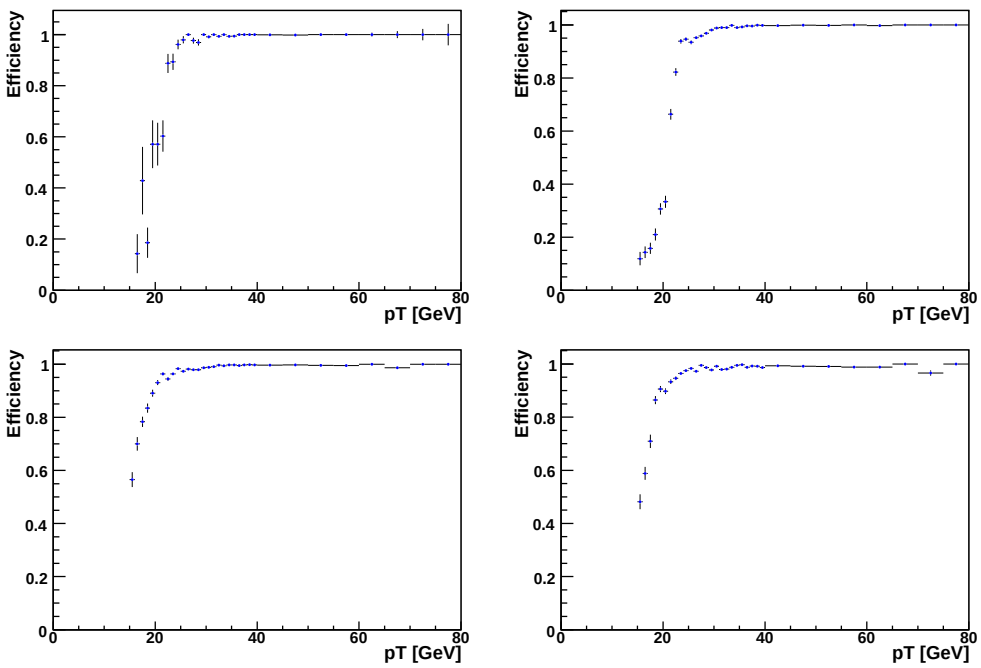

Figure 13.3. Trigger efficiency vs. electron p_T for four different trigger periods. Top left: v8-11, top right: v12, bottom left: v13 and bottom right: v14

13.5 Preselection Efficiency

This efficiency quantifies the probablity for reconstructing electrons as calorimeter clusters on the basis of EM fraction and isolation cuts only. No shower shape cuts are included in the selection criteria.

We use the $Z \rightarrow e^+e^-$ events collected from real data using the single EM trigger for deriving this efficiency. The tag electron for this efficiency is a well identified electron matched to a track, lies in the CC or EC calorimeter and has fired the electron trigger. The probe is an isolated track satisfying the isolation conditions in the tracker with a $p_T > 12$ GeV. The extrapolated track position

should lie either in the CC or EC region. The invariant mass of the EM cluster and the extrapolated track should lie between 70 and 110 GeV. This probe is then required to find a matching EM cluster with $p_T > 15$ GeV in $\Delta R = \sqrt{\Delta\eta^2 + \Delta\phi^2}$ space. The fraction of such events give the efficiency.

Figure 13.4 shows the preselection efficiency. For the purposes of this analysis it is fairly linear in the CC region from -1.05 $< \eta_{det} <$ 1.05. It drops off at the extremities of the CC ($|\eta_{det}| > 3.0$) and in the very forward EC regions. The dependence of the preselection efficiency on η_{det} is simulated in the FAST MC. The p_T and E_T thresholds used to measure the efficiency are well below the analysis threshold and have no impact.

13.6 EMID (HMatrix) Efficiency

This model of the electron identification efficiency quantifies the probability for reconstructing electrons on the basis of their EM fraction, isolation and shower shape requirements. The electrons being tested have already been reconstructed partially as clusters and have fired the single EM trigger in the real data. This modeling is done in two steps.

We first derive the electron efficiency as a function of detector η (η_{det}). For this electrons from $Z \rightarrow e^+e^-$ events are used. Electrons identified as track matched clusters (in the CC or EC regions of calorimeter and with $p_T > 25$ GeV) are considered as the tag whereas clusters matched to tracks are considered as the probe. Each probe is then tested to see if it satisfies the HMatrix criteria. The efficiency is defined as the fraction of events which pass the HMatrix requirement.

Figure 13.5 shows this HMatrix efficiency as a function of η_{det} and this histogram is used in the FAST MC to simulate the average HMatrix efficiency. It can

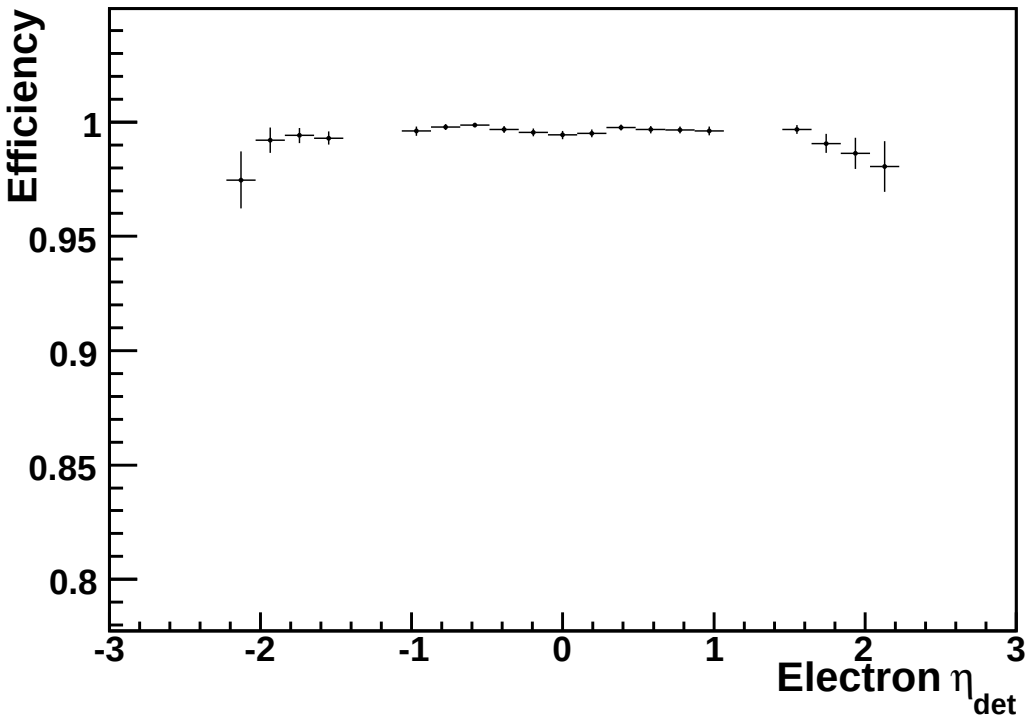

Figure 13.4. The efficiency for reconstructing a loose EM cluster. The efficiency is almost flat over the η region used here ($|\eta_{det}| < 1.05$)

be seen that the efficiency drops a little towards the forward EC regions. However since the dependence of the simulation on the detector eta is small, the drop does not have a significant impact.

The efficiency is re-derived as a function of electron p_T in different bins of detector η. This is done via a simple counting method, uses single electron FULL MC events and is defined as the number of events that pass all the identification (ID) requirements including EMF, isolation and HMatrix to the number which pass the preselection.

Figure 13.6 contains a set of diagrams showing this efficiency. Evidently there

are non-trivial inefficiencies and kinematic variations over the range of η.

As mentioned earlier, this electron ID efficiency is derived from simulated single electrons and not $Z \rightarrow e^+e^-$ events as in the earlier case. Hence the additional contribution from the effects due to the rest of the event comes by way of perturbative corrections and is explained in the Section 13.10.

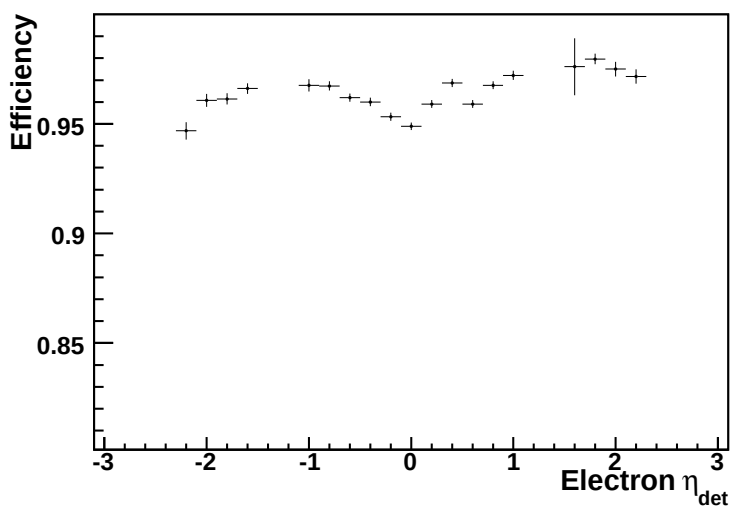

Figure 13.5. The η_{det} dependence of the final EM ID requirements relative to the preselection

13.7 Track Matching Efficiency

This efficiency characterizes the probability of the electrons to be reconstructed as a cluster matched to a track. The electrons being tested have already been partially reconstructed as clusters after qualifying all the calorimeter cuts (EM

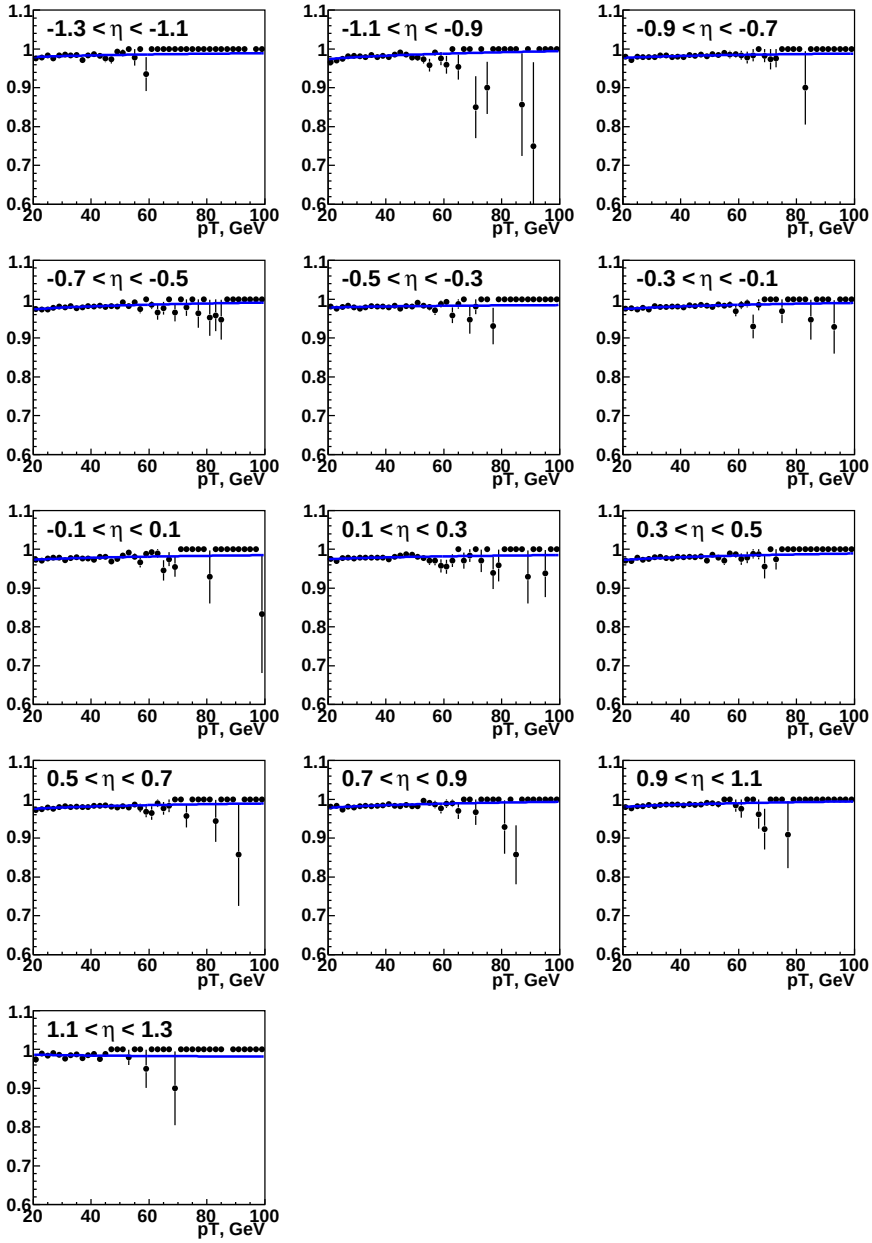

Figure 13.6. The η and p_T dependence of the EMID efficiency for single electrons relative to the preselection efficiency. Each pane shows the p_T efficiency in a given η bin. The bins are 0.2 units wide in η and cover the range $-1.3 \leq \eta \leq 1.3$, and the horizontal axes run from 20 GeV to 100 GeV

fraction, isolation, HMatrix). The track matching requirement is actually a combination of the efficiencies to reconstruct a track, match the track to a cluster and for the track to have a SMT hit. The probe track is required to have a SMT requirement and be located in the immediate vicinity of the cluster. The selection does not include a cut on the p_T of the track hence avoiding the efficiency of the cut. The tracking resolution and the p_T are modeled separately in FAST MC.

This modeling of the efficiency is also performed in two steps. We first quantify the efficiency as a function of detector η and primary vertex (vtx_z). The tag is an electron from $Z \rightarrow e^+e^-$ collider data that has satisfied all the criteria for a track matched electron. So it is located in the CC or EC regions of the CAL, has $p_T >$ 25 GeV and has fired the single EM trigger. The probe is a reconstructed cluster that has $p_T > 25$ GeV. It is then required to match to a track. The efficiency is given by the fraction of events in which there is a second track match.

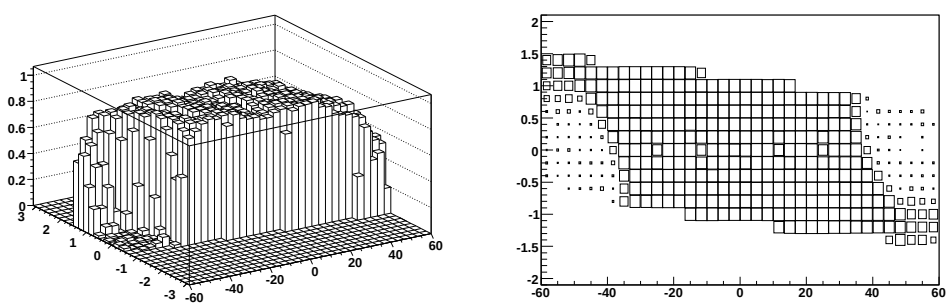

Figure 13.7. Left: The tracking efficiency as a function of η and vertex z position shown as a lego plot. Right: Shown as a box plot

Figure 13.7 shows this electron efficiency. As seen, this is a very important effect, mostly dependent on geometry. The SMT hit requirements are necessary for track reconstruction and points to the fact that tracking detectors seem to have a higher hit efficiency for non-normal tracks.

The second part of this efficiency involves its re-derivation showing its dependence on electron p_T in different bins of detector η. This is done via a simple counting experiment using the same single electron FULL MC events as in the EMID efficiency. The resulting efficiency is defined as the number of single electrons which pass the combined calorimeter and track requirements divided by the number which pass just the calorimeter requirements.

The efficiency has been shown in Figure 13.8. We notice significant ineffiencies and differences in p_T over our range of η. As in the EMID efficiency, the modeling of this efficiency also incorporates the effects from the "rest of the event". These are introduced as small corrections later on in Section 13.10.

Both the track matching efficiencies described here have been modeled as a function of η. Hence the inefficiencies related to η come in twice as a result of double counting. These η-related inefficiencies are removed by renormalizing the individual curves in Figure 13.8, so that they all predict the same efficiency at electron $p_T = 45$ GeV.

13.8 Overall Hadronic Activity (SET) Efficiency

This efficiency takes into account the effect of the "rest of the event" on the electron. Thus it contains the contributions from the hadrons that recoil against the vector boson (W or Z) and contributions from the multiple interactions of the spectator quarks and additional $p\bar{p}$ interactions. This hadronic activity is present

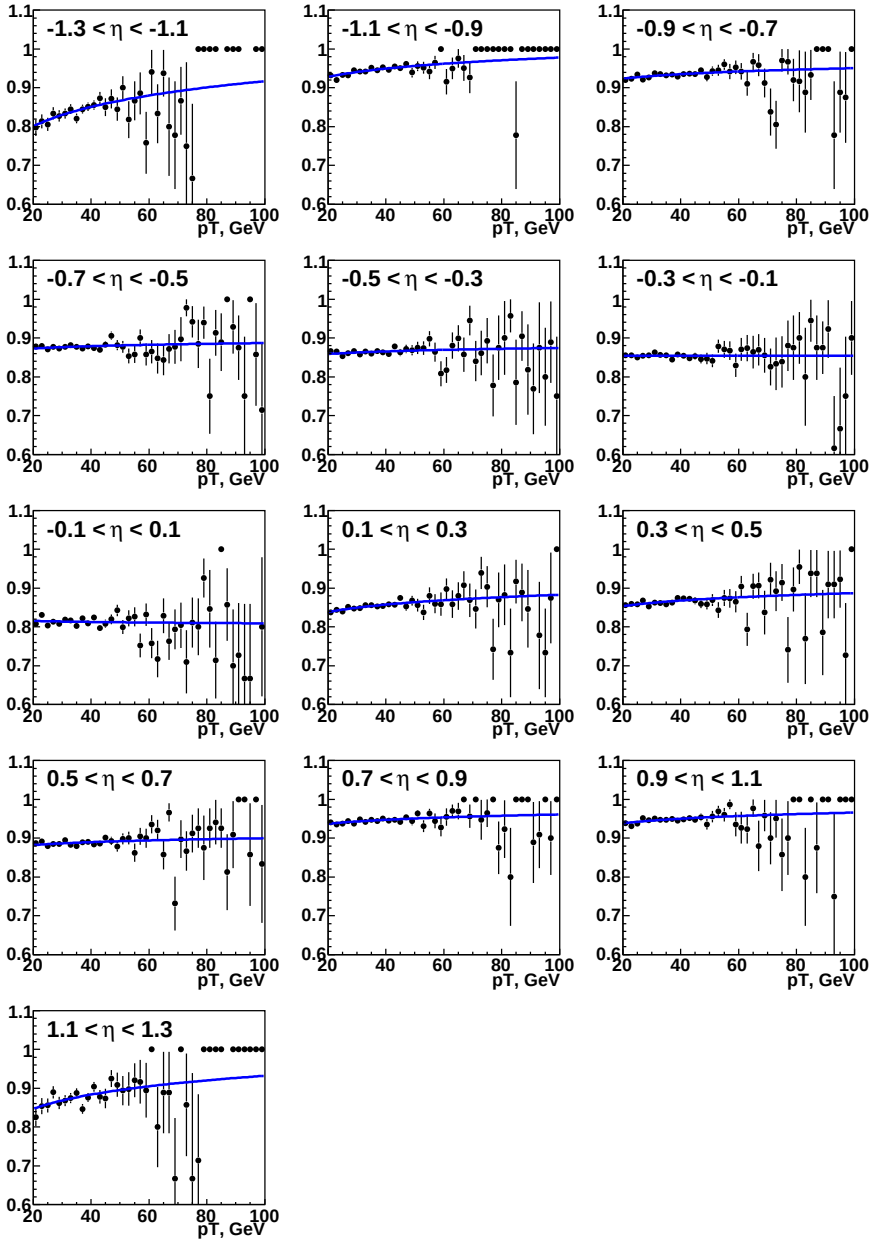

Figure 13.8. The tracking efficiency as a function of η and p_T determined using single electron events. Each panel shows the p_T efficiency in a given η bin. The η bins are 0.2 η-units wide and cover the range $-1.3 \leq \eta \leq 1.3$, and the horizontal axis in each figure runs from 20 GeV to 100 GeV

over large regions of the detector and so can easily overlap with the energy cluster of an electron and obscure its signature. We use the scalar E_T (SET) to quantify this hadronic activity in an event. Scalar E_T of an event is defined as the energy of all the calorimeter cells in the plane transverse to the beams, except those that belong to the electron clusters.

An initial estimate of the SET efficiency is in the form of a per-event efficiency as a function of the SET of the ZB events used for the overlay in the FULL MC. The advantage of using the FULL MC is that the SET contribution from the ZB event does not reduce the apparent SET as it comes from the ZB events only and is known beforehand. However, even though we construct the model using the SET of the ZB events, all parameterizations apply to the total SET of the event.

Thus FULL MC $Z \to e^+e^-$ events are used with the standard recoil (u_T) cut relaxed to 30 GeV and the reconstruction efficiency is defined simply as the number of selected events divided by the total. This efficiency is derived as a function of the SET of the ZB event on a per-event basis. However the implementation of this efficiency in the FAST MC requires one to consider the combined effects of the other electron efficiencies and an initial estimate of the $u_{\parallel}$ efficiency that are already present in the FAST MC. Hence the parameterization of the SET efficiency uses a simple polynomial function with coefficients. The coefficients are adjusted so that the SET efficiency of the FAST MC as a function of the ZB SET matches that observed in the FULL MC. This procedure is done separately for the $Z \to e^+e^-$ and $W \to e\nu$ events. The resulting polynomials are shown in Figure 13.9.

However this simple modeling of the SET efficiency turns out to be precise enough for obtaining closure in the W mass measurement but not in the measure-

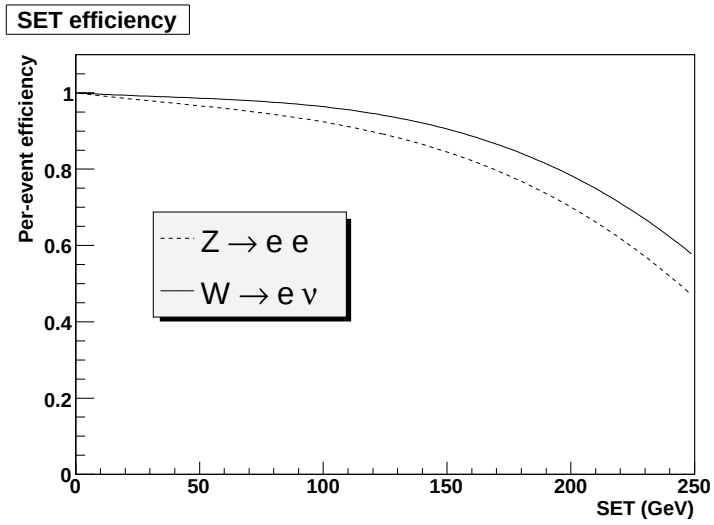

Figure 13.9. The event reconstruction efficiency as a function of SET shown separately for Z and W FULL MC events. The polynomial fits are used in the FAST simulation

ment of the W width. This arises due to the fact that the width measurement is very sensitive to the high p_T tail of the electron (p_T^e) or transverse mass (m_T) distributions.

It takes a trivial discussion to understand that the reconstruction of a high-p_T electron (say $p_T = 80$ GeV) is easier since it is more robust against the additional, unrelated hadronic energy in the event, compared to an electron with $p_T = 25$ GeV. The same amount of hadronic energy will have less impact on the shower shape or the estimate of the cluster position of a high-p_T electron cluster than a low p_T one, when superimposed on both of them.

Thus this simple efficiency model needs refinement. Small perturbations in the form of multiplicative correction factors depending on electron p_T and SET are added to this per-event efficiency. These perturbative corrections are obtained

for each electron (one for W, two for Z) by comparing the FULL and FAST MC as a function of ZB SET, in different bins of the p_T of reconstructed electrons. They are derived separately for the Z and W events. The resulting per-electron correction factors have been shown in Figure 13.10.

While some aspects of the shape of the correction functions might be trivial to understand, some might look confusing. This is because we are dealing with different competing physical effects. As we know, the SET contribution from the spectator quarks and the additional $p\bar{p}$ collisions in the same bunch are not correlated to the hard scatter that produces the vector boson and hence the electron direction. Hence an increase in the SET from these sources is likely to drown the electron signature. This is the effect seen in most p_T bins. However there is another underlying effect. This arises from the fact that the SET contribution from the recoil (due to the hard scatter) is correlated with the relative direction of the electron and the recoil. The vector boson tends to be highly boosted when the SET contribution from the recoil is large enough. In this event, if the electron is emitted in the direction of the travelling boson, the event possesses high electron p_T along with high SET and the recoil is directed away from the electron. Thus the effect of high p_T electrons having high SET efficiency are seen. In the alternative case, electrons are emitted against the boson direction. This leads to a high SET contribution but low electron p_T from the event and the hadronic recoil is closer to the electron on an average, thus drowning its signature. We now see the effects of low p_T electrons having low SET efficiency. We observe this in most bins of Figure 13.10.

As mentioned earlier, the incorporation of the p_T^e dependence into the SET efficiency has a minor impact on the W mass analysis. In addition the high-mass

events responsible for the shape of the high p_T correction distributions do not impact the W mass because these regions are far away from the Jacobian edge, the relevant region for the W mass. These effects are however non-trivial for the W width which includes the tail of the transverse mass distribution in its measurement. Thus the efficiency at high p_T and the uncertainties from data/MC in the relative weights of the different contributions to the SET are important for the W width analysis.

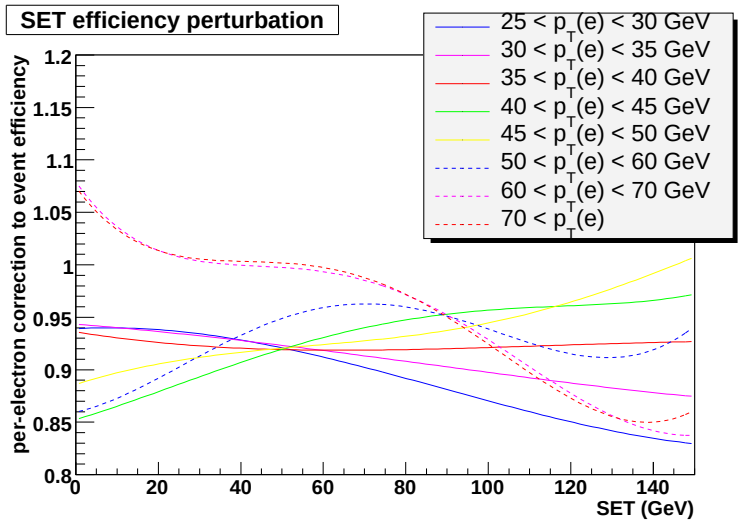

Figure 13.10. The electron p_T and SET based correction factors to the SET parameterization of event efficiency. Each curve corresponds to a different p_T range, and the horizontal axis is the SET

13.9 Recoil Related ($u_{\parallel}$) Efficiency

The effects described in the previous section arise mostly due to the overall energy content of the detector and are largely uncorrelated with the boson. However the proximity of the hadronic recoil to the electron also interferes with its identification and reconstruction. This impact of this is assessed by means of the $u_{\parallel}$ which is defined as the component of the recoil in the direction of the electron. The $u_{\parallel}$ efficiency and a "scaling law" that accounts for the difference between Z and W electrons are parameterized from the $Z \rightarrow e^+e^-$ and $W \rightarrow e\nu$ data and FULL MC samples.

The $u_{\parallel}$ efficiency is described for positive and negative values of $u_{\parallel}$. Figure 13.11 shows the $u_{\parallel}$ efficiency in data for the Z and W events. Negative values of $u_{\parallel}$ indicate that the recoil is directed almost opposite to the electron, hence it does not interfere with the electron identification and the efficiency is about 90%. Positive values of $u_{\parallel}$ imply that the recoil is close to the electron direction and hence the efficiency of identifying and reconstructing the electron decreases as the $u_{\parallel}$ component increases.

In the FAST MC an electron efficiency dependent solely on $u_{\parallel}$ will not work because the presence of the p_T and SET dependent efficiencies together with the kinematics of the vector boson decay leads to an apparent $u_{\parallel}$ related inefficiency. Events possessing FSR photons also lead to $u_{\parallel}$ inefficiencies. Events which have FSR photons possessing energies comparable (or greater than) to the energy of the mother electron might get misconstructed as electron clusters and eventually fail event selection thus counting as an inefficiency. However their recoils will possess large contributions from $u_{\parallel}$ due to the inclusion of the FSR-emitting electron. Thus the $u_{\parallel}$ efficiency needs to be modulated to take into account these

inefficiencies.

For the parameterizations in the FAST MC [140], the value of the "kink point" (between the flat line and slope) is determined from data (or FULL MC in the case of FULL MC analysis) and the slope is adjusted in such a way that the slope of the apparent (overall) $u_{\parallel}$ efficiency is the same in FAST MC as in data (or in FULL MC). In Figure 13.11, the agreement for the Z is very good over the full range. The non-trivial features at negative $u_{\parallel}$ are described well by the FAST MC. The "dip" at negative $u_{\parallel}$ is a result of the combined effects of the SET efficiency and FSR photons which result in some inefficiency. The agreement for the W is also remarkable. The minor disagreements beyond -15 GeV $< u_{\parallel} <$ 15 GeV are outside the range of our M_W analysis.

13.10 Final Efficiency Corrections Based on Electron p_T: Tag and Probe

We come to the end of modeling the different aspects of our electron reconstruction and identification inefficiencies. At this point we expect our model to describe all geometrical and p_T-dependent aspects of the electron efficiencies. For modeling the effects related to the p_T-dependences, we have used the detailed simulations extensively. For e.g. the correlations between the electron p_T, the electron η_{phys} and the event SET have been modeled in details in the FAST MC. However these tuning procedures cannot be repeated in data, mainly because we do not have the generator level information and there aren't enough events for detailed studies and parameterizations.

However since we've developed a FAST MC that models the FULL MC detector efficiencies well enough, we perform a check to see if there are any differences between the data and FULL MC, as regards to the p_T^e dependence of the selection

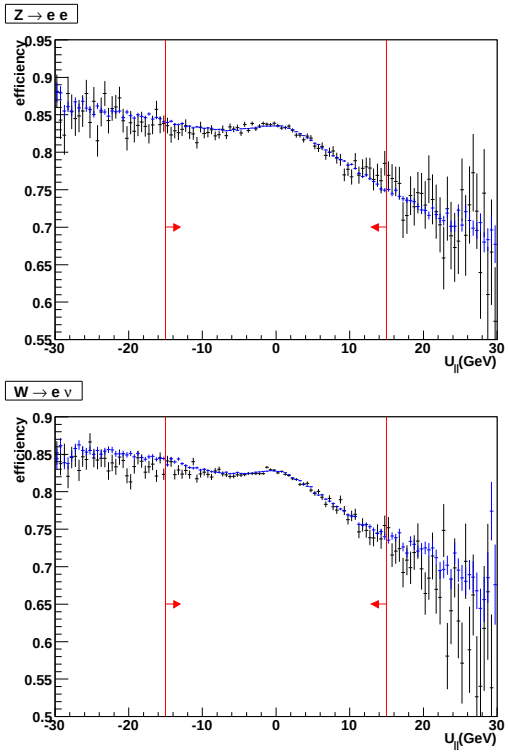

Figure 13.11. The efficiency as a function of $u_{\|}$ in FULL and FAST MC. Excellent agreement is found

efficiency. Any small discrepancies between the data and FULL MC simulation are parameterized as a function of electron p_T and η and incorporated into the FAST MC, in the form of a corrective ratio, for a better match.

We use the standard tag and probe method again on $Z \rightarrow e^+e^-$ events. We compare data and FULL MC and compare the p_T dependence of the efficiency. Figure 13.12 shows the p_T dependence of HMatrix for CC electrons in the data and FULL MC (left) and the corresponding ratio (right). It is evident that both the data and FULL MC have the same p_T dependence to within errors from limited data statistics and hence their ratio can be fit with a straight line with a good

χ^2/dof. A similar behavior is seen for the track match as shown in Figure 13.13.

With these tunings we can rest assured that the p_T dependence of the efficiencies measured from FULL MC is valid for the data measurement, over the range of interest.

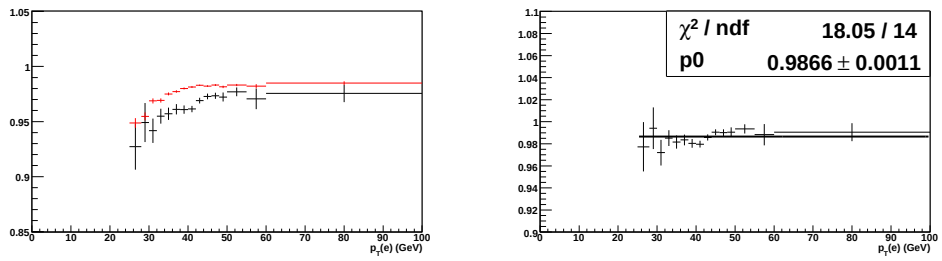

Figure 13.12. Left: p_T dependence of HMatrix for CC electrons in data(black) and FULL MC(red). Right: Ratio between the black and red curve in the left plot

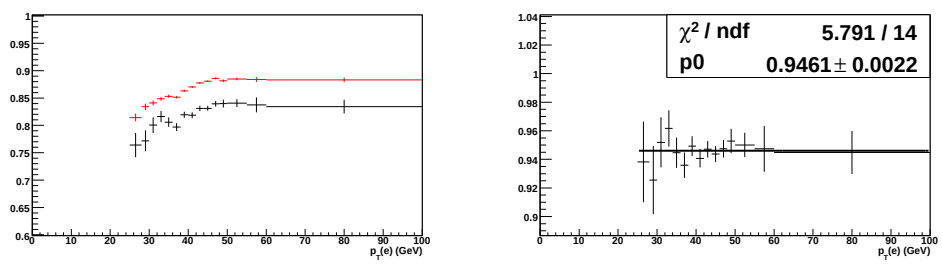

Figure 13.13. Left: p_T dependence of track match for CC electrons in data(black) and FULL MC(red). Right: Ratio between the black and red curve in the left plot

CHAPTER 14

SIMULATING THE ELECTRON ENERGY IN THE PMCS

14.1 A Brief Introduction

This chapter details the various steps undertaken to model the energy of the electron in the FAST MC for the collider data analysis. Since the FAST MC is a parameterized detector model, the generated (true) energy of the electron is smeared with the help of parameters to give a value corresponding to the reconstructed energy in data. Some corrections are also added. The chapter begins with a recap of the reconstruction of the electron energy in data and then details the parameterization of the electron energy response and resolution. The contributions from the underlying energy and FSR photons have also been described. The last section deals with the impact of the non-linearity of the energy-loss functions on the analysis.

14.2 Reconstruction of the Electron Energy in Data

As we have read earlier, both in collider data and FULL MC, energy clusters corresponding to electrons in the calorimeter are reconstructed by DØRECO to determine the electron energy in a W event. Energy content of the cells in all the four EM layers (EM1, EM2, EM3, EM4) and FH layer of the calorimeter are added up. This approximately corresponds to a simple cone algorithm that

considers the energy deposition in a cone of radius $\Delta R = 0.2$ in the $\eta - \phi$ space

$$\Delta R = \sqrt{\Delta\eta^2 + \Delta\phi^2} \tag{14.1}$$

This reconstructed or measured energy includes the effects of the detector on the incident electron, the non-electron energy (e.g. from recoil), the effects of zero suppression, energy lost due to the presence of significant amounts of uninstrumented material in front of the calorimeter, the multiple parton interactions, pile up and due to final-state radiation of photons. During the reconstruction process by DØRECO corrections are made to account for some of the effects due to zero suppression and energy lost in the dead material.

14.3 Parameterization of the Electron Energy in the FAST MC

In the FAST MC, the reconstructed (measured) energy of the electron is modeled with the help of some parameters. The effects of the detector that need to be considered here are its response to the energy of the electron, its smearing effect on the energy (resolution) and some other adjustments or corrections to the detected energy. The final, smeared energy is the corresponding equivalent of the reconstructed energy in data. The detector effects are applied to electrons generated from PYTHIA or RESBOS. Hence the various components that comprise the modeling of the electron in the detector can be expressed in the following way:

$$E_{\text{meas}} = E_{\text{response}} + E_{\text{resolution}} + \Delta E(\mathcal{L}, u_{\parallel}) \tag{14.2a}$$

which can also be expressed as follows:

$$E_{\text{meas}} = R_{EM}(E_0) + \sigma_{EM}(E_0) + \Delta E(\mathcal{L}, u_{\|}) \tag{14.2b}$$

here $R_{EM}(E_0)$ is the response and $\sigma_{EM}(E_0)$ is the resolution of the calorimeter. ΔE is the non-electron energy (from recoil) measured as part of the electron energy and needs to be subtracted from the measured energy.

14.3.1 Parameterization of the Electron Energy Response

We adopt a linear model to describe the electron energy response of the calorimeter in the FAST MC. It is given as follows:

$$E_{\text{response}} = \alpha \times E_{\text{true}} + \beta \tag{14.3}$$

α is the parameter denoting the scale while β is the offset for the electron energy. E_{true} is the energy that the electron is generated with in the FAST MC. However the above linear expression for describing the energy response is not the most general form of the parameterization.

Several sources can introduce non-linearities in the response of the detector to the electron energy thus yielding different values of the scale and offset. Most significant among these are the underlying event and the energy lost due to the material in front of the calorimeter. Extensive calibrations (*in-situ* and offline) that account for these two effects have been done beforehand using different data samples including the $Z \to e^+e^-$ sample. They are applied prior to the reconstruction procedure in data and FULL MC and are also modeled in FAST MC before the effects of the detector on the generated electrons are studied.

If the above calibrations are functioning effectively we should obtain a value of scale ~ 1 and offset ~ 0. Any large deviation from these values suggests a miscalibration or incorrect modeling of the electron energy.

The parameters α and β are determined with the help of two body decay kinematics. The invariant mass from a two-body decay can be determined from the decay products as:

$$M^2_{\text{meas}} = 2E_1^{\text{meas}} E_2^{\text{meas}}(1 - \cos\gamma) \tag{14.4}$$

where $E_{1,2}^{\text{meas}}$ are the measured energies of the two decay products and γ is the opening angle between them.

Substituting the expression for E_{meas} into 14.4 and assuming $\beta << (E_1^{\text{meas}} + E_2^{\text{meas}})$ we obtain:

$$M_{\text{meas}} \sim \alpha \times M_{\text{true}} + \beta \times f_Z \tag{14.5}$$

where f_Z is a variable that depends on the kinematics of the decay. Since the electrons from the Z decay are not monochromatic, it is possible to define the variable f_Z which relates the mass of the Z to the spread in electron energies from the Z decay. From the above equation 14.5 f_Z is expressed as follows:

$$f_Z = \frac{(E_1^{\text{meas}} + E_2^{\text{meas}})(1 - \cos\gamma)}{M_{\text{meas}}} \tag{14.6}$$

We notice that when β is small, f_Z is nearly equal to $\partial M_{\text{meas}}/\partial\beta$. Thus we see that the slope of the M_{meas} versus f_Z can be interpreted as the offset, implying that the sensitivities to β are dependent on f_Z.

In this way, the equation 14.5 relates the measured Z mass to both the scale and offset and also the true Z mass. Since α and β appear in a strongly correlated

way in E_{meas} they cannot be determined with the help of M_{meas} alone. The use of f_Z acts like an additional constraint and helps to separate the two terms for an independent determination of their values. The values of α and β are determined from events containing two-body decays for which M_{true} is known from other measurements.

The parameters α and β are determined with the help of physical observables derived from $Z \to e^+e^-$ data. Templates of kinematic distributions such as the invariant Z mass (M_Z) or p_T^e obtained from FAST MC are compared with the corresponding distributions from collider data. These templates of M_Z versus f_Z are obtained by varying both the scale and offset. The parameters α and β are then determined for the best tune and these describe the detector response to the energy of an electron. For a more detailed explanation of the method please refer to [141]. Figure 14.1 is a M_Z vs. f_Z distribution from FULL MC events.

14.3.2 Parameterization of the Electron Energy Resolution

The detector effects of smearing the incident energy of the electron is reflected by the resolution of the electron energy distribution. In the traditional sense of modeling the smearing effect of the calorimeter, the relative resolution is given as follows:

$$\frac{\sigma_E}{E} = \sqrt{C_{EM}^2 + \frac{S_{EM}^2}{E} + \frac{N_{EM}^2}{E^2}} \tag{14.7}$$

The term $\frac{\sigma_E}{E}$ represents the fractional energy resolution. The noise term (N_{EM}) accounts for the electronics noise, latent radioactivity from Uranium and the underlying events in the calorimeter. Due to its $1/E^2$ dependence in the resolution, it is an insignificant contribution at higher energies. The constant term (C_{EM}) incorporates the effects of imperfections in the relative channel-to-channel cali-

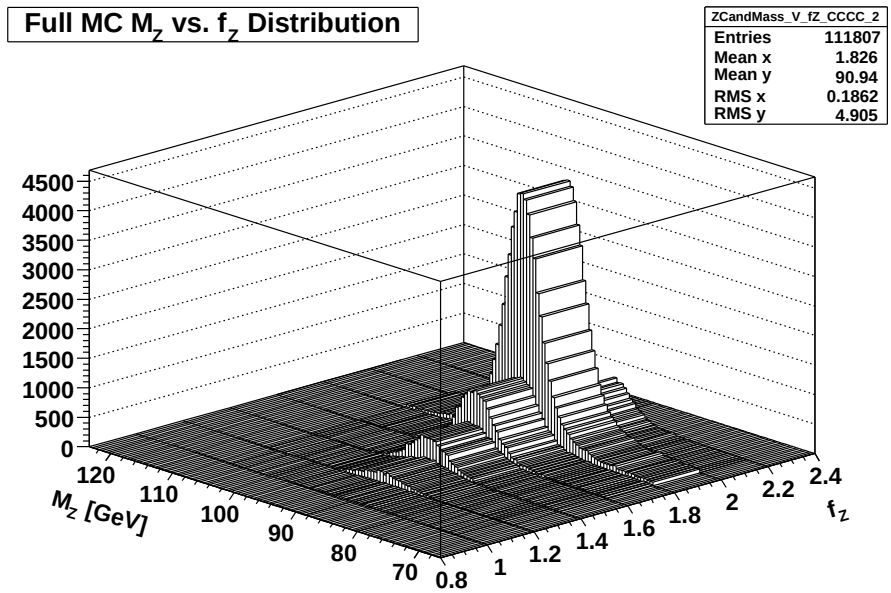

Figure 14.1. The distribution of M_Z vs. f_Z in FULL MC events

brations of the $\eta - \phi$ segmentations. Since this term is independent of energy, it does dominate at high energies. The sampling term (S_{EM}) accounts for the fact that we sample only a fraction of the total energy (signal) from the calorimeter. The effects of fluctuations in the shower development due to the material in front of the calorimeter are also included in this term. At high electron energies the contribution from the sampling term is suppressed due to its $1/E$ behavior.

However the effect of the significant amount of material present in front of the DØ Run II detector is to impart a dependence on the angle of incidence (η) and energy of the electron (E) to the sampling term of the calorimeter. Hence,

$$S_{EM} = \left(S_1 + \frac{S_2}{\sqrt{E}}\right) \times \frac{e^{S_{exp}/\sin\theta}}{e^{S_{exp}}} \tag{14.8a}$$

with

$$S_{exp} = S_3 - S_4/E - S_5^2/E^2 \tag{14.8b}$$

These parameters are tuned from special FULL MC $Z \to e^+e^-$ and J/ψ events. Once the resolution of the detector has been determined, its contribution is added to the energy of the electron in the following way:

$$E_{\text{meas}} = E_{\text{response}} + x * \sigma E + \Delta E(\mathcal{L}, u_{\parallel}) \tag{14.9}$$

where x is a random variable chosen from a gaussian distribution at zero mean and unit width. For a more detailed explanation of the method please refer to [142].

14.3.3 Parameterization of the Underlying Energy Corrections

Not all of the energy deposited in the calorimeter cells corresponds to the electrons. Contributions from the hadronic recoil, underlying event and additional energy from multiple interactions in the detector also creep into the electron window. Hence in the FAST MC simulation of the electron energy, this extra contribution needs to be subtracted from the smeared energy of the electron. This correction is dependent on the luminosity, pseudorapidity (η) and $u_{\parallel}$, the component of the recoil vector ($\vec{u}_T$) that is parallel to the direction of the electron. During reconstruction, the electron energy is also sensitive to the effects of zero-suppression when both the pure electron energy and the contribution from the additional energy in the detector are subject to the readout criteria involving zero-suppression in the calorimeter.

The compensation for the energy which does not belong to the electron but

lies beneath the electron window is done via an offset correction

$$\Delta E = \Delta UE_{\mathrm{rot}} / \cosh \eta \tag{14.10}$$

and is subtracted from the total smeared energy in the FAST MC. Here $\cosh \eta$ is the cosine of the electron pseudorapidity necessary to convert a transverse quantity (ΔUE_{rot}) to the total energy (ΔE).

The effect of zero-suppression arises from the fact that the presence of more energy in the electron window, some of which is non-electron related (such as underlying energy), pushes more calorimeter cells above the zero-suppression thresholds thus increasing the response of the detector to the electron.

The zero-suppression effect is eliminated with the help of two samples, one which contains the contribution from underlying events and is reconstructed using the zero-suppression and the other which is reconstructed using zero-suppression but does not contain the underlying events. The EM energy correction ΔUE_{rot} is the energy difference of the same electron from both the samples.

The underlying energy contributions are estimated by looking at the energy deposition in a 13 calorimeter cell tower lying adjacent to the cluster containing the electron energy but rotated from it by an angle $\Delta\phi$. Each rotated region is the same size in $\Delta\eta - \Delta\phi$ space as the EM cluster defining the electron and the centers of the adjacent regions are separated by five towers. The energy content from each region gives an idea of the non-electron energy deposition beneath the electron window, (denoted by ΔUE_{rot}). The value of ΔUE_{rot} for each event is stored in a 13×13 dimensional array binned in luminosity and $u_{\parallel}$. To avoid regions with enough energy that might cause the electron identification to fail, the ratio between the energy in the region to that of the electron in the event is

required to be less than 0.15. Figure 14.2 shows the transverse energy for a region of the calorimeter towers, $\Delta UE_{\rm rot}$.

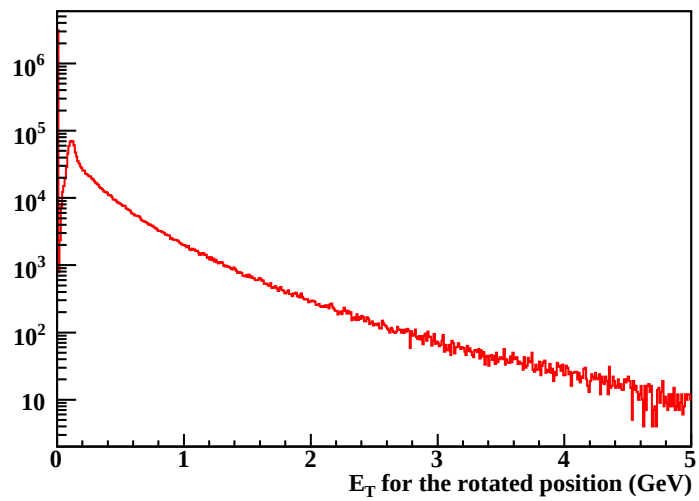

Figure 14.2. The $\Delta UE_{\rm rot}$ distributon in collider data

As expected, the mean values of $\Delta UE_{\rm rot}$ stored in the 13 $\times$ 13 bin array should increase in the higher bins which show an increase in luminosity. This is because an increase in luminosity signals more activity in the detector. Similarly the underlying energy should increase for larger values of $u_{\|}$, since more recoil energy finds its way under the electron window.

Figure 14.3 shows the average energy flow into a region as a function of instantaneous luminosity and the average as a function of $u_{\|}$.

The $\Delta UE_{\rm rot}$ correction in the FAST MC is implemented on a per-event basis, by choosing a value of $\Delta UE_{\rm rot}$ randomly for the event distributed according to the histogram in bins of luminosity and $u_{\|}$.

In the FAST MC simulation of the underlying energy contribution, a random value of ΔUE_{rot} is chosen from the energy information stored on a per event basis, for different values of luminosity and $u_{\|}$. This value is considered as the underlying energy beneath the electron window.

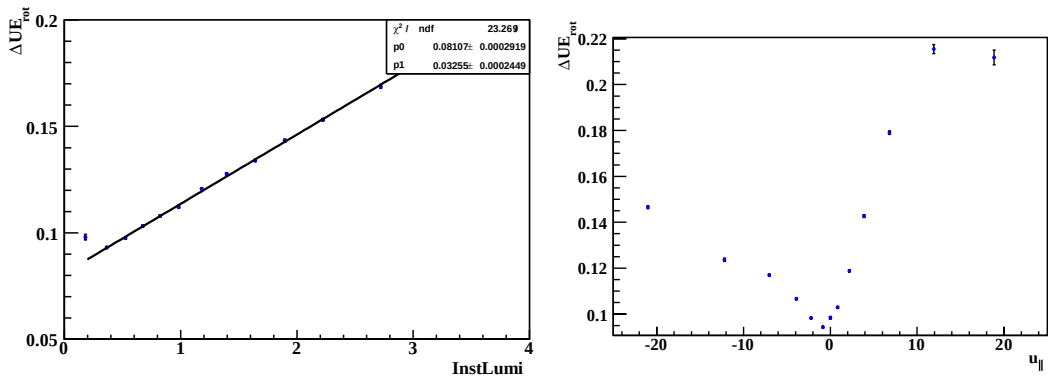

Figure 14.3. Average ΔUE_{rot} as functions of luminosity (left) and $u_{\|}$ (right) in collider data.

14.3.4 Parameterization of the Calorimeter Position Resolution

The electron energy in the calorimeter needs to have a matching track in order to distinguish it from photons and certify it as an electron cluster. The requirement of a track match also helps in lowering the background due to fake electrons. The direction of the matched track is assigned as the direction of the electron cluster. The position of the electron shower in the calorimeter is given by the centroid of the cluster which is determined as follows:

$$x_{\text{cal}} = \frac{\sum_i \omega_i \vec{x_i}}{\sum_i \omega_i} \tag{14.11}$$

The weights ω_i are given by:

$$\omega_i = \max(0, \omega_0 + \log\left(\frac{E_i}{E^e}\right)) \tag{14.12}$$

where E_i is the energy in cell i, ω_0 is a parameter that depends on η^e and E^e is the energy of the electron.

The position resolution of the calorimeter is determined as the root mean square of the difference in the track and calorimeter position distributions. The η and ϕ resolutions are $\sigma_\eta = 0.007$ and $\sigma_\phi = 0.007$ radians.

14.3.5 Electron Geometrical Acceptance - PhiMod

The detector ϕ (ϕ^{det}) of the particle is smeared with the help of the phimod shift. This shift arises due to the non-responsive module edges called "ϕ cracks" of the calorimeter. There is a bias towards the center of the module. Phimod shift is defined as ($\phi_{EM} - \phi_{trk}$), the difference between the ϕ of the position of the reconstructed EM cluster (ϕ_{EM}) and the ϕ of the track position (ϕ_{trk}) as defined by the extrapolation of the electron trajectory from the primary vertex to the third layer of the EM calorimeter (EM3). The corresponding cluster should fall within the allowed region comprising 80% of the width of an EM module (10 % is cut off from each side). More details on the geometrical acceptance for the electron has been given in Chapter 13.

14.4 Final State Photon Correction

The electrons arising from the W decay are capable of radiating photons. These final-state photons are radiated either at the time of generation of the electron (internal brehmsstrahlung) or during the interaction of the electron with

the material (external brehmsstrahlung). The effect of the photons coming from the external brehmsstrahlung are accounted for by the energy-loss corrections. Most of the photons from the internal brehmsstrahlung come from the radiation by the decay electron and are referred to as the FSR photons. If the energy of these photons are not included in the reconstructed energy of the electron, E_T, the W mass can be mismeasured. This problem occurs if the radiated photon is so far away from the electron that its energy does not fall within the electron cone and cannot be included in the reconstructed electron energy. The second reason is when the photon is absorbed by the material and does not reach the calorimeter.

FSR photons close to the electron reconstruction cone or inside the cone will effect the electron identification efficiency (isolation, shower shape and track matching) and energy measurement. Hence it is necessary to obtain a parameterization of the electron efficiency and energy as a function of the photon distance from the detected electron. This distance is given by

$$\Delta R(e\gamma) = \sqrt{[\phi(e) - \phi(\gamma)]^2 + [\eta(e) - \eta(\gamma)]^2} \tag{14.13}$$

This parameterization is achieved with the help of two FULL MC samples, one sample contains single electrons (possessing the kinematics of electrons from $W \rightarrow e\nu$) accompanied by FSR photons, the second sample contains the same electron events as the first one sans the FSR photons whose energy has been merged back with the electrons. The electron and photon responses from both samples are studied.

Figure 14.4 shows the reconstruction efficiency of the electron versus the fraction of the energy carried by the leading FSR photon (X). There are 12 plots for 12 bins in ΔR with an interval of 0.05.

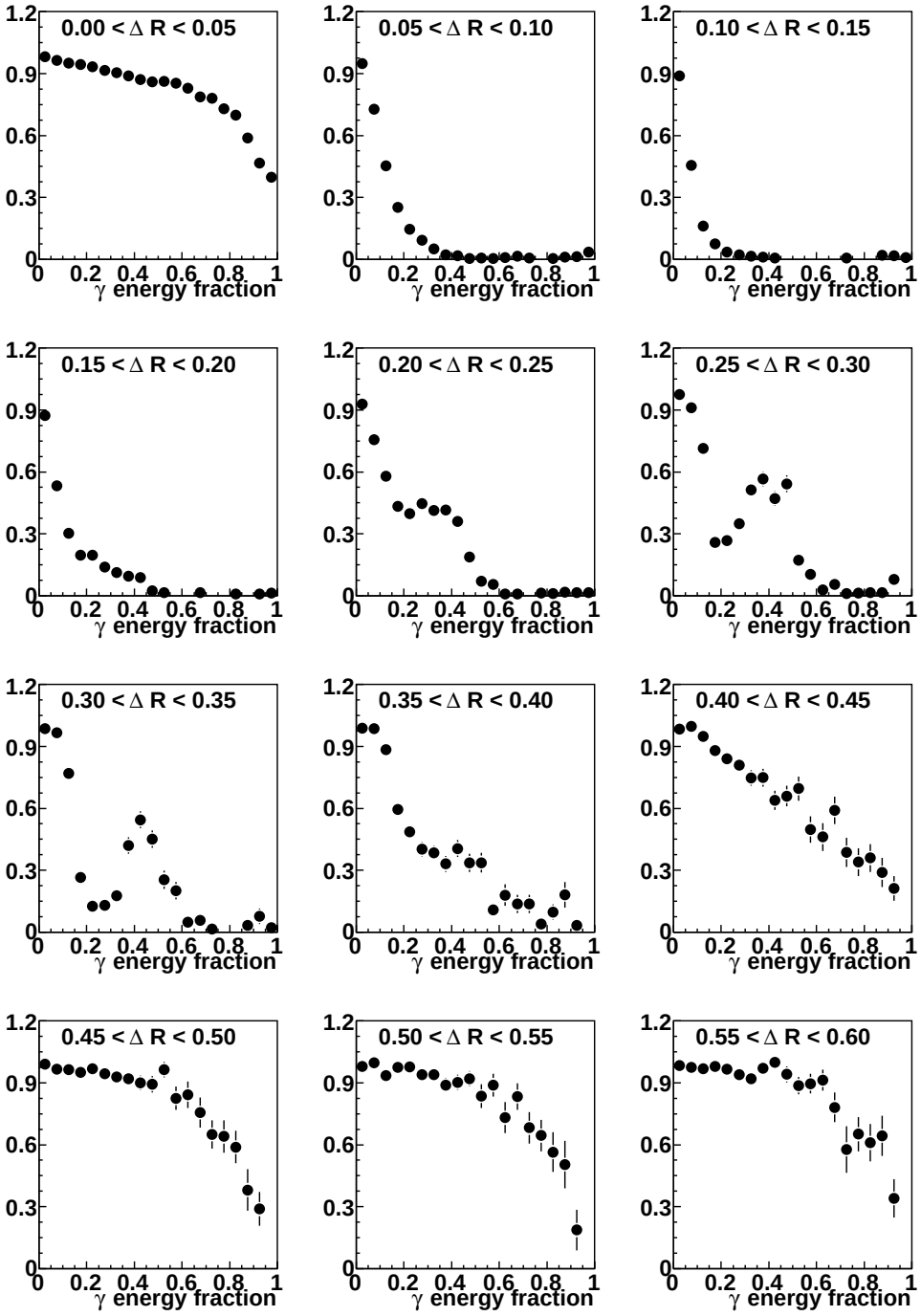

Figure 14.4. Electron identification efficiency as a function of the fractional energy carried by the leading photon

The average energy response difference between FSR and no FSR is given in Figure 14.5. The horizontal axis again represents the fraction of energy carried by the leading FSR photon (X) for all the twelve bins of ΔR. The vertical axis is a double ratio, it is the difference between the reconstructed energy with and without FSR divided by the true energy without FSR. This in turn is divided by the energy fraction of the leading FSR photon. Thus the double ratio can be represented by

$$\kappa = \frac{(E_{\text{true}}[\text{withFSR}] - \text{E}_{\text{true}}[\text{noFSR}])/(\text{E}_{\text{true}}[\text{noFSR}])}{X} \tag{14.14}$$

For large values of ΔR κ=-1 since the photon lies too far away from the electron and is lost. At low values of ΔR, large negative values of κ are expected due to the losses in the dead material and we expect these losses to be less important as X increases. All the distributions from Figures 14.4 and 14.5 are included in the FSR model in the parameterized FAST MC.

Both the Figures 14.4 and 14.5 carry a lot of embedded information. This is because the efficiency distributions are sculpted in different ways by different selection criteria. By considering only one criteria at a time we notice that the efficiency in the first three ΔR bins is influenced by the track matching requirement and to a lesser extent by the shower-shape requirement (HMatrix). When the photon is very close to the electron, the shower shape for a high X photon is too much for the HMatrix to handle because it has been tuned on single electrons. More importantly the calorimeter-based cluster position deviates significantly from the track-based expectation. In the last three ΔR bins, the photon is far away from the electron and does not interfere directly with its reconstruction. It interferes indirectly at large X values when the electron energy is so low that our high-p_T

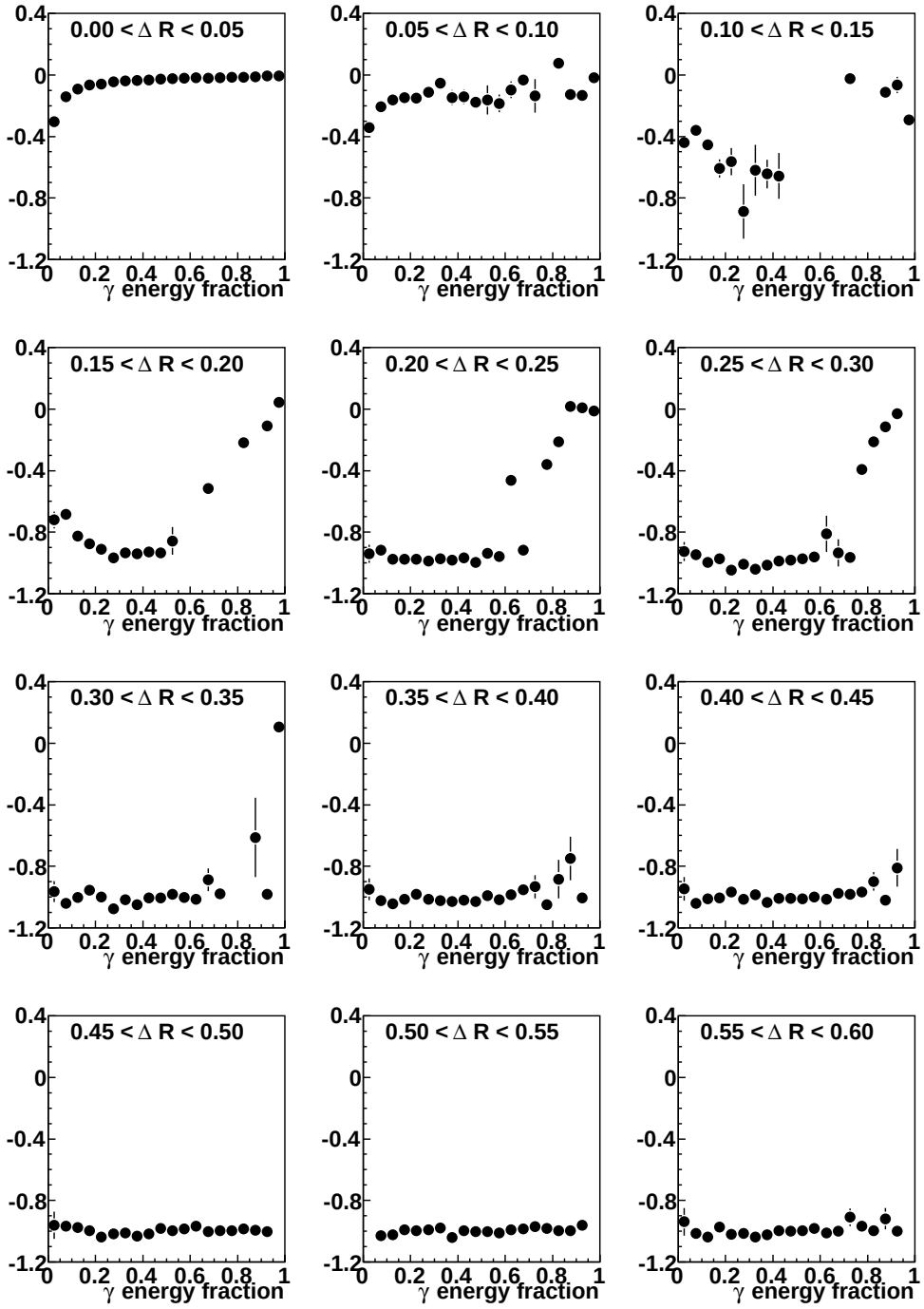

Figure 14.5. Electron energy correction as a function of the fractional energy carried by the leading photon

reconstruction algorithms fall out of scope and are thus inefficient.

In the transition region between the two p_T regimes, the effect of the cluster isolation requirement can be seen in the Figures for $0.30 < \Delta R < 0.35$. The equivalent of this plot obtained by dropping the track matching and shower shape requirements shows a flat at "perfect efficiency" except for two symmetric "holes" at $X \simeq 0.2$ and $X \simeq 0.8$. These "holes" separate three different regimes - at $X \lesssim 0.2$ the photon energy is included in the electron reconstruction cone, but the energy is not sufficiently large to cause the isolation cut to fail. At $X \gtrsim 0.8$ we reconstruct the photon cluster rather than the electron one. The electron does enter the isolation cone of the photon but its energy is insufficient for causing the isolation cut to fail. At $X \sim 0.5$ we are in the intermediate zone, dealing with two consecutive deposits of energy and the clustering algorithm places the cluster in such a way that it includes both deposits (the cluster is large enough to do that). The track matching requirement kills the photon clusters at large X and both the track matching and HMatrix requirements kill significant fractions of the remaining events, especially of unusual clusters at $X \sim 0.5$.

In conclusion, our FSR model not only models the QED effects at the four-vector level, it also describes the effects of the detector on the photons that are produced and pass through the material. It describes the probability of the photons reaching the calorimeter, probability of the photon and electron merging with each other, probability that the photon will interfere with the selection cuts of the electron and kill the event.

14.5 Primary Vertex Simulation

The primary vertex (z_{vtx}) is necessary for deriving the detector η (η_{det}) of the particle, which depends on the η_{phys} and primary vertex information. Hence the FAST MC should be able to model the primary vertex distribution as seen in data. The shape of the vertex distribution depends on the shape of the luminous region, thus the width of the primary vertex (σ_z) depends on the instantaneous luminosity. The σ_z is parameterized from zero-bias (ZB) events, by fitting the primary vertex distribution from ZB data for 15 different epochs with a multi-parameter formula. More details on the determination of the primary vertex of the event has been given in Chapter 13.

14.6 Luminosity Profile and Run Number

The luminosity and run number values are chosen randomly from a 2-dimensional histogram which stores the luminosity and run numbers for minimum-bias (MB) events that were recorded over the same run period as the W and Z data. The MB events will be discussed broadly in Chapter 15.

14.7 Quality of the Electron Energy Loss Functions

The energy loss correction functions describe the average energy loss of electrons in the dead material upstream of the calorimeter, parameterized as a function of energy and η (angle of incidence). The function possesses a statistical uncertainty due to the limited statistics of the FULL MC single electron samples that were used to derive it and uses a parameterization with limited flexibility that might not be able to fully describe all aspects of the energy-loss functions.

The electron energy scale described in Section 14.3.1 can absorb an error associated with the global scale of the energy loss functions. However it cannot absorb other imperfections. As evident from Figure 9.10 in the E-η space, the electrons from $Z \rightarrow e^+e^-$ populate one "band" while the electrons from $W \rightarrow e\nu$ populate another band. There is some overlap between the two bands, but they also probe distinct regions in E-η space. The incomplete overlap between the W and Z energies leads to the speculation that there is a dependence on the "transportation" of the energy scale from being measured at the Z down to the W. This depends on the quality of the energy-loss parameterization (extrapolation from one band to the other). This section deals with the precision of the E-loss functions for purposes of this "transportation of energy scales".

The quality of the energy loss functions needs to be assessed separately for each set of E-loss functions. This is done with the help of a sample of dielectron events that possess the kinematics of electrons from $Z \rightarrow e^+e^-$ events with no FSR. This sample is passed through the detailed simulation of the detector, just like the FULL MC samples used for deriving the energy-loss parameterizations. After reconstructing the $Z \rightarrow e^+e^-$ events using the same event selection criteria as for the W mass analysis, we determine the ratio of the difference between the reconstructed and true energy to the true energy. The same exercise is repeated for the electrons from the W without any FSR. A profile of each of these two fractional differences as a function of true energy indicates the imperfections in the energy-loss corrections. The bottom plot of Figure 14.6 shows a plot of the difference between the fractional energy deviations for the W and Z (difference of the above two) as a function of true energy. This indicates the presence of errors in "transporting" the energy-loss corrections from the Z to the W. The top

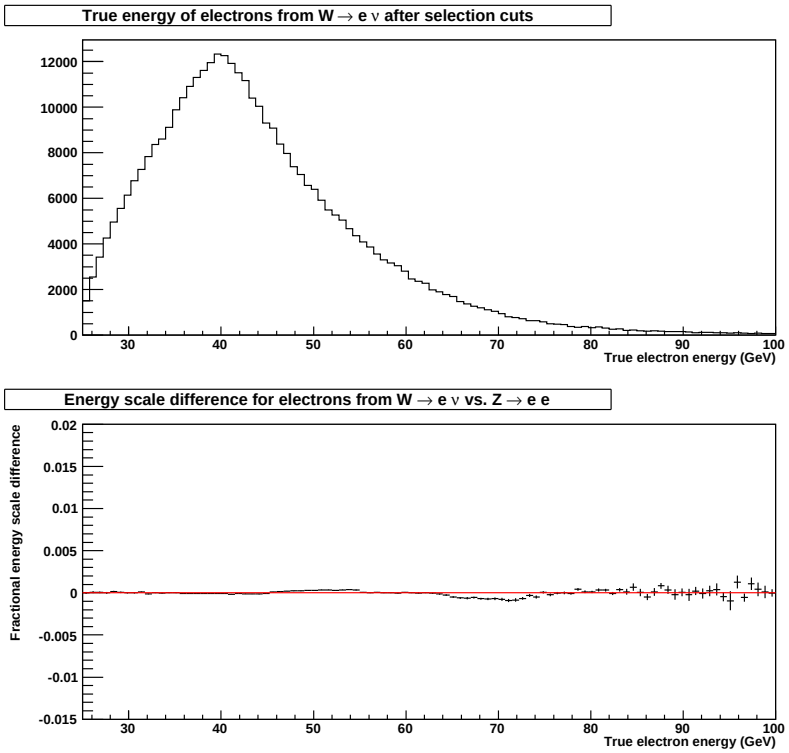

Figure 14.6. Top: The true energy spectrum for electrons in simulated W events which pass the full selection Bottom: The difference of the fractional difference of measured and true electron energies as a function of true energy in Z and W electrons

plot shows the true energy distribution of electrons from $W \rightarrow e\nu$ after the event selection conditions have been applied. The convolution of this distribution and the bottom plot is a measure of the impact of the imperfections in the energy-loss parameterizations on our measurement of the W mass. The convolution might result in the reconstructed electron energy from the W being higher than required by the analysis. This in turn would result in the fitted W mass values being low. We correct our measurements for this bias and quote the uncertainty due to the corrections as an additional systematic on the W mass measurement.

CHAPTER 15

SIMULATING THE RECOIL ENERGY IN THE PMCS

15.1 A Brief Introduction

This section details the modeling of the hadronic recoil for the Run IIa W mass measurement. It is sub-divided into an introduction followed by a discussion of the modeling of the various components of the recoil. Some minor tuning procedures that are done to help the modeled recoil match the real world recoil are also described.

The hadronic recoil in a hard scatter event that produces a vector boson from proton-antiproton collisions (and thus $q\bar{q}$ pairs), can be conceived as a "collective term used for everything detected" in the event, except for the vector boson and its decay products. This has been shown in the Figure 5.1 in Chapter 5.

15.2 Components of the Hadronic Recoil

The hadronic recoil possesses three main components. The first constituent represents the hadronizing fragments from the hard scatter that recoil against the vector boson, thus balancing the boson in the transverse plane. The second contribution comes from the interactions of the remaining partons of the same proton-antiproton that produced the vector boson. The additional interactions from the numerous proton-antiproton collisons in the same or previous beam

crossings constitute the third component of the hadronic recoil.

With these assumptions, the DØ Run IIa model of the hadronic recoil [143] in the FAST MC (PMCS), can be expressed mathematically in terms of its components as follows:

$$\vec{u}_T(\text{meas}) = \vec{u}_T^{\,\text{HARD}} + \vec{u}_T^{\,\text{SOFT}} + \vec{u}_T^{\,\text{ELEC}} + \vec{u}_T^{\,\text{FSR}} \tag{15.1}$$

We briefly introduce each of the terms in the above equation below. More details on them have been provided in section 15.3.

- $\vec{u}_T^{\,\text{HARD}} = \vec{f}(\vec{q}_T)$

  Here $\vec{u}_T^{\,\text{HARD}}$ denotes the recoil component associated with the hard scattering of the $q\bar{q}$ pair that resulted in the $W(Z)$ boson. This "hard" component balances the transverse momentum of the vector boson. Here $\vec{q}_T$ is the generator level momentum of the boson. The $\vec{f}(\vec{q}_T)$ is an ansatz function used for smearing the $\vec{q}_T$). It is derived from $Z \to \nu\nu$ GEANT (FULL) MC events as described in [143].

- $\vec{u}_T^{\,\text{SOFT}} = -\sqrt{\alpha}_{mb} \cdot \vec{\not{E}}_T^{\,\text{MB}} - \sqrt{\alpha}_{zb} \cdot \vec{\not{E}}_T^{\,\text{ZB}}$

  Here $\vec{u}_T^{\,\text{SOFT}}$, named the "soft" component, represents the other interactions that contribute to the hadronic recoil. As evident, there are two sub-components here. First is the "underlying event", the second is the "additional energy content in the event". The underlying event consists of the interactions of the remaining (or spectator) partons of the same $p\bar{p}$ pair that produced the vector boson. It is modeled with the help of minimum bias (MB) events. The additional energy content is associated with all the other interactions occuring in the $p\bar{p}$ pairs present in the same or previous

beam crossings. Interactions contributing to detector noise are also included in this sub-component. It is modeled using zero bias (ZB) events. We set α_{zb} to unity because the ZB events are a reliable control sample directly from collider data.

- $\vec{u}_T^{\text{ELEC}} = -\sum_e \Delta u_{\parallel} \cdot \hat{p}_T(e)$

  This component serves as a correction for the recoil energy that is parallel to the electron direction. It is present under the electron window, is measured as part of the electron energy and is thus subtracted from the recoil energy.

- $\vec{u}_T^{\text{FSR}} = \sum_\gamma \vec{p}_T(\gamma)$

  The FSR component contains the energy of the Final State Radiation (FSR) photons that are far away from the electron(s) and hence reconstructed as recoil energy.

15.3 Modeling the Hadronic Recoil

Each of the four components of the hadronic recoil are modeled separately and then combined. This section describes the process for modeling each of the components.

15.3.1 Modeling the "hard" Component

The ansatz function $\vec{f}(\vec{q}_T)$ is derived from "pure" $Z \to \nu\nu$ FULL MC events. This sample generated from PYTHIA has no underlying event contribution in it. The generated events have been propagated through the full chain of the DØ detector simulation and reconstruction software without adding any ZB overlay to them. In addition, since the decay products (neutrinos) escape undetected, all

the energy measured in the detector can be attributed to the recoil alone. Hence the term "pure" recoil sample is used. This FULL MC sample contains 600,000 $Z \rightarrow \nu\nu$ events. In order to obtain kinematics similar to the $Z \rightarrow e^+e^-$ events used in the fine-tuning procedure described later in sub-section 15.4, both the neutrinos from a Z boson decay are required to be centrally located (i.e. physics pseudorapidity $|\eta_\nu| < 1.3$).

In the Run I analyses low luminosity conditions and a better energy resolution for individual pions resulted in a situation where the resolution of the recoil direction was not significantly large. Hence only the magnitude of the transverse momentum of the generated recoil was smeared. However in the present experimental conditions of the Run IIa analysis, which include high luminosities and extra material in front of the detector, both the magnitude (q_T) and direction (ϕ) of the recoil need to be smeared. This implies that the correlations between the momentum and direction fluctuations also need consideration now.

The two main variables that are used to parameterize the hard component are the recoil p_T resolution (R) and the angular resolution ($\Delta\phi$).

$$R = \frac{u_T - q_T}{q_T} \qquad (R < 1) \tag{15.2}$$

$$\Delta\phi = \phi(\vec{u}_T) - \phi(\vec{q}_T) \qquad (|\Delta\phi| < \pi) \tag{15.3}$$

Here $\vec{q}_T$ (= - $\vec{p}_T^{\,Z}$) is the true recoil vector and q_T its magnitude. $\vec{u}_T$ is the smeared recoil vector and u_T its magnitude.

The parameterization of the hard component of the recoil is described in the following steps. More details have been provided in the recoil note [143].

1. The $Z \rightarrow \nu\nu$ sample is split into 32 variably sized bins of q_T from 0 to 100

GeV.

2. For each q_T bin a two-dimensional distribution as a function of R and $\Delta\phi$ is constructed. Two examples of such event *probability density functions (pdf)* are shown in Figures 15.1and 15.2 as coloured box histograms for $q_T \in [4.5,\ 5[\,GeV$ and $q_T \in [18,\ 20[\,GeV$ bins respectively. From here it is evident that for low values of q_T there is a correlation between R and $\Delta\phi$. Moreover the distributions of R for slices of $\Delta\phi = const$ are non-gaussian.

3. Each of these *pdf* distributions are fit with an ansatz parameterization. Five parameters are needed to describe the two-dimensional distributions. The fits are shown in Figures 15.1 and 15.2 as coloured contours. Details of the ansatz parametrization have been provided in [143].

4. A smearing function ($\vec{f}(\vec{q}_T)$) is built based on these 32 fits. Hence $\vec{f}(\vec{q}_T)$ determines the smeared momentum (or $\vec{u}_T$) of the boson from its generator level momentum (or $\vec{q}_T$) as the input. The smearing of the hadronic response and resolution (p_T and ϕ) are performed in a single step by $\vec{f}(\vec{q}_T)$, inherently including the correlations between them.

This parameterization for the hard component is derived only once, from the $Z \rightarrow \nu\nu$ FULL MC sample. The recoil model retains this hard component for the data measurement too. No explicit reweightings for emulating data such as corrections for beam vertex or RESBOS kinematics are applied to this parameterization when used for the data analysis. This is due to the fact that this method of parameterization preserves the fundamental characteristics of the hard component of the recoil by preserving information on the correlated momentum and direction resolutions (R and $\Delta\phi$) of the recoil vectors. These resolutions are used to model

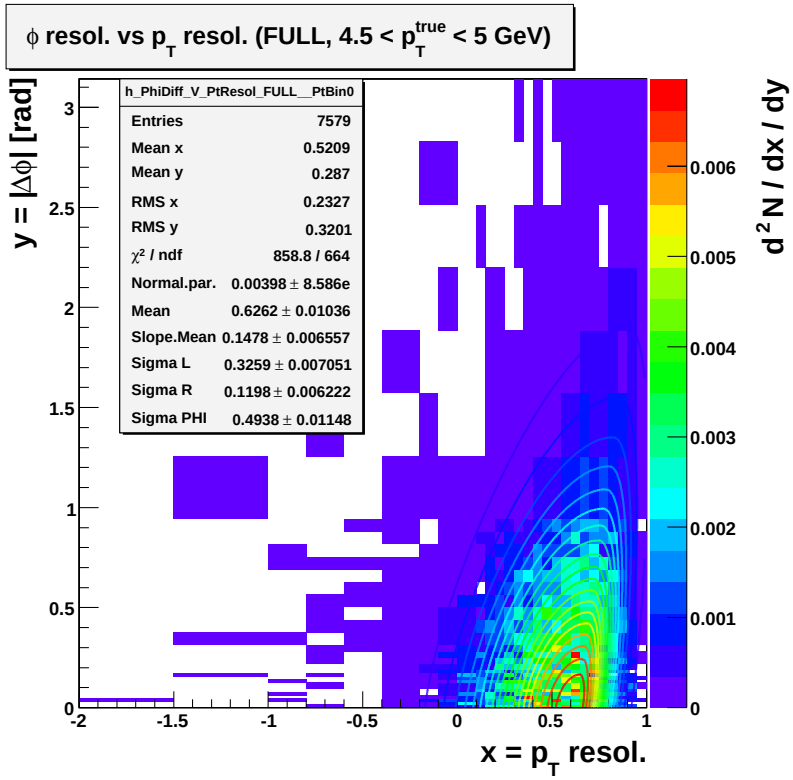

Figure 15.1. The two-dimensional distribution of the recoil p_T and ϕ resolutions for FULL MC (boxes) and fit (contours) for $q_T \in [4.5,\ 5[\, GeV$

the recoil, both for FULL MC and data thus keeping the basic model intact.

15.3.2 Modeling the "soft" or "semi-hard" Component

For the purposes of this analysis, the soft component consists of two major contributions, the first from the underlying event and the second from the additional $p\bar{p}$ interactions.

The "underlying event" contribution consists of the interactions of the spectator quarks in the same $q\bar{q}$ collision that produced the $W(Z)$ boson. It is indepen-

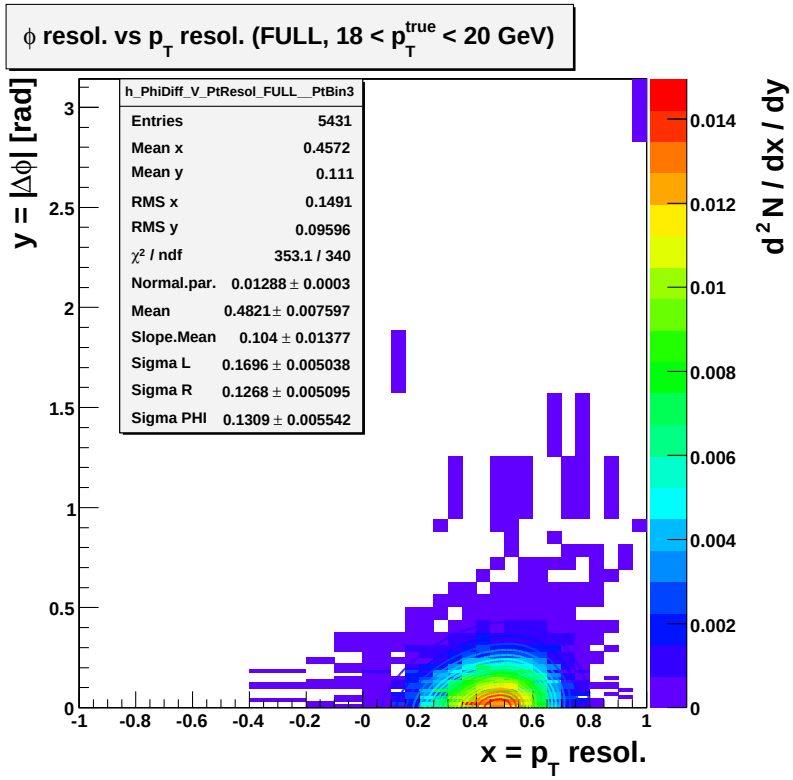

Figure 15.2. The two-dimensional distribution of the recoil p_T and ϕ resolutions for FULL MC (boxes) and fit (contours) for $q_T \in [18,\ 20[\, GeV$

dent of the instantaneous luminosity. We do not have a reliable first-principles method for modeling these interactions so we use minimum bias (MB) events as the starting point. In the data analysis, the MB events samples from collider data are used. These are selected via the minimal trigger requirement of an inelastic interaction so as to veto the empty beam crossings. Events possessing more than one reconstructed PV are vetoed from the MB samples. In the FULL MC analysis, MB events generated from a special run of PYTHIA are used. For this the underlying event generation "tune A" is turned on in PYTHIA.

Since MB events are not the perfect choice for modeling the underlying event, they are first reweighted in both the data and FULL MC analyses. The MB events are reweighted until their scalar E_T (SET) matches the scalar E_T of those $Z \rightarrow ee$ events from which the electron energy contribution has been removed. More details on this procedure have been provided in [143]. The reweighting helps the MB events model the underlying event better.

The reweighted MB event information is stored in an event library that is used as a lookup table and the $\not\!\!E_T$ of the MB events are used for modeling the underlying event.

To improve the underlying event model, a multiplicative scale factor called α_{mb} is also used in addition to reweighting the events.

An important point here is that this α_{mb} is a "multipurpose" *ad hoc* correction factor used in the modeling of our recoil. This single factor is used for three different purposes in our recoil model. The above is the first usage of α_{mb}. It is also used as a de-weighting factor to eliminate double-counting and as a fine-tuning parameter for the resolution of the "soft" component of the modeled recoil. Although it has multiple uses in our recoil model, α_{mb} is determined only once as described in sub-section 15.4. The latter two uses of α_{mb} will be discussed in the appropriate sub-sections that follow.

The "additional energy content" in the event is composed of the other $p\bar{p}$ interactions that occur in the same or previous beam crossings. Calorimeter noise and pileup also contribute to this energy content. In both the data and FULL MC analyzes, this contribution is modeled with the help of ZB events from the collider.

For the data analysis, the instantaneous luminosity profiles and run numbers

of the ZB overlay sets recorded in the non zero-suppressed mode and used in the modeling of the recoil match those of the $W(Z)$ data taking epochs. In the FULL MC analysis, the ZB events used for modeling the "soft" component of the recoil have the same instantaneous luminosity profile as the $W(Z)$ FULL MC sample. This is insured because the same ZB (recorded in non zero-suppressed mode) processing version (from d0raw2sim) is used for both.

The ZB event information is stored in an event library used as a lookup table. The $\not\!\!E_T$ of the ZB events model the additional energy contribution and are added to the underlying event.

An artifact of using two event information libraries to model the two sub-components of the "soft" component of the recoil is the double counting of some effects here. Effects such as detector noise and soft interactions which do not possess a primary vertex are being double counted. This double counting effect is eliminated by the use of the same multipurpose factor α_{mb} that has been applied to the MB events earlier. The α_{mb} serves to de-weight the MB events when they are used along with the ZB events.

15.3.3 The $u_{\parallel}$ Correction to the Modeled Recoil

This component is a correction for the transverse energy flow of the recoil into the electron(s) window. This energy gets measured as electron energy and cannot be considered as part of the recoil since calorimeter cells belonging to the electron clusters are excluded from the computation of the recoil $\vec{u}_T$. Here $\hat{p}_T(e)$ denotes the direction of a smeared electron. The $\Delta u_{\parallel}$ correction factor depends on the projection of $\vec{u}_T$ on the $\hat{p}_T(e)$ axis and on the instantaneous luminosity. We explicitly model the fact that $\Delta u_{\parallel}$ is related to the energy that gets added to

the electron, but not identical (because of zero suppression [144]).

15.3.4 The FSR Correction to the Modeled Recoil

This correction contains the energy of the Final State Radiation (FSR) photons that fall outside the electron reconstruction cone. The photons are radiated from the electron originally but reconstructed as part of the recoil due to their remoteness from the electron.

15.4 Fine-tuning/Over-smearing the Modeled Recoil

We know that the parameterized detector model of the hard component presented in sub-section 15.3 has been developed from a special FULL MC sample that contains "pure" $Z \rightarrow \nu\nu$ events only. It does not have any underlying event and additional energy contributions in it. The latter two increase the energy content of the calorimeter. Thus, both the response and resolution of the calorimeter for the recoil component arising due to the hard scatter (that produces the $W(Z)$), change in the presence of this additional activity. In other words, the hard and soft recoil components are not completely independent of each other, rather correlated.

However in our simulation model, both the "hard" and "soft" components of the hadronic recoil are modeled separately and then combined. To account for the correlations existing between these different components of our recoil, the parameterized model of the recoil needs some "fine-tuning" or "over-smearing". These small *ad-hoc* corrections, in the form of free tunable parameters, reflect the differences between our modeled recoil ($Z \rightarrow \nu\nu$ + MB + ZB) and the realistic one. They help us tune our modeled recoil to the real-world one (from the collider data or FULL MC simulation) in a more accurate way.

There are six floating parameters that are responsible for tuning the modeled recoil. Three are for the modeled response while three tune the recoil resolution. These tuning parameters are applied to the "hard" and "soft" components when they are combined to obtain the hadronic recoil. These parameters are determined by comparing the simulated recoil to the reference (collider data or FULL MC) for $Z \rightarrow ee$ events and then are plugged back into the FAST MC for modeling the recoil of the W boson.

The diagnostic variables of the η and ξ imbalance play an important role in the determination of the tuning parameters. Let us get aquainted with these diagnostics first.

The transverse momenta of the recoil ($\vec{u}_T$), and that of the Z boson as measured by the two decay electrons ($\vec{p}_T^{\,ee}$), are projected on the inner bisector of the angle between the two electrons (called η axis), as shown in Figure 15.3. The projection of these two momenta onto the η axis depends only on the directions of the electrons and not on their measured energy (the noise contributions to the momenta average out to zero and do not bias the results). By definition, η imbalance (η_{imb}) is the sum of these two projections:

$$\eta_{imb} = \vec{u}_T \cdot \hat{\eta} + \vec{p}_T^{\,ee} \cdot \hat{\eta} \tag{15.4}$$

We also project the recoil and Z p_T in the direction perpendicular to the η axis, called the ξ axis (defined in Figure 15.3). The ξ-imbalance (ξ_{imb}) is defined as:

$$\xi_{imb} = \vec{u}_T \cdot \hat{\xi} + \vec{p}_T^{\,ee} \cdot \hat{\xi} \tag{15.5}$$

The recoil response is fine-tuned by using the mean of the η_{imb} whereas the reso-

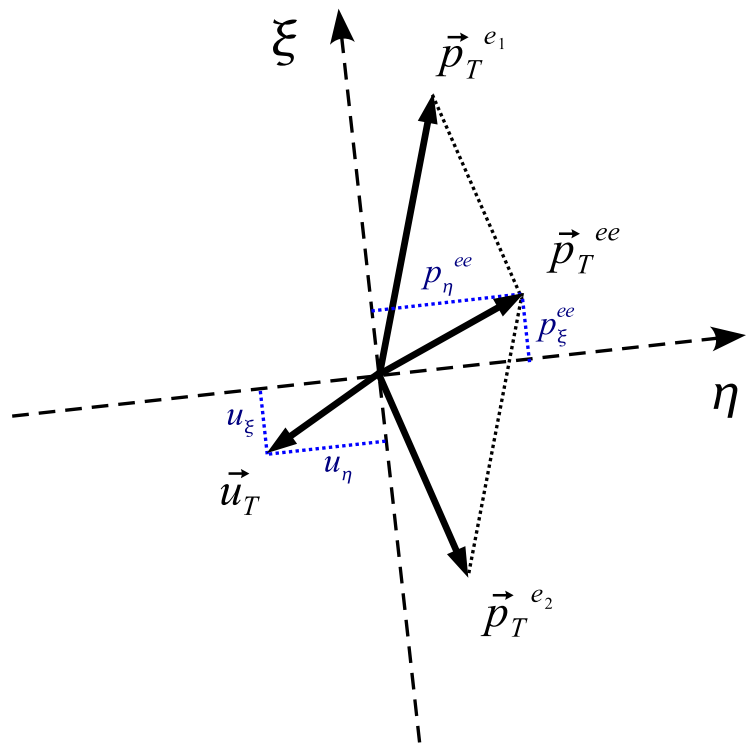

Figure 15.3. The $\eta - \xi$ coordinate system in a $Z \to ee$ event

lution is fine-tuned using the width of the η_{imb} distributions. The ξ_{imb} observable offers little additional statistical power and is therefore not used for the tuning.

A kinematical upper limit of 30 GeV is placed on the magnitude of the smeared recoil during the tuning of the response and resolution.

The η (or ξ) imbalances are most appropriate for the task of tuning the recoil since, by virtue of the construction of the $\eta - \xi$ coordinate system as shown in Figure 15.3, the effects of the electron energy resolution are minimal in the determination of the η (or ξ) imbalance. As evident, the η (or ξ) imbalance is an estimation of the hadronic recoil response with respect to the electromagnetic energy response. If both the responses were equal, there would be no imbalance.

Since the positive η axis is always in the direction of $\vec{p}_T^{\,ee}$, it is more sensitive to changes in the recoil. Hence any systematic bias in the measurement of $\vec{u}_T$ will manifest itself as a bias in the η_{imb}. This helps in determining the recoil tuning parameters in the best way.

15.4.1 Fine-tuning the Hadronic Response

The relative hadronic response `RelResp` is defined in terms of three tuning parameters named `RelScale`, `RelOffset` and $\tau_{\texttt{HAD}}$ as follows:

$$\texttt{RelResp} = \texttt{RelScale} + \texttt{RelOffset} \cdot \exp \frac{-\,q_T}{\tau_{\texttt{HAD}}} \tag{15.6}$$

This relative hadronic response is used to fine-tune the hard component of the modeled recoil. Here $\tau_{\texttt{HAD}}$ helps describe the response of the calorimeter at low values of the recoil momentum. q_T is the magnitude of the recoil momentum at the generator level. No tuning for the response of the soft component is needed. This is because the soft component is modeled from the type of events that closely match or actually constitute it by definition. Both in the reference (data or FULL MC) and FAST MC simulation, the η imbalance plots are constructed for ten different ranges of smeared Z boson momenta i.e. p_T^Z. For determining the fine-tuning parameters, high statistics templates of the η imbalance distribution are made for the same p_T^Z ranges by the FAST MC simulation by varying the values of the above three parameters. A χ^2 is defined by comparing the mean of the η imbalance from the reference with that from the FAST MC templates. This is done for each of the ten p_T^Z bins and the total χ^2 (which is the sum of all these individual ones) is minimized in the fitting procedure.

15.4.2 Fine-tuning the Hadronic Resolution

The tuning of the hadronic resolution involves the hard and soft components of the modeled recoil. This is because the width of the η imbalance obtained in the various smeared p_T^Z bins is sensitive to the hadronic resolution of the hard and soft components. The electron resolution is intrinsically better than its hadronic counterpart due to the choice of the η axis and thus makes a small contribution here.

The two parameters involved in the tuning of the hadronic resolution of the hard component in our recoil model are `RelSampA` and `RelSampB`. The relative resolution `RelResn` is defined as follows:

$$\texttt{RelResn} = \texttt{RelSampA} + \frac{\texttt{RelSampB}}{\sqrt{q_T}} \tag{15.7}$$

This relative resolution is used to tune the hard component of the modeled recoil. Here q_T is the magnitude of the recoil momentum at the generator level. For tuning the resolution of the soft component, the multipurpose *ad hoc* scale factor introduced as α_{mb} earlier in sub-section 15.3 is used here again. This is the third use of α_{mb}. The implementation of α_{mb} for the purpose of tuning the soft component is in the same step that has been shown earlier in sub-section 15.2 as follows :

$$\vec{u}_T^{\,\text{SOFT}} = -\sqrt{\alpha}_{mb} \cdot \vec{\not{E}}_T^{\,\text{MB}} - \sqrt{\alpha}_{zb} \cdot \vec{\not{E}}_T^{\,\text{ZB}} \tag{15.8}$$

The α_{mb} being a free tunable parameter adjusts MB events in the soft component thus helping the modeled recoil match the real-world recoil.

A notable point here is that although the factor α_{mb} is used as a tuning parameter at two different places and acts as a de-weighting factor for eliminating

the double counting, it is determined once and only once, here in this fine-tuning procedure. There are no multiple steps for determining this parameter.

The values of α_{mb} obtained in the data and FULL MC analyzes are quite different. This is because α_{mb} is used for scaling MB events obtained from two different sources. As a result the two event libraries (MB and ZB) are also different in each case. Since α_{mb} also eliminates the double-counting, its values differ in both measurements.

As in the earlier case of tuning for the hadronic response, determining the fine-tuning parameters for the hadronic resolution involves making high statistics templates of the η imbalance distribution for the same p_T^Z ranges as the reference, with the help of the FAST MC simulation by varying the values of the above three parameters. A χ^2 is defined again by comparing the width of the η imbalance from the reference with the templates. This is done for each of the ten p_T^Z bins and the total χ^2 (which is the sum of all these individual ones) is minimized in the fitting procedure.

The fine-tuned response and resolution of the modeled recoil are combined along with the other components ($\vec{u}_T^{\mathrm{ELEC}}$ and $\vec{u}_T^{\mathrm{FSR}}$) to give the smeared recoil $\vec{u}_T$. The details of this fine-tuned combination are available in chapter 5 of the recoil note [143].

CHAPTER 16

THE BACKGROUNDS IN THE ANALYSIS

16.1 A Brief Introduction

The $W \rightarrow e\nu$ events are subject to backgrounds mainly from QCD multi-jet (mostly di-jet) production, $W \rightarrow \tau\nu \rightarrow e\nu\nu\nu$ and $Z \rightarrow e^+e^-$ events. Backgrounds usually arise when these events fake a $W \rightarrow e\nu$ event due to poor reconstruction. So a jet could fake an electron or a high-p_T electron (positron) could fake a large amount of missing energy if poorly reconstructed. There is an irreducible background from the $W \rightarrow \tau\nu \rightarrow e\nu\nu\nu$ decay, especially if the electron acquires most of the energy. In our analysis the QCD and $Z \rightarrow e^+e^-$ backgrounds are estimated from collider data, while the $W \rightarrow \tau\nu \rightarrow e\nu\nu\nu$ background is estimated from GEANT (FULL) MC.

This chapter provides detailed descriptions on these various sources of backgrounds relevant for the W mass analysis and their estimations.

16.2 QCD Background

The di-jet events can pass the W selection cuts if one of the jets mimics an electron and the other is mismeasured thus posing as missing energy. Collider data is used for this study. The number of W events is extracted by solving the

following system of equations:

$$N = N_W + N_{QCD} \tag{16.1a}$$

$$N_{trk} = \epsilon_{trk} N_W + f_{QCD} N_{QCD} \tag{16.1b}$$

the two equations yield

$$N_W = \frac{N_{trk} - f_{QCD} N}{\epsilon_{trk} - f_{QCD}} \tag{16.1c}$$

where N_{trk} and N represent the number of W candidate events with and without the track matching requirements, N_W is the true number of real W bosons and N_{QCD} is the number of QCD events for W candidates without track matching requirements. f_{QCD} is the track match faking probability while ϵ_{trk} is the track match efficiency. f_{QCD} and ϵ_{trk} are measured using em+jet and diem events. An illustration of the concept for extracting the QCD background is given in Figure 16.1. The track matching requirement for our analysis is the good spatial track matching, which means that the matched track should possess at least one SMT hit and the track p_T should be > 10 GeV. Due to the track-matching requirement for the reconstructed clusters, the real W events and the QCD background in the sample we use can be expressed as:

$$\epsilon_{trk} N_W = \frac{\epsilon_{trk}(N_{trk} - f_{QCD} N)}{\epsilon_{trk} - f_{QCD}} \tag{16.2a}$$

$$f_{QCD} N_{QCD} = \frac{f_{QCD}(\epsilon_{trk} N - N_{trk})}{\epsilon_{trk} - f_{QCD}} \tag{16.2b}$$

Detail studies [145] show that the η_{det} and vertex dependence do not affect the final QCD background shape, even though the fake rate and electron efficiency are strongly dependent on them. We rely on the kinematic distributions to measure

the W mass. Hence the p_T^e dependence of f_{QCD} and ϵ_{trk} need to be considered while estimating the shape and fraction of the QCD background.

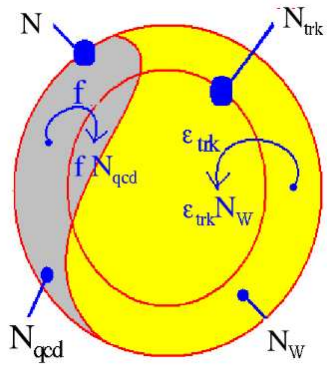

Figure 16.1. Concept of the method used to subtract QCD backgrounds from $W \to e\nu$ events

16.2.1 f_{QCD} and ϵ_{trk}

The track match faking probability, f_{QCD} is determined with the help of EM+jet events. These EM+jet events are actually those di-jet events where one of the jets fakes an EM object. The EM+jet samples are taken from the Run IIa data and possess an integrated luminosity of 1 fb^{-1}. We select events by requiring an EM cluster to satisfy the EM-identification requirements and lie back-to-back with a jet that passes the jet-identification requirements. The fake probability (f_{QCD}) is then given by the fraction of those EM objects that are found to have

a matching track. Figure 16.2 shows the p_T dependence of f_{QCD} in bins of η_{det}. The bins of η_{det} are given by (-∞, -1.3), (-1.3, -1.1), ..., (1.1, 1.3), (1.3, +∞).

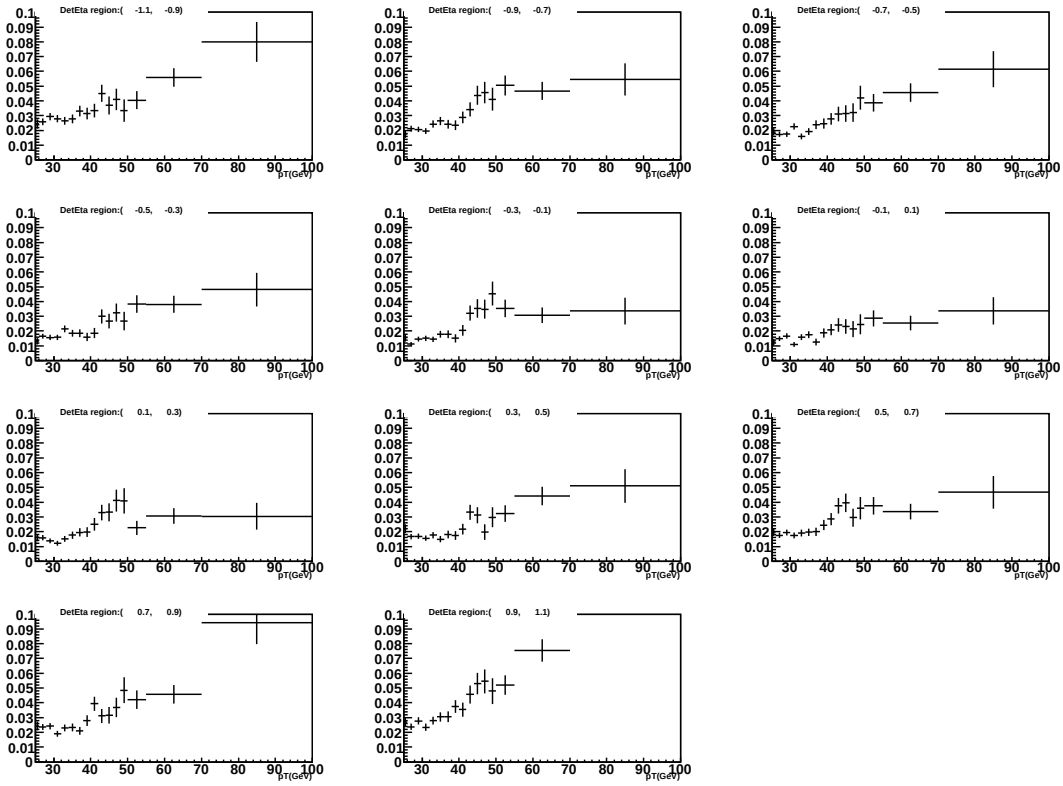

Figure 16.2. The p_T dependence of f_{QCD} in bins of η^{det}

$Z \rightarrow e^+e^-$ events are used to study the single electron track match efficiency with the help of the tag-and-probe method [146]. In the FULL MC studies, this method was found to have some bias. A 2% uncertainty due to this bias is attached as the systematic uncertainty of the track matching efficiency measured using the

tag-and-probe method. Figure 16.3 shows the p_T dependence of the ϵ_{trk} in bins of η_{det}.

With the help of the fake rate and electron efficiency, we determine the shape of the background using the above method. The QCD background fraction is $(1.49 \pm 0.03\%)$.

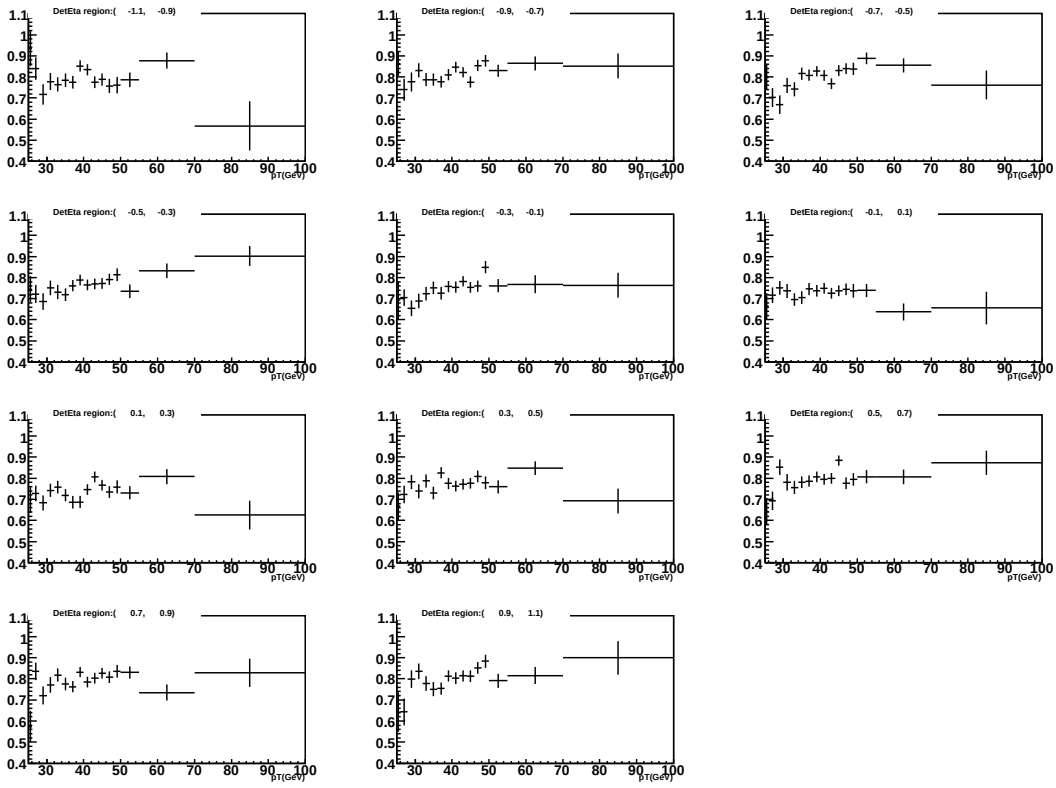

Figure 16.3. ϵ_{trk} in η^{det} bins

16.3 $Z \rightarrow e^+e^-$ Background

The $Z \rightarrow e^+e^-$ events can fake the W events when one of the electrons is mismeasured or not identified and it poses as a substantial amount of missing energy. If we plot the true η of the both the Z electrons from FULL MC $Z \rightarrow e^+e^-$ events which pass the standard $W \rightarrow e\nu$ selection criteria, as seen in Figure 16.4, we see that if one of the Z electrons falls into the ICR region, it gets lost (effectively) giving the impression of a large missing energy upon reconstruction. As we have read earlier, the ICR is not well instrumented and calibrated in Run IIa and so the detailed GEANT simulation of the detector does not describe it well either. Hence we resort to a different method to determine the $Z \rightarrow e^+e^-$ background - we extract it directly from collider $W \rightarrow e\nu$ data.

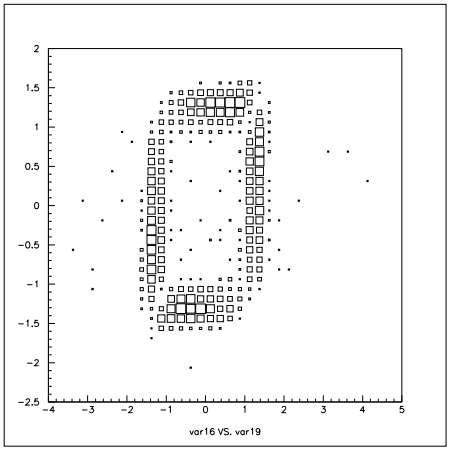

Figure 16.4. η^{det} of the two electrons in the $Z \rightarrow ee$ Background

The requirements for selecting $Z \rightarrow e^+e^-$ events out from $W \rightarrow e\nu$ data are listed below.

1. Event should pass standard $W \rightarrow e\nu$ selection criteria.

2. Require a track with the following properties

   - back to back with the electron
   - p_T of track > 25 GeV
   - $1.0 < |\eta| < 1.5$
   - $|z_0 - Z_{PV}| < 1$ cm
   - Track should have opposite charge as compared to electron
   - Scalar sum over p_T of all other tracks within a cone of $\Delta R < 0.4$ around the selected track should be less than 4 GeV. ΔR is the distance in $\eta - \phi$ space.
   - The reconstructed, invariant mass of the track and cluster should lie between 70 and 110 GeV.

Using this method, the fraction of $Z \rightarrow e^+e^-$ background is estimated to be (0.80 $\pm$ 0.01)%.

16.4 $W \rightarrow \tau\nu$ Background

The $W \rightarrow \tau\nu \rightarrow e\nu\nu$ is topologically indistinguishable from the $W \rightarrow e\nu$ decay. It is suppressed by the branching fraction of $\tau \rightarrow e\nu\nu$ and by the electron p_T cuts. Thus the $W \rightarrow \tau\nu$ events fake a $W \rightarrow e\nu$ signal when the τ decays into $e\nu\nu$. The electron from the τ decay is softer (has less energy) than from a typical $W \rightarrow e\nu$ decay. Hence instead of the typical Jacobian decay peak at $M_W/2$, the

peak appears at a lower momenta and falls off rapidly. The cross-sections for the W bosons decaying into electrons and τ leptons and neutrinos is the same, but the τ background is further reduced by the branching ratio of the subsequent $\tau \to e\nu\nu$ decay. Using a detailed simulation of this process, the $W \to \tau\nu \to e\nu\nu\nu$ background fraction is estimated to be $(1.60 \pm 0.02)\%$.

16.5 Normalization of the Backgrounds

The backgrounds from all the three main sources, i.e. QCD, $W \to \tau\nu$ and $Z \to ee$ are normalized in the same plot as shown in Figure 16.5, for each of the three kinematic distributions. This plot is used for determining the systematics by varying the background fractions by $\pm 1\sigma$.

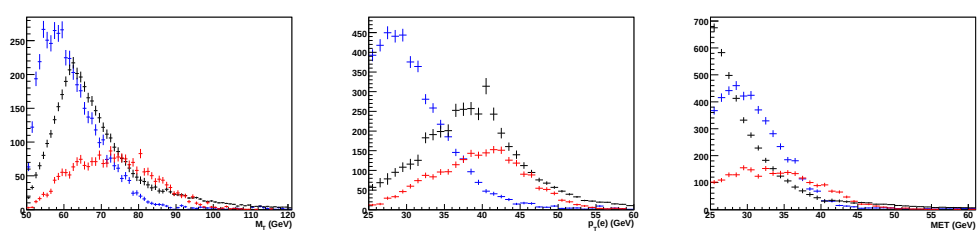

Figure 16.5. M_T, $p_T(e)$ and $\not{E}_T$ of three different backgrounds with the proper relative normalization. Black: QCD, Red: $Z \to ee$, Blue: $W \to \tau\nu$

CHAPTER 17

THE FULL (GEANT) MC ANALYSIS

17.1 A Brief Introduction

The *modus operandi* for the W mass analysis adopted by the group, is to first perform a FULL Monte Carlo (FULL MC) measurement [104] followed by the measurement performed on the collider data. The MC measurement serves as a good warm-up exercise, testing out the functionality, effectiveness and accurate performance of the various tools and procedures that have been developed by the group, for the analysis. Since the input W mass is known in the FULL MC, achieving closure in this analysis gives the green signal for proceeding with the analysis with the collider data samples.

However, the two different measurements, FULL MC and collider data require that our parameterized FAST MC model of the detector needs to be calibrated twice, first to reflect the effects of the FULL MC detector and later to reflect the effects of the actual detector. The forms of the parameterizations in the FAST MC are all derived using the FULL MC Z samples. Obviously for the FULL MC analysis the values of the parameterization constants are derived from the FULL MC $Z \to e^+e^-$ sample whereas for the collider data analysis, they are re-derived from collider $Z \to e^+e^-$ data.

For the FULL MC measurement we produce several MC samples containing

events generated by PYTHIA and processed through a full chain of the DØ detector simulation and reconstruction software. The full detector simulation is based on the GEANT3 program [108]. This FULL MC sample is treated just like data and the FAST MC model is tuned to it. Both the $W \to e\nu$ and $Z \to e^+e^-$ FULL MC samples are generated in this way. For the data measurement the constants of our FAST MC model are tuned to the collider data.

For the FULL MC measurement, the FAST MC templates are obviously generated from the PYTHIA MC generator. For the collider data measurement, they are generated from RESBOS. This stems from the fact that RESBOS describes the kinematics of the boson production and decay in a better way by incorporating gluon re-summation at low boson momenta and NLO perturbative QCD calculations at high boson momenta.

In both the measurements, the methodology is exactly the same. This means that $Z \to e^+e^-$ events are used for calibrating the different aspects of the FAST MC model of the detector, such as the electron energy scale and resolution, hadronic momentum response and resolution, selection efficiencies, etc. This is possible because the W and Z possess similar signatures, thus enabling the Z to act as an excellent control sample for the W. The effect of the different masses of the W ($\sim$ 80 GeV) and Z ($\sim$ 90 GeV) are duly taken into account in the parameterizations where they can have an impact. The FAST MC parameterization is preserved for analyzing the $W \to e\nu$ event samples and extracting the value of the W mass.

Thus in the FULL MC analysis, before extracting the value of M_W, it is important to compare the diagnostic variables from FULL and FAST MC for the Z events to ensure that the parameterizations in the FAST MC are working ef-

fectively. Next the same comparisons are necessary for the W events to assure ourselves that the parameterization developed on the basis of $Z \rightarrow e^+e^-$ event information is also valid when extrapolated down to the $W \rightarrow e\nu$ events. Obtaining a good comparison for all the diagnostic variables is essential for proceeding with the determination of the W mass from the m_T, p_T^e and $\not{E}_T$ distributions in the FULL MC.

17.2 FULL MC Samples

The $Z \rightarrow e^+e^-$ FULL MC sample is used for tuning the FAST MC for the FULL MC analysis of the W mass. It contains approximately 1.8 million events, corresponding to about 6 fb^{-1} of data before any acceptance or selection cuts are applied in the analysis. The $W \rightarrow e\nu$ FULL MC sample contains about 5.8 million events before the application of any acceptance or selection cuts. It is equivalent to about 2.3 fb^{-1} of data.

17.3 Electron Response and Resolution Terms

We have read about the overall energy scale and offset for the electron model in the FAST MC in Chapter 14. The best fit values that describe the electron energy scale and offset for the FULL MC analysis are obtained from the $Z \rightarrow e^+e^-$ FULL MC sample. The Z events are selected with the standard EM requirements and both electrons are required to have a matching track. The other event selection criteria are the same as those used for the W analysis. The Z mass (M_Z) versus f_Z distributions (see Chapter 14) from the FULL MC are compared to the corresponding templates generated from the FAST MC, each template generated

for a grid point on the $\alpha - \beta$ grid. The results obtained from the fit are:

$$\alpha = 0.9997 \pm 0.0013; \qquad \beta = 0.009 \pm 0.063 \quad \text{GeV} \tag{17.1}$$

with a correlation of -0.995. The left side of Figure 17.1 shows the central value and one-sigma contour for the optimum value of the fit while the right side shows a comparison of the reconstructed Z mass distribution from the FULL and FAST MC using the fit results for the α and β. The fitted Z mass obtained from the FULL MC is 91.197 ± 0.011 GeV which is in good agreement with the input value of 91.188 ± 0.0021 GeV.

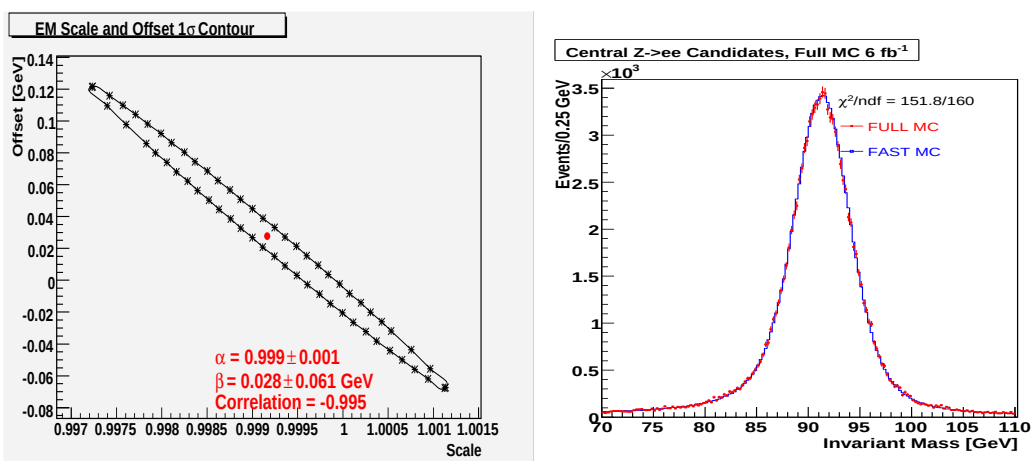

Figure 17.1. Left: Central value and one-sigma contour of electron energy scale and offset resulting from the fit. Right: $Z \to ee$ comparison between FULL MC and FAST MC

The parameterization of the electron energy resolution as shown in Chapter 14 differs from that of an ideal sampling calorimeter due to the $4X_0$ of material infront of the calorimeter. The sampling term as shown in equation 14.8 depends on the

electron energy and angle of incidence now. The values of the smearing parameters S_1 to S_5 determined for the FULL MC are:

$$S_1 = 0.152035; S_2 = 0.151266; S_3 = 1.39247; S_4 = 1.45474; S_5 = 10.3506 \quad (17.2)$$

These parameters are determined from a comparison of the energies of a special sample of single FULL MC electrons at the generator and fully reconstructed output levels. For the FULL MC analysis, the constant and noise term, C_{EM} and N_{EM}, are set to zero. The former results mainly from the channel-to-channel gain variations while the latter is basically the electronics noise, both of which are not simulated in the GEANT3-based FULL MC.

17.4 Recoil Response and Resolution Terms

We have read about the tuning parameters for the recoil model in the FAST MC in Chapter 15. In the FULL MC analysis, the recoil is tuned to the $Z \to e^+e^-$ FULL MC events. The best fit values of the tuning parameters are obtained for `RelScale` $= 1.0475 \pm 0.0059$, `RelOffset` $= 0.3063 \pm 0.0359$ and $\tau_{\texttt{HAD}} = 6.6110 \pm 1.8464$.

Figure 17.2 shows the central value and the one standard deviation contour for the `RelScale` and `RelOffset` from the tuning of the hadronic response. Figure 17.3 shows a comparison of the mean of the η imbalance between the FULL MC and FAST MC, for the ten different p_T^Z bins.

The optimal values of the parameters from the fit are for `RelSampA` $= 0.9912 \pm 0.0262$, `RelSampB` $= 0.3715 \pm 0.1764$ and $\alpha_{mb} = 0.9306 \pm 0.0185$.

Figure 17.4 shows the central value and one sigma contour of the α_{mb} and `RelSampA` from the tuning of the hadronic resolution. Figure 17.5 shows a com-

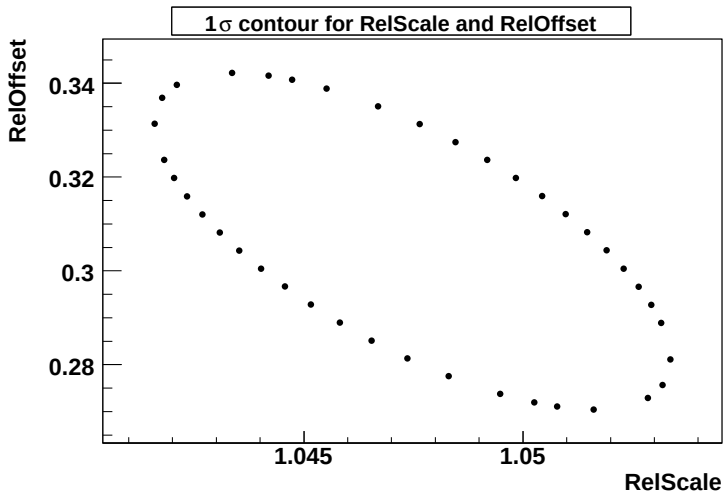

Figure 17.2. Central value and one sigma contour plot for `RelScale` and `RelOffset` corresponding to an optimum value of $\tau_{\mathtt{HAD}} = 6.6110$

parison of the width of the η imbalance between the FULL and FAST MC, for the ten different p_T^Z bins.

Now that we have parameterized the FAST MC model of the detector for the FULL MC analysis, most notably the electron and recoil systems, let us take a look at a comparison of the diagnostic plots from the control Z and the actual W samples. These comparisons are between the distributions obtained from the FULL MC samples and the FAST MC, to ensure that the latter describes the effects of the FULL MC (GEANT3) detector as accurately as necessary for this analysis. Attainment of an excellent agreement between the two sets of distributions in terms of χ^2 values and the absence of any systematic trend gives us the go ahead for extracting the value of M_W from the FULL MC $W \to e\nu$ sample.

17.5 Z Boson Comparison Results

Figure 17.6 shows the comparison and level of agreement between the FULL and FAST MC plots for $Z \to e^+e^-$ events. The FULL MC sample is the one with

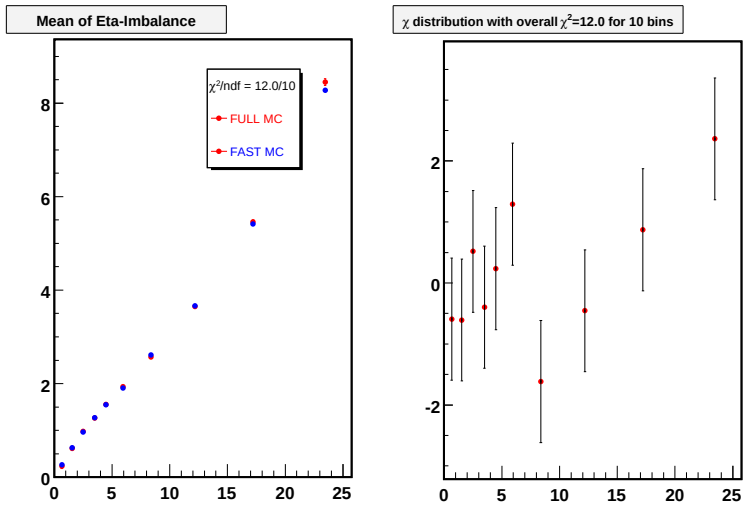

Figure 17.3. FULL and FAST MC comparison of the mean of the η imbalance for the ten different bins in p_T^Z

which the tuning has been performed. In the figure the Z mass is shown on the top left, the Z p_T on the top right, the electron p_T (p_T^e) on the bottom left and the hadronic recoil momentum on the bottom right.

Figure 17.7 shows the $u_{\parallel}$ on the top left, the $u_{\perp}$ on the top right, the η imbalance on the bottom left and the azimuthal difference between the directions of the electron and the recoil on the bottom right, for FULL and FAST MC comparisons for the $Z \rightarrow e^+e^-$ events. These plots serve as important diagnostic variables for the tuning of the recoil model in the FAST MC to match the FULL MC. Note the good χ^2 distribution for all fits which reflect that a good modeling for the recoil in the case of the FULL MC has been obtained.

17.6 W Boson Comparison Results

Figure 17.8 show the comparisons between the FULL MC and FAST MC for the diagnostic variables from $W \rightarrow e\nu$ events. The transverse mass of the W

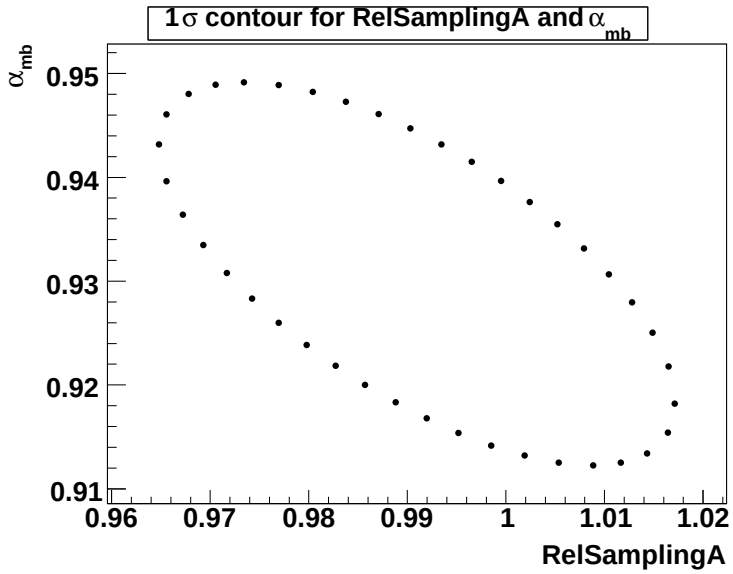

Figure 17.4. Central value and one sigma contour plot for α_{mb} and `RelSampA` corresponding to an optimum value of `RelSampB` = 0.3715

is shown on the top left while the electron p_T is shown on the top right. The transverse missing energy is shown at the bottom left of the Figure and the W p_T is shown on the bottom right.

Figure 17.9 shows a comparison of the $u_{\parallel}$, $u_{\perp}$, the recoil momentum (u_T) and the scalar E_T (SET) distributions for the W events. These are important diagnostic variables for ensuring that the recoil for the W events has been modeled as accurately as possible for the FULL MC analysis.

17.7 Fitting Procedure for Determining the W Mass

As mentioned earlier, the W mass is determined by fitting each of the three kinematic distributions of m_T, p_T^e and $\not{E}_T$ to the corresponding template distributions generated with the help of the FAST MC simulation. The templates are produced for a range of input W mass values, in steps of 10 MeV. The backgrounds

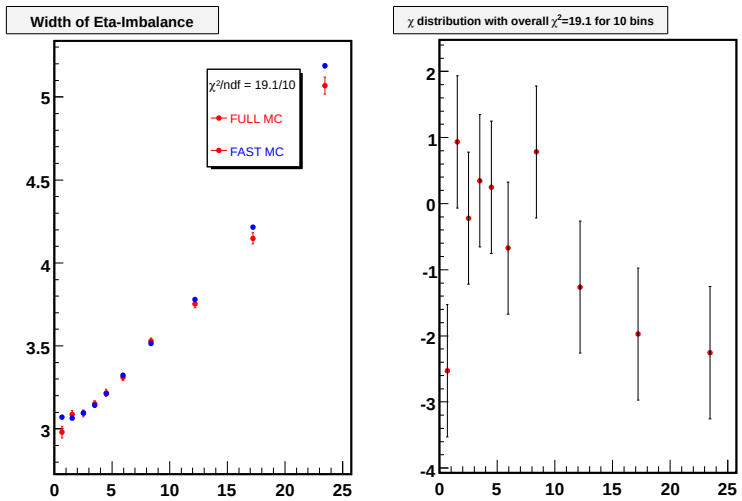

Figure 17.5. FULL and FAST MC comparison of the width of the η imbalance for the ten different bins in p_T^Z

are added to the simulated distributions.

A binned likelihood is computed between the FULL MC distribution and each template. This is done by calculating the product of the Poisson probability for each bin, with n_i observed events and m_i expected events. The probability is given by:

$$\mathcal{L} = \prod_{i=1}^{N} \frac{e^{-m_i} m_i^{n_i}}{n_i!} \tag{17.3}$$

The negative log likelihood is given as follows:

$$-\ln\mathcal{L} = \sum_{i=1}^{N} (-n_i \ \ln \ m_i + m_i + \ln \ n_i!) \tag{17.4}$$

Using the standard MINUIT [106] minimization package we find the mass that minimizes -ln $\mathcal{L}$ and the $\pm 1\sigma$ values that increase -ln $\mathcal{L}$ by 0.5. The fits are performed separately for the m_T, p_T^e and $\not{E}_T$ distributions.

17.8 W Mass Results

In the FULL MC analysis the input W mass is known. It is 80.450 GeV. Unlike the data analysis these results were not blinded. The results obtained from the fits to the W mass distributions are as follows. From a fit to the transverse mass distribution (m_T) we measure:

$$M_W = 80.441 \pm 0.015(\text{stat}) \pm 0.011(\text{syst}) \pm 0.010(\text{e} - \text{loss corr.}) \qquad \text{GeV} \quad (17.5)$$

A fit to the distribution of the transverse momentum of the electron yields:

$$M_W = 80.441 \pm 0.017(\text{stat}) \pm 0.007(\text{syst}) \pm 0.010(\text{e} - \text{loss corr.}) \qquad \text{GeV} \quad (17.6)$$

while a fit to the transverse missing energy distribution yields:

$$M_W = 80.429 \pm 0.017(\text{stat}) \pm 0.010(\text{syst}) \pm 0.010(\text{e} - \text{loss corr.}) \qquad \text{GeV} \quad (17.7)$$

These results are in excellent agreement with each other and consistent with the input value of M_W.

Each of the three kinematic FULL MC distributions along with the FAST MC template that fits best have been shown in Figures 17.10, 17.11 and 17.12. The figures also show the bin-by-bin χ values defined as the difference between the FULL MC and template divided by the uncertainty of the FULL MC.

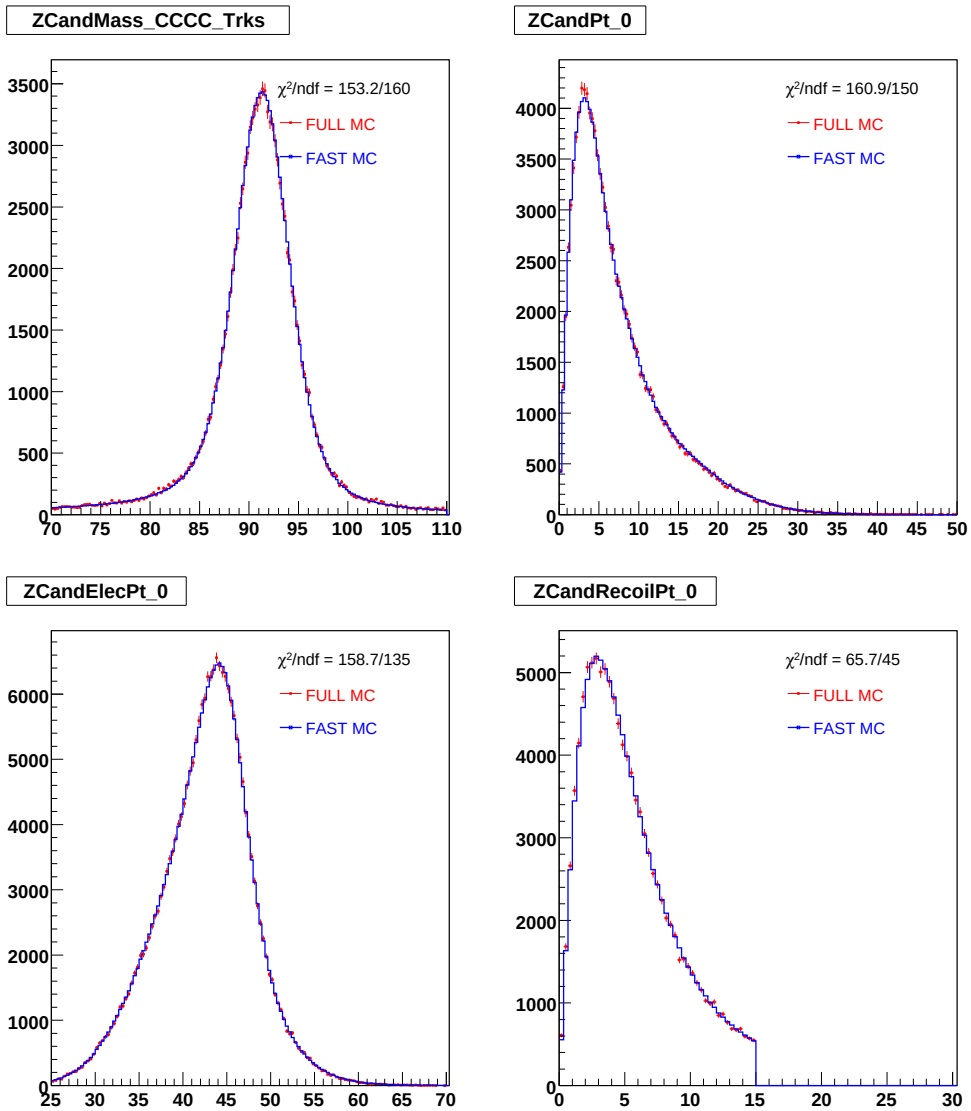

Figure 17.6. Top left: Z mass for FULL and FAST MC. Top right: Z p_T for FULL and FAST MC. Bottom left: Electron p_T for FULL and FAST MC. Bottom right: Recoil p_T for FULL and FAST MC

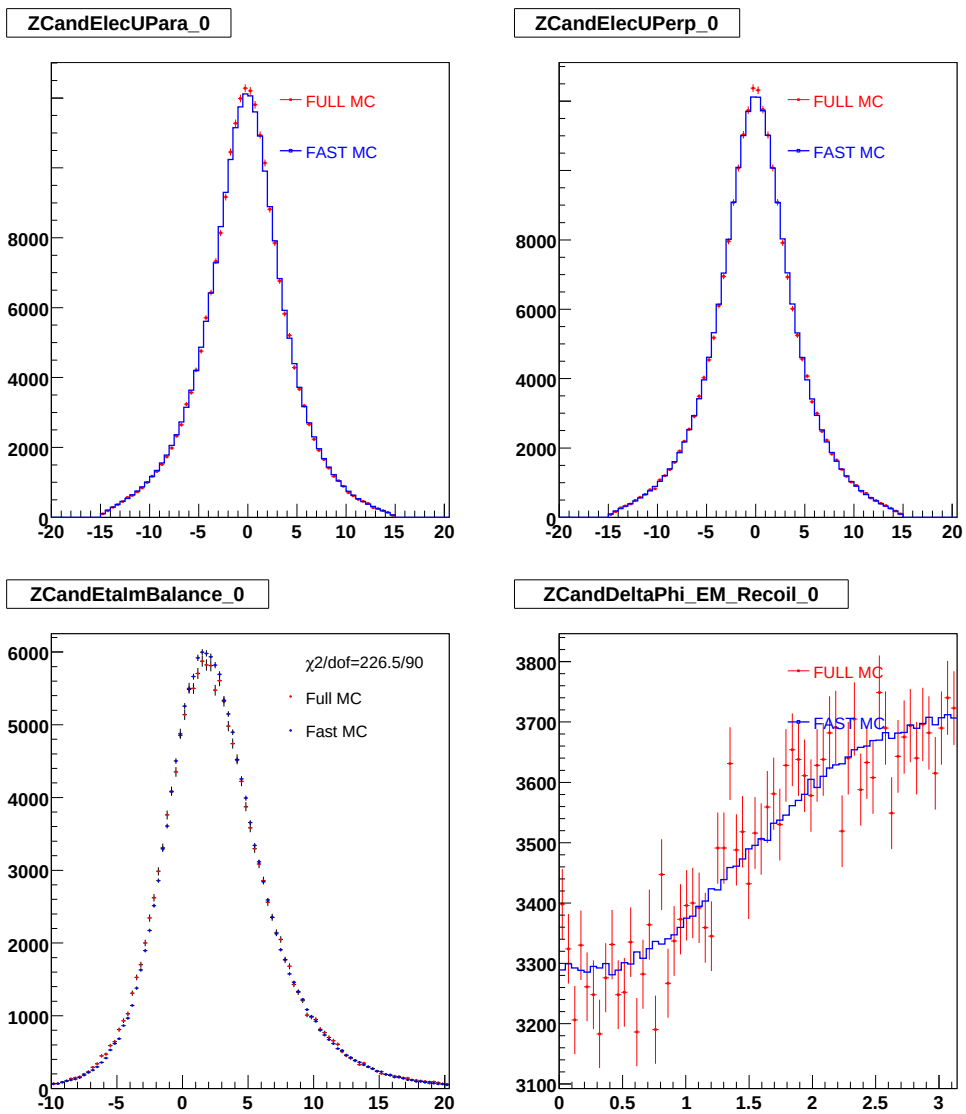

Figure 17.7. Top left: $u_{\parallel}$ for FULL and FAST MC. Top right: $u_{\perp}$ for FULL and FAST MC. Bottom left: η imbalance for FULL and FAST MC. Bottom right: $\Delta\phi$ between electron and recoil for FULL and FAST MC

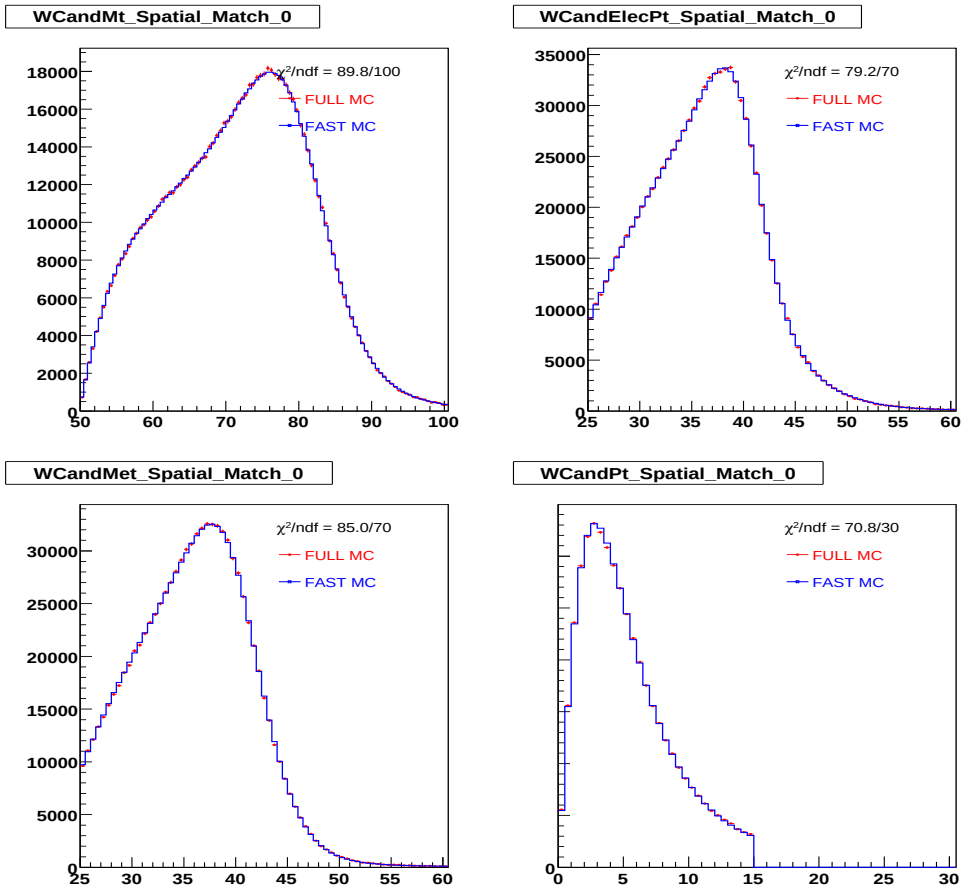

Figure 17.8. Top left: Transverse mass of W boson (m_T) for FULL and FAST MC. Top right: Electron p_T for FULL and FAST MC. Bottom left: Transverse missing energy ($\not{E}_T$) for FULL and FAST MC. Bottom right: W boson p_T for FULL and FAST MC

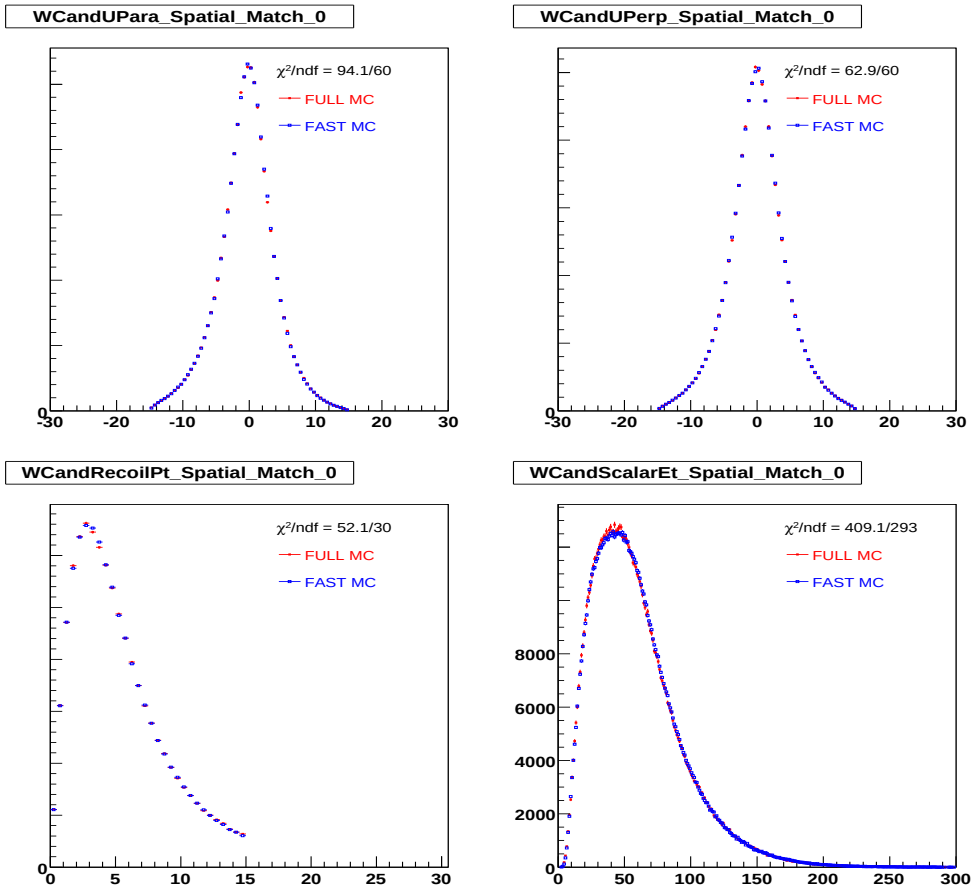

Figure 17.9. Top left: $u_{\parallel}$ for FULL and FAST MC. Top right: $u_{\perp}$ for FULL and FAST MC. Bottom left: Recoil p_T (with statistical errors only) for FULL and FAST MC. Bottom right: Scalar E_T for FULL and FAST MC

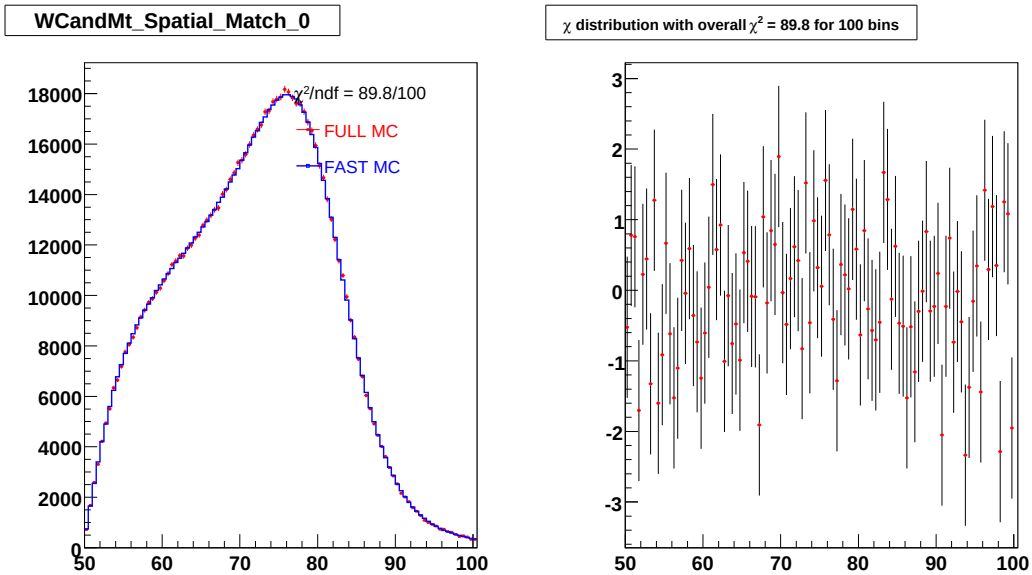

Figure 17.10. Left: The m_T distribution for FULL MC and FAST MC. Right: The χ value for each bin of the mass plot

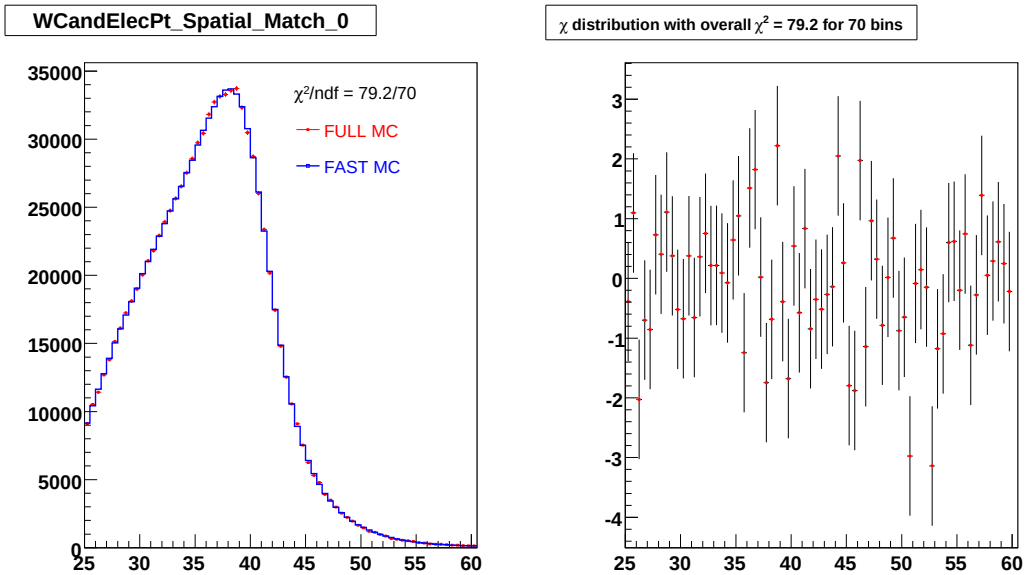

Figure 17.11. Left: The p_T^e distribution for FULL MC and FAST MC. Right: The χ value for each bin of the mass plot

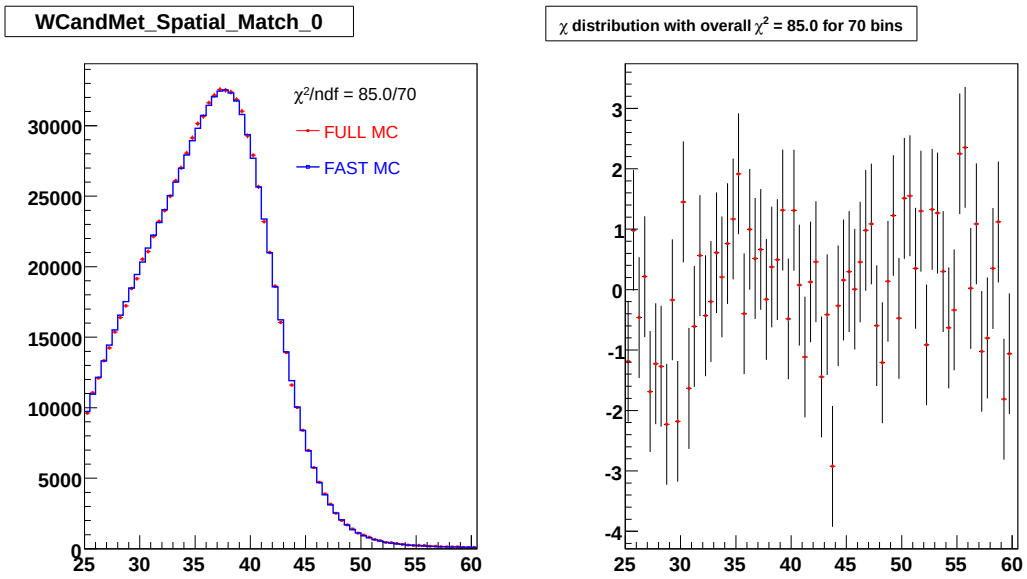

Figure 17.12. Left: The $\not{E}_T$ distribution for FULL MC and FAST MC. Right: The χ value for each bin of the mass plot

CHAPTER 18

W MASS RESULTS FROM THE COLLIDER DATA

18.1 A Brief Introduction

Before extracting the W mass from the kinematic distributions (p_T^e, m_T and $\not{E}_T$) of the $W \to e\nu$ event we need to ensure that all the parameterizations derived so far are capable of modeling the detector as accurately as necessary for the analysis. The forms of the parameterizations have been derived earlier for the FULL MC analysis, which serves as a mock analysis for making sure that each and every step of the analytical procedure is functioning effectively. For the analysis with the collider data, the values of the parameters describing the FAST MC model of the detector (e.g. the electron and recoil systems) are rederived from $Z \to e^+e^-$ collider data, which again acts as a control sample for the W data. After all the parameterization procedures with Z data are complete and have been implemented, it is necessary to check if the diagnostic observables from FAST MC match the corresponding ones from collider data for the $Z \to e^+e^-$ events. A comparison of the diagnostic plots accurate to within statistical fluctuations and a measured Z mass that is consistent with its standard world average value of 91.1876 ± 0.0021 GeV ensures that our parameterizations in the FAST MC are working effectively. It gives the signal for proceeding with the W data analysis.

The parameterizations obtained from the $Z \to e^+e^-$ events are used for the W analysis. This follows from the fact that the W and Z possess similar signatures,

thus enabling the Z to act as an excellent control sample for the W. The effect of the different masses of the W ($\sim$ 80 GeV) and Z ($\sim$ 90 GeV) are duly taken into account in the parameterizations where they can have an impact.

Thus before fitting for the W mass, a major step in the analysis is to compare the diagnostic observables from the FAST MC with those from collider data $W \rightarrow e\nu$ events, to ensure that the parameterization developed on the basis of $Z \rightarrow e^+e^-$ event information is also valid when extrapolated down to the $W \rightarrow e\nu$ events. Obtaining a good comparison for all the diagnostic variables is essential for proceeding with the determination of the W mass from the m_T, p_T^e and $\not{E}_T$ distributions.

18.2 Electron Response and Resolution Terms

We have read about the overall energy scale and offset for the electron model in the FAST MC in Chapter 14. The best fit values that describe the electron energy scale and offset for the data analysis are obtained from the $Z \rightarrow e^+e^-$ collider data sample which acts as an excellent control sample for the $W \rightarrow e\nu$ events. The Z events are selected with the standard EM requirements and both electrons are required to have a matching track. The other event selection criteria are the same as those used for the W analysis. The Z mass (M_Z) versus f_Z distributions (see Chapter 14) from the data are compared to the corresponding templates generated from the FAST MC, each template generated for a grid point on the $\alpha - \beta$ grid. The results obtained from the fit are:

$$\alpha = 1.0111 \pm 0.0043; \qquad \beta = -0.40 \pm 0.21 \quad \text{GeV} \tag{18.1}$$

with a correlation of -0.997. Figure 18.1 shows the projections of the χ^2 onto the α and β axes and the one-sigma contour for the optimum position of the fit. Details of the determination of the response parameters can be found in [141].

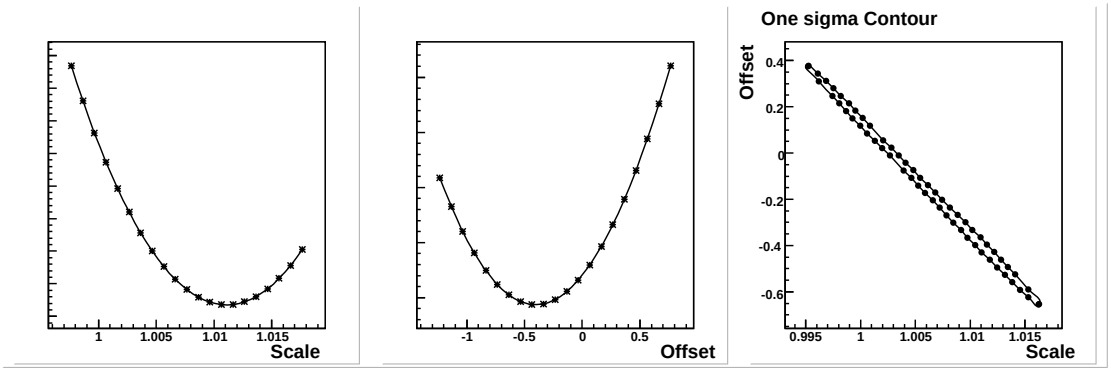

Figure 18.1. χ^2 projections on the α and β axes; Correlation between the α-β values

Just like in the FULL MC, the parameterization of the electron energy resolution here in data, as shown in Chapter 14 differs from that of an ideal sampling calorimeter. It now depends on the electron energy and angle of incidence as shown in equation 14.8. The values of the smearing parameters S_1 to S_5 determined for the data analysis are:

$$S_1 = 0.1633; \quad S_2 = -10.0; \quad S_3 = 0.0; \quad S_4 = 0.0; \quad S_5 = 0.0 \tag{18.2}$$

The values of these parameters are derived from $Z \rightarrow e^+e^-$ data. The main contribution to the electron energy resolution at high energies such as the Z and W comes from the constant term (see Chapter 14), C_{EM}. The value of C_{EM} is derived from a fit to the width of the Z mass distribution with the sampling and

noise terms fixed. The fit can be done either by using a Voight function to fit the width of the M_Z distribution or by using templates similar to the method used to determine the response parameters (α and β). For the latter, templates of the Z mass are produced for different values of the constant term and the optimum value of C_{EM} is extracted from the template that fits the corresponding data distribution best. For the Run IIa data, the value of the constant term is found to be:

$$C_{EM} = 2.04 \pm 0.13\% \tag{18.3}$$

The noise term (N_{EM}) is found to be 0.29 GeV. This term has a negligible contribution at high energies due to its $1/E^2$ dependence. The contribution from the sampling term is also suppressed due to its $1/E$ dependence. More details of the determination of C_{EM} can be found in [142].

18.3 Recoil Response and Resolution Terms

We have read about the tuning parameters for the recoil model in the FAST MC in Chapter 15. In the M_W analysis with the collider data, the recoil is tuned to the $Z \to e^+e^-$ events from data. The best fit values are obtained for `RelScale` = 0.9413 ± 0.0109, `RelOffset` = 1.2016 ± 0.1783 and $\tau_{\texttt{HAD}}$ = 3.1758 ± 0.8981. For details of the tuning procedure please refer to [143].

Figure 18.2 shows the central value and the one standard deviation contour for the `RelScale` and `RelOffset` from the tuning of the hadronic response. Figure 18.3 shows a comparison of the mean of the η imbalance between the data and FAST MC, for the ten different p_T^Z bins.

The optimal values of the parameters from the fit are for `RelSampA` = 1.0839 ± 0.0573, `RelSampB` = 0.0 and α_{mb} = 0.6180 ± 0.0662.

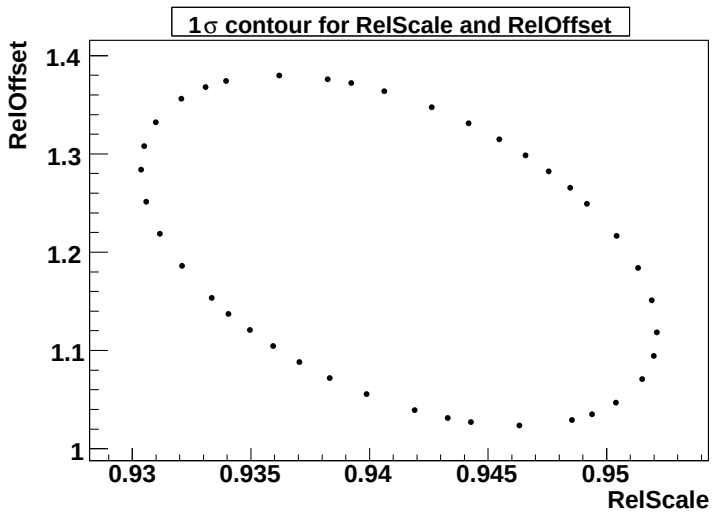

Figure 18.2. Central value and one sigma contour plot for `RelScale` and `RelOffset` corresponding to an optimum value of $\tau_{\mathtt{HAD}} = 3.1758$

Figure 18.4 shows the central value and one sigma contour of the α_{mb} and `RelSampA` from the tuning of the hadronic resolution. Figure 18.5 shows a comparison of the width of the η imbalance between the data and FAST MC, for the ten different p_T^Z bins.

Now that we have parameterized the FAST MC model of the detector for the collider data analysis, most notably the electron and recoil systems, let us take a look at a comparison of the diagnostic plots from the control Z and the actual W samples. These comparisons are between the distributions obtained from the data samples and the FAST MC, to ensure that the latter describes the effects of the real detector as accurately as necessary for the analysis. An excellent agreement between the distributions of the W and Z in terms of χ^2 values and the absence of any systematic trend is important for obtaining the go ahead to extract the value of M_W from the data.

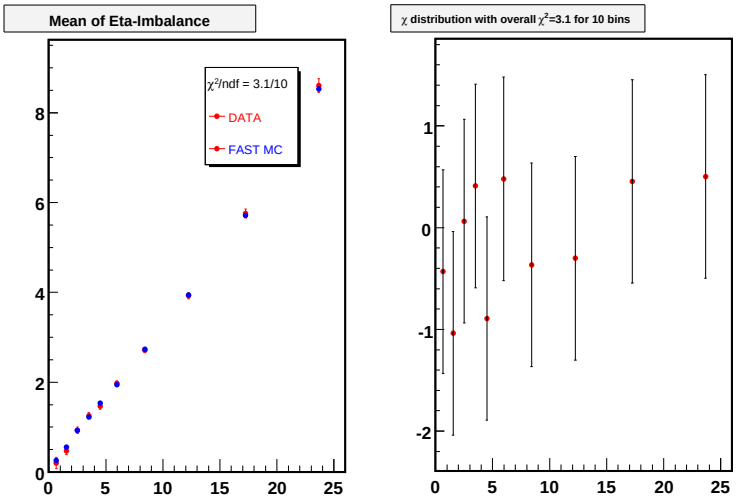

Figure 18.3. DATA and FAST MC comparison of the mean of the η imbalance for the ten different bins in p_T^Z

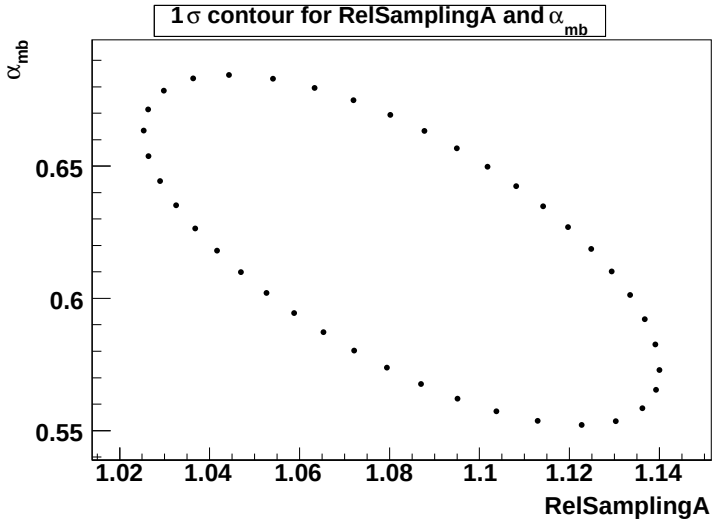

Figure 18.4. Central value and one sigma contour plot for α_{mb} and `RelSampA` corresponding to an optimum value of `RelSampB` $= 0.0$

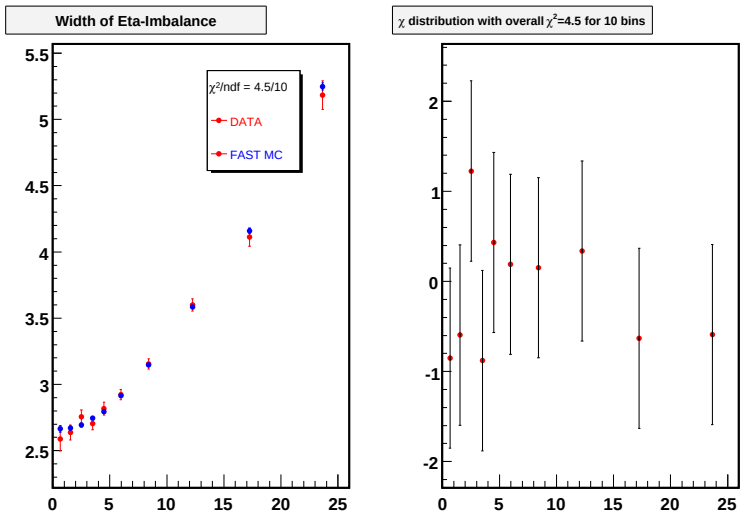

Figure 18.5. DATA and FAST MC comparison of the width of the η imbalance for the ten different bins in p_T^Z

18.4 Z Boson Comparison Results

The Figure 18.6 shows the comparison and level of agreement between the collider data and FAST MC for diagnostic variables from $Z \rightarrow e^+e^-$ events. The collider data sample is the one with which the tuning has been performed. The Z mass is shown on the top left, the Z p_T on the top right, the electron p_T (p_T^e) on the bottom left and the hadronic recoil momentum on the bottom right.

We notice a slight discrepancy in the Z p_T plot which also has a large χ^2/dof. A detailed probe into this momentum plot has shown disagreement in the low p_T region. Figure 18.7 shows the χ distribution with the systematic uncertainties from the theoretical parameter g_2, the "Phimod corrections" due to the less responsive intermodular regions of the calorimeter and the errors from the parton distribution functions (PDF) included. This combined systematic covers the possible variation

seen in the low p_T region and helps explain the discrepancy.

Figure 18.8 shows the $u_{\parallel}$ on the top left, the $u_{\perp}$ on the top right, the η imbalance on the bottom left and the azimuthal difference between the directions of the electron and the recoil on the bottom right, for data and FAST MC comparisons for the $Z \to e^+e^-$ events. These plots serve as important diagnostic variables for the tuning of the recoil model in the FAST MC to match the data. Note the good χ^2 distribution for all fits which reflect that a good modeling for the recoil in the case of the data has been obtained.

18.5 W Boson Comparison Results

The Figure 18.9 shows the comparisons between the collider data and FAST MC for the diagnostic variables from $W \to e\nu$ events. The transverse mass of the W is shown on the top left while the electron p_T is shown on the top right. The transverse missing energy is at the bottom left of the Figure and the W p_T is shown on the bottom right.

Figure 18.10 shows a comparison of the $u_{\parallel}$, $u_{\perp}$ and the recoil momentum (u_T) distributions for the W events. These are important diagnostic variables for ensuring that the recoil for the W events has been modeled as accurately as possible for the analysis. At a first glance it seems like the distributions show a significant disagreement between the data and FAST MC, particularly in the recoil variables. This is because the error bars reflect the fluctuations due to the W statistics only and do not reflect the effects of the limited Z statistics that have been used for the calibration of the recoil model. When we take into account the fluctuations due to the recoil parameters (e.g. `RelScale`, `RelOffset`, `RelSamplingA`, etc.) that were tuned with the help of the Z data, we see that the

discrepancy narrows down. This has been shown in a more quantitative way in the bottom right plot of Figure 18.10.

18.6 Fitting Procedure for Determining the W Mass

As mentioned earlier, the W mass is determined by fitting each of the three kinematic distributions of m_T, p_T^e and $\not{E}_T$ to the corresponding template distributions generated with the help of the FAST MC simulation. The templates are produced for a range of input W mass values, in steps of 10 MeV. The backgrounds are added to the simulated distributions.

A binned likelihood is computed between the data and each template. This is done by calculating the product of the Poisson probability for each bin, with n_i observed events and m_i expected events. The probability is given by:

$$\mathcal{L} = \prod_{i=1}^{N} \frac{e^{-m_i} m_i^{n_i}}{n_i!} \tag{18.4}$$

The negative log likelihood is given as follows:

$$-\ln\mathcal{L} = \sum_{i=1}^{N} (-n_i \ln m_i + m_i + \ln n_i!) \tag{18.5}$$

Using the standard MINUIT minimization package we find the mass that minimizes -ln $\mathcal{L}$ and the $\pm 1\sigma$ values that increase -ln $\mathcal{L}$ by 0.5. The fits are performed separately for the m_T, p_T^e and $\not{E}_T$ distributions.

18.7 W Mass Results

The values of the W mass as obtained from the fits were blinded in the early stages of the collider data analysis. The blinding was achieved with the help of

a constant but hidden offset embedded in the fitter, that shifted the central W mass values by that amount [109]. The uncertainties, both for the Z and W were never obscured so that the various tuning procedures could be carried out to their maximum accuracy and the internal consistency checks could be performed without any knowledge of the final W mass result. The results were unblinded once the analysis had been approved by the collaboration.

Since the Z has been used extensively as a control sample for the W, for calibrating the electron and recoil systems for the data analysis, it is important to fit for the reconstructed Z mass first. The Z mass fit obtained from the collider data $Z \to e^+e^-$ sample is shown in Figure 18.11. For an input value of $M_Z = 91.188 \pm 0.0021$ GeV used in the tuning, the value returned from the fit after all the tuning procedures was 91.185 ± 0.033 (stat) GeV. This result is in agreement with its input, reiterating the fact that the forms and values of the parameterizations for the FAST MC have been derived quite accurately and are working effectively for the analysis. We now proceed to fit confidently for the M_W using the $W \to e\nu$ collider data sample and W mass templates made from the FAST MC. For details on the data analysis of the W mass please refer to [147].

The ranges for the W mass fits are important, they help us extract the maximum information from the kinematics of the W decay. The fit ranges are chosen such that they minimize the detector effects on the kinematic variable (for small values of the variable) and the effects of a finite decay-width (for large values of the variable). The m_T distribution is fit in the range 65-90 GeV, while each of the p_T^e and $\not{E}_T$ distributions have a fit range of 32-48 GeV. Each of the distributions is fit separately. The W mass results obtained after the unblinding are as follows.

From a fit to the transverse mass distribution (m_T) we measure:

$$M_W = 80.401 \pm 0.023(\text{stat}) \pm 0.037(\text{syst}) \qquad \text{GeV} \tag{18.6}$$

A fit to the distribution of the transverse momentum of the electron yields:

$$M_W = 80.400 \pm 0.027(\text{stat}) \pm 0.040(\text{syst}) \qquad \text{GeV} \tag{18.7}$$

while a fit to the transverse missing energy distribution yields:

$$M_W = 80.402 \pm 0.023(\text{stat}) \pm 0.043(\text{syst}) \qquad \text{GeV} \tag{18.8}$$

These results are in excellent agreement with each other.

Each of the three kinematic data distributions along with the FAST MC template that fits best have been shown in Figures 18.12, 18.13 and 18.14. The figures also show the bin-by-bin χ values defined as the difference between the data and template divided by the uncertainty of the data and show the likelihood as a function of the assumed W mass.

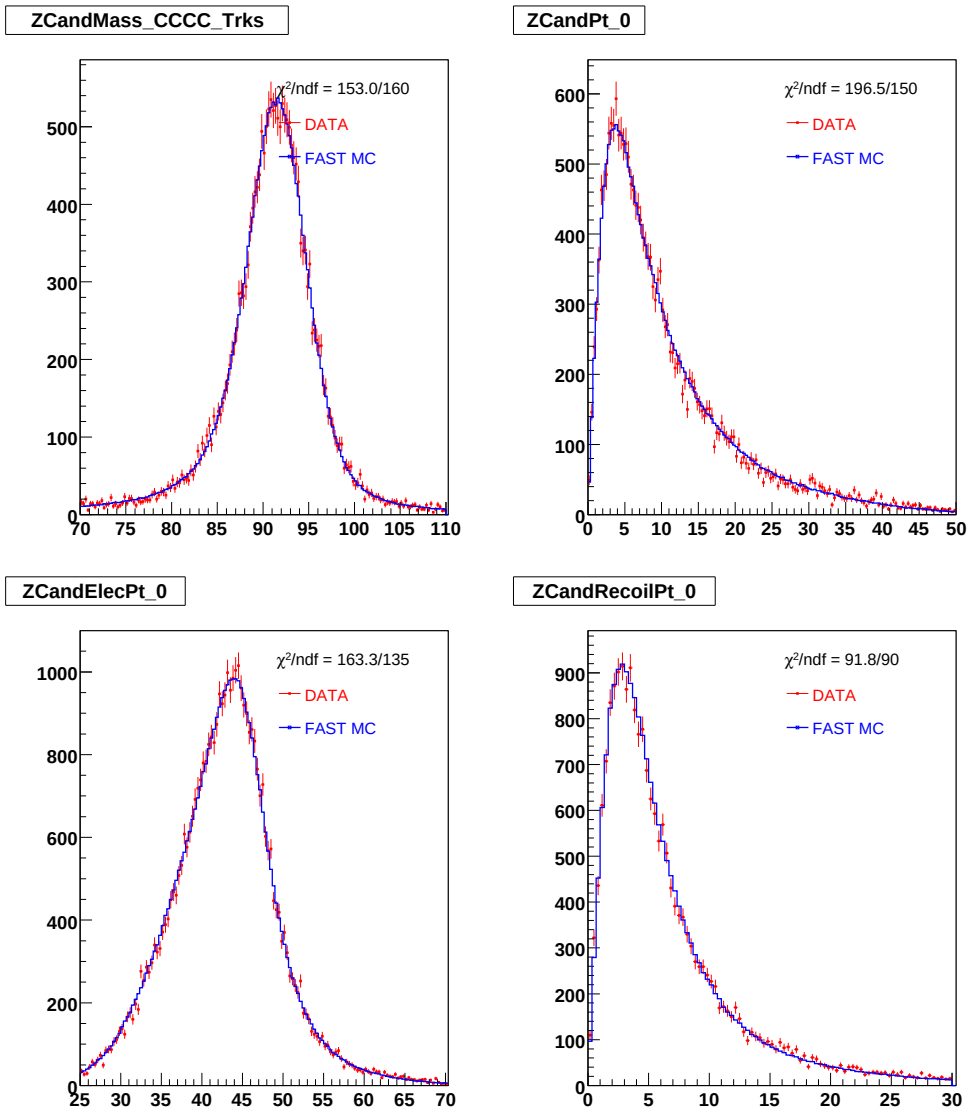

Figure 18.6. Top left: Z mass for data and FAST MC. Top right: Z p_T for data and FAST MC. Bottom left: Electron p_T for data and FAST MC. Bottom right: Recoil p_T for data and FAST MC

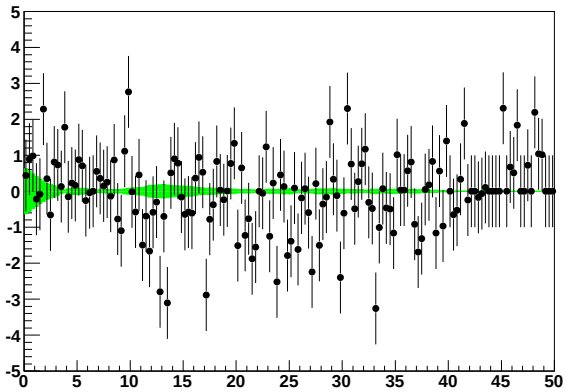

Figure 18.7. Contribution of the g_2, PDF and ϕ-crack position-correction systematics (green band) to the χ of the Z p_T comparison between data and FAST MC. The Poisson probability of statistical agreement (no systematics considered) between data and FAST MC corresponds to $\chi^2/dof = 168/150$

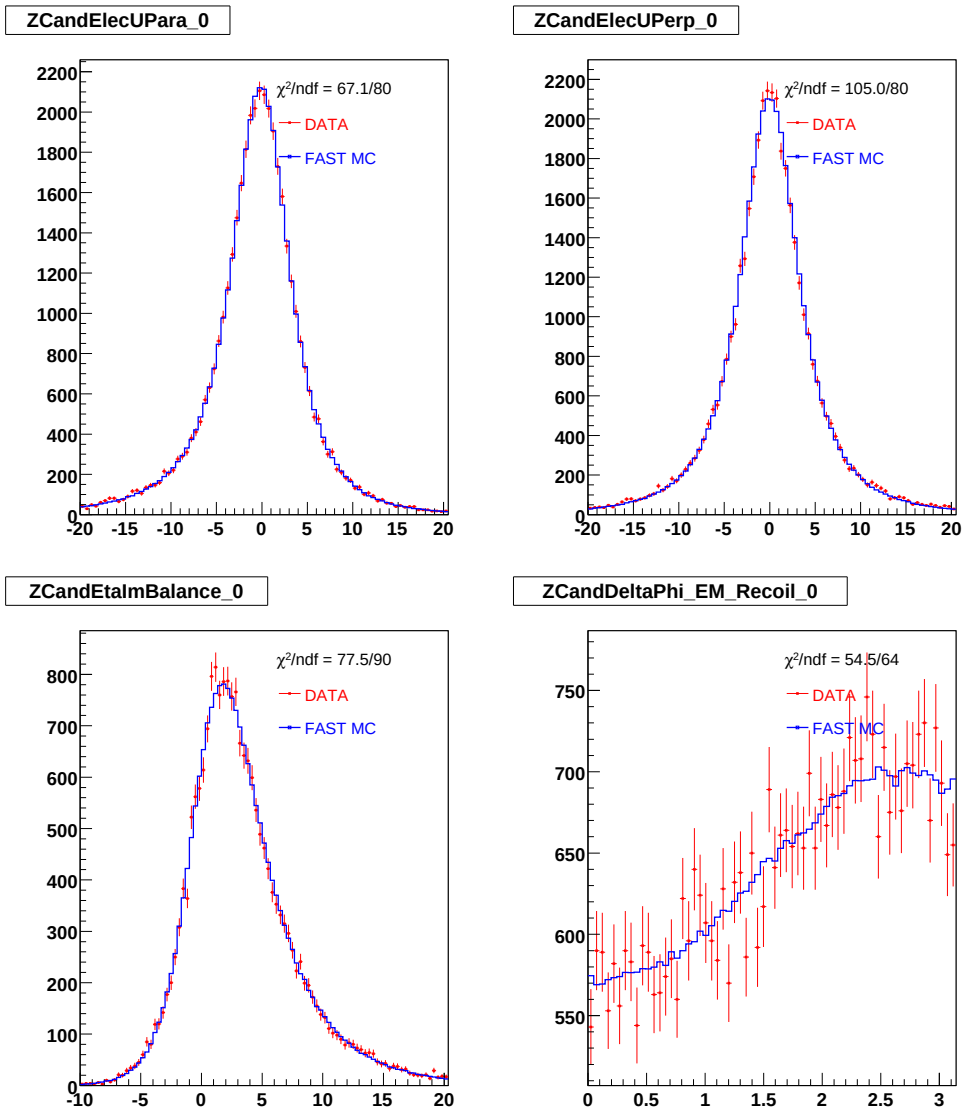

Figure 18.8. Top left: $u_{\parallel}$ for data and FAST MC. Top right: $u_{\perp}$ for data and FAST MC. Bottom left: η imbalance for data and FAST MC. Bottom right: $\Delta\phi$ between electron and recoil for data and FAST MC

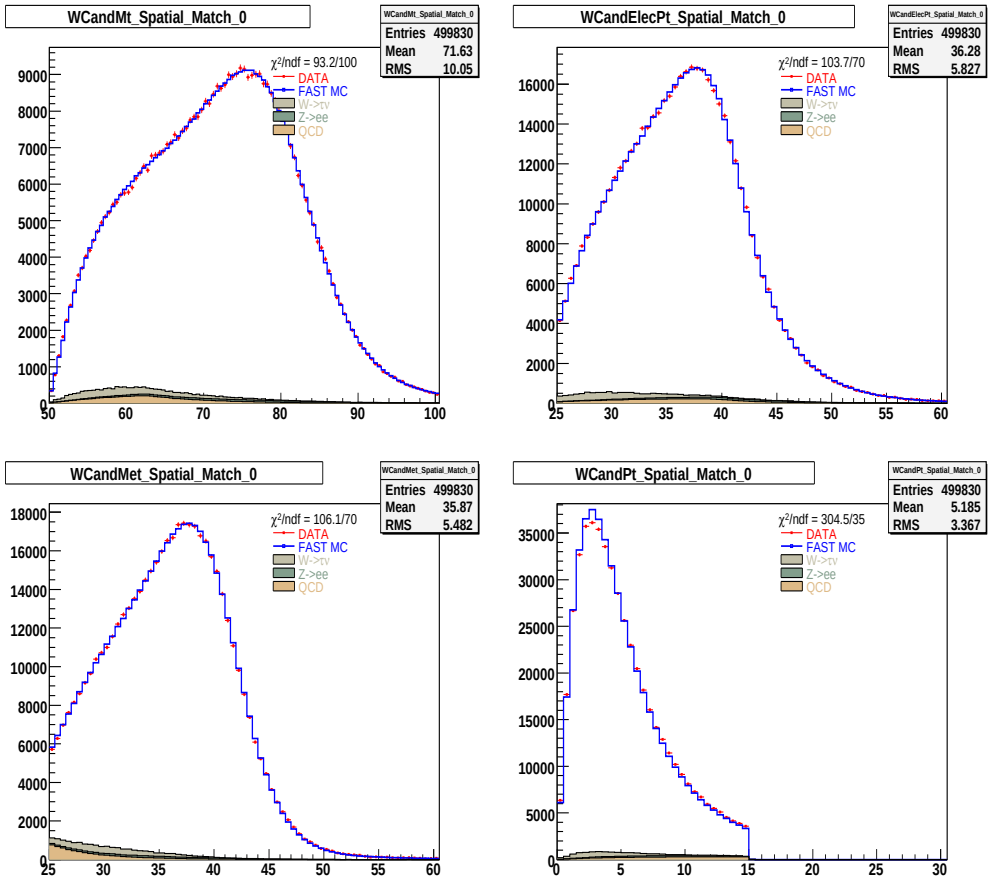

Figure 18.9. Top left: Transverse mass of W boson (m_T) for data and FAST MC. Top right: Electron p_T for data and FAST MC. Bottom left: Transverse missing energy ($\not{E}_T$) for data and FAST MC. Bottom right: W boson p_T for data and FAST MC

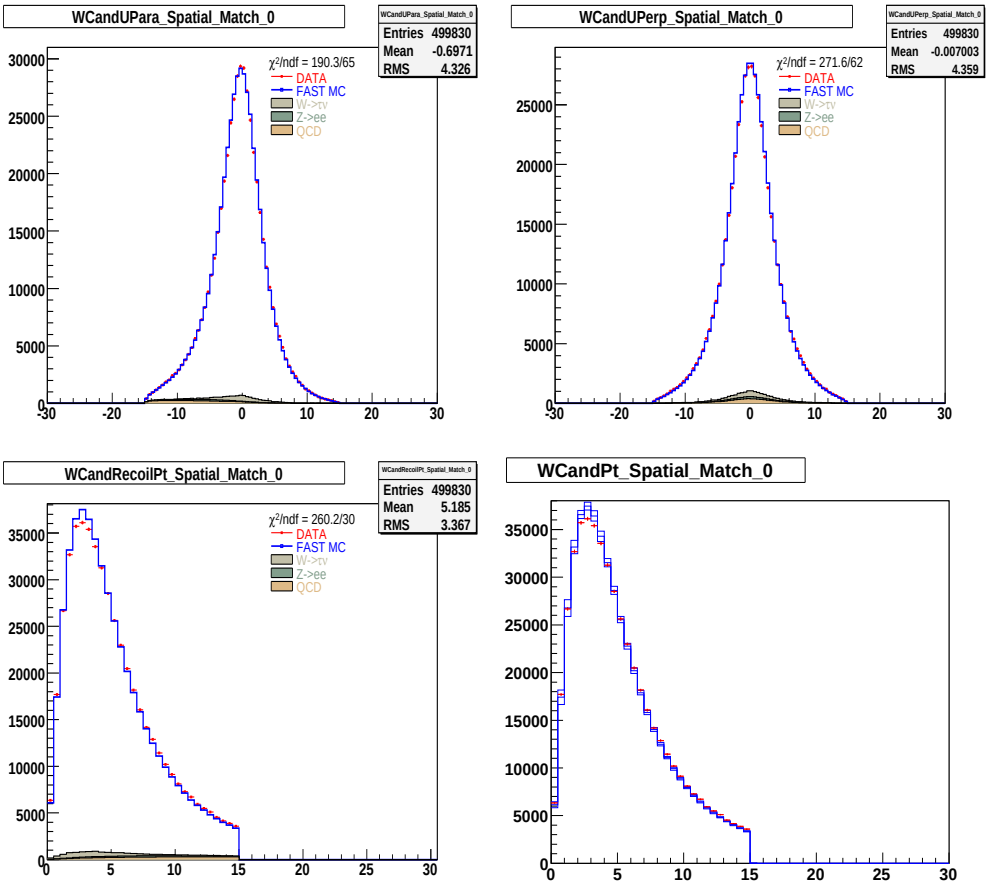

Figure 18.10. Top left: $u_{\parallel}$ for data and FAST MC. Top right: $u_{\perp}$ for data and FAST MC. Bottom left: Recoil p_T (with statistical errors only) for data and FAST MC. Bottom right: Recoil p_T (now including errors of tuning parameters) for data and FAST MC

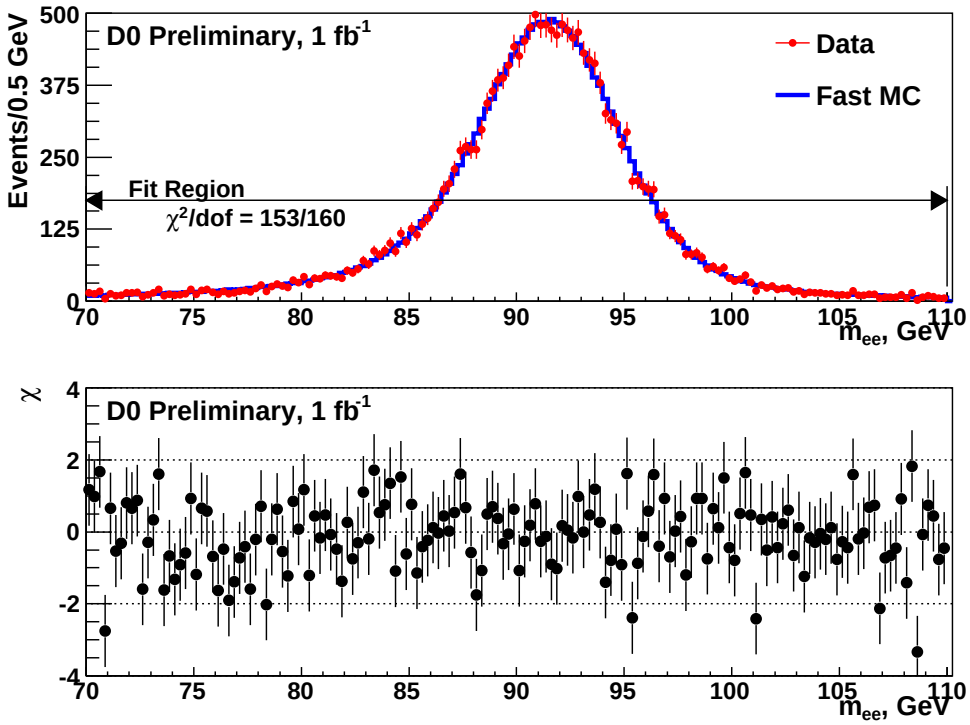

Figure 18.11. Top: The reconstructed Z mass from data and from the FAST MC. Bottom: The χ values for each bin of the mass plot. The agreement is quite good, giving $\chi^2/\text{dof} = 153/160$

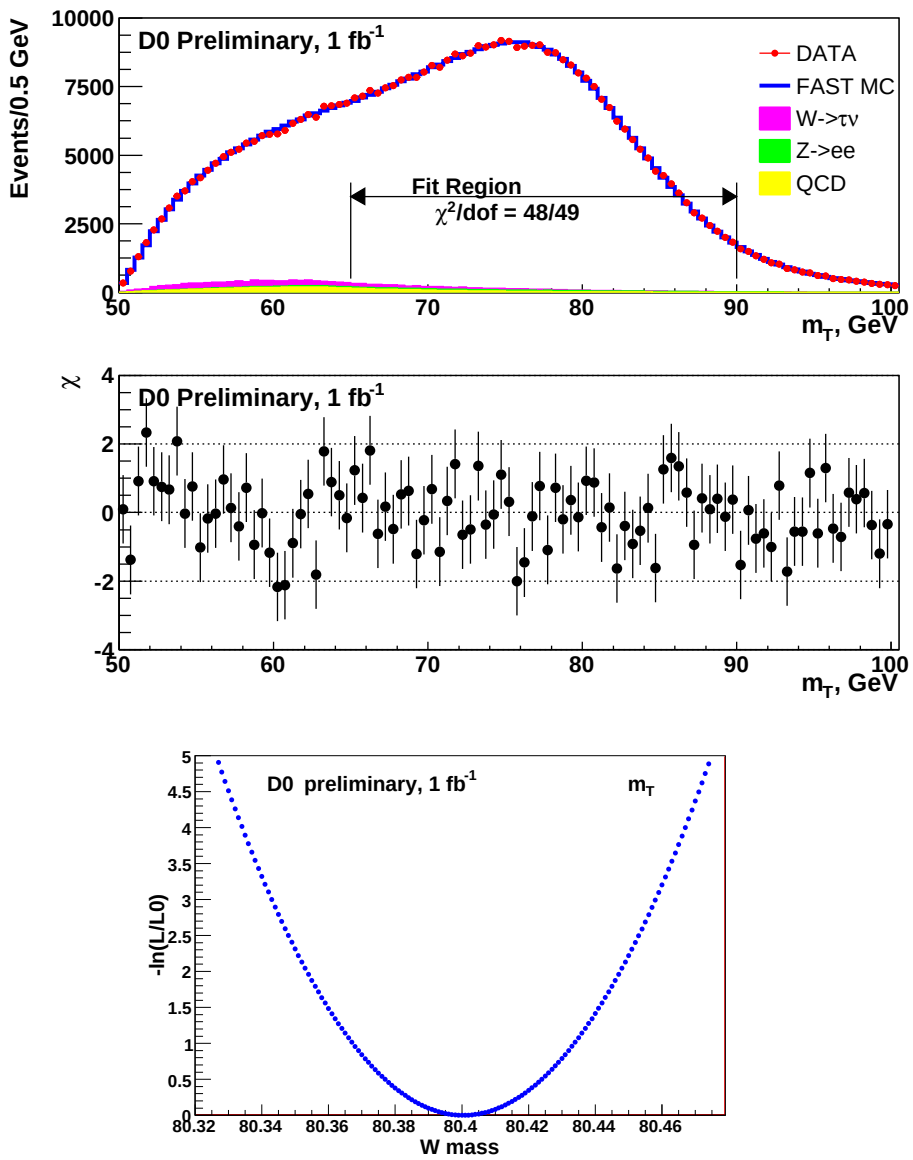

Figure 18.12. Top: The m_T distribution for data and FAST MC with the backgrounds added. Center: The χ value for each bin of the mass plot. Bottom: The negative log of the likelihood ratio L/L_0 where L_0 is the maximum likelihood as a function of M_W

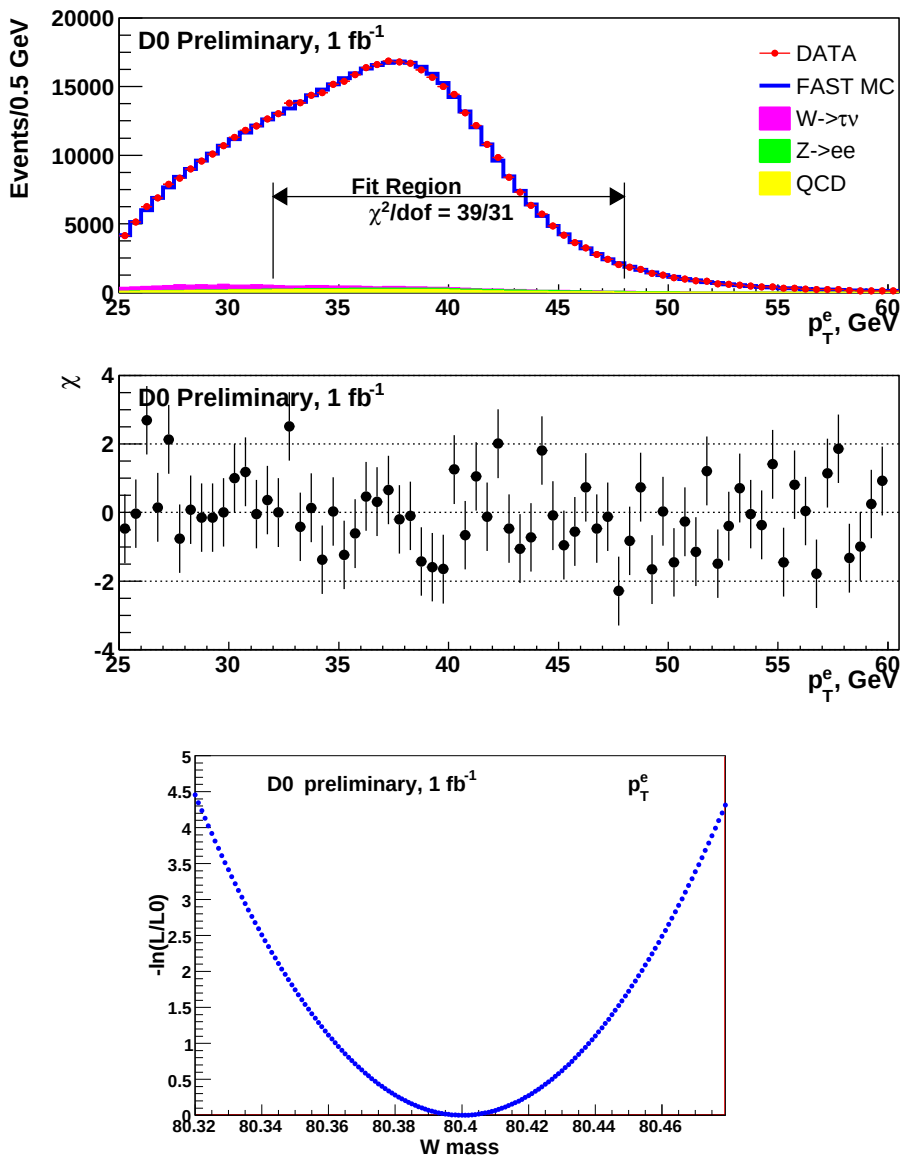

Figure 18.13. Top: The p_T^e distribution for data and FAST MC with the backgrounds added. Center: The χ value for each bin of the mass plot. Bottom: The negative log of the likelihood ratio L/L_0 where L_0 is the maximum likelihood as a function of M_W

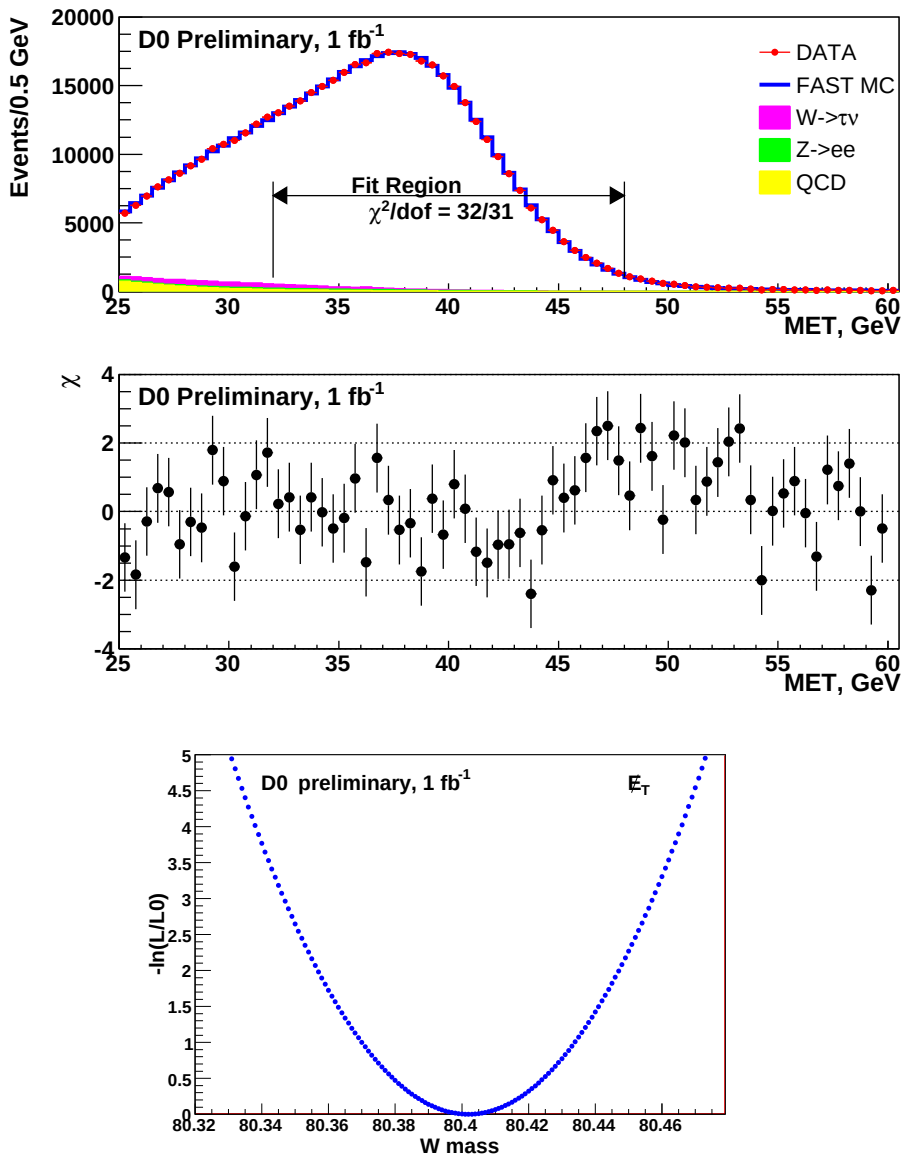

Figure 18.14. Top: The $\not\!\!E_T$ distribution for data and FAST MC with the backgrounds added. Center: The χ value for each bin of the mass plot. Bottom: The negative log of the likelihood ratio L/L_0 where L_0 is the maximum likelihood as a function of M_W

CHAPTER 19

SYSTEMATIC UNCERTAINTY ON THE W MASS MEASUREMENT

19.1 An Introduction

In a precision measurement like this one, uncertainties associated with the measured W mass value play a very important role. In most experimental measurements there are two major sources of uncertainties, statistical and systematic. Statistical as the name suggests comes from the size or statistical limit on the W or Z sample. The systematics uncertainties arise from all possible sources associated with the measurement, such as theoretical predictions of the process and event kinematics, to experimental ones like the energy scales and resolution, etc. The combined uncertainty indicates the precision of a particular measurement.

In our analysis the W mass can be obtained from fits to three different variables obtained from the collider data. These are the distributions of the transverse mass (m_T), transverse momentum of the electron (p_T^e) and the transverse momentum of the neutrino (p_T^ν or $\not{E}_T$). Hence in this chapter we refer to them as the MT, PT and MET methods respectively, when we mention the systematics for a particular source derived from each of these distributions.

As we know, the W mass is extracted from the above mentioned observables with the help of templates produced by the parameterized FAST MC. The FAST MC has to describe the effects of the actual DØ detector to within reasonable

accuracies if it is to be used for producing all of the required templates. Hence it is important to know what the effect on the W mass would be if the parameters that help emulate the various detector effects in the FAST MC were not as accurate as they should be for an ideal measurement of the W mass. In other words, this chapter discusses the uncertainties on the measured W masses that could arise from the mis-measurements of the various parameters. As we know some of the parameters are essential for sculpting the energies of the leptons and hadrons while some contribute in other ways to retrieving the correct value of the W mass from the signatures of the $W \to e\nu$ events.

The standard procedure for determining the shifts in the W mass due to the various uncertainties of the measured parameters here is by performing FAST MC studies. The main steps of these studies can be outlined as follows:

1. A large ensemble of high statistics FAST MC $W \to e\nu$ samples are generated by varying the optimal value of the relevant parameter, in steps of its standard deviation ($\pm 1\sigma$, $\pm 2\sigma$). The other parameters are held constant, only one parameter is varied at a time. These FAST MC samples are also called pseudo-experiments or "fake data" samples and are referred to as "FAST MC toys" in this chapter.

2. One hundred high statistics, FAST MC templates are made by varying the W mass in a range, in steps of 10 MeV. The templates are made at the optimal settings of all the parameters (including the relevant one).

3. The W mass is determined by fitting the FAST MC toys to the templates, in this way we have at least five average values of M_W for the optimal value of the parameter and for the steps of its standard deviation. The errors on these fits reflect the statistical error on the simulation.

4. The slope or "sensitivity" is denoted as $\Delta M_W/\Delta P$, where P is the parameter that has been varied. ΔM_W is the difference between the true value of M_W and the M_W values obtained from the FAST MC toys made by varying the parameter P. ΔP is the variation of the parameter P ($\pm 1\sigma$, $\pm 2\sigma$) in a range about its optimal value. The sensitivity is determined from a linear fit to the values of ΔM_W versus ΔP.

This sensitivity is then used in the usual formula for error propagation and is given by:

$$\sigma^2_{M_W}(P) \simeq \left(\frac{\Delta M_W}{\Delta P}\right)^2 \sigma^2_P \tag{19.1}$$

where $\frac{\Delta M_W}{\Delta P}$ is the slope and σ_P is the uncertainty on parameter P. The $\simeq$ sign indicates that instead of using the actual error $(P_0 - P)$ on the parameter that contributes to the final error, we estimate the error on the final result by the product of the error on the parameter and the effect that the parameter has on the final value of M_W. The above formula can be used to propagate the errors for parameters that are not correlated with each other.

In the event of determining errors on the W mass due to correlated parameters (P_1, P_2, P_3, ...) for any of the three methods mentioned above, we utilize the correlation coefficients or covariance matrices obtained from the fit results for the correlated parameters. This ensures that the correlation between the parameters is accounted for correctly. The general expression [148] for combining the standard deviations of individual parameters for estimating the total uncertainty on the M_W result is given as:

$$\sigma^2_{M_W}(P_1, P_2, ...) \simeq \sigma^2_{P_1}\left(\frac{\Delta M_W}{\Delta P_1}\right)^2 + \sigma^2_{P_2}\left(\frac{\Delta M_W}{\Delta P_2}\right)^2 + 2\cdot\sigma^2_{P_1P_2}\left(\frac{\Delta M_W}{\Delta P_1}\right)\left(\frac{\Delta M_W}{\Delta P_2}\right) + ... \tag{19.2}$$

where

- $\sigma^2_{M_W}$ is the square of the uncertainty on the final result i.e. M_W
- $\sigma^2_{P_1}$ and $\sigma^2_{P_2}$ are the individual variances of the correlated variables P_1 and P_2
- $\sigma^2_{P_1 P_2}$ is the covariance between the variables P_1 and P_2
- $\frac{\Delta M_W}{\Delta P_1}$ and $\frac{\Delta M_W}{\Delta P_2}$ are the slopes or sensitivities when variables P_1 and P_2 are varied

With these definitions, the standard deviation on the final result (in this case the W mass) is determined by making use of the determined sensitivities and uncertainties and covariance matrices in the case of correlated parameters.

The systematics on the W mass are broadly categorized into the experimental and theoretical uncertainties. The theoretical uncertainties mainly arise from the errors associated with modeling the production and decay of the vector bosons such as errors on the parton distribution functions, uncertainty on the W and Z boson p_T and errors associated with the electroweak corrections. The experimental systematics are mostly associated with the understanding of the energy of the leptons, recoil momentum, backgrounds and efficiencies. We look at each of these sources of systematics in detail in this chapter.

Table 19.1 provides a compilation of the various uncertainties associated with this W mass measurement.

19.2 Experimental Uncertainties

19.2.1 Electron Energy Scale

The precision with which we measure the absolute energy scale and offset ($E_{\text{response}} = \alpha \times E_{\text{true}} + \beta$) for the electron is the source of the dominant systematic. The uncertainties on the electron energy scale and offset (Chapter 14) are individually large and both the parameters are highly anti-correlated (-99.7 %) as shown in the Figure 18.1. Using this correlation the uncertainty on the W mass due to these two scale factors is estimated to be 33 MeV, from any of the three, m_T, p_T^e or $\not{E}_T$ distributions. Most of this uncertainty comes from the statistical limit of the $Z \rightarrow e^+e^-$ sample that is used to fit for the scale and offset here. With only $\sim$ 19,000 CC Z events for this measurements, more statistics in this sample would certainly help in lowering the uncertainty due to the scale.

19.2.2 Electron Energy Resolution

The systematic due to the energy resolution $\left(\frac{\sigma_E}{E} = \sqrt{C_{EM}^2 + \frac{S_{EM}^2}{E} + \frac{N_{EM}^2}{E^2}}\right)$ requires the measurement of the constant term (C_{EM}) in the FAST MC toys. Since the constant term is correlated with the sampling term (which has been parameterized as a function of X_0 for the calorimeter), part of the uncertainty introduced by the sampling term will be compensated for by the determination of the constant term. The uncertainty on the W mass due to the uncertainty in the constant term is small, 2 MeV for the PT method and 3 MeV each for the MT and MET methods.

19.2.3 Electron Energy Non-Linearity

The precision with which the material upstream of the calorimeter has been determined also contributes directly to the W mass by way of the electron energy. As we have read earlier, the energy-loss corrections are determined from $Z \rightarrow e^+e^-$ events. The fact that we are effectively measuring a ratio of M_W/M_Z depends on the critical assumption that the calibration and tuning done at the Z mass can be scaled down to the W mass. A mis-measurement in the material distribution could be a potential source of a non-linearity in this scaling. The determination of this systematic is complicated by the fact that the energy-loss corrections are used in the calibration and reconstruction of the electron energies, besides the tuning of the Parameterized Monte-Carlo Simulation.

For determining the systematics we basically make a large ensemble of FAST MC toy samples by "undoing" the energy-loss corrections determined for the amount of material nX_0 first and then applying energy-loss corrections for $\pm 1\sigma_{\Delta nX_0}$. Since the constant term of the EM calorimeter is sensitive to changes in X_0, it is redetermined from $Z \rightarrow e^+e^-$ FAST MC events. Thereafter, $W \rightarrow e\nu$ FAST MC toy samples are made using the alternative energy loss corrections and the new constant term. The systematic is derived from the measurements of the W mass from the toy samples for the change in material (ΔnX_0). The uncertainty in the determination of the material upstream of the calorimeter results in an uncertainty of 6 MeV from the PT method, 4 MeV from the MT method and 7 MeV from the MET methods, on the measured W mass.

19.2.4 Recoil Momentum Scale and Resolution

The uncertainties on the measured W mass arising from the mis-measurements of the recoil tuning parameters and systematic biases in the recoil simulation procedure is known as the systematic error here. As we have read earlier, the recoil tuning parameters (`RelScale`, `RelOffset` and $\tau_{\texttt{HAD}}$ for the response and `RelSampA`, `RelSampB` and α_{mb} for the resolution) are tuned with the help of the $Z \to e^+e^-$ collider data sample.

The systematic is determined by generating a high ensemble of FAST MC toy samples by varying the relevant parameter in steps of $\pm 1\sigma$ and $\pm 2\sigma$. The sensitivity $\frac{\Delta M_W}{\Delta P}$ is determined from the W masses of these toys and the uncertainty on the W mass from data is then given by the product of the sensitivity and the uncertainty on the relevant parameter. The tuning parameters of the recoil model are correlated and hence the equation 19.2 is used here. The corresponding systematics are 12 MeV from the PT method, 6 MeV from the MT method and 20 MeV from the MET method.

19.2.5 Efficiencies

The dominant efficiency related uncertainty results from the $u_{\parallel}$ efficiency (see Chapter 13). This uncertainty has two components, first comes the determination of the efficiency itself from $Z \to e^+e^-$ events and secondly the scaling of this efficiency to the $W \to e\nu$ events. In the combined form, the systematic is estimated at 6 Mev for the PT method, 5 MeV for the MT method and 5 MeV for the MET method.

19.2.6 Backgrounds

The backgrounds from three main sources, QCD, $W \to \tau\nu$ and $Z \to e^+e^-$, for the three distributions of m_T, p_T^e and $\not{E}_T$ are normalized on the same plot as shown in Figure 16.5 of Chapter 16. The uncertainties on the W mass due to the backgrounds are estimated by varying the backgrounds by $\pm 1\sigma$. The systematics from the backgrounds are 5 MeV from the PT method, 2 MeV from the MT method and 4 MeV from the MET method. They represent a small contribution to the overall uncertainty.

19.3 Theoretical Uncertainties

19.3.1 Parton Distribution Functions

The parton distribution functions (PDF) used in the description of the cross-sections in the event generators also have an uncertainty associated with them. The systematic uncertainty on the mass of the W boson due to the uncertainty in the PDF sets is estimated by using the $W \to e\nu$ events generated by the PYTHIA Monte-Carlo generator.

The "fake data" consists of FAST MC toy samples generated using PYTHIA and the central PDF set as defined in the Chapter 3. The generated $W \to e\nu$ events are passed through the FAST MC simulation of the detector. Upon satisfying all the requirements for selecting events deemed ideal for the analysis, these events make up the FAST MC toy samples.

The templates are also generated using the same procedure, but they are reweighted using the standard PDF reweighting method. By varying each of the 20 parameters by a $\pm 1\sigma$, 40 additional PDF sets are defined (see Chapter 3). A set of 100 templates represents each of those 40 variations. The template sets

are used to extract the W mass from the fake data samples and the systematic (σM_W) is determined with a 68% confidence level as follows:

$$\sigma M_W = \frac{1}{2 \times 1.6} \sqrt{\sum_{i=1}^{20} (M_i^+ - M_i^-)^2} \tag{19.3}$$

where M_i^+ and M_i^- denote the W mass obtained from the use of templates made from the $+1\sigma$ and -1σ of the ith orthogonal PDF set [149].

The systematic on the W mass due to the PDF is estimated for all the three distributions (m_T, p_T^e and $\not{E}_T$), they are found to be 11 MeV from the PT method, 10 MeV from the MT method and 14 MeV from the MET method.

19.3.2 W and Z Boson p_T

At the Tevatron, the uncertainty due to the theoretical description of the transverse momenta of the vector bosons (p_T^Z and p_T^W) is most sensitive to the value of g_2, it has limited sensitivity to g_1 and is almost insensitive to g_3. These parameters are used in the BLNY [150, 151] parameterization of the non-perturbative region of the p_T spectrum. This has been discussed in detail in Chapter 3 and 11.

A change in the value of g_2 changes the mean of the boson p_T, most effectively. For the purposes of this analysis we use the global fit value of g_2=0.68 $\pm$ 0.02 GeV^2 and estimate the uncertainty on the W mass due to g_2. The uncertainties due to g_1 and g_3 are negligible.

The systematic uncertainty due to g_2 is estimated by making FAST MC toy samples for different parameter values of g_2, ranging from g_2=0.64 to g_2=0.72 in steps of 0.02. The templates are made with the global value of g_2=0.68. The W mass is then extracted from the m_T, p_T^e and $\not{E}_T$ distributions. These W mass

values for each value of g_2 determine the slope or sensitivity ($\Delta M_W/\Delta g_2$). The uncertainties are estimated to be 5 MeV from the PT method, 2 MeV from the MT method and 2 MeV from the MET method.

19.3.3 Electroweak and FSR Photon Corrections

As mentioned in Chapter 11 photons can be radiated in the intial or final-state of the processes forming W/Z bosons. These impact the energy of the electron from the W/Z and consequently the W mass. Hence the impact on the W mass due to the uncertainties associated with all these corrections is an important systematic. It is estimated with the help of WGRAD and ZGRAD. The two are parton level Monte-Carlo programs for calculating the electroweak radiative corrections to W/Z boson production at hadron colliders.

WGRAD and ZGRAD are well equipped to study the effects of initial and final state photon radiation for upto one photon. There are 2 parameters in WGRAD/ZGRAD that control the radiated photons, one is the minimum transverse momentum of the radiated photon, $p_T^{min}(\gamma)$, which is denoted by the δs variable in WGRAD/ZGRAD, the other is the minimum distance, ΔR between the photon and electron, denoted by the δc variable in the WGRAD/ZGRAD generators.

The procedure for determining the systematics is similar to the other cases. "Fake data" $W \rightarrow e\nu$ samples are generated using the event generator and the FAST MC simulation of the detector, for a range of δs (or δc) values. W mass templates are also made in the same way for a certain value of δs (or δc). The W mass is determined with the help of both these sets of events and the shift of the W mass from its optimum for each δs (or δc) value gives us a gradient for

predicting the systematic. Since we are effectively measuring the ratio of the W to Z masses, we also determine the relative shift of the Z mass due to shifts in δs (or δc).

Tables 19.2 and 19.3 show the effect of the minimum photon $p_T^{min}(\gamma)$ cut on the W mass measurement and on the ratio M_W/M_Z for all the three distributions. As δs decreases, the $p_T^{min}(\gamma)$ also decreases allowing more photons to be radiated from the W propagator and the final-state electron. This leads to a reduction of their energies and thus to a lower W mass value. However the Z mass gets lowered too and so the ratio between the two masses remains stable for $\delta s < 0.02$. We use δs=0.01 as the default value for our analysis and the systematic uncertainties on the M_W measurement due to the $p_T^{min}(\gamma)$ cut has been estimated for δs between 0.00025 and 0.02. These correspond to values of $p_T^{min}(\gamma)$ between 10 MeV and 800 MeV respectively. The systematic uncertainties are estimated to be 2 MeV from the m_T distribution, 1 MeV from the p_T^e distribution and 3 MeV from the $\not{E}_T$ distribution.

The distance of proximity of the radiated photon and electron does not have an appreciable effect on the W mass. The effect of the cone size for merging the electrons and photons is larger. This effect is estimated in the same way as for δs. "Fake data" W samples were generated for different values of ΔR ranging from 0.2 to 0.4. Templates were made for ΔR=0.2. The uncertainty on the W mass was estimated from the deviations in the W mass obtained for the different values of ΔR. The systematic uncertainties are 1 MeV for m_T method, 1 MeV for p_T^e method and 5 MeV for $\not{E}_T$. The electron-photon merging cone size affects the electrons from both the W and Z decays and since we are measuring the relative

impact (ratio of W to Z) the uncertainty for the $\not{E}_T$ method is larger.

The WGRAD generator is also used for estimating the effect of ISR, ISR-FSR interference and other EW corrections. This is possible because WGRAD has provisions to allow us to study the effect of FSR-only corrections or the full EW corrections. To estimate the above systematic "fake data" $W \to e\nu$ samples are made from WGRAD with the full EW corrections implemented in them. Then W mass templates are made from WGRAD with the effects of FSR-only related corrections incorporated in them. The deviation of the resulting W mass from its input shows the effect of ISR, ISR-FSR interference and other EW corrections. The final uncertainties are obtained as 5 MeV from the m_T distribution, 5 MeV from the p_T^e distribution and 5 MeV from the $\not{E}_T$ distribution.

Since PHOTOS is more adept at dealing with the corrections due to one or more final-state photons we use RESBOS interfaced with PHOTOS as the main event generator for our W mass analysis. However since the RESBOS-PHOTOS combination neglects higher order QED processes such as ISR-FSR interference and W/Z self-energy box diagrams, we also estimate the difference between using PHOTOS and WGRAD for the FSR-only corrections. This is done by making "fake data" sample using WGRAD with contributions from the FSR-only corrections. Thereafter W mass templates are made by using PHOTOS. The difference between the measured W mass and the input indicates the systematic uncertainty due to the event generators. The final uncertainty stands at 5 MeV from the m_T distribution, 5 MeV from the p_T^e distribution and 5 MeV from the $\not{E}_T$ distribution.

The final systematic uncertainty due to all the electroweak corrections needs to include the uncertainties from all the above sources and is found to be 7 MeV from the m_T distribution, 7 MeV from the p_T^e distribution and 9 MeV from the

$\not{E}_T$ distribution.

19.4 Concluding Remarks on the Uncertainties

The uncertainties on the present measurement of the W mass are mainly due to statistical limitations. Both the W and Z data samples at 1 fb^{-1} cannot be considered to be large samples, especially when compared to the 10 fb^{-1} of integrated luminosity data that the Tevatron plans to record. More statistics could help bring down most of the major systematics like the electron energy and the recoil scales. The dominant theoretical uncertainty is the PDF. Their determination from the "global fits" to the world's data will also benefit from more data being available as the parameters describing the PDF sets can be determined much more accurately. For example the determination of the W forward-backward charge asymmetry that helps constrain the PDFs will benefit directly from an increase in statistics.

TABLE 19.1

SYSTEMATIC UNCERTAINTIES ON THE W MASS RESULTS

Source	$\sigma(m_W)$ MeV m_T	$\sigma(m_W)$ MeV p_T^e	$\sigma(m_W)$ MeV $\not{E}_T$
Experimental			
Electron Energy Scale	34	34	34
Electron Energy Resolution	2	2	3
Electron Energy Nonlinearity	4	6	7
W and Z Electron energy loss differences	4	4	4
Recoil Model	6	12	20
Electron Efficiencies	5	6	5
Backgrounds	2	5	4
Experimental Total	35	37	41
W production and decay model			
PDF	10	11	11
QED	7	7	9
Boson p_T	2	5	2
W model Total	12	14	14
Total	37	40	43

TABLE 19.2

MASS SHIFT OF W AND Z DUE TO δs VARIATION

δs	E_γ *cut* (MeV)	ΔM_W (m_T) (MeV)	ΔM_W (p_T^e) (MeV)	ΔM_W ($\not{E}_T$) (MeV)	ΔM_Z (MeV)
0.00025	10	-25 ± 3	-23 ± 4	-22 ± 4	-34 ± 2
0.0005	20	-29	-29	-27	-30
0.0006	24	-24	-27	-24	-32
0.0007	28	-24	-29	-19	-32
0.0008	32	-21	-23	-20	-33
0.001	40	-20	-20	-20	-27
0.003	120	-17	-22	-14	-21
0.005	200	-10	-13	-12	-15
0.01	400	0	0	0	0
0.015	600	5	8	6	11
0.02	800	18	20	15	26

TABLE 19.3

MASS RATIO OF W AND Z DUE TO δs VARIATION

δs	E_γ *cut* (MeV)	$\Delta(\frac{M_W}{M_Z})$ (m_T) $(\times 10^{-5})$	$\Delta(\frac{M_W}{M_Z})$ (p_T^e) $(\times 10^{-5})$	$\Delta(\frac{M_W}{M_Z})$ $(\not{E}_T)$ $(\times 10^{-5})$
0.00025	10	5.5	7.7	8.8
0.0005	20	-2.8	-2.8	-0.6
0.0006	24	4.6	1.3	4.6
0.0007	28	4.6	-0.85	10.0
0.0008	32	8.9	6.7	10.0
0.001	40	4.2	4.2	4.2
0.003	120	1.7	-3.8	5.0
0.005	200	3.5	0.25	1.3
0.01	400	0	0	0
0.015	600	-5.2	-1.9	-4.1
0.02	800	-5.4	-3.2	-8.7

CHAPTER 20

CONSISTENCY CHECKS

20.1 A Brief Introduction

In this chapter we present the consistency checks on the analysis. By changing one aspect of the analysis at a time, we check to see if the measurement is consistent or stable under that change. These aspects could be a cut on an event selection criterion such as the p_T of the electron, or splitting up the data sample into two subsets on the basis of a criterion such as the luminosity, etc. The splitting is typically done on a variable that is either considered difficult to describe or one that is sensitive to many aspects of the parameterized simulation.

The first set of consistency checks is performed by varying the fit ranges to observe the affect of varying fit ranges on the W mass values. We also perform additional checks which are more fundamental to the analysis and technically harder to implement. An important thing to keep in mind is the fact that we are able to attain the desired precision on the W mass because we are measuring the ratio of the W to the Z mass, effectively. Hence many systematic effects cancel out as a result of this ratio. This implies that when we change a selection criterion or condition for a particular consistency check, we should retune the EM energy scale and the recoil model to the Z electrons. Similarly, when we split the sample into two subsamples, we should retune the EM energy and recoil systems

to the Z, separately for each subsample, before using it to determine the W mass. However retuning of the electron and recoil systems is a very time intensive and arduous procedure. Hence this is not exactly what we do here. In our consistency checks we study the impact of a variation (of a selection criterion or a sample splitting) on the W and Z masses separately. This is facilitated by the FAST MC templates which can be produced relatively quickly. Hence instead of carrying out the entire parameterization with the Z and then determining the W mass, we study the impact as a function of W and Z masses, the latter being equivalent to the former. The relevant figure of merit now is not the W mass alone, but the ratio of the measured W and Z masses.

20.2 Fitting Intervals

The fit intervals (or ranges) are important for all the three W mass distributions (m_T, p_T^e and $\not{E}_T$) as they enable us to extract the W mass information from the W decay. The effects of the detector compete with the kinematic effects of the event in each of the observables. The fit range needs to be chosen in a way that optimizes the effects of both, thus helping in an accurate determination of M_W. For this consistency check we vary the fit ranges, both upper and lower values, one at a time and observe the change in the fitted W mass from the nominal value. The nominal value is defined as the M_W obtained (80.011 GeV, it is blinded) with the default fit ranges of 65-90 GeV for the m_T and 32-48 GeV for each of the p_T^e and $\not{E}_T$ distributions, as quoted in the Chapter 18.

Figures 20.1, 20.2 and 20.3 show the variations of the fitted W mass obtained for different choices of the fitting intervals with respect to the nominal results (indicated by the blue dots), both from the collider data. Since the data sample

used for all the measurements is the same, these measurements are correlated. This needs to be taken into account. While determining the stability of the variations in M_W, we determine the uncorrelated statistical error between the M_W obtained from the chosen fit range and that of the nominal. This uncorrelated error (σ_{uncorr}) is given by:

$$\sigma_{\text{uncorr}} = \sigma^2_{\text{nominal}} + \sigma^2_{\text{fr}} + 2 \times \rho \times \sigma_{\text{nominal}} \times \sigma_{\text{fr}} \tag{20.1}$$

where σ_{fr} stands for the statistical error from the M_W fit with the chosen fit range while σ_{nominal} is the corresponding value for the nominal fit range. ρ is the correlation coefficient between σ_{nominal} and σ_{fr}.

The yellow band displays this uncorrelated error. This error is estimated from the M_W values from fits to FAST MC toys which are like pseudo data samples. The two dashed lines on each figure indicate the statistical uncertainty obtained from using the nominal (default) fit range.

20.3 Instantaneous Luminosity

We split the data sample on the basis of instantaneous per-tick luminosity, into a "low lumi" subsample (per-tick lumi $< 1 \times 10^{30}$ cm^{-2} s^{-1}) and a "high-lumi" subsample (per-tick lumi $> 1 \times 10^{30}$ cm^{-2} s^{-1}). The value of the cut has been chosen in such a way that both subsamples are almost of the same size. Since the high-lumi regime leads to more activity in the detector, this consistency test is important for checking the capability of the event reconstruction algorithms for extracting the information related to W and Z bosons, both in clean and hyper active detector conditions. The W and Z masses are measured from each of the subsamples and the resulting ratios are computed. Figure 20.4 shows the W and Z masses along with the "relative change in the mass ratio". The relative

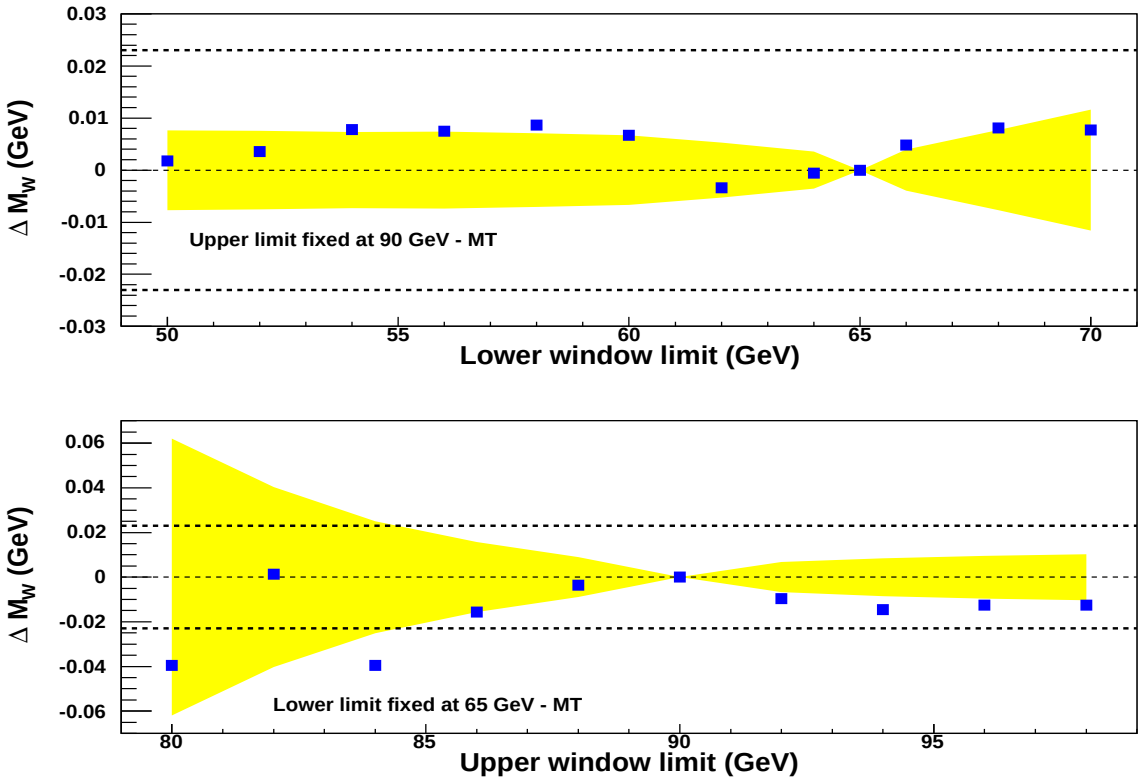

Figure 20.1. Top: Sensitivity of the fitted M_W values to the choice of fit interval for m_T distributions when upper edge is fixed. Bottom: Sensitivity of M_W when the lower edge is fixed. The yellow band indicates the expected statistical variations

change is defined as the ratio of measured W and Z masses (taking into account their statistical uncertainties) divided by the ratio of the nominal result for the W mass from the m_T observable (80.011 GeV) and the nominal result for the Z mass (91.185 GeV), without the uncertainties on the nominal values. The relative change in the mass ratio is expected to be consistent with unity. As seen in Figure 20.4, the ratios are consistent, thus implying that our measurements are stable.

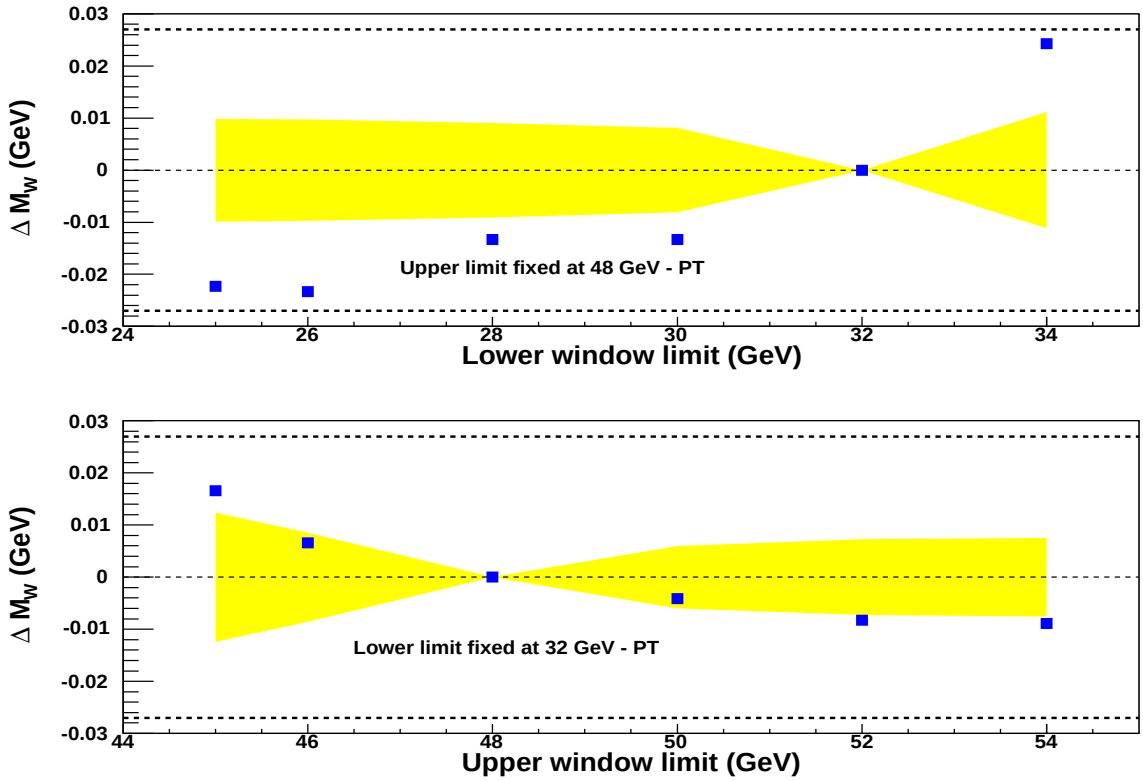

Figure 20.2. Top: Sensitivity of the fitted M_W values to the choice of fit interval for p_T^e distributions when upper edge is fixed. Bottom: Sensitivity of M_W when the lower edge is fixed. The yellow band indicates the expected statistical variations

From Figure 20.4 it is evident that there is an "apparent lowering trend" present for both the W and Z masses at higher luminosities. This is a real effect and not a statistical oddity because it is expected from first principles [152] and has been confirmed with more data at higher luminosities in Run IIb [153].

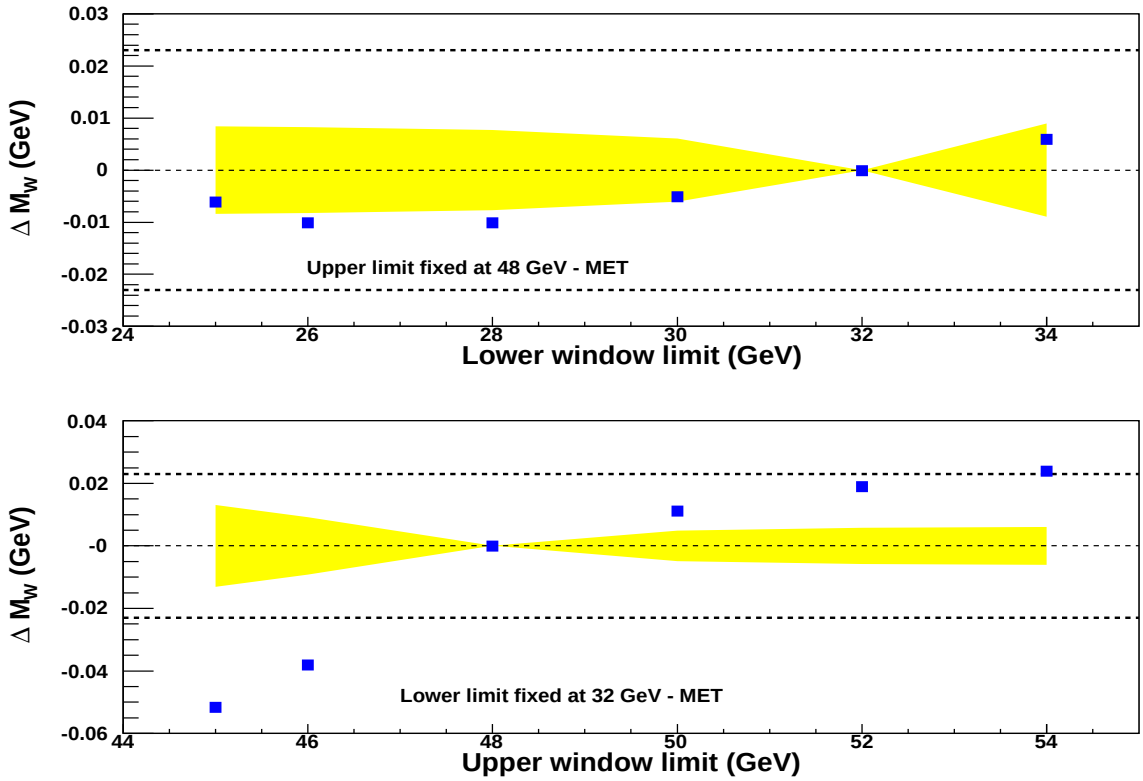

Figure 20.3. Top: Sensitivity of the fitted M_W values to the choice of fit interval for $\not{E}_T$ distributions when upper edge is fixed. Bottom: Sensitivity of M_W when the lower edge is fixed. The yellow band indicates the expected statistical variations

20.4 Time

We now split our sample according to "time" or data-taking period, into an "early" subsample (run number < 202471) and a "late" subsample (run number ≥ 202471). The cut separates the data collected before and after the August 2004 shutdown. The early subsample has been recorded at a lower instantaneous luminosity than the late subsample, on an average. The stability of the reconstruction and analysis procedure is tested out in different time regimes by this consistency

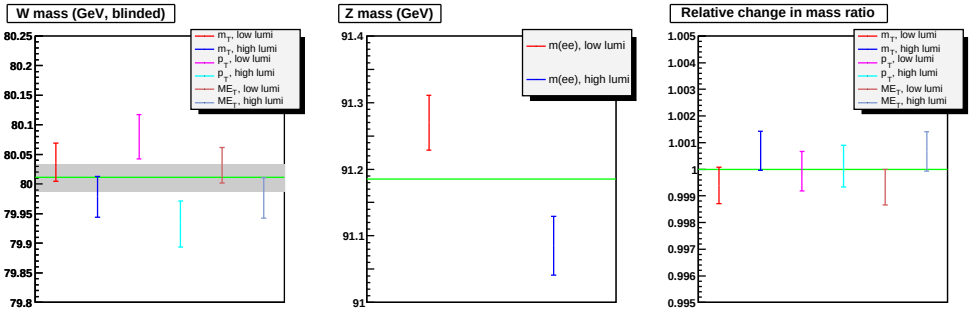

Figure 20.4. Left: W mass as measured from the m_T, $p_T(e)$ and $\not{E}_T$ observables, separately for the "low lumi" and the "high lumi" subsamples. The green line and grey band indicate the nominal result from the m_T observable and its uncertainty. Middle: Z mass as measured from the di-electron invariant mass spectrum, separately for the two subsamples. The green line shows the nominal result from the fit to the full Z sample. Right: The resulting mass ratios, separately for the m_T, $p_T(e)$ and $\not{E}_T$ observables and for the two subsamples, divided by the nominal mass ratio. The green line indicates unity

check. Any time-dependent effects, changes in any calibration or degradation in the detector readout if present, will reveal themselves in the values of the W and Z masses obtained herein. The W and Z masses as well as the relative change in the mass ratios are presented in Figure 20.5. The relative change in the mass ratio is consistent with unity, proving that our measurements are stable. The trend to an apparent lower mass at higher instantaneous luminosities, is also visible here and has also been reported from the second data-taking period (Run IIb).

20.5 Scalar E_T

The data sample is now split up according to scalar E_T (SET). We divide our data into a "low SET" subsample (SET $<$ 50 GeV) and a "high SET" subsample

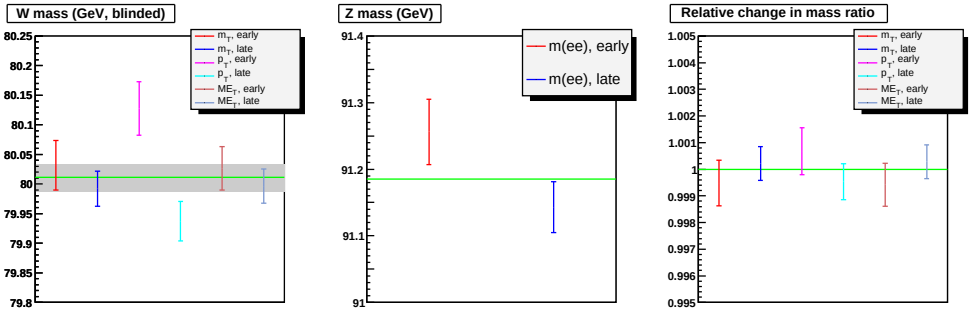

Figure 20.5. Left: W mass as measured from the m_T, $p_T(e)$ and $\not{E}_T$ observables, separately for the "early" and the "late" subsamples. The green line and grey band indicate the nominal result from the m_T observable and its uncertainty. Middle: Z mass as measured from the di-electron invariant mass spectrum, separately for the two subsamples. The green line shows the nominal result from the fit to the full Z sample. Right: The resulting mass ratios, separately for the m_T, $p_T(e)$ and $\not{E}_T$ observables and for the two subsamples, divided by the nominal mass ratio. The green line indicates unity

(SET $>$ 50 GeV). Scalar E_T of an event is defined as the energy flow in the transverse plane of the beams and excludes the energy of the electron clusters. Hence an increase of SET indicates more energy in the event and could interfere with the detection of the event (W/Z) signatures. However this consistency test reveals the robustness of our reconstruction procedure in the analysis, even in the cases of increased activity in the event. The W and Z masses along with the resulting relative change in mass ratio are shown in Figure 20.6. Our measurements are stable as seen from the consistency of the mass ratio plots around unity.

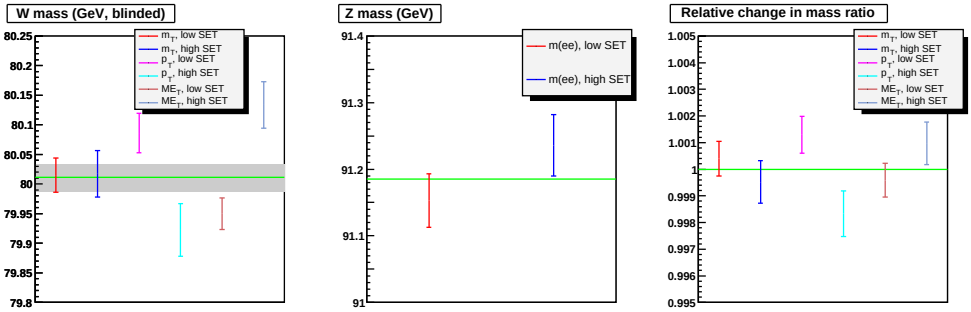

Figure 20.6. Left: W mass as measured from the m_T, $p_T(e)$ and $\not\!\!E_T$ observables, separately for the "low SET" and the "high SET" subsamples. The green line and grey band indicate the nominal result from the m_T observable and its uncertainty. Middle: Z mass as measured from the di-electron invariant mass spectrum, separately for the two subsamples. The green line shows the nominal result from the fit to the full Z sample. Right: The resulting mass ratios, separately for the m_T, $p_T(e)$ and $\not\!\!E_T$ observables and for the two subsamples, divided by the nominal mass ratio. The green line indicates unity

20.6 Phi Fiducial Cut

We now vary the ϕ fiducial requirement. Our nominal requirement, ϕ mod $<$ 0.80, cuts away 10% of the phase space at each edge of each CCEM module. The analysis is also performed for two tighter versions of this requirement, namely ϕ mod $<$ 0.75 and ϕ mod $<$ 0.70. As we have read in Chapter 13 we avoid EM clusters near the edges of the module boundaries. This could lead to a significant bias in the reconstructed energy clusters thus impacting the electron p_T. Hence this is a very important cross-check to verify if our nominal requirement of excluding 10% of each module edge is appropriate for minimizing the above bias in the analysis. The effects of these cuts on the W and Z masses are summarized in the plots shown in Figure 20.7. We notice that the relative change in the mass

ratio is consistent with unity.

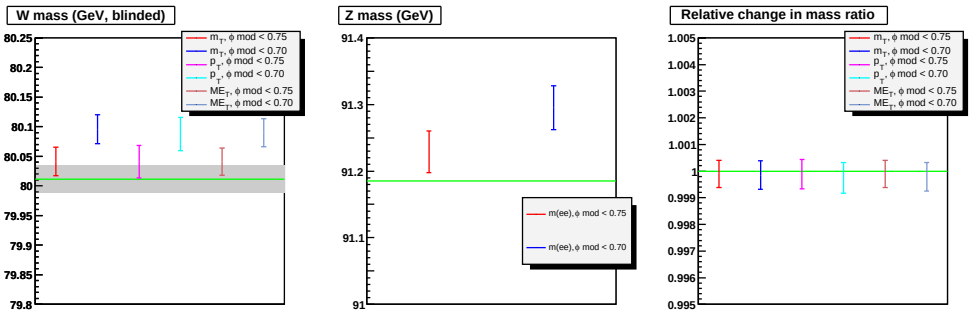

Figure 20.7. Left: W mass as measured from the m_T, $p_T(e)$ and $\not{E}_T$ observables, separately for two variations of the phi fiducial cut. The green line and grey band indicate the nominal result from the m_T observable and its uncertainty. Middle: Z mass as measured from the di-electron invariant mass spectrum, separately for the two cut variations. The green line shows the nominal result from the fit to the default Z sample. Right: The resulting mass ratios, separately for the m_T, $p_T(e)$ and $\not{E}_T$ observables and for the two cut variations, divided by the nominal mass ratio. The green line indicates unity

While it is irrelevant for the measurement of the W mass, we notice that the measured W and Z masses are not stable separately. This signifies that our rudimentary model of the energy response variation across the EM modules of the CC is not precise to the per-mil level. This is not surprising because the parameters describing the model have never been tuned precisely.

20.7 u_T Cut

The magnitude of the transverse momentum of the recoil is denoted as u_T. Our nominal requirement is $0 < u_T < 15$ GeV. As part of the consistency check, we perform the analysis with two different cuts of u_T, a tighter version with $u_T < 10$ GeV and a loose one with $u_T < 20$ GeV. The recoil cut helps sculpt the electron p_T spectrum, thus impacting the p_T^e and m_T measurements of the W mass. This consistency check shows the impact of relaxing this cut on the W and Z masses. The effects of these cut variations on the W and Z masses and the ratio can be seen in Figure 20.8. The consistency of the relative change in the mass ratio plot with unity, indicates that our measurements are stable with respect to this variation.

Although it is irrelevant for our measurement of the W boson mass, one could in principle conceive a very small increase in the measured masses as the u_T cut is relaxed due to the larger flux of positive energy in the selected events. While the central values for the masses follow this pattern, we do not see evidence of any statistically significant trend. Within the precision levels of our current statistics, the measured W and Z masses are stable individually.

20.8 $u_\parallel$

$u_\parallel$ is defined as the projection of the transverse momentum of the recoil in the direction parallel to the direction of the electron. We split the data sample into a subsample of negative $u_\parallel$ and a subsample of positive $u_\parallel$. There is no direct equivalent of this splitting for the Z sample.[1] However this is not pertinent for the

[1]Since there are two electrons from each Z decay that are reconstructed in roughly opposite directions in the transverse plane.

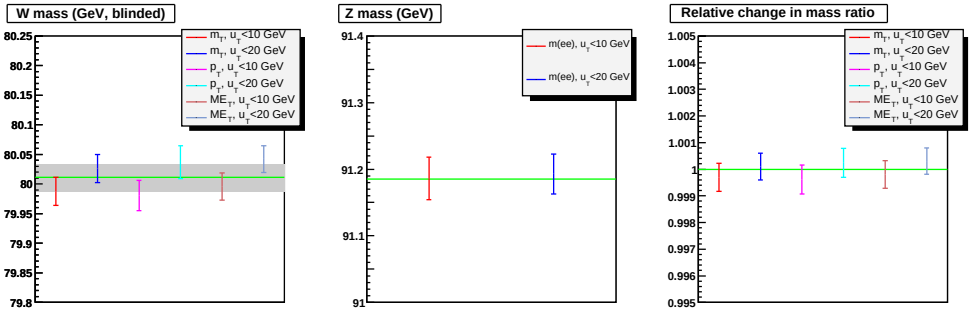

Figure 20.8. Left: W mass as measured from the m_T, $p_T(e)$ and $\not{E}_T$ observables, separately for two variations of the u_T cut. The green line and grey band indicate the nominal result from the m_T observable and its uncertainty. Middle: Z mass as measured from the di-electron invariant mass spectrum, separately for the two cut variations. The green line shows the nominal result from the fit to the default Z sample. Right: The resulting mass ratios, separately for the m_T, $p_T(e)$ and $\not{E}_T$ observables and for the two cut variations, divided by the nominal mass ratio. The green line indicates unity

consistency check since we expect the W mass to be stable on its own under this splitting and not just with respect to the mass ratio. As we've seen earlier, the $u_{\|}$ denotes the component of the recoil in the direction of the W/Z electron and thus an increase of $u_{\|}$ increases the probability of the electron signature getting drowned in the recoil. In a high luminosity regime this situation is very probable and thus this consistency check is important for testing the robustness of the electron reconstruction algorithms and procedures. The W mass results from the two subsamples as shown in Figure 20.9, indicate that the two subsets agree with each other and that our measurement is stable.

The difference in central values for the m_T and $\not{E}_T$ observables is somewhat larger than that for the p_T^e observable. Upon inspection one finds that this dif-

ference is related to the same events that cause the fluctuation in the earlier Figure 20.8. The events responsible for these higher values "live" at $\not{E}_T \geq 45$ GeV and $m_T \geq 90$ GeV. The difference in central values from these two distributions (m_T and $\not{E}_T$) vanishes almost completely when the fitting range is slightly reduced to a lower value at the upper end, as indicated by the last four points of Figure 20.9.

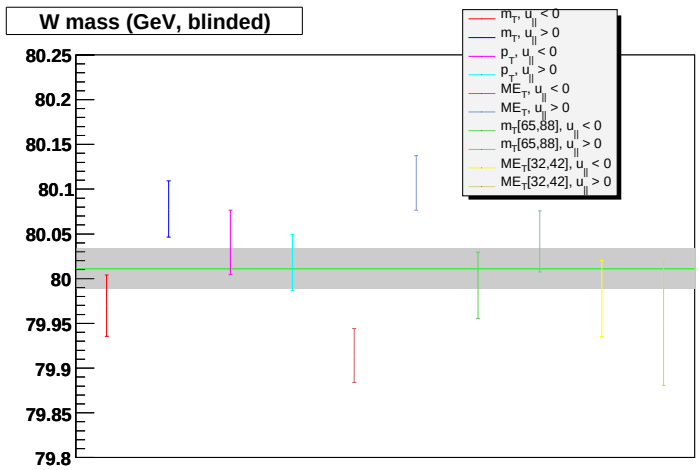

Figure 20.9. W mass as measured from the m_T, $p_T(e)$ and $\not{E}_T$ observables, separately for the subsamples of negative and positive $u_{\parallel}$. For the m_T observable, in addition to the results obtained using the nominal fitting range ($65 - 90$ GeV), we also report results from the slightly more restricted fitting range $65 - 88$ GeV. Similarly, for the $\not{E}_T$ observable additional results from the more restricted fitting range $32 - 42$ GeV are included

CHAPTER 21

THE COMBINATION OF THE W MASS RESULTS

21.1 A Brief Introduction

The W mass results obtained from the three kinematic distributions (m_T, p_T^e and $\not{E}_T$) are correlated, both statistically and systematically. This chapter will describe the determination of the statistical and systematic correlations between them. These three measurements are later combined using the BLUE (Best Linear Unbiased Estimate) method [154, 155] which takes into account the correlations between the different measurements. A more detailed presentation of the procedure of combining the three W masses is given in [157].

21.2 Determination of Statistical Correlations for the Three M_W Measurements

The same collider data sample is used for obtaining all the three W mass measurements. This gives rise to statistical correlations between the three measured values depending on the size of the data sample.

The procedure for determining the statistical correlations can be outlined as follows:

1. A large number of $W \to e\nu$ FAST MC (PMCS) samples are made with the help of the RESBOS event generator. Each is generated at a W mass of

80.403 GeV (input value for RESBOS) and is the size of our collider data sample. Three hundred data-like samples were made in this way.

2. One hundred high statistics, FAST MC templates are made by varying the W mass in a range, in steps of 10 MeV.

3. The W mass is measured by fitting each of the FAST MC samples with the templates, using the three distributions (p_T^e, m_T and $\not{E}_T$), one at a time. The results of these fits are used to determine the statistical correlation between the three measurements.

The statistical correlations were determined using the expression from the "Pearson's product-moment correlation coefficient" [148]. Here the correlation coefficient $\rho_{X,Y}$ between two random variables X and Y with expected values μ_X and μ_Y and standard deviations σ_X and σ_Y is defined as:

$$\rho_{xy} = \frac{N\sum x_i y_i - \sum x_i \sum y_i}{\sqrt{N\sum x_i^2 - (\sum x_i)^2}\,\sqrt{N\sum y_i^2 - (\sum y_i)^2}} \tag{21.1}$$

where the summation is from i = 1,2, ... N. Here x_i and y_i are a series of N measurements of X and Y.

Table 21.1 shows the coefficients that represent the correlations on our three W mass measurements due to the statistics of our data $W \to e\nu$ sample.

21.3 Determination of Systematic Correlations for the Three M_W Measurements

In the experimental domain, the dominant systematics for the W mass measurement arise from the uncertainties in the parameterizations of the electron response and the recoil response and resolution. Amongst the uncertainties re-

TABLE 21.1

CORRELATION COEFFICIENTS FOR THE W MASS MEASUREMENTS DUE TO THEIR STATISTICS

	m_T	p_T^e	$\not{E}_T$
m_T	1	0.699467	0.62245
p_T^e	0.699467	1	0.357875
$\not{E}_T$	0.62245	0.357875	1

lated to the vector boson production and decay model, the parton distribution functions (PDFs) are the chief source of systematics. Hence the systematic correlations between the three W mass measurements due to the electron, recoil and PDFs have been determined here. It should be kept in mind that the parameterizations for these three are also obtained from the same data sample and are used for all three measurements of the W mass, hence the correlations between them.

The "covariance matrix for the W mass measurement" is determined as the first step towards estimating any of the systematic correlations. The correlation coefficients for the three measurements can then be determined from these covariance terms. The various terms of this matrix are determined using the following general expression [53]:

$$C_{QR}^{M} = \sum_{k,l=1}^{N_p} D_{Qk}^{M} C_{kl}^{P} D_{Rl}^{M} \tag{21.2}$$

Here indices Q and R denote any two of the three W mass measurements. C_{kl}^{P} is the parameter covariance matrix for the electron or recoil. This matrix is a product of the fits that are performed for obtaining the electron response or the

recoil tuning parameters. N_p denotes the number of relevant parameters for the electron, recoil or PDF. D^M_{Qk} and D^M_{Rl} are the derivatives or "sensitivities" of the W mass with respect to the parameter being considered. These derivatives are obtained by noting the change in W mass due to a deviation of the parameters from their optimal values and are assumed to be linear with the change in the relevant parameters. They are obtained in the same way as the sensitivities mentioned in the Chapter 19 and hence:

$$D^M_{Qk} = \frac{\Delta M_Q}{\Delta P_k} \tag{21.3}$$

Here ΔM_Q is the change in the W mass from a measurement Q, for a change of ΔP_k in the parameter P_k.

The derivatives for the electron and recoil shown here have been obtained beforehand during the course of determining the systematics on the W mass by the usual method of an error propagation, as described in Chapter 19.

The parameter covariance matrix and the derivatives of the parameters obtained in each case are plugged into equation 21.2 to determine the correlations between the three W mass measurements arising from the systematics of the electron, recoil or PDF. The correlation coefficients are then determined from the respective covariance matrices.

Table 21.2 shows the correlation coefficients on our three W mass measurements due to the electron systematics, while Table 21.3 shows the same for the recoil systematics.

The correlations between the W mass measurements due to the PDF uncer-

TABLE 21.2

CORRELATION COEFFICIENTS FOR THE W MASS MEASUREMENTS DUE TO ELECTRON SYSTEMATICS

	m_T	p_T^e	$\not{E}_T$
m_T	1	0.900887	0.998228
p_T^e	0.900887	1	0.925122
$\not{E}_T$	0.998228	0.925122	1

tainties were estimated using the formula below:

$$\Delta M_W = \sqrt{C_Q^M} = \sqrt{\sum_i^{N_p} \frac{(M_{Q,i}^+ - M_{Q,i}^-)^2}{(2 * 1.6)^2}} \tag{21.4}$$

This is obtained from the basic equation 21.2 by way of some simplifications. Table 21.4 shows the correlations between the three W mass measurements due to the PDF systematics.

21.4 Combining the three measurements using BLUE

BLUE, the standard method of combining results from different measurements, is used here for combining our three different (p_T^e, m_T, $\not{E}_T$) W mass measurements by taking into account the correlations due to the statistics, electron energy response, recoil model and the PDF systematics that exist between them. All other sources of systematics (such as QED, backgrounds, efficiencies) have been considered to be 100% correlated.

TABLE 21.3

CORRELATION COEFFICIENTS FOR THE W MASS MEASUREMENTS DUE TO RECOIL SYSTEMATICS

	m_T	p_T^e	$\not{E}_T$
m_T	1	0.648404	0.247175
p_T^e	0.648404	1	0.0759881
$\not{E}_T$	0.247175	0.0759881	1

With the numbers shown in Table 19.1 of Chapter 19, the combined W mass comes out to be:

$$80.401 \pm 0.043 \quad \text{GeV} \qquad (\text{Stat} : 0.021, \text{Syst} : 0.038) \tag{21.5}$$

The overall χ^2 is 0.003 for these three measurements and correponds to a probability of 99.87%. A small shift in the combined value of M_W comes in the form of a correction due to Γ_W. The M_W value is corrected to the same assumed W boson width value for achieving consistency between results from DØ and CDF. The standard value of the Γ_W used is 2093.2±2.2 MeV. The combined value of M_W when corrected to this value [156] increases by 1 MeV to:

$$80.402 \pm 0.043 \quad \text{GeV} \tag{21.6}$$

The overall correlation coefficients are shown in Table 21.5.

TABLE 21.4

CORRELATION COEFFICIENTS FOR THE W MASS MEASUREMENTS DUE TO PDF SYSTEMATICS

	m_T	p_T^e	$\not{E}_T$
m_T	1	0.990215	0.987714
p_T^e	0.990215	1	0.999794
$\not{E}_T$	0.987714	0.999794	1

TABLE 21.5

FINAL CORRELATION COEFFICIENTS FROM BLUE

	m_T	p_T^e	$\not{E}_T$
m_T	1.0	0.83	0.82
p_T^e	0.83	1.0	0.68
$\not{E}_T$	0.82	0.68	1.0

21.5 Future Prospects of the M_W analysis

Precision measurements of the W mass are very important for establishing the validity of the electroweak theory of the Standard Model. As we have read in Chapters 1 and 2, higher order contributions, in the form of the electroweak radiative corrections, augment the value of the W mass. Within the framework of the Standard Model, these corrections are dominated by loops involving the top

quark and the Higgs boson. They are proportional to m_t^2 and $\ln M_H$ for large values of the masses of the top quark (m_t) and Higgs boson (M_H) respectively. Thus the measured W mass can be compared with the value calculated from the theoretical models for a study of the impact of the radiative corrections. Besides, if there are new particles that couple to the W, they may give rise to additional corrections to the W (e.g. the MSSM extension to the Standard Model can increase M_W by up to 250 MeV) [68]. Hence a measurement of the W mass is extremely important not only as a rigorous test of the Standard Model but as an excellent probe for searches for new physics.

The result presented in this analysis of the W mass measurement (80.401 ± 0.043 GeV) has been combined with the previous results from other experiments, by taking into account the correlations that might exist between any two experiments. The new world average value determined by the Tevatron Electroweak Working Group is 80.399 ± 0.023 GeV and is shown in Figure 21.1.

In conjunction with the measurements of the mass of the top quark, the W mass also imposes significant constraints on the mass of the elusive Higgs boson. The latest constraints on the Higgs mass from the most recent (2009) measurements of the top and W masses are $M_H < 157$ GeV without the direct LEP constraints (was 163 GeV) and $M_H < 186$ GeV with the direct LEP constraints (was 191 GeV).

As we have read earlier, the dominant systematics in this 1 fb^{-1} measurement of the W mass (electron response, recoil response and resolution, parton distribution functions) are mainly due to the statistical limitations ($\sim$ 20000 events) of the Z samples that were used to derive them. With the Tevatron planning to deliver about 10 fb^{-1} of data over the next few years, the statistical component of

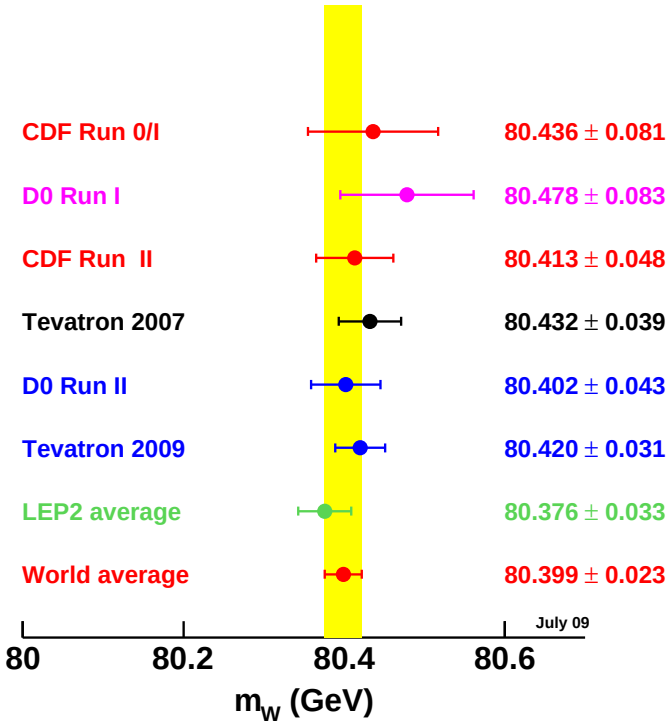

Figure 21.1. The world average value of the W mass including this DØ Run IIa measurement

these uncertainties should scale down by a factor of $\sqrt{10}$. After this it might reach the regime where the systematic contribution becomes the major factor in these uncertainties. Besides, this huge increase in the data will also effect other measurements, the results of which have a significant impact on the W mass analysis. For example, the W forward-backward charge asymmetry which helps constrain the PDFs and a measurement of the transverse momentum of the Z boson which is pertinent for modeling the p_T in the W events will also benefit from more data for their determination.

Future particle colliders like the LHC (Large Hadron Collider) will see an increased cross-section of the production of the W and Z bosons with collisions at $\sqrt{s}$=14 TeV. However, given the high instantaneous luminosity conditions in the detector, it will take awhile for these experiments to achieve an accurate understanding of the response of their subsystems and the precision on the calibrations of the electron and hadronic systems of these events, to the level desired for a precise analysis like the M_W. Colliders like the ILC (International Linear Collider) will have a much cleaner environment due to their e^+e^- beams and thus will not be sensitive to the effects of the parton model. However the construction and commissioning of the ILC might be a reality in the distant future compared to the time scale for probes into new physics and making interesting discoveries.

The analyses at the Tevatron have only begun. This is the first W mass measurement of the Run IIa data taking period at DØ. The W mass group at DØ is in the process of analyzing ~ 4 fb^{-1} of data at present and hopes to publish a new result in time for the Winter 2010 conferences. As noted earlier, the CDF experiment has also performed a first measurement of the mass of the W boson in 2007 and is currently analyzing more data. Both these experiments will contribute significantly towards laying the foundations for any discoveries or new and exciting physics that exists both within and beyond the scope of the Standard Model.

REFERENCES

1. D.J. Griffiths, *Introduction to Elementary Particles*, John Wiley & Sons Inc. (1987), (2008).

2. D.H. Perkins, *Introduction to High Energy Physics*, Addison Wesley Publishing Company, Inc. (1982).

3. H. Becquerel, *Emission de radiations nouvelles par l'uranium metallique*, Comptes Rendus des Sances de l'Academie des Sciences, Paris, **120**, 1086-1088, (1896).

4. H. Becquerel, *Sur les radiations invisibles mises par les corps phosphorescence*, Comptes Rendus des Sances de l'Academie des Sciences, Paris, **122**, 501-503, (1896).

5. H. Becquerel, *Recherches sur une proprit nouvelle de la matire*, Mmoires de l'Academie des Sciences de l'Institut France, vol. 46. Paris: Firmin-Didot (1903).

6. L. Badash, *The Discovery of Radioactivity*, Physics Today **49**, 21 (1996).

7. P. Curie, M. Curie and G. Bmont, *Sur une nouvelle substance fortement radioactive contenue dans la pechblende*, Comptes Rendus des Sances de l'Academie des Sciences, Paris, **127**, 1215-1217, (1898).

8. H. Becquerel and P. Curie, *Action Physiologique des rayonms du radium*, Comptes Rendus des Sances de l'Academie des Sciences, Paris, **132**, 1289-1291, (1901).

9. R.F. Mould, *The discovery of radioactivity in 1898 by Maria Sklodowska-Curie (1867-1934) and Pierre Curie (1859-1906) with commentary on their lives and times*, The British Journal of Radiology, **71**, 1229-1254, (1998).

10. J.J. Thomson, *Cathode rays - Discovery of the electron*, Philosophical Magazine, **44**, 293 (1897).

11. J.J. Thomson, *On the Structure of the Atom*, Philosophical Magazine Series 6, Volume 7, Number 39, 237-265.

12. E. Rutherford, *The Scattering of α and β particles by Matter and the Structure of the Atom*, Philosophical Magazine, vol. 6, 21, (1909).

13. E. Rutherford, *The Scattering of α and β particles by Matter and the Structure of the Atom*, Philosophical Magazine, Series 6, vol. 21, 669-688, (1911).

14. N. Bohr, *On the Constitution of Atoms and Molecules*, Philosophical Magazine vol. 26, 1-24, (1913).

15. J. Chadwick, *Possible Existence of a Neutron*, Nature, **129**, 312, (1932).

16. M. Planck, *Über das Gesetz der Energieverteilung im Normalspectrum*, Annalen der Physik **4**, 553-563 (1901).

17. A. Einstein, *Über einen die Erzeugung und Verwandlung des Lichtes betreffenden heuristischen Gesichtspunkt*, Annalen der Physik, **17**, 132-148 (1905).

18. A. Einstein, *Über die Entwicklung unserer Anschauungen ber das Wesen und die Konstitution der Strahlung*, Physikalische Zeitschrift **10**, 817-825 (1909).

19. R.A. Millikan, *A Direct Photoelectric Determination of Planck's "h"*, Physical Review, **7**, 355-388, (1916).

20. A. Compton, *A Quantum Theory of the Scattering of X-rays by Light Elements*, Physical Review **21**, 483-502, (1923).

21. H. Yukawa, *Interaction of Elementary Particles*, Part I, Proc. Physico-Math. Soc. Japan, **17**, 48, (1935).

22. H. Yukawa, *Models and Methods in the Meson Theory*, Reviews of Modern Physics, **21**, 474, (1949).

23. C.D. Anderson, *The Positive Electron*, Physical Review **43**, 491-494, (1933).

24. P.A.M. Dirac, Proc. R. Soc. London A **126**, 360, (1930); Proc. Cambridge Philos. Soc. **26**, 361, (1930).

25. W. Pauli, *Pauli's Letter - Dear Radioactive Ladies and Gentlemen*, Tübingen, December 4, 1930.

26. E. Fermi, *Tentativo di una teoria dei raggi β*, Il Nuovo Cimento, (1934); *Versuch einer Theorie der β-Strahlen.I*, Zeitschrift für Physik, (1934).

27. C.M.G. Lattes, H. Muirhead, G.P.S. Occhialini and C.F. Powell, *Processes Involving Charged Mesons*, Nature **159**, 694-697 (1947).

28. F. Reines and C.L. Jr. Cowan, Physical Review, **92**, 8301, (1953); C.L. Cowan *et al.*, Science, **124**, 103, (1956).

29. R. Davis and D.S. Harmer, Bulletin of the American Physical Society, **4**, 217, (1959).

30. G. Danby, J.M. Gaillard, K. Goulianos, L.M. Lederman, Nari B. Mistry, M. Schwartz and J. Steinberger, *Observation of High-Energy Neutrino Reactions and The Existence of Two Kinds Of Neutrinos*, Physical Review Letters, **9**, 36, (1962).

31. M. Gell-Mann, Physical Review, **92**, 883, (1953); Nuovo Cimento **4** (Suppl. 2), 848, (1956).

32. T. Nakano and K. Nishijima, Progress in Theoretical Physics, **10**, 581, (1953).

33. T.D. Lee and C. N. Yang, *Question of Parity Conservation in Weak Interactions*, Physical Review **104**, 254 (1956).

34. M. Gell-Mann and Y. Ne'eman, *The Eightfold Way:A theory of strong interaction symmetry*, Westview Press, pg. 11, ISBN 0-7382-0299-1, (1964).

35. M. Gell-Mann, *A Schematic Model of Baryons and Mesons*, Physics Letters **8** (3), 214-215, (1964).

36. G. Zweig, *An SU(3) Model for Strong Interaction Symmetry and its Breaking*, CERN Report No.8181/Th 8419, (1964).

37. G. Zweig, *An SU(3) Model for Strong Interaction Symmetry and its Breaking: II*, CERN Report No.8419/Th 8412, (1964).

38. O.W. Greenberg, Physical Review Letters, **13**, 598, (1964).

39. J.J. Aubert *et al.*, Physical Review Letters, **33**, 1404, (1974); J.E. Augustin *et al.*, Physical Review Letters, **33**, 1406, (1974).

40. E.G. Cazzoli *et al.*, Phys. Rev. Lett. **34**, 1125, (1975).

41. G. Goldhaber *et al.*, Phys. Rev. Lett. **37**, 255, (1976); I. Peruzzi, Phys. Rev. Lett. **37**, 569, (1976).

42. S.W. Herb *et al.*, Physical Review Letters, **39**, 252, (1977).

43. F. Abe *et al.*, Physical Review Letters, **74**, 2626, (1995); S. Abachi *et al.* Physical Review Letters, **74**, 2632, (1995).

44. C.S. Wu, E. Ambler, R.W. Hayward, D.D. Hoppes and R.P. Hudson, *Experimental test of parity conservation in beta decay*, Physical Review **105**, 1413 (1957).

45. G. Backenstoss *et al.*, Physical Review Letters, **6**, 415, (1961); M. Bardon *et al.*, Physical Review Letters, **7**, 23, (1961); M. Goldhaber, L. Grodzins and A.W. Snyder, Physical Review, **109**, 1015, (1958).

46. S.L. Glashow, *Partial-symmetries of weak interactions*, Nuclear Physics, **22**, 579-588, (1961).

47. A. Salam, *Eighth Nobel Symposium*, Elementary Particle Physics: Relativistic Groups and Analyticity edited by Nils Svartholm, Almquvist and Wiksell, Stockholm, pg. 367, (1968).

48. S. Weinberg, *A Model of Leptons*, Physical Review Letters, **19**, 1264-1266, (1967).

49. G. Arnison *et al.*, Physics Letters, **122B**, 103, (1983); G. Arnison *et al.*, Physics Letters, **126B**, 398, (1983);

50. P.W. Higgs, *Broken Symmetries and the Masses of Gauge Bosons*, Physical Review Letters **13**, 508-509, (1964).

51. B. Abbott *et al.*, *Measurement of the W boson mass*, Physical Review D **58**, 092003 (1998).

52. B. Abbott *et al.*, *Determination of the Mass of the W Boson Using the DØ Detector at the Tevatron*, Physical Review D **58**, 012002 (1998).

53. V.M. Abazov *et al.*, *Improved W boson mass measurement with the D0 detector*, Physical Review D **66**, 012001 (2002).

54. W.J. Marciano and A. Sirlin, *Radiative corrections to neutrino-induced neutral-current phenomena in the SU(2)L × U(1) theory*, Physical Review D **22**, 2695, (1980).

55. The Tevatron Electroweak Working Group, *Combination of CDF and DØ Results on the Mass of the Top Quark*, CDF Note 9717, DØ Note 5899, (2009).

56. DØ Collaboration, B. Abbott *et al.*, Phys. Rev. Lett. **80**, 3008, (1998); DØ Collaboration, B. Abbott *et al.*, Phys. Rev. Lett. **84**, 222-227, (2000); DØ Collaboration, V.M. Abazov *et al.*, Phys. Rev. D **66**, 012001, (2002); DØ Collaboration, B. Abbott *et al.*, Phys. Rev. D **62**, 092006, (2000).

57. CDF Collaboration, F. Abe *et al.*, Phys. Rev. Lett. **65**, 2243-2246, (1990); CDF Collaboration, F. Abe *et al.*, Phys. Rev. D **43**, 2070-2093, (1991); CDF Collaboration, F. Abe *et al.*, Phys. Rev. Lett. **75**, 11-16, (1995); CDF Collaboration, F. Abe *et al.*, Phys. Rev. D **52**, 4784-4827, (1995); CDF Collaboration, T. Affolder *et al.*, Phys. Rev. D **64**, 052001, (2001).

58. ALEPH Collaboration, S. Schael *et al.*, Eur. Phys. J. C **47**, 309, (2006).

59. DELPHI Collaboration, J. Abdallah *et al.*, Eur. Phys. J. C **55**, 1, (2008).

60. L3 Collaboration, P. Achard *et al.*, Eur. Phys. J. C **45**, 569, (2006).

61. OPAL Collaboration, G. Abbiendi *et al.*, Eur. Phys. J. C **45**, 307, (2006).

62. LEP Electroweak Working Group, Report No. CERN-PH-EP/2008-20, 2008; Tevatron Electroweak Working Group, Report No. FERMILAB-TM-2415, 2008; URL (http://tevewwg.fnal.gov/)

63. CDF Collaboration, T. Aaltonen *et al.*, Phys. Rev. Lett. **99**, 151801, (2007); CDF Collaboration, T. Aaltonen *et al.*, Phys. Rev. D **77**, 112001, (2008).

64. SLD Collaboration, K. Abe *et al.*, Phys. Rev. Lett. **84**, 5945-5949, (2000); Phys. Rev. Lett. **86**, 1162-1166, (2001).

65. NuTeV Collaboration, G.P. Zeller *et al.*, Phys. Rev. Lett. **88**, 091802, (2002).

66. C. N. Yang and R. Mills, *Conservation of Isotopic Spin and Isotopic Gauge Invariance*, Physical Review **96**, 191, (1954).

67. A. Sirlin, Physical Review D **22**, 971, (1980).

68. P. Chankowski *et al.*, Nucl. Phys. B **417**, 101 (1994); D. Garcia and J. Sola, Mod. Phys. Lett. A **9**, 211 (1994); A. Dabelstein, W. Hollik and W. Mosle, *Perspectives for Electroweak Interactions in e^+e^- Collisions*, edited by B.A. Kniehl, World Scientific Singapore, 345 (1995); D. Pierce *et al.*, Nucl. Phys. B **491**, 3 (1997).

69. J.M. Campbell, J.W. Houston and W.J. Stirling, *Hard Interactions of Quarks and Gluons: a primer for LHC physics*, Rep. Prog. Phys. **70**, 89-193, (2007).

70. W.K. Tung, *Perturbative QCD and the Parton Structure of the Nucleon.*

71. G.A. Ladinsky and C.P. Yuan, Physical Review D **50**, 4239 (1994).

72. P.B. Arnold and R.P. Kauffman, Nuclear Physics B **349**, 381 (1991).

73. P.B. Arnold and M.H. Reno, Nuclear Physics B **319**, 37 (1989); Nuclear Physics B **330**, 284E (1990).

74. J.C. Collins and D.E. Soper, Nuclear Physics B **193**, 381 (1981); Nuclear Physics B **213**, 545E (1983); J.C. Collins, D.E. Soper and G. Sterman, Nuclear Physics B **250**, 199 (1985).

75. G. Altarelli *et al.*, Nuclear Physics B **246**, 12 (1984).

76. D.E. Soper, *Basics of QCD Perturbation Theory*, arXiv:hep-ph/9702203 v1, (1997).

77. Tevatron Electroweak Working Group, URL (http://tevewwg.fnal.gov/wz/).

78. J. C. Collins, *Renormalization*, Cambridge University Press, Cambridge (1994).

79. J. Pumplin, D.R. Stump, J. Huston, H.L. Lai, P. Nadolsky and W.K. Tung, JHEP **0207**, 012 (2002). [e-print Archive hep-ph/0201195].

80. A.D. Martin, R.G. Roberts, W.J. Stirling and R.S. Thorne, Eur. Phys. J. C **4**, 463 (1998). [arXiv:hep-ph/9803445].

81. D. Stump *et al.*, *Inclusive jet production, parton distributions, and the search for new physics*, JHEP **0310**, 046 (2003). [e-Print Archive hep-ph/0303013].

82. G. Sterman, Nuclear Physics B **281**, 310 (1987).

83. S. Catani and L. Trentadue, Nuclear Physics B **327**, 323 (1989).

84. S. Catani and L. Trentadue, Nuclear Physics B **353**, 183 (1991).

85. G. Parisi and R. Petronzio, Nuclear Physics B **154**, 427 (1979).

86. J.C. Collins and D.E. Soper, Nuclear Physics **197**, 446 (1982).

87. C. Balazs and C.P. Yuan, Physical Review D **56**, 5558 (1997).

88. C. Davies, B. Webber and W.J. Stirling, Nuclear Physics B **256**, 413 (1985); C. Davies and W.J. Stirling, Nuclear Physics B **244**, 337 (1984);

89. T. Cole *et. al.*, *Technical Report*, Fermilab TM-1909, (1994).

90. S. Mishra, *Presented at Particle Accelerator Conference (PAC 03)*, Fermilab CONF-03-194, (2003).

91. DØ Collaboration, V.M. Abazov *et al.*, *The Upgraded DØ Detector*, Nucl. Instrum. Methods in Phys. Res. A **565**, 463 (2006).

92. United Technologies Microelectronics Center, Inc. is not part of Aeroflex.

93. E. Kajfasz, *The DØ Silicon Microstrip Tracker for Run IIa*, February 27, 2003.

94. A.G. Degussa, Düsseldorf, Germany, URL (www.rohacell.com).

95. M.D. Petroff and M.G. Stapelbroek, IEEE Trans. Nucl. Sci. NS-36, 158 (1989).

96. M.D. Petroff and M. Atac, IEEE Trans. Nucl. Sci. NS-36, 163 (1989).

97. A. Bross *et al.*, Nucl. Instr. and Meth. A **477**, 172 (2002).

98. Altera Corporation, 101 Innovation Drive, San Jose, CA 95134, document part number DS-F10K-4.2, URL (www.altera.com).

99. Xilinx, Inc., 2100 Logic Drive, San Jose, CA 95124-3400, URL (www.xilinx.com).

100. S. Rapisarda, N. Wilcer and R. Yarema, IEEE Trans. Nucl. Sci. NS-50, 878 (2003).

101. J.R. Vlimant, U. Bassler, G. Bernardi and S. Trincz-Duvoid, *Technical description of the T42 algorithm for the calorimeter noise suppression*, DØ Note 4146, (2003).

102. D. Edmunds, M. Johnson, R.D. Schamberger, *"Purple Haze" Noise*, DØ Note 5829, (2009).

103. U. Baur, *Measuring the W Boson mass at Hadron Colliders*

104. The DØ W mass group, *W mass measurement in Full Geant Monte Carlo*, DØ Note 5659, (2008).

105. LEP Electroweak Working Group, URL (http://lepewwg.web.cern.ch/LEPEWWG/).

106. F. James, *MINUIT - Function Minimization and Error Analysis*, Ver. 94.1 (1998).

107. T. Sjöstrand *et al.*, *High-Energy-Physics Event Generation with PYTHIA 6.1*, Computer Phys. Commun. **135**, 238 (2001).

108. R. Brun and F. Carminati, *CERN Program Library Long Writeup*, W5013, 1993 (unpublished).

109. P. Petroff and J. Stark, *Proposal to perform a blind measurement of the W mass in Run II*, DØ Note 5388, (2007).

110. M. Wetstein, *Using the* `wzfitter` *Utility*, DØ Note 5663 (2007).

111. C. Grupen, *Particle Detectors*, Cambridge University Press (1996).

112. D. Green, *The Physics of Particle Detectors*, Cambridge University Press (2005).

113. E. Fermi, *Über die Theorie des Stoßes zwischen Atomen und elektrisch geladenen Tilchen*, Z. Phys. **29**, 315-327 (1924).

114. C.F. von Weizsäcker, *Ausstrahlung bei Stößen sehr schneller Elektronen*, Z. Phys. **88**, 612-625 (1934).

115. E. J. Williams, *Correlation of Certain Collision Problems with Radiation Theory*, Kgl. Danske Videnskab. Selskab Mat.-fys. Medd. **13**, No. 4 (1935).

116. H. Greenlee, *The DØ Kalman Track Fit*, DØ Note 4303 (2003).

117. A. Schwartzman and M. Narain, *Vertex Fitting by means of the Kalman Filter technique*, DØ Note 3907 (2001).

118. J. Zhu, *Direct Measurement of the W Boson Decay Width in Proton-Antiproton Collisions at* $\sqrt{s}$ *=1.96 TeV*, Ph.D. Thesis, (2004).

119. G. Grindhammer and S. Peters, *The Parameterized Simulation of Electromagnetic Showers in Homogeneous and Sampling Calorimeters*, hep-ex/0001020 (1993).

120. G. Grindhammer, M. Rudowicz, and S. Peters, Nucl. Instrum. Meth. A **290**, 469, (1990).

121. W. R. Nelson, H. Hirayama and D.W.O. Rogers, *The EGS4 Code System*, SLAC-265, Stanford Linear Accelerator Center (1985).

122. D.E. Wagoner and D.J. Judd, *Using the EGS Electromagnetic Shower Simulation Program for SSC Calculations*

123. J. Stark, *A few questions and comments on ICD data quality*, Calorimeter Operations Meeting, August 25, 2005, Fermilab.

124. J. Hays *et al.*, *Electron Trigger Efficiencies using Calorimeter Information in p17 Data*, DØ Note 5138, (2006).

125. J. Andr and T. Sjöstrand, *Matching of matrix elements and parton showers*, Phys. Rev, D **57**, 5767-5772, (1998).

126. M. Lefebvre, *QCD Multijet Event Generation*, October 25, 2006.

127. M.H. Seymour, *Matrix-Element Corrections to Parton shower Algorithms*, hep-ph 9410414.

128. D.E. Soper, *The physics of parton showers* , CTEQ School, Madison, June 2009.

129. J. Heinonen, *Monte Carlo Simulations:Partons, Showers and all that*, April 2, 2009.

130. U. Baur, S. Keller and D. Wackeroth, Phys. Rev. D **59**, (1999).

131. U. Baur, S. Keller and D. Wackeroth, *A Monte Carlo program for the calculation of electroweak radiative corrections to Z boson production at hadron colliders*.

132. E. Barbiero and Z. Was, *PHOTOS: A Universal Monte Carlo for QED radiative corrections*, Version 2.0, Comput. Phys. Commun **79**, 291, (1994).

133. S.D. Drell and T.M. Yan, *Massive Lepton-Pair Production in Hadron-Hadron Collisions at High Energies*, Physical Review Letters **25** (5), 316-320 (1970).

134. J. Zhu, *The* `wzepmcs` *simulation package"*, DØ Note XXXX (2008).

135. H. Schellman, *The longitudinal shape of the luminous region at DØ*, DØ Note 5142, (2006).

136. J. Stark, *Manoeuvre critique:Status of fast/full MC comparison*, W Mass Meeting, May 23, 2007, Fermilab.

137. H. Schellman and D. Chapin, *Biases in calorimeter phi*, W/Z to Electrons Meeting, March 23, 2004, Fermilab.

138. H. Schellman and D. Chapin, *Study of shower centroid bias in ϕ - Version 0.0*, DØ Note XXXX (March 22, 2004).

139. M. Hildreth, J. Hobbs, J. Osta, H. Schellman, J. Stark and J. Zhu, *Studies of EM PhiMod efficiency and shift for M_W Measurement*, DØ Note 5914, (2009).

140. T. Andeen, F. Guo, J. Guo and J. Zhu, *Effect of Recoil on Electron Identification Efficiency*, DØ Note 5686, (2008).

141. T. Andeen and A. Melnitchouk, *Fit for the Electron Response Model* DØ Note 5662, (2008).

142. A. Melnitchouk and M. Wetstein, *Determination of the constant term of the electron resolution*, DØ Note 5879, (2009).

143. T. Andeen, M. Cwiok, J. Guo, J. Hobbs, J. Osta, J. Stark and J. Zhu, *Modeling the Hadronic Recoil for the W Mass Measurement in Run IIa*, DØ Note 5668, (2008).

144. F. Guo, J. Hobbs, R. McCarthy, P. Petroff, M. Rijssenbeek, J. Stark and J. Zhu, *Studies of energies below electron window for W mass measurement*, DØ Note 5661, (2008).

145. J. Guo, J. Zhu, J. Hobbs and R. McCarthy, DØ Note 5665, (2008).

146. J. Hays, J. Mitrevski, C. Schwanenberger and T. Toole, *Single Electron Efficiencies in p17 Data and Monte-Carlo Using p18.05.00 d0correct* , DØ Note 5105, (2006).

147. The DØ W mass group, *Measurement of the W Boson mass using Run IIa Data*, DØ Note 5868, (2009).

148. P.R. Bevington, *Data Reduction and Error Analysis for the Physical Sciences*, Mc-Graw Hill Inc.

149. J. Guo, J. Zhu, J. Hobbs and R. McCarthy, *PDF Uncertainty for W Mass Measurement*, DØ Note 5078, (2006).

150. R. Brock, F. Landry, P. Nadolsky and C.P. Yuan, *Tevatron Run I Z boson data and Collins-Soper-Sterman Resummation Formalism*, Physical Review D **67**, 073016 (2003).

151. P. Nadolsky, *Theory of W and Z boson Production*, AIP Conf. Proc. **753**, 158 (2005).

152. C. Biscarat, *Calorimeter Operations Meeting*, September 7, 2007, Fermilab.

153. J. Stark and A. Melnitchouk, *CAL calibration meeting*, February 12, 2009, Fermilab.

154. L. Lyons *et al.*, *How to combine correlated estimates of a single physical quantity*, Nuclear Instruments and Methods in Physics Research A **270**, 110-117 (1998).

155. A. Valassi, *Combining correlated measurements of several different physical quantities*, Nuclear Instruments and Methods in Physics Research A **500**, 391-405 (2003).

156. The Tevatron Electroweak Working Group for the CDF and DØ Collaborations, it Updated Combination of CDF and DØ Results for the Mass of the W Boson, FERMILAB-TM-2439-E, (2009).

157. J. Osta, *Combination of the Run IIa W boson mass measurements*, DØ Note 5913, (2009).

This document was prepared & typeset with LaTeX 2_ε, *and formatted with* NDdiss2_ε *classfile (v3.0[2005/07/27]) provided by Sameer Vijay.*